Interactions in driven double quantum dots

Dissertation der Fakultät für Physik
der Ludwig-Maximilians-Universität München

vorgelegt von
Florian Forster
geboren in Essen

München, den 14. Dezember 2015

Erstgutachter:	PD Dr. Stefan Ludwig
Zweitgutachter:	Prof. Dr. Jan von Delft
Tag der mündlichen Prüfung:	12.02.2016

Inhaltsangabe

In dieser Doktorarbeit wurde die Wechselwirkung zwischen Elektronen in einem getriebenen Doppelquantenpunkt und seiner Umgebung untersucht. Ein Quantenpunkt ist eine nanoskopische Struktur, in der Elektronen in allen drei Raumrichtungen lokalisiert sind, sodass sie ähnlich wie in einem Atom ein diskretes Energiespektrum aufweisen. Dieses System kann benutzt werden, um fundamentale Quanteneigenschaften wie den Elektronenspin oder Superpositionszustände im Festkörper zu untersuchen. Die hier betrachteten Quantenpunkte wurden mittels Feldeffekt elektrostatisch in einem zweidimensionalen Elektronensystem basierend auf einer GaAs/AlGaAs-Heterostruktur defininiert. Diese Methode erlaubt Kontrolle über das Einschlusspotential der Elektronen, da die Elektrostatik über Spannungen an metallischen Gattern während des Experiments beeinflusst werden kann, sowie die direkte Messung von Elektronentransport durch die Quantenpunkte. In dieser Arbeit wurde ein System von zwei zu einem Doppelquantenpunkt gekoppelten Quantenpunkten studiert. Das theoretische Konzept des quantenmechanischen Zwei-Niveau-Systems kann durch bestimmte Kombinationen der Molekülzustände im Doppelquantenpunkt in guter Näherung realisiert werden. Doppelquantenpunkte stellen daher ein mögliches System zur Implementierung von Qubits im Kontext der Quanteninformationsverarbeitung dar. Da das Zwei-Niveau-System von seiner Umgebung jedoch nicht völlig isoliert ist, spielen Wechselwirkungen für die Zeitentwicklung des Quantenzustands im Festkörper eine wichtige Rolle.

Der erste Teil der Arbeit untersucht die Wechselwirkung von Zwei-Elektron-Spinzuständen in einem inhomogenen, d.h. am Ort der beiden Quantenpunkte unterschiedlichen, Magnetfeld. Dieses inhomogene Magnetfeld wurde erstmalig mit zwei eindomänigen magnetischen Gattern realisiert und mittels direkter Strommessung sowie Elektronspin-Resonanz charakterisiert. Da die Atome des GaAs-Kristalls, in dem der Doppelquantenpunkt realisiert ist, einen Kernspin aufweisen, können Elektronen in einem Quantenpunkt mit typischerweise 10^6 Kernspins über Hyperfeinwechselwirkung interagieren. Unter bestimmten Bedingungen können die Kernspins durch die Hyperfeinwechselwirkung dynamisch polarisiert werden, was im Hinblick auf die Wechselwirkung mit den Elektronen in semiklassischer Näherung als effektives Magnetfeld beschrieben werden kann. Wegen des komplexen elektronischen Spektrums der Quantenpunkte und der Vielzahl an Kernspins ergibt sich hieraus eine bislang noch nicht vollständig verstandene Dynamik, die zu verschiedenen Fixpunkten in der Polarisationsdynamik führt. Es gelang, verschiedene Fixpunkte durch Messung des effektiven Magnetfeldes mittels Elektronspin-Resonanz zu charakterisieren und mit ihrer Hilfe eine hohe Kernspin-Polarisation direkt nachzuweisen.

Der zweite Teil der Arbeit beschäftigt sich mit einem Qubit bestehend aus zwei gekoppelten Ladungszuständen, die mithilfe einer periodischen Gatterspannungsmodulation durch Landau-Zener-Übergänge in Superposition gebracht wurden. Die dadurch entstehenden Landau-Zener-Stückelberg-Majorana-Interferenzmuster wurden durch die Dekohärenz des Zwei-Niveau-Systems modifiziert. Es konnte gezeigt werden, dass die Ladungszustände in Quantenpunkten in erster Linie an Ladungsfluktationen in ihrer Nähe, sowie an das Phononenspektrum des Kristalls koppeln. Über ein theoretisches Modell, das die beiden auf sehr unterschiedlichen Zeitskalen stattfindenden Wechselwirkungen berücksichtigt, konnten die Interferenzmuster im Detail analysiert und die Kohärenzzeit des individuellen Qubits und die Dephasierung des Zeitensembles getrennt bestimmt werden, ohne dass auf eine experimentell kompliziertere Echomessung zurückgegriffen werden musste. Darüber hinausgehend wurde der Einfluss von komplexeren Antrieben auf das Interferenzmuster am Beispiel von bichromatischen Antrieben mit unterschiedlichen Frequenzverhältnissen und Phasenbeziehungen untersucht. Die Symmetrieeigenschaften der unterschiedlichen Interferenzmuster konnten auf die des jeweils zugrunde liegenden Antriebs zurückgeführt werden.

Contents

1 Introduction

> *If, in some cataclysm, all of scientific knowledge were to be destroyed, and only one sentence passed on to the next generations of creatures, what statement would contain the most information in the fewest words? I believe it is the atomic hypothesis [...] that all things are made of atoms – little particles that move around in perpetual motion, attracting each other when they are a little distance apart, but repelling upon being squeezed into one another.* (Richard Feynman [1])

It is this sentence that Richard Feynman put in the beginning of his famous Lectures on Physics with which he has influenced the perception of the world around us of a number of undergraduate students including myself. While the concept of atoms goes back to ancient philosophy, the starting point of the scientific atomic theory is often attributed to John Dalton in the early 1800s [2, p. 131]. In the following years, many observations could be explained by theories following from the atomic hypothesis and the classical Newtonian mechanics, such as the kinetic gas theory. However, a question which is not answered by the atomic hypothesis as phrased by Feynman remains: why do atoms actually do what they do, how do they interact, and do atoms consist maybe of other particles? In the beginning of the 20th century, this question lead to what is among the most significant achievements in modern science: the theory of quantum mechanics, which can describe physics on very small length scales comparable to the size of atoms and molecules. It has since then lead to numerous advances in understanding the atomic nature of matter and also shed light on the quantum world which continuously disappoints our intuitive expectations drawn from classical mechanics in exciting ways.

As building blocks of bulk materials, the physics of atoms is highly relevant for macroscopic solid state systems. The theory of quantum mechanics, which is able to predict the movement of electrons in semiconductors, enabled the development of what is perhaps the most influential technology in our everyday lives: the transistor. Its invention made a multitude of applications in electronic circuits possible, from simple switches built from a single transistor to modern microprocessors, highly integrated circuits composed of billions of transistors connected to a complex digital logic. Advanced fabrication techniques allow us nowadays to engineer artificial structures with nanometre precision. At the heart of this thesis is one of these artificial nano systems, the quantum dot. In a quantum dot, electrons are confined in all three spatial dimensions similar to an atom, and the fundamental quantum mechanics for these so called artificial atoms is the same as for actual atoms. Interestingly, we returned to a point similar to where quantum mechanics started over a hundred years ago; but as the modern fabrication techniques provide control over the confinement potential defining the quantum dots, their properties can be tailored. This makes quantum dots excellent model systems to research fundamental quantum mechanics, such as the spins of single electrons, superposition states, and multi-particle interactions in a solid state environment [3–5]. However, quantum dots are more than just model systems, as state-of-the-art experiments demonstrate a high degree of quantum control which makes them possible candidates for quantum bits (qubits), the analogue in quantum computing to the bit in boolean logic [6, 7].

While quantum dots exist in many realizations, the quantum dots investigated in this thesis are electrostatically defined in a semiconductor crystal [3]. This type of quantum dot is particularly suited for studying the transport of electrons through the quantum dot structure and offers a high degree of control over the confinement potential during the experiment. The thesis is devoted to interactions of electrons in a driven double quantum dot (DQD) with the solid state system the quantum dot is embedded in. It studies

the impact on the electron transport through the double quantum dot system, which is a system of two coupled quantum dots. More specific, I investigated the influence of an inhomogeneous magnetic field across the DQD produced by an on-chip nanomagnet in the regime of spin-dependent transport (Pauli spin blockade) by means of direct current measurements as well as electron spin resonance (chapter 5). With these methods, I also studied the electron-nuclear hyperfine interaction between the electrons in the DQD and the nuclei of the GaAs host crystal. Employing a dynamic polarization technique developed in a preceding PhD thesis [8], the polarization of the $\sim 10^6$ nuclear spins at the position of the double quantum dot exceeded 50% and, as a novel aspect in this structure, was also significant in its surroundings (chapter 6). The understanding of the nuclear dynamics is of high interest for quantum information applications, where the nuclear spins are the main decoherence source for spin qubits [9]. As a second part of this thesis, I probed the quantum coherence of charge states in a periodically driven double quantum dot utilizing Landau-Zener-Stückelberg-Majorana interference [10] of two-electron charge states. The charge states in this system are mainly influenced by two interactions: On the one hand, Coulomb interaction with fluctuating charges in the environment of the quantum dot, and electron-phonon interaction on the other hand. The applied method allows us to separate both contributions and identify the coherence time for the single qubit as well as the dephasing time of the time ensemble (chapter 7). Furthermore, I investigated the influence of more complex bichromatic drivings on the symmetry of the Landau-Zener-Stückelberg-Majorana interference patterns (chapter 8).

This thesis is written as a cumulative thesis, i.e. the main content of this work presented in chapters 5 to 8 consists of several articles published in peer-reviewed journals during the course of the PhD research. In the beginning, each of these chapters provides an overview about the contents of the respective publication. This overview is followed by a theory section which is intended to make the non-specialist reader familiar with the main aspects of the particular physics discussed later on in this chapter, and a section describing the measurement setup of the experiment. The complete list of publications is included in appendix D and also provides detailed information about the contribution of each author. Preceding this main part of the thesis is an introductory part structured as follows: First, I give an introduction to transport spectroscopy in quantum dots with the main focus on double quantum dots in chapter 2. This chapter is written with a broad readership in mind who might not be familiar with quantum dots or want to refresh their knowledge about the concepts used to describe the principal quantum dot physics. Chapter 3 explains the basic material system used to realize the double quantum dots studied in this thesis and contains an overview about the fabrication process with details on the fabrication of the single-domain nanomagnets. Chapter 4 covers the low-temperature measurement setup and concludes this part.

2 Transport spectroscopy of quantum dots

The confinement of a particle inside a potential with dimensions comparable to its De-Broglie wavelength is a text book example of quantum mechanics. It leads to the quantization of the particle's energy while the details of the spectrum depend on the form of the confinement potential. Electrons in quantum dots (QDs) are confined within all three spatial dimensions similar to an atom. In fact, even though there are quite large differences for example in size (~1 Å for an atom compared to ~100 nm for a QD), they share a lot of the electronic properties such as the shell-like filling according to Hund's rules, so that quantum dots are often referred to as artificial atoms [11].

2.1 Semi-classical description

2.1.1 Single quantum dots

While QDs exist in different realizations, the QDs investigated in this thesis are embedded in a semiconductor crystal. They are coupled via tunnel barriers to electron reservoirs with which electrons can be exchanged and which can be used to probe the electronic properties of the QD in transport experiments. Furthermore, the QD is coupled capacitively to metallic gates which can be used to tune the electrostatic energy inside the quantum dot with respect to the electron reservoirs. A straightforward approach to the understanding of the main features of the system is given by the constant interaction model. This model makes two assumptions [4]: First, the Coulomb interaction of electrons inside the dot with each other as well as with other charges outside of the QD can be parametrized by a single capacitive constant C. C is the sum of all capacitances between the dot and its environment, usually the source and drain contacts and multiple gates. Even though there is typically more than one gate present, we will simplify our model by capturing the influence of all gates in one representative gate. As the second assumption, the quantum mechanical single-particle spectrum with the energies ϵ_n is independent of these interactions. The electrostatic energy of n electrons in the quantum dot is given by

$$U(n) = \frac{[-en + (V_G C_G + V_L C_L + V_R C_R)]^2}{2C}, \tag{2.1}$$

where e is the electron charge, and V_i are voltages to the gate and contacts which are coupled to the QD by capacitances C_i, as depicted in the sketch 2.1(a) [3]. The chemical potential is a particularly useful concept for determining the electron ground state of the system as a function of external parameters, since the system to consider is the grand canonical ensemble of the QD connected to the leads. The chemical potential $\mu(n)$ of the electron n in the QD can be defined based on (2.1) as

$$\mu(n) = \epsilon_n + U(n) - U(n-1) = \epsilon_n + \frac{e^2}{C}(n - 1/2) - \frac{|e|}{C}(V_G C_G + V_L C_L + V_R C_R), \tag{2.2}$$

which is the energy needed to add the nth electron to the QD. Here, we included the quantum mechanical single-particle spectrum ϵ_n. Note that $\mu(n)$ is a discrete function of the particle number n, in contrast to the one of e.g. a Fermi liquid. A direct consequence of this relation is the possibility to modify the chemical potential inside the QD by changing the voltages V_i in the system. Here, we introduce the concept of a lever arm $\alpha_i = \partial\mu(n)/\partial V_i$ to relate a change in voltage to the change in chemical potential. From equation (2.2), we find $\alpha_i = -|e|C_i/C$. Only if the chemical potential of the dot is below or equal to one of the chemical

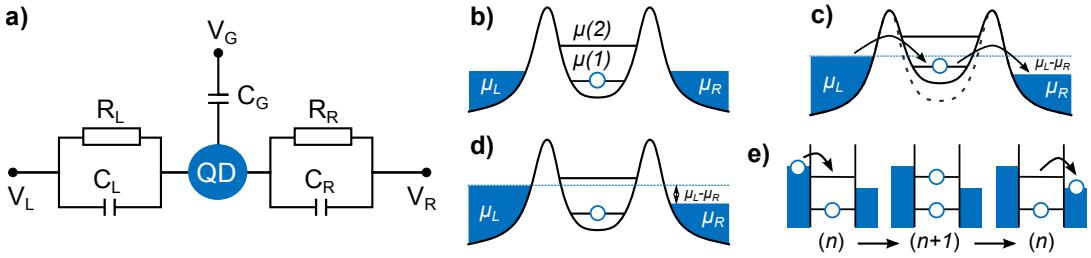

Figure 2.1: Semi-classical model of a single quantum dot. (a) Equivalent circuit of a quantum dot (blue) coupled to a gate (index G), a left (L) and a right (R) reservoir at voltages V_i. The capacitive coupling constants are denoted by C_i. The reservoirs are also coupled resistively by R_i to the quantum dot which enables electron exchange under the conditions sketched in (d, e). (b) Sketch of the quantum dot with the chemical potential of two electron levels μ_1 and μ_2 and the tunnel barriers connecting the dot to the two reservoirs. Only the first level is occupied by an electron (blue circle) since its chemical potential lies beneath the one of the reservoirs. (c) The same as (b) but with $\mu_L - \mu_R > 0$. Electrons can be exchanged between the two reservoirs via the electron states n for which $\mu_L > \mu_n > \mu_R$ is valid. The dashed gray line shows the confinement potential of (d), where the chemical potentials inside the dots are shifted by a gate voltage V_G. (d) Coulomb blockaded quantum dot, where no electron state is energetically available for transport. (e) Reduced scheme of the $(n) \rightarrow (n+1) \rightarrow (n)$ electron transport cycle, where n denotes the number of electrons in the dot. In the reduced scheme, tunnel barriers are drawn as vertical lines and not necessarily all n states are shown.

potentials of the reservoirs, i.e. $\mu(n) \leq \mu_{L,R}$, an electron will eventually tunnel from the correspondent reservoir into the dot. Figure 2.1(b) shows an example of a few-electron dot with two electron states, where $\mu(1)$ is occupied but $\mu(2)$ remains unoccupied. In the same spirit, if one of the reservoirs' chemical potentials is lower or equal compared to the one inside the dot, i.e. $\mu(n) \geq \mu_{L,R}$, the electron occupying the nth level will move out of the quantum dot into the reservoir. By modifying the chemical potential of the dot, the number of electrons inside the dot can be tuned from hundreds of electrons down to a single one [12].

We define the charging energy E_C as difference between the chemicals potentials of n and $n+1$ electrons on the QD,

$$E_C(n) = \mu(n+1) - \mu(n) = \frac{e^2}{C} + \Delta\epsilon,$$

where $\Delta\epsilon = \epsilon_{n+1} - \epsilon_n$ is the contribution of the single-particle spectrum. For lateral QDs discussed in this thesis, the Coulomb energy e^2/C of around 1–10 meV is typically more than a magnitude larger than the contribution of the single-particle spectrum and hence clearly dominates the level splitting [12] so that we can neglect $\Delta\epsilon$ in most of our discussions such that E_C is independent of n. To resolve the spectrum of a QD, the broadening of the single electron levels in the QD has to be smaller than E_C. For the conditions of the experiment, this implies a low noise level, suitable tunnel barriers (lifetime broadening), and that the Fermi edge in the leads is sufficiently sharp, i.e. $k_B T \ll E_C$ [(1)], which means cryogenic temperatures $T \lesssim 1\,\mathrm{K}$.

Electrons can be exchanged from one to the other reservoirs by sequential tunnelling through the QD, if one or more electron states are energetically between the chemical potentials of the reservoirs, i.e. $\mu_L > \mu(n) > \mu_R$ [figure 2.1(c)] or $\mu_L < \mu(n) < \mu_R$. The size of this current is determined by the time scales of the individual electron transfer processes from and to the reservoirs, modelled semi-classically by the size of the resistors $R_{L,R}$ and capacitances in figure 2.1(a). A very distinct feature of the current is the so called Coulomb blockade which is a direct consequence of the large charging energy E_C. If the difference of the chemical potentials of the reservoirs, realized by a bias voltage $e(V_L - V_R) = \mu_L - \mu_R \neq 0$, is fixed and much smaller than the charging energy, this condition is only satisfied at very distinct gate voltages. So whenever $|e|(V_L - V_R) \ll E_C$ is valid, the system is in a blockaded state for most gate voltages, where no first-order current will flow despite of an applied bias. Figure 2.2(a) shows a typical measurement of the gate voltage

[(1)] k_B denotes the Boltzmann constant.

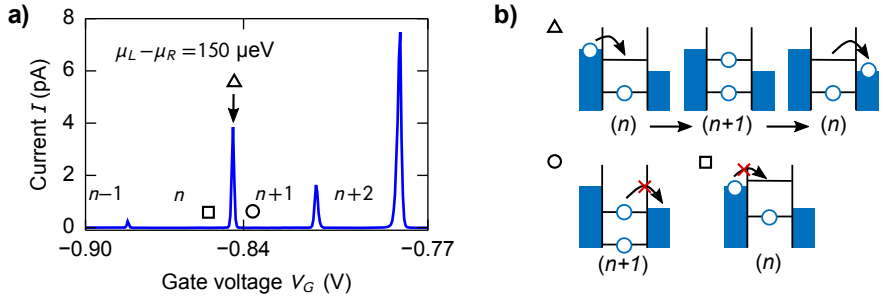

Figure 2.2: (a) Measurement of the gate voltage dependent current through a single QD. The inset numbers indicate the numbers of electrons in the ground state. At most gate voltages, current is suppressed due to the Coulomb blockade which is only lifted at the transition of the electronic ground states. The dot's state at the position of the markers is sketched in (b). (b) Chemical potentials at the voltages marked in (a). Circular and square markers: The chemical potential of the electron is too low to find an unoccupied state, hence the electron cannot move into (square) or out of (circle) the dot (Coulomb blockade). Triangular marker: The chemical potentials of the reservoirs and the dots are aligned accordingly, such that the Coulomb blockade is lifted.

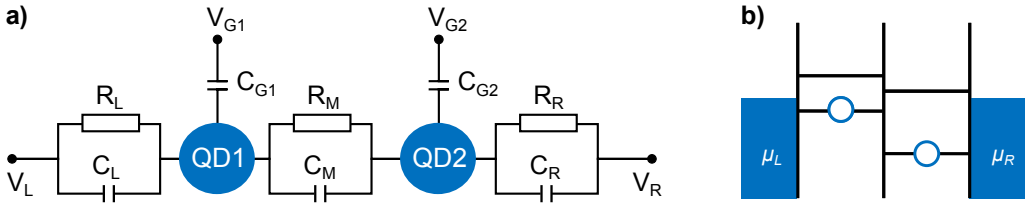

Figure 2.3: Model of a double quantum dot. (a) The equivalent circuit of the single quantum dot (QD1) in figure 2.1(a) is extended by a second quantum dot (QD2) which leads to a series of two QDs connecting the two reservoirs. The quantum dots are coupled by the capacitance C_M and resistance R_M which enables tunneling of the electrons between the dots. (b) Scheme of the chemical potentials for a DQD and its leads similar to figure 2.1(e).

dependency of current through a QD. It shows the characteristic features of large regions of V_G in which no current flows due to the Coulomb blockade in addition to very distinct current peaks separated by ΔV_G for which holds $\alpha_G \Delta V_G = E_C$, as sketched in figure 2.2(b).

2.1.2 Double quantum dots

A straightforward extension of a single quantum dot is the combination of two quantum dots to a double quantum dot (DQD) connecting the two reservoirs in series. Extending the single QD discussed above, each quantum dot is now coupled to a gate, to one of the reservoirs and to the other quantum dot as depicted in the equivalent circuit diagram 2.3(a). The derivation of the lengthy term for the electrostatic energy can be found in many review papers, e.g. in reference [3, p. 20], and is omitted here. The chemical potential μ_i of dot i[(2)] with the electron occupation (n_1, n_2) can be calculated to

$$\begin{aligned}
\mu_1(n_1,n_2) &= \left(n_1 - \frac{1}{2}\right) E_{C1} + n_2 E_{CM} - \frac{1}{|e|}\left(C_{G1} V_{G1} E_{C1} + C_{G2} V_{G2} E_{CM}\right) \\
\mu_2(n_1,n_2) &= n_1 E_{CM} + \left(n_2 - \frac{1}{2}\right) E_{C2} - \frac{1}{|e|}\left(C_{G1} V_{G1} E_{CM} + C_{G2} V_{G2} E_{C2}\right) \\
\text{with} \qquad & E_{Ci} = \frac{e^2}{C_i}\left(1 - \frac{C_M^2}{C_1 C_2}\right)^{-1}, \quad E_{CM} = \frac{e^2}{C_M}\left(\frac{C_1 C_2}{C_M^2} - 1\right)^{-1},
\end{aligned}$$

[(2)] $i \in 1,2$

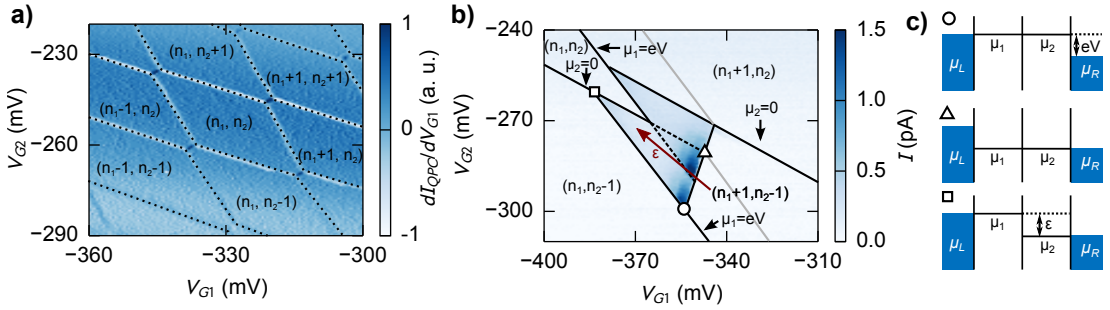

Figure 2.4: (a) Charge stability diagram of a GaAs-based double quantum dot investigated in section 5. (n_1, n_2) denotes the number of electrons in the ground state. Charge transition lines at which electrons are exchanged with the reservoirs are emphasized by dotted lines. (b) Triple points of a similar DQD as in (a) with a bias of 1 meV between the two reservoirs. Solid and dashed black lines mark the resulting current triangle originating from the alignment of the chemical potentials inside the quantum dot with the reservoirs. Labels for chemical potentials μ_i relate to the ground state of the charge diagram's section in which the labels are positioned. Gray lines mark the transition lines for $\mu_1 = V = 0$. The brown arrow marks the detuning axis ε. (c) Alignment of chemical potentials $\mu_1(n+1, n_2-1)$ and $\mu_2(n_1, n_2)$ for three special cases for the corresponding markers in (b). For the circle and the triangle markers, the detuning ε is zero and the chemical potentials are resonant with the one of the reservoirs. At the square marker, the detuning is equal to eV which is the largest detuning for which current can still be measured.

where C_i is the sum of all capacitances connected to dot i, e.g. $C_1 = C_L + C_{G1} + C_M$. E_{Ci} is the charging energy for each individual dot i, e.g. $\mu_1(n_1+1, n_2) - \mu_1(n_1, n_2) = E_{C1}$. The capacitive coupling between the quantum dots C_M has two effects: First, the chemical potential of one dot is dependent on the number of electrons in the other dot since electrons on the other quantum dot act like charges on a gate. Second, the gate of one dot is effectively cross-coupled to the other quantum dot meaning the chemical potential in each dot depends on both gate voltages. A finite C_M enables a finite E_{CM}, which is the electrostatic coupling energy, i.e. the change of energy in one dot when an electron is added to the other dot [4, p. 29]. For $C_M \to 0$, hence $E_{CM} \to 0$, all cross-coupling terms in (2.5) vanish and the relation (2.2) for the single dot is recovered.

The diagram showing the ground state configuration of the quantum dot in dependence of the gate voltages is called charge stability diagram. A non-vanishing C_M leads to a hexagonal pattern as depicted in figure 2.4(a). The lines separate regions of different electronic ground states, e.g. (n_1, n_2) and (n_1+1, n_2). Along lines with negative slope, the charging lines, emphasized by dotted lines in figure 2.4(a), the respective chemical potential inside one of the dots is equal that of the reservoir. The slope of the line gives information about which dot is affected: Lines with a steeper slope in figure 2.4(a) indicate a stronger coupling to V_{G1} marking a transition in QD1, whereas lines with a small slope indicate a stronger coupling to V_{G2} and hence mark transitions in QD2. The lines with positive slope at the narrowest region between two hexagons mark interdot transitions – along these lines, the chemical potentials of both dots are aligned and electrons can be exchanged between the dots. The size and the proportions of width and length of each individual cell depend on the lever arms connected to the capacitive constants and therefore the charging energies of the system and can be used to determine these constants for a real system. However, the exact procedure is quite technical and gives no further insight into the physical properties of the system. References [3, 13, 14] contain comprehensive summaries and step by step instructions how to carry out the energy calibration in detail.

The most prominent points of the charge stability diagrams are the connecting points of three neighbouring cells. At these so called triple points, the chemical potentials of both dots and both reservoirs are aligned. Since the current condition is similar as for the case of a single dot, e.g. current can only flow from the left to the right reservoir[3] if $\mu_L \geq \mu_1 \geq \mu_2 \geq \mu_R$, current can only occur in the vicinity of these triple points. Applying a bias between the two reservoirs will shift their chemical potentials and

[3] For a directed current, at least one condition must satisfy > if no other asymmetry exists in the system.

therefore also the charging lines in the stability diagram. For the simplest and experimentally most relevant case we consider a voltage $V = -(\mu_L - \mu_R)/e$ and assume $\mu_R = 0$ independent of V. This increases the chemical potential connected to QD1 and shifts all lines with steep slopes in figure 2.4(a) to the left by the energy $eV = \alpha_{G1}\Delta V_{G1}$ while leaving the lines with smaller slopes untouched as they belong to the dot connected to the other reservoir. This leads to triangular regions of allowed current around the triple points, as shown in figure 2.4(b). Each triangle belongs to a transport cycle involving the three charge configurations at the respective triple point; e.g. the lower triangle in figure 2.4(b) belongs to the cycle $(n_1, n_2) \rightarrow (n_1, n_2 - 1) \rightarrow (n_1 + 1, n_2 - 1) \rightarrow (n_1, n_2)$. Outside of the current triangles, the QD system remains in Coulomb blockade.

To understand the triangular shape, we look at the alignment of the chemical potentials inside the dots. Let us define the difference between the two chemical potentials inside the dots, $\mu_1 - \mu_2 = \varepsilon$, as detuning. Along the baseline of the triangle, the chemical potentials in both dots are equal and hence $\varepsilon = 0$. Starting at the lowest point of the baseline of a triangle (circle marker in figure 2.4(b)), μ_1 and hence also μ_2 is resonant with $\mu_L = eV$. By following the baseline, we shift μ_1 as well as μ_2 gradually down in energy by making both V_{G1} and V_{G2} more positive until we reach the other tip (triangular marker), where $\mu_2 = \mu_R = 0 = \mu_1$. At the tip opposing the baseline, the lines for $\mu_1 = eV$ and $\mu_2 = 0$ cross each other, marking the point of maximum detuning $\varepsilon = eV$ at which current is possible. The chemical potentials for the three configurations just discussed are sketched in figure 2.4(c). In general, along each line connecting the baseline and the tip the detuning increases linearly. For example, along the edge between the circle and the square marker in fig. 2.4(b), μ_2 is reduced from eV to 0 while μ_1 remains at eV. However, the symmetric case in which μ_1 is increased, $eV/2 \rightarrow eV$, and μ_2 is decreased, $eV/2 \rightarrow 0$, is often defined as the detuning axis ε. As a consequence of the symmetry, the line crosses the baseline exactly at the center, as depicted in figure 2.4(b) by a brown arrow. Note that only the transitions at $\varepsilon = 0$, i.e. the baseline of the current triangles, are elastic; so it is essential that the system is connected to a dissipative bath to comply with energy conservation for inelastic transitions at $\varepsilon > 0$.

2.1.3 Spin dependent transport

So far, we have neglected quantum mechanical properties to a large extent and reduced our considerations mainly to the Coulomb interaction between electrons on the dot. In fact, many features of the DQD system can be readily explained by this simplification, since the Coulomb interaction is by far the biggest energy scale in the system. Indeed, one has to look more closely to discover the intriguing and surprisingly complex influence of quantum mechanics. The first major step is to include the electron spin into the picture. This already leads to a multitude of consequences for the QD physics about which reference [4] gives a comprehensive overview. As a start, we focus on the phenomenon of Pauli spin blockade (PSB) which is a main feature for transport in the few electron regime of a DQD and remains important throughout all chapters of this thesis.

It is instructive to think again about QDs as artificial atoms. Just as real atoms form molecules, two QDs which are coupled to each other form a DQD system which is different from two separate single QDs. At this point, we focus on a DQD charged by two electrons, since this will be the relevant case for all our experiments.

To model the spin properties of our DQD system, we will separate its total quantum state $|\Psi\rangle$ into an orbital part and a spin part, such that $|\Psi\rangle = |\Psi_{\text{orbit}}\rangle \otimes \left|\Psi_{\text{spin}}\right\rangle$. $|\Psi_{\text{orbit}}\rangle$ is determined primarily by the confinement potential and therefore the Coulomb interaction, while all the spin physics is included in $\left|\Psi_{\text{spin}}\right\rangle$. In the following, I will briefly recapitulate the main properties for a system of two indistinguishable spin-1/2 Fermions, such as the two interacting electrons inside a DQD. The derivation and a more comprehensive discussion of these properties can be found in any standard text book of quantum mechanics, for instance in reference [15, p. 997ff].

We use the expressions $|\uparrow\rangle$ for a spin-up state, and $|\downarrow\rangle$ for a spin-down state in Dirac notation. Two-particle

spin states are mathematically described by the tensor product of the single spins; $|\uparrow\rangle \otimes |\downarrow\rangle \equiv |\uparrow\downarrow\rangle$ for example denotes a spin-up state of the first particle and a spin-down state of the second particle. The quantum mechanical operator associated with a spin-1/2 particle is $\mathbf{s}_i = \frac{h}{2}\boldsymbol{\sigma_i}$, where $\boldsymbol{\sigma_i}$ can be represented by a vector of Pauli matrices in the Cartesian basis, which satisfy the standard commutation relations of a momentum operator. Since the particles are indistinguishable and form a two-electron state, the accessible commuting observables are not the individual spins, but the total spin of the system and its projection on one axis, commonly to be chosen as z-axis. The operator for two spin-1/2 particles is just the sum of two spin operators, each acting on the subspace of its own spin, $\mathbf{s} = \mathbf{s_1} + \mathbf{s_2}$. While the states $|\uparrow\uparrow\rangle$, $|\uparrow\downarrow\rangle$, $|\downarrow\uparrow\rangle$, $|\downarrow\downarrow\rangle$ are the eigenstates of the spin projection operator $s_z = s_{1,z} + s_{2,z}$, where $s_{i,z}$ is the spin projection operator for the electron i, the situation is more difficult for the total spin angular momentum, $\mathbf{s^2} = (\mathbf{s_1} + \mathbf{s_2})^2$. The diagonalization of this operator, which is carried out as a part of appendix A.2, yields its four eigenstates, namely

$$\begin{aligned} |T_+\rangle &= |\uparrow\uparrow\rangle, \\ |T_0\rangle &= \frac{1}{\sqrt{2}}(|\uparrow\downarrow\rangle + |\downarrow\uparrow\rangle), \\ |T_-\rangle &= |\downarrow\downarrow\rangle, \\ |S\rangle &= \frac{1}{\sqrt{2}}(|\uparrow\downarrow\rangle - |\downarrow\uparrow\rangle). \end{aligned} \tag{2.6}$$

The quantum number s commonly defined for each state is connected to the eigenvalue of the total spin operator, $\mathbf{s}^2 \left|\Psi_{\text{spin}}\right\rangle = s(s+1)\hbar^2 \left|\Psi_{\text{spin}}\right\rangle$. The three states $|T_\pm\rangle$ and $|T_0\rangle$ are called triplet states with $s = 1$, and therefore have a finite total spin momentum. The state $|S\rangle$, a singlet, has the quantum number $s = 0$ and its total spin therefore vanishes. In the same spirit, the quantum number m is connected to the eigenvalue of the spin projection, $s_z \left|\Psi_{\text{spin}}\right\rangle = m\hbar \left|\Psi_{\text{spin}}\right\rangle$. For $|T_+\rangle$, both spins add up to $m = 1$, whereas $|T_-\rangle$ with both spins pointing in the other direction yields $m = -1$. For $|T_0\rangle$, the z-components of the spin cancel each other such that $m = 0$. For $|S\rangle$, the total spin momentum is 0 and therefore the projection onto the z-axis also vanishes, $m = 0$.

The triplet states of equation (2.6) are symmetric with respect to the exchange of the two spins, while the singlet state is antisymmetric. Since the entire wavefunction $|\Psi\rangle$ is always antisymmetric due to the Pauli principle of Fermions, the symmetry of $|\Psi_{\text{orbit}}\rangle$ and the symmetry of $\left|\Psi_{\text{spin}}\right\rangle$ depend on each other. If one is symmetric, the other one must be antisymmetric to achieve antisymmetry in $|\Psi\rangle$. This directly implies an exchange energy difference J between the singlet and the triplets due to their orbital wavefunctions. In the systems discussed in this thesis, this exchange energy is positive such that triplets have a higher energy than singlet states at zero magnetic field. In the following and throughout the thesis, we will denote the total wavefunction just by their spin part, albeit that *singlet* has to be read as *singlet state including its orbital part*.

In summary, the inclusion of spin to the system yields for each occupation configuration four different two-electron spin states that make up the lowest-lying energy eigenstates: For two electrons, the orbital part is either (2,0), (1,1) or (0,2), adding up to a total of 12 eigenstates. At zero magnetic field, the three triplet states of each occupation configuration are degenerate and separated from the singlet state by the exchange energy. The exchange energy of the (2,0) and (0,2) states, where both electrons are confined to a single dot, is significantly larger than the one of the (1,1) states, since the exchange energy increases with the overlap of the two-electron wavefunctions.

Even if no magnetic field is present, the existence of singlet and triplet states has a severe impact on the electron transport. The main reason is the selection rule which forbids transitions between pure singlet and triplet states in first order, because of spin angular momentum conservation. First, we consider the transport cycle of a two-electron double quantum dot $(2,0) \rightarrow (1,1) \rightarrow (1,0) \rightarrow (2,0)$ as depicted in fig. 2.5(a). Here, the current remains undisturbed compared to the case without spin discussed before, since the triplet

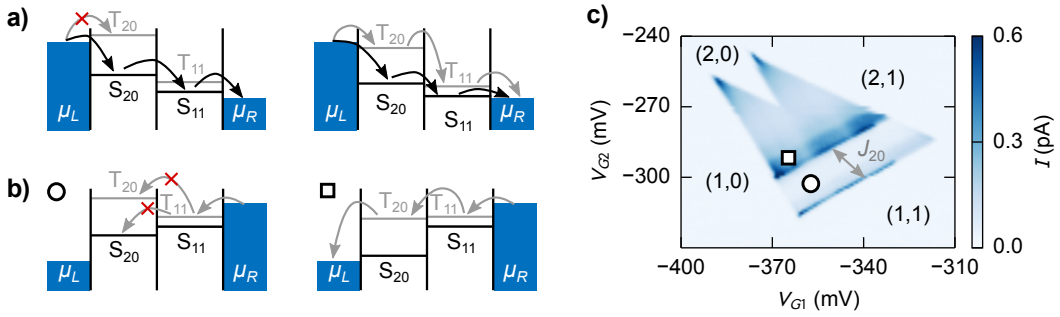

Figure 2.5: (a) Transport cycle for a two-electron DQD for the sequence $(2,0) \rightarrow (1,1) \rightarrow (1,0) \rightarrow (2,0)$. Triplets T_{20} and singlet S_{20} are separated by a large exchange energy J_{20}. Left panel: T_{20} is not in the bias window $\mu_L - \mu_R$; only singlet states contribute to transport. Right panel: T_{20} is now inside the bias window and can contribute to the transport. (b) Reverse bias as in (a) leading to the transport cycle $(1,1) \rightarrow (2,0) \rightarrow (1,0) \rightarrow (1,1)$. Left panel: Eventually the triplet T_{11} is occupied blocking further transport since T_{20} are energetically not accessible and the transition between pure singlet and triplet states is forbidden (Pauli spin blockade). Right panel: Lifting of the Pauli spin blockade when T_{20} has a lower chemical potential than T_{11}. (c) Charge stability diagram similar to fig. 2.4(b) in the presence of Pauli spin blockade (almost vanishing current in the lower region of the triangle). Markers correspond to the sketches of (b). The exchange interaction of the singlet and triplet (2,0) states is marked by J_{20}.

state T_{20} either is not accessible (left panel of fig. 2.5(a)) and the transport only involves singlet states or can transition to the triplet T_{11} state due to the lower exchange energy J_{11} (right panel). The situation changes drastically for the reverse transport cycle, namely $(1,1) \rightarrow (2,0) \rightarrow (1,0) \rightarrow (1,1)$. The initial (1,1) occupation can either be S_{11} or T_{11} with equal probability in good approximation. If the initial state is S_{11}, it can transition to S_{20} and contribute to the current as before. However, if the initial state is T_{11}, it can neither transition to T_{20} due to the high exchange energy J_{20}, nor to a singlet because of the selection rule of spin conservation. Since the electron cannot leave the QD and no other electron can enter because of the charging energy, T_{11} becomes a metastable state which will eventually block the current as shown in the left panel of figure 2.5(b). This so called Pauli spin blockade is visible as a region of highly suppressed current at the lower part of the stability diagram in 2.5(c) (marked by a circle). For higher detuning ε, T_{20} enters the transport window and lifts the blockade [right panel in 2.5(b)] resulting again in a sizeable current in the upper part of the current triangle in 2.5(c) (marked by a square). Since $J_{20} \gg J_{11}$, the region of suppressed current is mainly given by J_{20} as indicated in figure 2.5(c) by a grey arrow.

Importantly, there are mechanisms to lift the Pauli spin blockade even if T_{20} remains energetically inaccessible. The main mechanisms include the presence of an inhomogeneous magnetic field across the DQD [16], hyperfine interaction between the DQD's electrons and the nuclei of the host material [17] , and co-tunneling via the energetically forbidden T_{20} state [18]. In all presented experiments, the DQD was tuned to be only weakly coupled to the leads, such that the latter is only a minor effect compared to the others: The inhomogeneous magnetic field, which is provided by on-chip single-domain nanomagnets in the vicinity of the DQD, is by far the largest contribution and will be discussed in section 2.2.2. The lifting of PSB via hyperfine interaction provides the exciting possibility to manipulate the state of the nuclear spins of the host material and is a topic of chapter 6.

2.2 Quantum mechanical description of a two-electron double quantum dot

We will now discuss the quantum mechanical description of our two-electron DQD in the local basis $\{|T_+\rangle, |T_0\rangle, |T_-\rangle, |S_{11}\rangle, |S_{20}\rangle\}$. Here, the three triplet states are the triplet states of the (1,1) occupation and we neglect the triplets (2,0) due to their large exchange energy as discussed before, because we only work

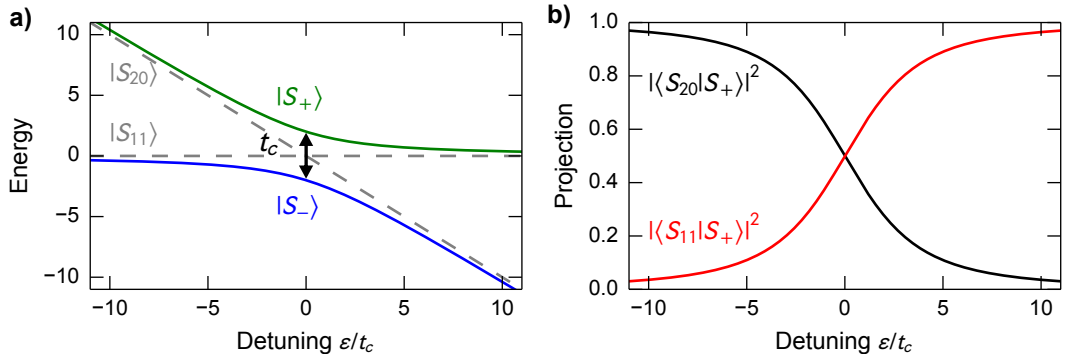

Figure 2.6: (a) Term scheme of a two-level system where the basis states $|S_{20}\rangle$ and $|S_{11}\rangle$ are coupled to each other by a coupling t_c (see Hamiltonian (2.7)). Eigenstates in eq. (2.8) are shown in green and blue, the unperturbed levels are shown in grey and form asymptotes to the eigenstates. (b) Projection of the eigenstate $|S_+\rangle$ onto the basis states. For $|S_-\rangle$, the projections are equal with respect to the other eigenstate, e.g. $|\langle S_{11}|S_-\rangle|^2 = |\langle S_{20}|S_+\rangle|^2$.

in the regime of $\varepsilon < J_{20}$. We will also approximate $J_{11} \approx 0$ which otherwise would cause a small shift of the triplet energies. We already introduced the detuning ε as difference between the two chemical potentials of the quantum dot during the semi-classical description of the DQD. We now denote it more precisely as the energy difference between the two singlet states, $\varepsilon \equiv E(S_{11}) - E(S_{20})$ and will further choose our energy scale such that $E(S_{11}) \equiv 0$.

2.2.1 Tunnel coupling

First, we will take into account the possibility of electrons to tunnel from one dot to the other. This couples the two singlet states by a (real) coupling constant t_c, such that the two-level Hamiltonian in singlet subspace reads

$$H_{\text{el}} = -\varepsilon\,|S_{20}\rangle\langle S_{20}| + \frac{t_c}{2}\left(|S_{20}\rangle\langle S_{11}| + |S_{11}\rangle\langle S_{20}|\right) \doteq \begin{pmatrix} 0 & t_c/2 \\ t_c/2 & -\epsilon \end{pmatrix}, \tag{2.7}$$

where we chose the representation $|S_{11}\rangle \doteq \begin{pmatrix}1\\0\end{pmatrix}$ and $|S_{20}\rangle \doteq \begin{pmatrix}0\\1\end{pmatrix}$. Diagonalizing this Hamiltonian yields the two eigenstates $|S_\pm\rangle$ with their respective eigenvalues $\varepsilon_\pm$,

$$\begin{aligned} |S_+\rangle &= \sin\theta\,|S_{20}\rangle + \cos\theta\,|S_{11}\rangle, \quad \varepsilon_+ = \frac{1}{2}\left(-\epsilon + \sqrt{\varepsilon^2 + t_c^2}\right), \\ |S_-\rangle &= \cos\theta\,|S_{20}\rangle - \sin\theta\,|S_{11}\rangle, \quad \varepsilon_- = \frac{1}{2}\left(-\epsilon - \sqrt{\varepsilon^2 + t_c^2}\right), \end{aligned} \tag{2.8}$$

and $2\theta = \arctan(t_c/\varepsilon)$ (see appendix A.1 for details of the calculation). For a better understanding, these results are visualized in figure 2.6. We find that both eigenstates become equal to the basis states at high positive and negative detunings, e.g. for $\varepsilon/t_c \ll 0 \Rightarrow \theta \to \pi/2$, $|S_+\rangle \to |S_{20}\rangle$ and $|S_-\rangle \to |S_{11}\rangle$. We further find that each eigenstate undergoes a transformation from one basis state to the other basis state by increasing the detuning, e.g. $|S_+\rangle \to |S_{20}\rangle$ at high negative detuning becomes $|S_+\rangle \to |S_{11}\rangle$ at high positive detuning. At $\varepsilon = 0, \Rightarrow \theta \to \pi/4$, both eigenstates become superpositions with equal ratio of each basis state, as seen in panel (b). At this value, the eigenstates are $|S_\pm\rangle = 1/\sqrt{2}\,(|S_{20}\rangle \pm |S_{11}\rangle)$ and their energy splitting becomes minimal and equal to t_c.

In summary, the local basis states remain unperturbed for large detunings $|\varepsilon| \gg t_c$ and the coupling only plays a major role at small detunings $|\varepsilon| \lesssim t_c$, where the singlets form a so called avoided crossing and the singlet eigenstates become superposition of the local basis states (which are resonant at $\varepsilon = 0$). These avoided crossings are of crucial importance since they enable transitions between the local basis states, as

we will further discuss later. The Hamiltonian (2.7) is a representative example of quantum mechanical two-level systems, which are called qubits in the context of quantum computing.

2.2.2 Magnetic field

We will now introduce a magnetic field to our double quantum dot system. We allow the magnetic field to be different in each quantum dot, which yields the total energy of the two-electron spin system

$$H_{\mathrm{mag}} = \frac{g\mu_B}{\hbar}\left(\mathbf{B_1}\cdot\mathbf{s_1} + \mathbf{B_2}\cdot\mathbf{s_2}\right) = \frac{g\mu_B}{\hbar}\left[\overline{\mathbf{B}}\cdot(\mathbf{s_1}+\mathbf{s_2}) + \Delta\mathbf{B}\cdot(\mathbf{s_1}-\mathbf{s_2})\right], \tag{2.9}$$

where we defined $\overline{\mathbf{B}} = (\mathbf{B_1}+\mathbf{B_2})/2$ and $\Delta\mathbf{B} = (\mathbf{B_1}-\mathbf{B_2})/2$ and used the g-factor g and the Bohr magneton μ_B. We can calculate the representation of H_{mag} in the singlet-triplet basis of the (1,1) state, which is carried out in appendix A.2, and find

$$H_{\mathrm{mag}} \doteq g\mu_B \begin{array}{c} \begin{matrix} |T_+\rangle & |T_0\rangle & |T_-\rangle & |S_{11}\rangle \end{matrix} \\ \begin{pmatrix} \overline{B}_z & \overline{B}_-/\sqrt{2} & 0 & -\Delta B_-/\sqrt{2} \\ \overline{B}_+/\sqrt{2} & 0 & \overline{B}_-/\sqrt{2} & \Delta B_z \\ 0 & \overline{B}_+/\sqrt{2} & -\overline{B}_z & \Delta B_+/\sqrt{2} \\ -\Delta B_+/\sqrt{2} & \Delta B_z & \Delta B_-/\sqrt{2} & 0 \end{pmatrix} \end{array} \begin{matrix} |T_+\rangle \\ |T_0\rangle \\ |T_-\rangle \\ |S_{11}\rangle \end{matrix}$$

for the general case, where we used the abbreviations $\overline{B}_\pm = \overline{B}_x \pm i\overline{B}_y$ and $\Delta B_\pm = \Delta B_x \pm i\Delta B_y$. As the most important result, we find that the singlet and triplet subsystems are connected via the off-diagonal terms $\Delta B_\pm$ and ΔB_z, i.e. the inhomogeneous components of the magnetic field. Hence, the singlet $|S_{11}\rangle$ forms avoided crossings with all three triplets depending on different components of $\Delta\mathbf{B}$. It is important to understand that the triplet states chosen as basis were defined by the z-axis as the quantization axis of the system. This leads to the direct conclusion that transitions between the different triplet states are facilitated by $\overline{B}_\pm$. While this is true for chosen basis states, it can be misleading for the interpretation of our experiments: There, the eigenstates are defined by the sum field $\overline{\mathbf{B}}$ whose orientation might not be parallel to the z-axis and remains fixed on the time scale of the measurement. Therefore, it is more intuitive to define the quantization axis parallel to $\overline{\mathbf{B}}$, where the terms $\overline{B}_\pm$ vanish and the triplet states of our new basis are orthogonal. In this spirit, we can choose $\overline{\mathbf{B}}$ as the canonical quantization axis, and for the case of $\mathbf{B_1} = \mathbf{B_2}$ reduce H_{mag} to the simple Hamiltonian of two spin-1/2 particles in a magnetic field, yielding the singlet and triplet states of equation (2.6) as the eigenstates of the system. A finite $\Delta\mathbf{B}$, however, breaks the symmetry and introduces off-diagonal elements to the Hamiltonian coupling $|S_{11}\rangle$ to its triplets as discussed.

2.2.3 Energy spectrum

The Hamiltonian for the DQD system accounting for the electron spin in a magnetic field and the tunnel coupling between the dots is the sum of the two just discussed contributions H_{el} (2.7) and H_{mag}. In the singlet-triplet basis, where we defined the quantization axis of the triplets parallel to $\overline{\mathbf{B}}$, the Hamiltonian reads

$$H = H_{\mathrm{el}} + H_{\mathrm{mag}} \doteq g\mu_B \begin{array}{c} \begin{matrix} \left|\widetilde{T}_+\right\rangle & \left|\widetilde{T}_0\right\rangle & \left|\widetilde{T}_-\right\rangle & |S_{11}\rangle & |S_{20}\rangle \end{matrix} \\ \begin{pmatrix} \overline{B}_z & 0 & 0 & -\Delta B_-/\sqrt{2} & 0 \\ 0 & 0 & 0 & \Delta B_z & 0 \\ 0 & 0 & -\overline{B}_z & \Delta B_+/\sqrt{2} & 0 \\ -\Delta B_+/\sqrt{2} & \Delta B_z & \Delta B_-/\sqrt{2} & 0 & t_c/2g\mu_B \\ 0 & 0 & 0 & t_c/2g\mu_B & -\varepsilon/g\mu_B \end{pmatrix} \end{array} \begin{matrix} \left|\widetilde{T}_+\right\rangle \\ \left|\widetilde{T}_0\right\rangle \\ \left|\widetilde{T}_-\right\rangle \\ |S_{11}\rangle \\ |S_{20}\rangle \end{matrix}. \tag{2.10}$$

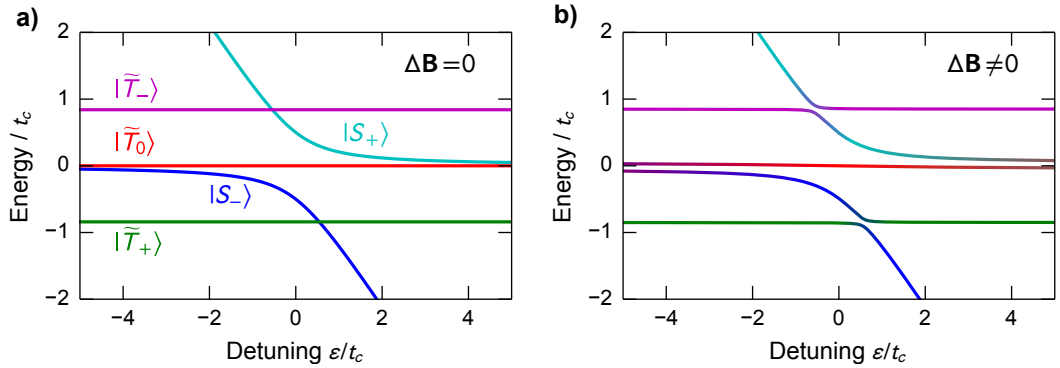

Figure 2.7: Eigenenergies of all energetically available states of a two-electron DQD calculated from Hamiltonian (2.10) with g=-0.36 of GaAs. (a) In a homogeneous magnetic field with $\overline{\mathbf{B}} = (0 \;\; 0 \;\; 200)^T$ mT, $\Delta\mathbf{B} = 0$, $t_c = 5\,\mu$eV. $|\widetilde{T}_\pm\rangle$ are split by the Zeeman energy, but the singlets do not mix with the triplets. (b) In an inhomogeneous magnetic field with $\overline{\mathbf{B}} = (0 \;\; 40 \;\; 205)^T$ mT, $\Delta\mathbf{B} = (0 \;\; 40 \;\; 5)^T$ mT, $t_c = 5\,\mu$eV. $|\widetilde{T}_\pm\rangle$ are split by the Zeeman energy, and the singlets mix with all triplets when their energies are close.

Without an inhomogeneous magnetic field, the terms with $\Delta\mathbf{B}$ vanish, the singlets are not coupled to the triplet subsystem, and the energies of singlets and triplets remain unperturbed as in the term-scheme of figure 2.7(a). The degeneracy of triplets, however, is still lifted by the Zeeman energy $g\mu_B|\overline{\mathbf{B}}|$. Figure 2.7(b) shows the term-scheme for a finite inhomogeneous field $\Delta\mathbf{B}$. Here, all triplets couple to the singlet subsystem via $|S_{11}\rangle$ and introduce avoided crossings. The avoided crossing between $|S_\pm\rangle$ and $|\widetilde{T}_0\rangle$ is mediated by the z-component of $\Delta\mathbf{B}$ and causes a splitting for $|\varepsilon| \gg t_c$. The x,y-components of $\Delta\mathbf{B}$ mix $|S_\pm\rangle$ and $|\widetilde{T}_\pm\rangle$. For a given t_c, the detuning ε at which these avoided crossings occur depends on the Zeeman energy and can hence be tuned by $\overline{B}_z$. This fact can be harnessed experimentally to measure t_c with a high precision [19], see also section 7. The coupling of the singlet and triplet states in general is an important property of the system and has lead to active research not only related to quantum information processing. At the time of this thesis, a variety of robust quantum gate operations has been demonstrated rendering a DQD system as one of the most important systems to explore the concepts of a quantum computer [20–22]. As a direct impact for the electron transport through a DQD, the Pauli spin blockade is partly lifted in the vicinity of the avoided crossings, since the pure singlets and triplets are no longer the eigenstates of the system. This leads to a complex dependency of the current on $\Delta\mathbf{B}$, $\overline{B}_z$, ε, and t_c, because the actual mixing depends on all of these parameters [17, 23], as will be discussed later in chapter 5.

3 System and fabrication process

All nano structures studied during this PhD thesis are fabricated in a top-down process starting from a semiconductor heterostructure. The band structure of the heterostructure is engineered to incorporate an intrinsic two-dimensional electron system (2DES) in a layer parallel to the surface. This electron system can be locally depleted by the field effect by applying voltages to gates on the wafer surface to build for instance one-dimensional channels or zero dimensional constrictions, i.e. quantum dots. Since the growth of such heterostructures itself is a complex research field and is constantly improved even after tens of years of experience, the wafers originate from collaborating research groups in Regensburg and Zürich.

3.1 Electron confinement

The aim of combining semiconducting materials with different electronic properties is the targeted design of a bandstructure with tailored properties. The main experiments presented in this thesis investigate quantum dots based on the GaAs/AlGaAs heterostructure shown in figure 3.1(a). The bandgap of pure GaAs (1.42 eV) can be increased by replacing a fraction of Ga with Al; in this case $Al_{0.3}Ga_{0.7}As$ with a bandgap of 1.79 eV is used [24]. Since the relative mismatch of the lattice constants is smaller than 10^{-3} [24], both materials can be grown epitaxially on top of each other facilitating a mono-crystalline structure with a low defect density.

The thus engineered conduction band forms a triangular confinement potential at the interface between the AlGaAs layer to the pristine GaAs as depicted in figure 3.1(a). The system is designed in such a way that the triangle potential's first subband energy lies below the Fermi energy E_F, is populated by charge carriers from the nearby silicon δ-doping, and forms a two-dimensional electron system 85 nm below the surface. Contact to the 2DES is provided by a eutectic AuGe composition deposited on the surface. The material is heated up to enable thermal diffusion of the metal down to the 2DES as sketched in figure 3.1(b). Inside the 2DES, local potential barriers can be created by applying negative voltages on nanometer-sized gates on top by the electric field effect in the spirit of a field effect transistor. By applying a voltage, the chemical potentials $\mu_{L,R}$ on both sides of the barriers can be different, enabling a tunnel current through the barrier. The combination of barriers of various individual gates can confine the electrons to potentials of designed shape. In particular, quantum dots with the properties discussed in chapter 2 can be defined as small coupled islands (figure 3.1(c)). This type of electrostatically defined quantum dots is called lateral quantum dots due to their 2D geometry. The shape of their electrostatic confinement potential is coarsely predefined by the shape of the gates, but remains tunable by the actual value of voltages applied. Compared to quantum dots which are primarily defined during the growth process, e.g. self-assembled quantum dots [5], this type of quantum dots shows a higher degree of flexibility during the experiment and can be used to explore a wide range in the parameter space (such as coupling parameters, different geometries, and more) within one and the same structure.

3.2 Fabrication

The cleanroom fabrication process uses standard lithography procedures. All of those methods were highly optimized during the last years of our group's research in the field of nano structures. Since no new methods have been developed during this thesis, this section only briefly outlines the process flow to provide an

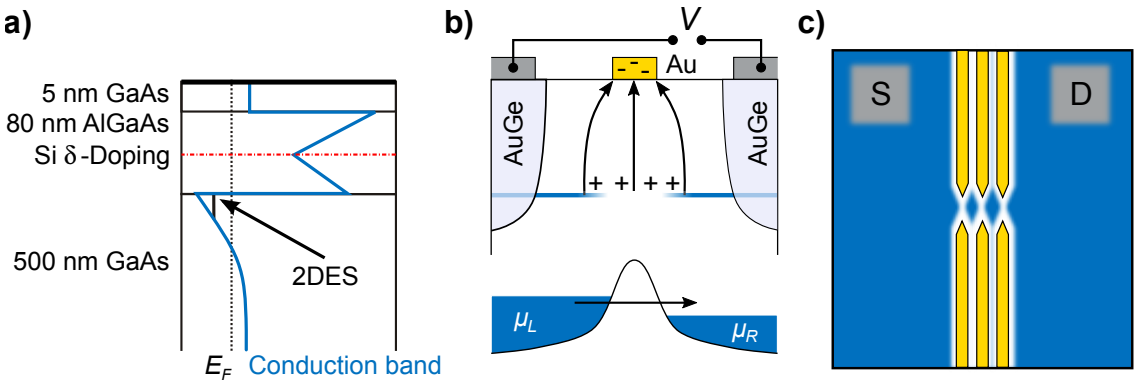

Figure 3.1: Electron confinement. (a) Sketch of the GaAs/AlGaAs based heterostructure used in this thesis. The conduction band (blue) is bended at the semiconductors' interface forming two-dimensional electron system (2DES) with charge carriers from the nearby Si doping inside a triangular potential. (b) Schematic of the essential part of a transport measurement: The 2DES (blue) is contacted by AuGe contacts (grey) diffused into the wafer. Gold gates (yellow) on top provide local potential barriers for the electrons by the field effect. An applied voltage V shifts the chemical potentials of the Fermi seas on both sides of the barrier $\mu_{L,R}$ in respect to each other and a tunneling current will flow (lower panel). (c) Combination of barriers form quantum dots as small islands inside the 2DES.

overview to non-expert readers of how the samples were fabricated. For more advanced readers, details of the fabrication including the process parameters are given in appendix B. References to previous theses which significantly contributed to the establishment of methods and provide in-depth descriptions are given at the appropriate passages.

There are five main steps from the wafer to the finished nanostructure. All of these steps involve a separate lithography step during which a pattern is written into a resist layer on top of the sample surface. A suitable resist is exposed locally either to UV light through a mask or to electrons of a controlled focused beam. Coarse structures are typically created by UV photo lithography which reaches its limits at around 1 µm, while smaller structures are written by an electron beam. After dissolving the exposed areas with a development chemical, the structure is transferred onto the surface of the sample by either etching or by depositing a metallic material which only remains at the patterned locations when finally removing the resist (lift-off). The lithography process is sketched in figure 3.2, for a detailed step-by-step description, the reader is advised to references [8, 13, 25].

An overview of the different lithography layers as well as a finished sample is shown in figure 3.3(a) and (b). The first structure processed onto the unpatterned chip is the Mesa structure. The Mesa consists of a squared area, where the nanostructures will be defined later on, as well as adjacent contact areas. The contact areas are well separated from each other and only connected by the central square which defines a pathway for electrons flowing between two contacts. The Mesa is defined by etching the surface elsewhere down to the Si dopant layer which removes all free charge carriers from the 2DES. As the second step, the contacts to the 2DES are fabricated. They consist of approximately rectangular pads with a meander edge structure to ensure a lower resistance through a large contact area after thermal diffusion [8]. The fabrication process of these Ohmic contacts is optimized to ensure a nearly linear I-V behaviour at cryogenic temperatures for voltages up to ~1 mV typically used in our quantum transport experiments. The third layer consists of bondpads and microstrip lines with which the nano meter sized gates processed in the subsequent step on the Mesa center are connected to the experimental setup. The design of the four gates optimized for rf modulations located at the bottom in figure 3.3 differs from the others; these gates have a large distance between each other as well as other gates to reduce cross-talk effects [8]. The last, but most advanced steps are the fabrication of the nano meter sized gold gates and on-chip cobalt magnets (details see below). Figure 3.3(c) shows a scanning electron micrograph of typical double quantum dot gate layout which was investigated in chapter 7.

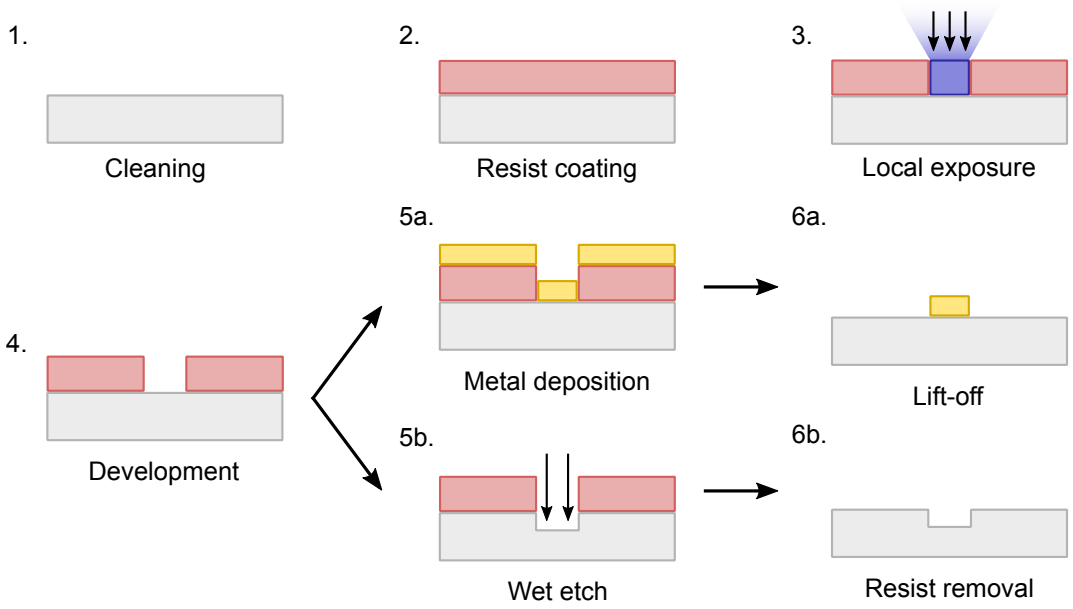

Figure 3.2: Standard lithography procedures. The clean sample (grey in 1) is spin-coated with a photo- or electron-sensitive resist (red in 2). The resist is locally exposed (blue areas in 3) to either ultraviolet light through a mask or to a controlled electron beam. The development (4) of the positive resist removes the resist at the exposed areas. The local structure is then fabricated by either metal deposition or wet etching. The initially globally deposited metal (yellow in 5a) only remains at the previously exposed areas when removing the resist during the lift-off (6a). For wet etching (5b), the etchant is selective, i.e. it does not etch the resist, so that the sample is etched only at the previously exposed areas. The sample is ready for further fabrication after resist removal (6b).

3.3 Single-domain nanomagnets

The on-chip magnet is the newest addition to our chip designs and its fabrication process was initially developed by G. Petersen [8] and further optimized by M. Mühlbacher [26].

The nanomagnets are designed to provide a strong inhomogeneous magnetic field at the site of the quantum dots to enhance the coupling of certain electronic states inside the dot, as discussed in all detail in chapters 5 and 6. As opposed to the concept of larger magnets with possibly many magnetic domains so far used in such structures (e.g. [27]), our bar-shaped nanomagnets have a strong anisotropy in geometry: While their length is around 2 µm, their height (50 nm) and width (100–250 nm) are significantly smaller. This leads to a single-domain magnetization along the long axis of the these magnets without the presence of any external magnetic field[(1)]. In our setup, where the external magnetic field is oriented along the long-axis of the bar-shaped magnet, the single-domain magnet is always fully polarized and the external magnetic field can only change the magnetization M as a whole; therefore, only two configurations, $M = \pm M_{\max}$, exist. The coercive field needed to reverse the magnetization of such a magnet depends on details in the geometry, for example a smaller width (and otherwise unchanged geometry) leads to a higher coercive field, since the anisotropy is increased. In multi-domain magnets, in contrast, the domains become aligned one by one until the maximum polarization $M_{\max}$ is reached, as sketched in figure 3.4(a) and (b). Compared to multi-domain magnets, the full magnetization facilitates a sizeable inhomogeneous field across the two QDs provided by the nanomagnet even at small external magnetic fields. Furthermore, its magnetization is straightforward to control during an experiment, because of the particularly simple hysteresis where the magnetization remains constant during a large range of external magnetic field values (even near zero external magnetic field) and switches direction almost instantly at well defined magnetic field values. By

[(1)] For a more detailed discussion of the theory which leads to the single-domain character of the magnets, see [8, p. 29ff]

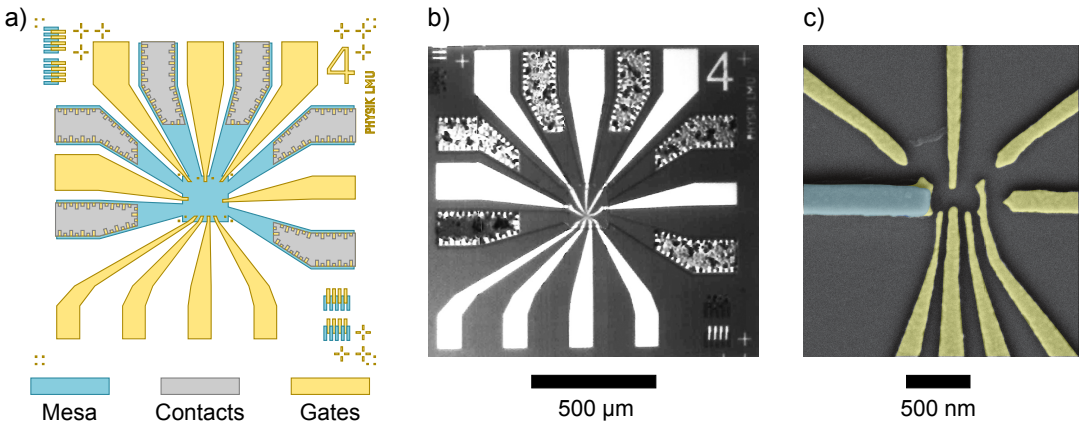

Figure 3.3: Example device structure. (a) Layout of the different lithographic layers of the micrometer-sized chip. (b) Microscope image of the finished chip layout. (c) False-colored electron micrograph of the center area of (b) including a double quantum dot layout with a nanomagnet investigated in chapter 7. Gold gates are colored in yellow, the Cobalt nanomagnet in blue.

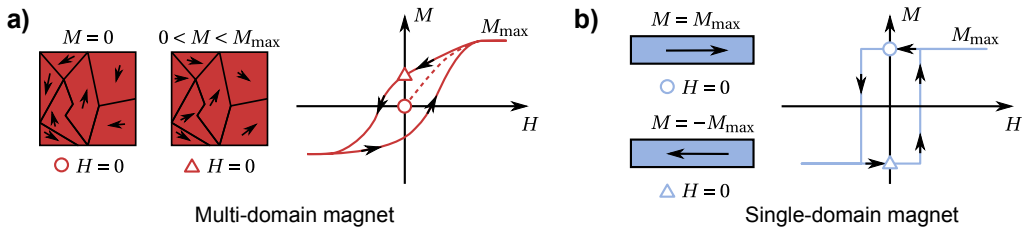

Figure 3.4: Comparison of the magnetization behaviour of (a) a multi-domain magnet and (b) a bar-shaped single-domain magnet in an external magnetic field along its long axis. (a) Before exposure to an external magnetic field H, the domains of a multi-domain magnet have no preferred magnetization axis and hence the overall magnetization M of the magnet vanishes (square marker). When exposed to an external magnetic field, the magnet's magnetization increases as more and more domains become aligned. The magnetization eventually reaches its maximum M_{max} when all domains are aligned. When ramping back to zero external field, the magnetization exhibits a hysteresis and shows a leftover magnetization, which is smaller than M_{max} (triangular marker). (b) The bar-shaped single-domain magnet is always fully magnetized, with the magnetization orientation along its long axis given by the shape anisotropy. The magnetization is initially at one of the values $\pm M_{\mathrm{max}}$ (square and triangular markers), which remain the only values exhibited depending on the hysteresis.

combining multiple magnets of different width, one can tailor their coercive fields and realize different stable configurations of the magnets' field, since the magnetization of each magnet switches at a different field value. We realized two parallel magnets width the width of 100 and 230 nm, whose magnetizations can be aligned parallel or anti-parallel to each other. Including the two different directions of an external magnetic field, this facilitates four different configurations in the experiment, which are characterized in chapter 5. A crucial step during the design of the nanomagnets is the calculation of their stray field. The magnetic field of a homogeneously polarized bar-shaped magnet can be calculated analytically [28] and was the basis for the design in reference [8]. However, a more advanced numeric treatment with the OOMMF framework [29], revealed that the magnetization, even though single-domain, shows a bending near the corners, and resulted in a non-negligible difference of up to 30 % [26, p. 15]. Details on the numeric simulations can be found in chapter 5 and in reference [26, pp. 11ff.]

In the following, I will provide a short summary of the latest results regarding the fabrication of the nanomagnets. Obviously, the effect of the magnets is larger the closer they are located to the DQD. However, it is vital that the magnet does not interfere with the gate layout defining the DQD in the first place, e.g. by shortening neighbouring gates. For larger magnets, this is commonly achieved by depositing an insulating

layer on top of the gate layer and put the magnet right on top of the DQD [27], since there is not enough space in the gate layer. For nanomagnets, this is not a suitable concept: First, the nanomagnets are thin compared to the larger magnets (e.g. 250 nm [27]) and can break apart if placed across a step on the surface[(2)]. Second, due to far less magnetic material deposited, the overall stray field is smaller and would be additionally reduced at the DQD due to the insulation layer. The initial concept to bring the nanomagnet closer to the DQD gate layout was to put it as a whole on top of a gold gate [8]. On the particular sample shown in 3.3(c), the nanomagnet is placed on the gate parallel to the axis connecting the dots. Though this concept has proven to be successful [30], it is still not ideal in terms of field strength at the position of the DQD, since the magnet and the QDs are separated not only by the depth of the 2DES but also additionally by the thickness of the gate[(3)]. A new concept developed during this thesis and described in reference [26] involves the replacement of individual gold gates by cobalt gates of the same shape thus directly integrating nanomagnets into the gate layout. This facilitates higher magnetic fields because of the reduced distance to the quantum dots and also allows more complex field distributions while still providing a good scalability. Both concepts require a lithographic positioning accuracy of around 10 nm which we achieved by usage of special markers on the surface [13].

The main problem which already occurred during the fabrication of the first nanomagnets and still remains, is the deformation of resist during the deposition of cobalt [figure 3.5(a)]. This leads to thin residual films near the actual magnet after lift-off [fig. 3.5(b, c)], as well as to deviations of the magnets' desired shape [fig. 3.5(d)]. The reasons for the deformation of the resist are so far still unknown: The initial hypothesis [8, p. 13] of a thermal deformation by the heat of the evaporation process is supported by the observations that a water-cooled aperture [8, p. 14] as well as a slow evaporation process (low deposition rates, frequent pauses during the process) [26, p. 32] reduced the effect. However, a thermometer connected to the substrate holder did not show an increased temperature compared to the evaporation of gold which succeeded without any problems, and an improved thermal connection between substrate chip and its holder via a copper tape did not yield any positive results. A transition from e-beam deposition, where the target material is locally heated by an electron beam, to simple thermal evaporation, which should in principle worsen the effect due to higher temperatures if the hypothesis is accurate, showed no significant difference. In addition, lower pressures in the evaporation chamber also reduced the effect significantly, which is not apparently connected to the sample's temperature. Recent attempts during where we forced a melting of the entire cobalt material inside the crucible during thermal evaporation showed the most promising results. So far, we have not been able to reliably solve the problem; however, we were able to remedy its symptoms. The residual films can be mechanically removed to a satisfying extent in an ultrasonic bath at low powers [compare figs. 3.5(b) and (d)] and the desired shape of the nanomagnet can be recovered by modifying the design to allow for the resist deformation, as depicted in figure 3.5(d).

[(2)] Note that the surface of the insulating layers mimics the profile of the underlying gates.
[(3)] 40 nm compared to a typical 2DES depth of 85 nm

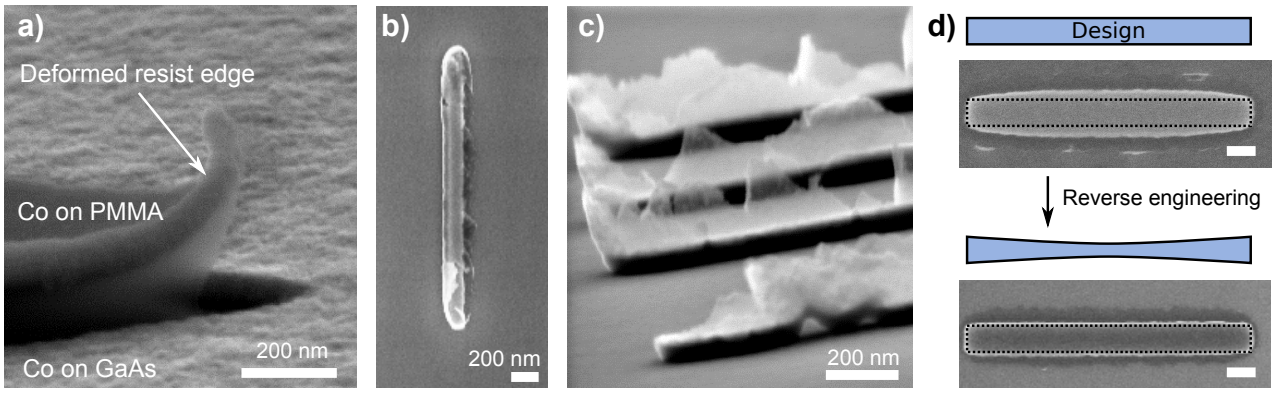

Figure 3.5: Nanomagnets' fabrication problems occurring during and after the evaporation of cobalt. (a) Scanning electron micrograph of a cobalt test structure after evaporation but before lift-off. The PMMA resist is deformed at the edges where it is bended upwards. This results in thin residual films after lift-off [panels (b) and (c)], but also a deformation of the whole magnet [panel (d)]. (b) Top-down view of a nanomagnet after lift-off. Residues are visible mainly as white regions near the actual magnet. (c) Side view on a test-structure of four magnets after lift-off. The residues have a significant height exceeding the one of the actual magnets, but are almost transparent and very thin. Ultrasonic cleaning removes most parts of the residues [compare magnets in (d)]. (d) The deformation of the resist leads also to a deviation from the desired geometry of the magnet (design in blue, desired shape sketched with dotted lines in the SEM pictures). The desired geometry is realized by reverse engineering, i.e. modifying the actual design in a number of iterations until the result matches the initial design. Scale bars are 200 nm. Figures reproduced from [8, 26].

4 Measurement setup

The purpose of this chapter is to give the reader an overview about the measurement setup and its most crucial components. For a detailed characterization of the low temperature measurement setup, the reader is advised to reference [25, p. 51–92].

4.1 Overview

The main requirements to perform coherent quantum transport measurements in DQDs are demanding. First of all, the DQD needs to be electrostatically defined by applying dc voltages to the nano-metre sized gates on top of the wafer. To ensure a high tunability and stability of the confinement potential, a high resolution and stability of these voltages is needed. In our setup, we achieve a voltage resolution of 100 µV at gate voltages of around −1 V and a voltage stability of $\lesssim 35\,\mu V$ during the measurement time of ∼200 ms [(1)]. To do so, we use a sophisticated wiring and low pass filtering scheme connecting high precision voltage sources to the gates on the sample which we will discuss in detail in section 4.2. As the second requirement, we want to probe and manipulate coherent electron dynamics by modulating some of the voltages defining the electron levels in the DQD with rf voltages. This requires special lines which transmit frequencies in the order of 1 GHz while not introducing noise compromising the overall voltage stability. The third requirement is the capability to measure small currents down to 10 fA flowing through the nano structure. To ensure a low noise floor, we again use an optimized wiring and filtering scheme (sec. 4.2) to connect the needed electronic devices, such as an operational amplifier and a multimeter. Furthermore, to prevent parasitic current flows via ground loops, all electronic devices are galvanically decoupled from the ground of the power line and connected to a common ground.

Importantly, as discuss in chapter 2, the relevant energy scales ∼1 µeV are exceeded by the thermal energy at room temperature of 25 meV by far. Therefore, all experiments are carried out in a low-temperature controlled environment, in our case a dilution refrigerator [31]. The base of the system is a commercially available *Oxford Kelvinox 100* which reaches a base temperature of 20 mK in the present setup. To provide a tunable magnetic field during the experiment, the sample is placed at the center of a superconducting magnet, which can supply a field up to 9 T parallel to the 2DES.

In the following section, we will focus on the general wiring and filtering scheme with which we are able to meet the requirements of tunable and stable dc voltages, a high current sensitivity, and rf voltage modulation. The specific setup of each experiment which makes use of these capabilities, is described separately in each chapter.

4.2 Wiring and filtering

A central part of the electrical measurement setup are the lines which connect the electronic devices controlling the experiment with the sample at low temperatures. The setup, schematically depicted in figure 4.1, provides three different types of wiring, each optimized for its special purpose. All the wires reach from the coldest point of the cryostat, namely the sample thermally coupled to the mixing chamber temperatures of around 20 mK by a silver rod, all the way up to room temperature. To minimize their heating effect on the

[(1)] Estimated from the inhomogeneous broadening of electron levels (3.5 µeV, chapter 7) and the lever arm of 0.1 eV/V. Note that the estimated value is only an upper limit for the voltage stability, since it neglects other contributions to the broadening.

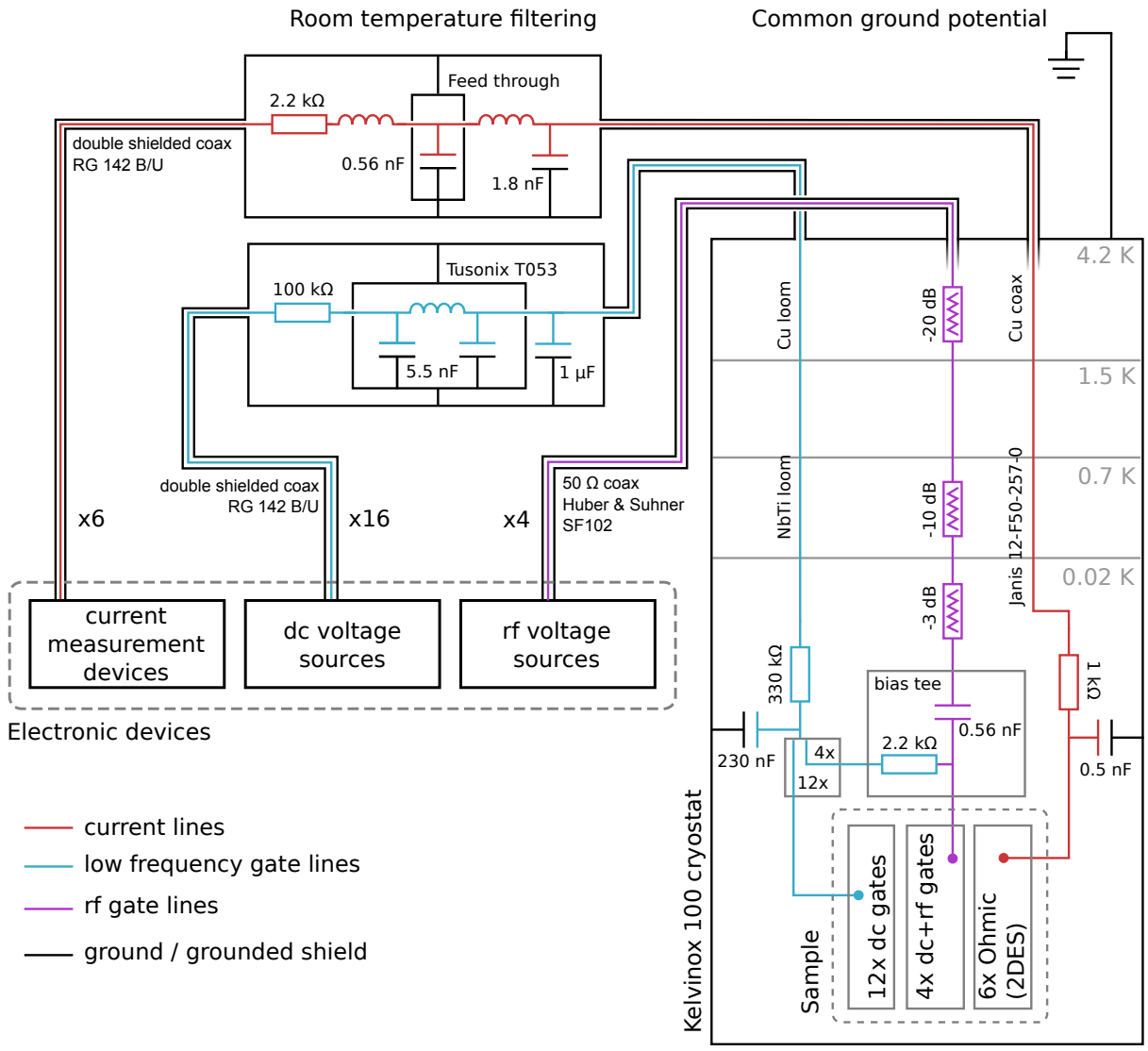

Figure 4.1: Scheme of the low-temperature transport setup used in all experiments. The sample inside the cryostat is electrically connected to the room temperature measurement equipment by different types of wiring each optimized for its purpose. All electronic measurement devices are galvanically isolated from the power lines and connected to the common ground potential at the cryostat. Between the sample and the measurement devices are two stages of filtering, the room temperature filters and the low-temperature filters inside the cryostat. All wires are thermally anchored at different temperature stages of the cryostat to minimize heating effects and ensure low electron temperatures. The sample inside the cryostat can be exposed to a magnetic field of a superconducting coil up to 9 T (not shown). The scheme depicts capabilities rather than details of a particular experiment; not all wires are necessarily used in each experiment. The details of the actual measurement schemes and which electronic devices have been used to realize them are given separately in each chapter. Figure adapted from [8].

sample and cool down the wires themselves, they are thermally anchored at several points of the cryostat (details in [8, 25]).

Low frequency gate lines

Up to sixteen low frequency gate lines (blue in fig. 4.1) connect the high precision voltage sources to the gates to electrostatically define the nano structures. At room temperatures, double shielded coax cables are used to prevent significant noise pick-up between the voltage sources and the cryostat. The cryostat itself is shielded by a metallic dewar such that the wires inside, Cu and NbTi looms, are not additionally shielded. The NbTi becomes superconductive at low temperatures and is a efficient thermal insulator. The line consists of two low-pass filter stages, one at room temperature (cut-off frequency $f_C = 1/2\pi RC = 1.6\,\mathrm{Hz}$) and the other one near the base temperature ($f_C = 2.1\,\mathrm{Hz}$) of the cryostat. Since the voltages applied on these lines are quasi-static, both filters are designed to restrictively damp any high frequency components, i.e. noise. Since the resistance of the sample, $> 10\,\mathrm{G\Omega}$, is by far the biggest one in the line ($\sim 430\,\mathrm{k\Omega}$ for filters and wiring[(2)]), it is ensured that no significant voltage drop occurs before reaching the sample. In principle, one could even lower the cut-off frequency further and still maintain this condition. However, the cut-off frequencies determine the maximum voltage sweep rate during an experiments, where these voltages are frequently swept. The chosen cut-off frequencies are a compromise between an efficient noise filtering and a reasonable measurement time.

rf gate lines

To modulate the voltages on the gates with rf voltage signals, the setup includes four rf gate lines (purple in fig. 4.1). The signal of each line is mixed with the one of a low frequency gate line on a bias tee at low temperatures. These lines consist of $50\,\Omega$ coax cables and impedance matched strip lines at the bias tee to ensure a high signal transmission. As these lines should provide a broad frequency range (100 kHz to 10 GHz), we cannot apply restrictive filters. Therefore, we apply an a priori strong modulation signal and include several attenuators at different stages of the cryostat (overall $-33\,\mathrm{dB}$). With this method, we can efficiently suppress noise which is significantly smaller than the initially strong output of the signal generator[(3)].

Current lines

Similar to the low frequency gate lines, the six current lines (red in fig. 4.1) outside of the cryostat consist of double shielded coax cables and feature in total two filter stages, one at room temperature and one at low temperatures. In contrast, the cut-off frequencies ($f_C = 31\,\mathrm{kHz}$ at room temperature, $f_C = 318\,\mathrm{kHz}$ at low temperatures) are significantly higher. The higher cut-off frequencies arise from to conditions: First, the resistance of the sample should be the largest one in the line ($R = 2 \cdot 3.4\,\mathrm{k\Omega}$ for wires and filters, see table C.2) to ensure the current signal predominantly shows the response of the sample (and not, e.g. the thermal noise of the filter). For DQDs ($R \gtrsim 1\,\mathrm{M\Omega}$), the limit is not reached, but for other nano structures such as quantum point contacts with $R \lesssim h/e^2 \approx 26\,\mathrm{k\Omega}$ it is. Second, to measure currents in the order of 10 fA, we use an operational amplifier which does not allow large capacitances to ground at its input [25, p. 57], which restricts the allowed capacitances to a few nF. Consequently, the cables inside the cryostat are shielded coax cables to avoid additional noise pick-up which might not be filtered out by the low temperature filter.

(2) See table C.1 for a detailed breakdown into each component.

(3) Note that noise scaling with the output level of the signal generator cannot be suppressed this way.

5 A double quantum dot inside a strongly inhomogeneous magnetic field

This chapter presents the results of

- Forster, F. *et al. Phys. Rev. B. 91.* 195417 (2015)

See section D for the contributions of each author.

5.1 Overview

The magnetic field at the position of the quantum dots plays a major role for its transport properties [16]. We already established in section 2.2.3 that an inhomogeneous magnetic field leads to couplings between the singlet and triplet subspace in the Hamiltonian (2.10) partly lifting the Pauli-spin blockade (PSB). In the following experiment, we introduce a double quantum dot incorporating two single domain nanomagnets and investigate the complex physics in the PSB regime enabled by the non-trivial magnetic field distribution. We discuss our dc transport spectroscopy as well as radio frequency electric-dipole-induced spin resonance (EDSR) experiments and demonstrate the capability and advantages of hybrid devices containing multiple single domain nanomagnets compared to devices with only one usually larger on-chip magnet. In dc current measurements, we explore the four possible configurations of the nanomagnet magnetizations (which can be polarized parallel or anti-parallel relative to each other and relative to an external field). Since the coupling of the states involved in the electron tunneling depend on the details of the magnetic field and thus the polarization of the nanomagnets, we are able to realize two very different coupling regimes in a single well controlled experiment. In our EDSR measurements we find two resonances which correspond to transitions in the two QDs. The combination of dc data and EDSR data compared to simulations of the magnetic stray field of the nanomagnets allows us to localize the positions of our two QDs. We have done this for two different double QDs corresponding to two different gate voltage configurations. A comparison of these data with a second sample containing only one single domain nanomagnet reveals an important advantage of multiple nanomagnets, namely a straightforward possibility to control spins in adjacent QDs separately.

5.2 Theory

5.2.1 Electron dipole-induced spin resonance

A central new aspect introduced in this chapter is the method of EDSR. Here, an electron spin in one quantum dot can be flipped, effectively driving transitions from $|S_{11}\rangle$ to $|T_{\pm}\rangle$ and thus lifting the PSB. In a typical EDSR setup, each electron spin is exposed to a combination of a static magnetic field $\mathbf{B}_{\text{ext}}$, which splits the electron levels by the Zeeman energy, and an oscillating field $\mathbf{B}_{\text{ac}}$ perpendicular to $\mathbf{B}_{\text{ext}}$:

$$\mathbf{B}(t) = \mathbf{B}_{\text{ext}} + \mathbf{B}_{\text{ac}}(t) = B_z \begin{pmatrix} 0 \\ 0 \\ 1 \end{pmatrix} + B_0 \begin{pmatrix} \cos\omega t \\ \sin\omega t \\ 0 \end{pmatrix}. \tag{5.1}$$

In principle, the model for our system is the full five-state Hamiltonian (2.10), which leads to complex time-dependent problem, especially because B_z and B_0 are not necessarily equal in both dots. However, in all relevant experiments, we perform EDSR in the (1,1) charge state at large detuning $|\varepsilon| \gg t_c$ in an inhomogeneous magnetic field with $-g\mu_B \Delta B_z \gg J_{11}$. Here, the eigenstates become $|T_+\rangle = |\uparrow\uparrow\rangle$, $\frac{1}{\sqrt{2}}(|T_0\rangle + |S_{11}\rangle) = |\downarrow\uparrow\rangle$, $\frac{1}{\sqrt{2}}(|T_0\rangle - |S_{11}\rangle) = |\uparrow\downarrow\rangle$, and $|T_-\rangle = |\downarrow\downarrow\rangle$, which are the single spin states of the DQD. We can therefore consider each spin separately, substantially reducing the complexity of the problem to a single spin in an oscillating magnetic field,

$$H(t) = \frac{g\mu_B}{\hbar}\mathbf{s}\cdot\mathbf{B}(t) = \omega_z s_z + \omega_0(\cos(\omega t)s_x + \sin(\omega t)s_y)$$

with $\omega_i = g\mu_B B_i/\hbar$. We can immediately see that the oscillating field with amplitude B_0 introduces off-diagonal terms to the Hamiltonian and couples $|\uparrow\rangle$ and $|\downarrow\rangle$ by a time dependent coupling constant. The calculation of the time dependent solution $\big|\psi(t)\big\rangle$ of the Schrödinger equation is covered in appendix A.3.1. In the rotating frame, which rotates about the z-axis with the same frequency as $\mathbf{B}_{\text{ac}}$, i.e. ω, the Hamiltonian becomes time-independent with a constant coupling. The Bloch vector of the system[1] then describes Rabi oscillations around $\mathbf{B}_{\text{ac}}$ which remains fixed on a constant direction, as depicted in figure 5.1(a). In the stationary frame, the direction of $\mathbf{B}_{\text{ac}}$ rotates and hence the Bloch vector describes a spiral precession on the sphere, see 5.1(b). For resonant driving, i.e. $\Delta\omega = \omega_z - \omega = 0$, the state vector can reach every point on the Bloch sphere; in fact, coherent control of quantum states for quantum computing by EDSR has already been demonstrated [27, 33, 34]. For the scope of this thesis, we are less interested on the exact position of the state vector on the Bloch sphere, but more so on the possibility to flip the electron spin. Assuming no decoherence, the transition probability from $|\uparrow\rangle \rightarrow |\downarrow\rangle$, when starting in the pure state $\big|\psi(0)\big\rangle = |\uparrow\rangle$, is given by Rabi's formula, also derived in appendix A.3.1:

$$\big|\langle\downarrow|\psi(t)\rangle\big|^2 = \frac{\omega_0^2}{\omega_0^2 + \Delta\omega^2}\sin^2\left(\frac{1}{2}\sqrt{\omega_0^2 + \Delta\omega^2}\,t\right).$$

We find that the probability to measure a spin-flip oscillates in time and that the amplitude of these Rabi oscillations is given by a typical Lorentz resonance: For $\Delta\omega = 0$, i.e. $\hbar\omega$ is equal to the Zeeman splitting of the spin states, the maximum amplitude of 1 is reached. For $\Delta\omega \neq 0$, the amplitude decreases as shown in 5.1(c). In the typical experimental situation in this thesis, the driving field is weak compared to the static field, i.e. $|\mathbf{B}_{\text{ext}}| \gg |\mathbf{B}_{\text{ac}}|$. This leads to a sharp resonance[2] which makes EDSR a useful tool to measure the local magnetic field in a quantum dot to high precision, since ω is well controlled and a spin-flip is in good approximation only measured for $\hbar\omega = g\mu_B|B_z|$. Since both quantum dots are independent in this measurement scheme, we can determine $\overline{\mathbf{B}}$ and $\Delta\mathbf{B}$ of the Hamiltonian (2.10) for a complex field distribution. Furthermore, because B_z includes the Overhauser field and thus the polarization state of the nuclei, EDSR poses an elegant method to investigate the dynamics of the nuclei, which is the topic of chapter 6.

5.2.2 Generation of the rf magnetic field

It is difficult to realize sizeable oscillating magnetic fields in the GHz regime in a low temperature experiment, since a globally applied ac field leads to heating via eddy currents and mechanical instabilities of magnetic parts in the cryostat. In quantum dots, the Oersted field of current through an on-chip conductor loop has been successfully used to drive EDSR, but an undesired heating effect still remains [33]. Other approaches harness the spin-orbit coupling [34] or the electron-nuclei hyperfine interaction [35] to provide an effective magnetic ac field, but they pose additional requirements on the host material. In our approach, we adapt a

[1] Refer to section 7.2.3 for an introduction to the Bloch sphere representation of a quantum state.

[2] Note that in the extreme case of $\omega_0 \rightarrow 0$, the Lorentz curve becomes the Delta distribution.

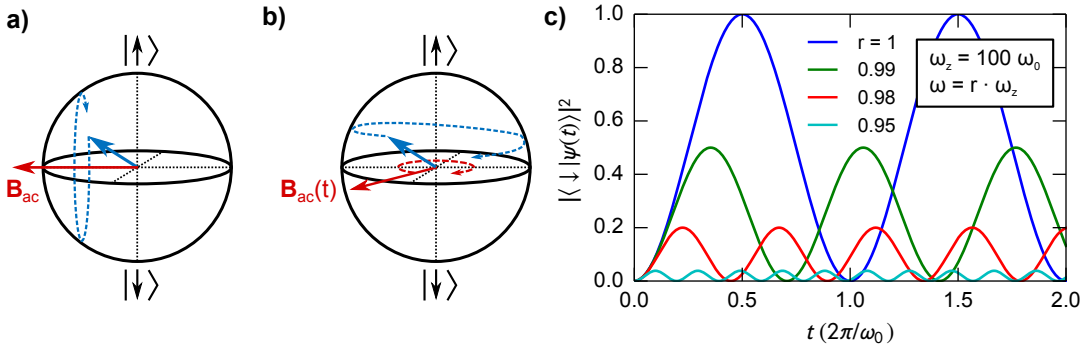

Figure 5.1: Electron spin resonance of an electron in a static magnetic field $\mathbf{B}_{\text{ext}}$ with a perpendicular driving field $\mathbf{B}_{\text{ac}}$, rotating with a frequency ω, as in equation (5.1). (a) Time evolution of the state vector on the Bloch sphere in the rotating frame, where $\mathbf{B}_{\text{ac}}$ is a static vector and the state vector exhibits a Rabi precession about $\mathbf{B}_{\text{ac}}$. (b) The same as a) for the stationary laboratory frame. The state vector spirals down over the surface of the Bloch sphere. (c) Time-dependent probability of a spin-flip for a typical experimental situation, in which $|\mathbf{B}_{\text{ext}}| = B_z \simeq 100|\mathbf{B}_{\text{ac}}|$ and different resonance situations $\omega = r \cdot g\mu_B B_z/\hbar$. (a, b adapted from [4].)

method already successfully applied to DQDs with micromagnets [36]: We capitalise on the incorporated inhomogeneous field, $\mathbf{B} = \mathbf{B}(\mathbf{r})$, provided by our already present nano magnets and move the electron periodically through their field gradient, i.e. $\mathbf{r} = \mathbf{r}(0) + \Delta\mathbf{r}(t)$. This is realised by applying a sine voltage $V_{\sim}(t)$ at one of the quantum dot gates. Using a Taylor expansion to first order in $\Delta\mathbf{r}$ explicitly carried out in appendix A.3.2, the magnetic field becomes

$$\mathbf{B}(t) = \mathbf{B}_{\text{ext}} + \mathbf{B}_{\text{ac}}(t) = B_z \begin{pmatrix} 0 \\ 0 \\ 1 \end{pmatrix} + 2B_0 \begin{pmatrix} \cos wt \\ 0 \\ 0 \end{pmatrix}.$$

The difference between the ideal driving field $\mathbf{B}_{\text{ac}}(t)$ of (5.1) and the one here is two-fold: In the ideal case, the driving field has a time-independent absolute value, $|\mathbf{B}_{\text{ac}}(t)| = B_0$, but its orientation rotates about the z-axis. Here, the absolute value is proportional to $\cos\omega t$ and hence oscillates in time, while its orientation remains fixed in one direction. Therefore, the Hamiltonian is not time independent in the rotating frame we used before, but consists of an additional time-dependent term (see appendix A.3.2 for details). However, this additional term oscillates fast compared to all other dynamics such that it can be dropped within the rotating wave approximation. The Hamiltonian then becomes identical to the one of the ideal driving and therefore leads to the same Rabi oscillations discussed above.

5.3 Measurement setup

The experiment described below has three main requirements: First, we need to measure the single electron leakage current in PSB. Second, we need to pulse the double quantum dot to the Coulomb blockade, i.e. a large negative detuning ε, to minimize effects of other PSB lifting mechanisms during EDSR. We also need to pulse back to the transport window if the EDSR drive flipped a spin, which yields an enhanced current in PSB, and to reinitialize the system in the blocked state $|T_{11}\rangle$. Third: We need to be able to apply the driving field only when in Coulomb blockade. The basic setup which complies with all three requirements is depicted in figure 5.2. The first requirement is fulfilled by using a highly sensitive I/V converter, the Ithaco 1211, with an amplification factor of 10^{10}. Together with the sophisticated filtering and ground concept already discussed in chapter 4, we are able to measure down to a noise floor of ~20 fA. The second requirement is matched by using the arbitrary waveform generator Tektronix 5014B, which can easily provide the slow pulses in the range of ~MHz required for our measurement scheme. The final

requirement is met by connecting the sine generator R&S SMP02 to one of the gates and modulate its output by another pulse sequence from the waveform generator, which modulates the output of the sine generator to 1 during the Coulomb blockade and to 0 during PSB, thus effectively switching on and off the driving whenever needed. In our setup, the sine driving signal is mixed to the slow pulse sequence of one of the gates via a Weinschel WA1515 resistive combiner, however this is not necessarily needed and was done for convenience.

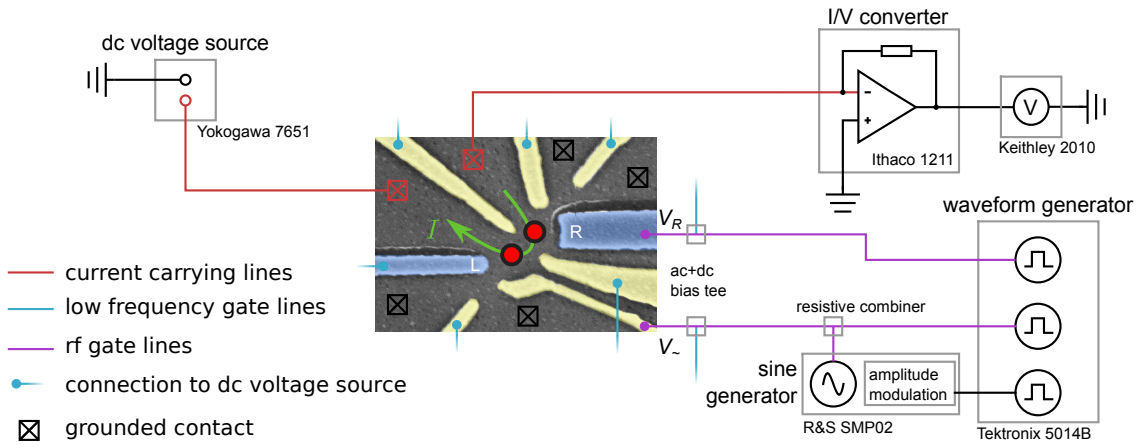

Figure 5.2: Electrical measurement setup for the EDSR experiment. The single electron tunneling current I through the double quantum dot defined by dc voltage sources connected to all gates is measured by an I/V converter, which amplifies current by a gain of 10^{10} and converts it to a voltage measured by a voltmeter. A waveform generator with independent output applies rf pulses in the ~1 MHz range to two high-frequency gates. The signal of one output is combined with a sine signal of ~1 GHz via a resistive combiner. A third output of the waveform generator modulates the output of the sine generator which serves as a fast switch to turn on and off the sine signal at given times during the pulse sequence of the waveform generator.

PHYSICAL REVIEW B **91**, 195417 (2015)

Electric-dipole-induced spin resonance in a lateral double quantum dot incorporating two single-domain nanomagnets

F. Forster,[1] M. Mühlbacher,[1] D. Schuh,[2] W. Wegscheider,[2,3] and S. Ludwig[1,*]
[1]*Center for NanoScience & Fakultät für Physik, LMU-Munich, 80539 München, Germany*
[2]*Fakultät für Physik, Universität Regensburg, 93040 Regensburg, Germany*
[3]*Solid State Physics Laboratory, ETH Zurich, 8093 Zurich, Switzerland*
(Received 6 March 2015; revised manuscript received 13 April 2015; published 14 May 2015)

On-chip magnets can be used to implement relatively large local magnetic field gradients in nanoelectronic circuits. Such field gradients provide possibilities for all-electrical control of electron spin qubits where important coupling constants depend crucially on the detailed field distribution. We present a double quantum dot (QD) hybrid device laterally defined in a GaAs/AlGaAs heterostructure which incorporates two single-domain nanomagnets. They have appreciably different coercive fields which allows us to realize four distinct configurations of the local inhomogeneous field distribution. We perform dc transport spectroscopy in the Pauli-spin blockade regime as well as electric-dipole-induced spin resonance (EDSR) measurements to explore our hybrid nanodevice. Characterizing the two nanomagnets we find excellent agreement with numerical simulations. By comparing the EDSR measurements with a second double QD incorporating just one nanomagnet we reveal an important advantage of having one magnet per QD: It facilitates strong field gradients in each QD and allows us to control the electron spins individually for instance in an EDSR experiment. With just one single-domain nanomagnet and common QD geometries EDSR can likely be performed only in one QD.

DOI: 10.1103/PhysRevB.91.195417 PACS number(s): 73.63.−b, 03.67.−a, 73.63.Kv

I. INTRODUCTION

At cryogenic temperatures semiconductor based quantum dots (QDs) can be used to create well defined quantum states of arbitrarily few localized electrons. The electron spins of these states provide a playground for exploring quantum mechanics in an interacting solid state environment and are heavily studied for possible applications in quantum information processing [1–19]. The coherent dynamics of electron spins can be accessed in an electron spin resonance (ESR) experiment. To control a QD based spin qubit on a time scale shorter than its dephasing time such an ESR experiment would require a magnetic field modulated at radio frequencies (rf) with an amplitude of a few millitesla. Combining such a large rf modulation to an (externally applied) macroscopic magnetic field with cryogenic temperatures of $T \ll 1$ K, required for long spin lifetimes, is a major technical challenge. Obstacles are oscillating strong mechanical forces between macroscopic perpendicular magnets and eddy currents caused by induction, both causing severe heating and mechanical oscillations. To overcome these problems, on-chip methods to locally manipulate electron spins have been developed. A breakthrough in locally controlling QD based spin qubits was based on the exchange coupling between two electrons located in adjacent tunnel coupled QDs [2]. This all-electrical method makes use of the direct dependence of the singlet-triplet splitting on gate voltages, while the latter can be rf modulated in a straightforward way [2,4,14–17]. Because the exchange coupling between two electrons is subject to fluctuations of the local potential, it is, however, desirable to be able to manipulate the spin of a single electron localized in a QD as well. In a standard ESR approach this is, in principle, possible with an on-chip magnetic antenna [4,6]. This approach has the disadvantage of needing a relatively strong current through an on-chip microwire which causes parasitic heating of the sample. The capacitive coupling between the strongly driven antenna and the QD leads can furthermore cause electron pumping via an unwanted modulation of the leads chemical potentials. Alternative methods are based on electric-dipole-induced spin resonance (EDSR) where a periodic spatial motion of an electron gives rise to an oscillating (effective) magnetic field, an rf driving force. The rf spatial oscillation of an electron is thereby induced by modulating the voltage of one of the metal gates defining the QD. It has been demonstrated that the necessary inhomogeneous effective magnetic field can be provided by the spin-orbit interaction [8,11] or even the spatial fluctuations of the hyperfine interaction between the electron and many nuclei [7]. Unfortunately, both these interactions also promote dephasing of the qubit; the spin-orbit interaction via coupling electrons and phonons, while the hyperfine interaction couples the electron spin dynamics to the thermal fluctuations of nuclear spins [20,21]. Consequently, it would be beneficial for spin qubit applications to use materials combining a small spin-orbit interaction with no nuclear spins, e.g., ^{28}Si and ^{12}C. However, this would require another mechanism to facilitate EDSR.

An elegant option employs the inhomogeneous stray field near the edge of an on-chip magnet. A spatial oscillation of an electron localized in such an inhomogeneous field then directly translates into a modulation of the magnetic field. In past experiments, relatively wide (width of $\sim$1 μm) on-chip magnets in the vicinity of double QDs have been used in order to create a strong field gradient [5,7,10,12,13,18,19]. The disadvantage of such a large magnet are its multiple

*Present address: Paul-Drude-Institut für Festkörperelektronik, Hausvogteiplatz 5–7, 10117 Berlin, Germany; ludwig@pdi-berlin.de

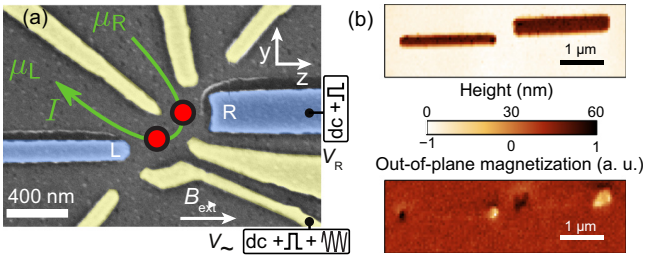

FIG. 1. (Color online) Sample layout: (a) Scanning electron microscope image of the wafer surface. The GaAs surface is dark gray, gold gates are shown in yellow, magnetic cobalt gates in blue. Both magnets are $\simeq$2 μm long and $\simeq$60 nm high, the left one (L) is $\simeq$100 nm and the right one (R) $\simeq$230 nm wide. Red filled circles indicate possible QD positions in the two-dimensional electron system 85 nm beneath the surface; actual positions depend on gate voltages and disorder potential. The voltages applied to gates R and $\sim$ are radio frequency modulated for EDSR measurements. (b) Magnetic force microscopy measurement of the magnets before the gold gates were processed; height profile in the upper panel and out-of-plane magnetization in the lower panel indicating single-domain magnetization of both magnets.

magnetic domains at zero external magnetic field $\mathbf{B}_{\text{ext}}$, which lead to a small and rather uncontrolled stray field. A sizable $\mathbf{B}_{\text{ext}}$ on the order of a Tesla is then needed to align the domains and thereby create a strong inhomogeneous magnetic field at the QD. Multiple domains can be avoided by reducing the on-chip magnet's lateral dimensions until its shape anisotropy yields a single-domain ground state. In a previous project we have already realized an on-chip single-domain nanomagnet. It yields a sizable inhomogeneous stray field $\mathbf{B}_{\text{nm}}$ independent of $\mathbf{B}_{\text{ext}}$ and, therefore, provides interesting possibilities for nanoelectronic circuits, in particular at $\mathbf{B}_{\text{ext}} \simeq 0$. As an example we have demonstrated that this new regime can be utilized for very efficient hyperfine induced nuclear spin manipulation and have indeed reached much stronger nuclear spin polarizations than previously reported for lateral QDs [22].

Here we present an innovative double QD hybrid design which incorporates two single-domain nanomagnets. We replaced two of the usual gold gates with ferromagnetic cobalt gates [Fig. 1(a)]. At small $\mathbf{B}_{\text{ext}}$, the two magnets can be magnetized in a parallel [as in Fig. 1(b)] or antiparallel configuration, giving rise to two very different inhomogeneous magnetic field distributions, an interesting possibility for spintronics applications. The double QD is defined in the two-dimensional electron system (sheet density: 1.19×10^{11} cm^{-2}, mobility: 0.36×10^6 cm^2/V s) of a GaAs/AlGaAs heterostructure 85 nm beneath its surface [Fig. 1(a)]. We have prepared the double QD in the two-electron Pauli-spin blockade regime with one electron in each dot, in order to employ spin-to-charge conversion. To determine static properties such as the coercive fields of the two magnets we have used dc measurements and have explored the electron spin dynamics with EDSR measurements.

Depending on the double QD geometry we have found either one or two electron-spin resonances. Two resonances corresponding to different $\mathbf{B}_{\text{nm}}$ in the two dots would allow us to study coupled spin qubits in a double QD. However, two resonances can only be resolved under three conditions: (i) a sizable magnetic field difference between the dots, (ii) a sufficiently large magnetic field gradient in each dot, and (iii) a strong enough capacitive coupling between each dot and an rf-driven gate. While (iii) is straightforward to fulfill, in this article we demonstrate that the remaining conditions (i) and (ii) can be met by employing two single-domain nanomagnets. As we merely replace gold gates by magnetic cobalt gates our scenario can be scaled up to multiqubit systems. Because single-domain magnets are also useful at $\mathbf{B}_{\text{ext}} = 0$ they allow spintronics experiments beyond the scope of previous experiments with only one (usually multidomain) on-chip magnet.

II. EXPERIMENTAL SETUP

Our measurements probe the dc current I [green arrow in Fig. 1(a)] which passes through the double QD in response to a constant voltage $V = (\mu_R - \mu_L)/e = 1$ mV applied across it. Figure 2(a) illustrates the double QD configuration by sketching the chemical potentials $\mu_{L,R}$ of the leads and those of the relevant double QD states as horizontal lines, while vertical lines indicate tunnel barriers. We denote (n,m) the charge configuration of the double QD with n electrons in the left and m in the right dot and consider the single electron charge transfer characterized by the following tunneling cycle: $(1,0) \rightarrow (1,1) \rightarrow (2,0) \rightarrow (1,0)$, where the transition $(1,1) \rightarrow (2,0)$ constitutes a bottleneck: Both configurations, $(1,1)$ and $(2,0)$, are composed of three triplets, collectively denoted by T_{11} and T_{20}, and one singlet, S_{11} and S_{20}. We define the detuning ϵ as the energy difference between S_{11} and S_{20}. For $\epsilon < 0$ tunneling processes $(1,1) \rightarrow (2,0)$ are blocked by energy conservation (Coulomb blockade) and I is close to zero. The exchange splitting between singlets and triplets is much higher if two electrons are in the same dot, $J_{20} \gg J_{11}$. Hence, at $\epsilon \simeq 0$ the T_{20} states are highly elevated compared to T_{11}. As a consequence, for $0 < \epsilon < J_{20}$ the transition $T_{20} \rightarrow S_{11}$ is forbidden by the Pauli principle (Pauli-spin blockade), as long as S_{11} and T_{11} remain decoupled. In our case the inhomogeneous $\mathbf{B}_{\text{nm}}$ mixes S_{11} and T_{11} states near where their eigenenergies are equal [22]. In the stability diagram plotted in Fig. 2(b) this coupling gives rise to a narrow stripe of $|I| > 0$ near $\epsilon = 0$. We stress that the hyperfine interaction, which also couples S_{11} and T_{11}, is only a weak perturbation compared to the effect of $\mathbf{B}_{\text{nm}}$. For $\epsilon \geqslant J_{20}$ the transition $T_{11} \rightarrow T_{20}$ lifts the Pauli-spin blockade and a sizable current flows (in our double QD $J_{20} \simeq 300$ μeV). The tiny but nonvanishing current visible in Fig. 2(b) for $0 < \epsilon < J_{20}$ is approximately constant as expected for higher order processes such as the cotunneling $T_{11} \rightarrow T_{20} \rightarrow (1,0)$, where T_{20} is energetically forbidden.

In the stability diagram in Fig. 2(b), the current carrying region corresponding to the absence of Coulomb blockade is composed of two overlapping triangles. Above we have described the tunneling cycle which gives rise to the lower left triangle; the second triangle corresponds to an alternative

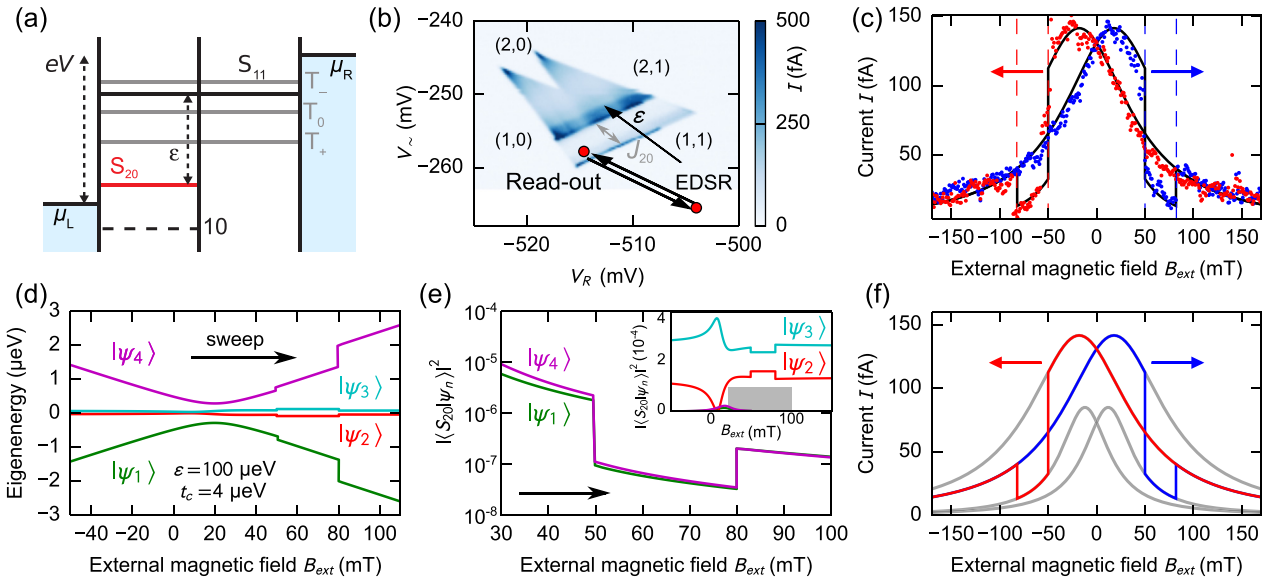

FIG. 2. (Color online) (a) Sketch showing the relevant two-electron levels of the double QD in Pauli-spin blockade and the lead chemical potentials ($\mu_R - \mu_L = 1$ meV). All horizontal lines depict chemical potentials, vertical lines indicate tunnel barriers, blue areas correspond to occupied states of the degenerate Fermi liquid in the leads. (b) Corresponding charge stability diagram at $\mathbf{B}_{ext} = 0$, presenting the current through the double QD. The numbers of electrons charging the left, right dot in stable areas of the stability diagram are indicated in parentheses. For our EDSR measurements the system was pulsed between the two red dots; details in main text. (c) Current at $\epsilon \simeq 100$ μeV as function of $\mathbf{B}_{ext}$, which was swept at a rate of 30 mT/min. Arrows indicate the sweep directions. (d) Numerically calculated eigenenergies of the (1,1) states of the system Hamiltonian (1) as a function of $\mathbf{B}_{ext}$. $|\psi_{1,4}\rangle$ are almost identical to $T_\pm$ and $|\psi_{2,3}\rangle$ are superpositions of T_0 and S_{11}. For the used parameters, $\epsilon = 100$ μeV and $t_c = 4$ μeV, the (2,0) state has a much lower energy. Vertical steps at $\mathbf{B}_{ext} \simeq 50$, 80 mT indicate discontinuities of $\mathbf{B}_{nm}$ caused by the numerically included switching of the nanomagnets. (e) Overlap of the (1,1) eigenstates shown in (d) with the S_{20} state (which would be zero for the T_{11} states in a homogeneous field): all four states in the inset. The main panel is a magnified view of the gray area. It contains the two states with the smallest overlap, the current limiting bottleneck states (almost $T_\pm$). (f) Sketch of the four current resonances belonging to the four different magnets' configurations. The red and blue line resemble the switching behavior of the actual current in (c) (arrows indicate sweep directions).

cycle $(2,1) \to (1,1) \to (2,0) \to (2,1)$. Nevertheless, the above explanations apply to both cycles, as they are both bottlenecked by the same transition $(1,1) \to (2,0)$ [23].

In previous devices on-chip magnets were separated from the heterostructure by a layer of metal gates and, with the exception of Ref. [22], in addition by a second electrically isolating layer. Here we simplify the structure and bring the magnets closer to the QDs by replacing two gold gates [yellow in Fig. 1(a)], used to define the double QD, by ferromagnetic cobalt gates (blue). Based on simulations with OOMMF [24] we have tailored the stray fields of the magnets and have optimized their geometries and positions to maximize stray field and field gradient between the two dots on the one hand and to guarantee full tunability of the double QD by applying gate voltages on the other hand. The advantage of using two instead of just one magnet is twofold: First, two magnets can be positioned to provide strongly inhomogeneous and different magnetic fields in two adjacent dots [conditions (i) and (ii) above] which facilitates EDSR measurements in both dots. Second, at moderate $\mathbf{B}_{ext}$ two separate magnets allow for two very different stray field distributions across the double QD corresponding to either parallel or antiparallel magnetization of the two magnets (see Fig. 5). The magnetization of each nanomagnet can thereby be reversed by sweeping $\mathbf{B}_{ext}$ beyond its coercive field and antiparallel to its present magnetization. The different width of the two magnets gives rise to individual coercive fields. Consequently, we can choose between parallel and antiparallel magnetization at relatively small $\mathbf{B}_{ext}$.

III. SYSTEM HAMILTONIAN

To model the dynamics of our double QD we assume that an electron localized in the left respective right dot experiences the local magnetic field $\mathbf{B}^{L,R} = \mathbf{B}_{ext} + \mathbf{B}^{L,R}_{nm}$. We thereby neglect the hyperfine interaction between the electron and nuclear spins, the spin-orbit interaction, and the exchange interaction which in our case are all small perturbations compared to the coupling induced by the inhomogeneous $\mathbf{B}_{nm}$. For simplicity we define the average field in the two dots $\overline{\mathbf{B}} = (\mathbf{B}^L + \mathbf{B}^R)/2$, their difference field $\Delta\mathbf{B} = \mathbf{B}^L - \mathbf{B}^R$, and the field operators $\overline{B}_\pm = \overline{B}_x \pm i\overline{B}_y$, $\Delta B_\pm = \left(\Delta B_x \pm i \Delta B_y\right)/2$ akin to spin raising and lowering operators. With the quantization axis $\hat{z}$ defined parallel to $\mathbf{B}_{ext}$, the matrix representation of the (semiclassical) total Hamiltonian in the basis spanned by the diabatic singlet and triplet states $\{T_+, T_0, T_-, S_{11}, S_{20}\}$

is then

$$H = g\mu_B \begin{array}{c} \begin{array}{ccccc} \mathrm{T}_+ & T_0 & \mathrm{T}_- & \mathrm{S}_{11} & \mathrm{S}_{20} \end{array} \\ \left(\begin{array}{ccccc} \overline{B}_z & \overline{B}_-/\sqrt{2} & 0 & -\Delta B_-/\sqrt{2} & 0 \\ \overline{B}_+/\sqrt{2} & 0 & \overline{B}_-/\sqrt{2} & \Delta B_z/2 & 0 \\ 0 & \overline{B}_+/\sqrt{2} & -\overline{B}_z & \Delta B_+/\sqrt{2} & 0 \\ -\Delta B_+/\sqrt{2} & \Delta B_z/2 & \Delta B_-/\sqrt{2} & 0 & t_c/2g\mathbf{B} \\ 0 & 0 & 0 & t_c/2g\mathbf{B} & -\epsilon/g\mathbf{B} \end{array} \right) \end{array} \quad \begin{array}{l} \mathrm{T}_+ = |\uparrow\uparrow\rangle \\ T_0 = (|\uparrow\downarrow\rangle + |\downarrow\uparrow\rangle)/\sqrt{2} \\ \mathrm{T}_- = |\downarrow\downarrow\rangle \\ \mathrm{S}_{11} = (|\uparrow\downarrow\rangle - |\downarrow\uparrow\rangle)/\sqrt{2} \\ \mathrm{S}_{20} = |0,\uparrow\downarrow\rangle, \end{array} \tag{1}$$

where t_c denotes the interdot tunnel coupling between the two dots. The matrix representation (1) illustrates that the x and y components of the difference field $\Delta B_\pm$, mix $T_\pm$ with S_{11}, while the z-component ΔB_z mixes T_0 (which has no spin component along the z axis). The average field $\overline{\mathbf{B}}$ yields the Zeeman splitting of the spin-up versus spin-down states. Note that the off-diagonal terms $\overline{B}_\pm$, which mix $T_\pm$ with T_0, vanish if the quantization axis is chosen parallel to $\overline{\mathbf{B}}$ instead of $\mathbf{B}_{\mathrm{ext}}$.

Hyperfine and spin-orbit interaction would both contribute to various matrix elements including the singlet-triplet coupling constants. In our case, however, the latter are far dominated by the time independent difference field (and we formally neglect the former contributions). In this way the nanomagnets provide a stabilization mechanism for appropriate qubit implementations which could increase the qubit coherence time in spite of the presence of nuclear spins or spin-orbit interaction. To fully determine our double QD hybrid system we need to know the nanomagnet's strayfield as a function of $\mathbf{B}_{\mathrm{ext}}$ at the position of the two dots, the interdot tunnel coupling t_c and the Lande g factor inside the dots g. In the following we will employ dc current measurements and EDSR experiments to achieve this goal.

IV. DIRECT CURRENT MEASUREMENTS

To experimentally determine the coercive fields of our nanomagnets we have measured the leakage current I through the spin-blockaded double QD while slowly sweeping $\mathbf{B}_{\mathrm{ext}}$ at constant detuning $\epsilon \simeq 100$ μeV. The current at this configuration is sensitive to the mixing of the singlet and triplet states [3] and can be used to detect changes of the magnetic field differences between the QDs [22].

In such a sweep experiment the current $I(\mathbf{B}_{\mathrm{ext}})$ might be influenced by dynamic nuclear spin polarization (DNSP) which can give rise to hysteresis as a function of the sweep direction of $\mathbf{B}_{\mathrm{ext}}$ [22,25,26]. However, it is also possible to avoid DNSP effects by preparing a fixed point at very weak polarization [22]. The presence of DNSP effects generally gives rise to specific long time dependencies in the current upon changing $\mathbf{B}_{\mathrm{ext}}$, ϵ, or V [22,25,26]. We indeed found intriguing DNSP effects under certain conditions in this sample which will be the topic of a future publication. We carefully assured that here and in the EDSR experiments discussed below, DNSP is unimportant and the apparent hysteresis of the measured $I(\mathbf{B}_{\mathrm{ext}})$ visible in Fig. 2(c) has a different reason: it is related to the four distinct configurations of the magnets, each of which can be magnetized parallel or antiparallel to $\mathbf{B}_{\mathrm{ext}}$.

In Fig. 2(c) we present $I(B_{\mathrm{ext}})$ for two sweeps in opposite directions ($dB_{\mathrm{ext}}/dt = \pm 30$ mT/min). We have started the sweeps at large $|B_{\mathrm{ext}}|$ to ensure that both magnets are magnetized parallel to $\mathbf{B}_{\mathrm{ext}}$. The current maxima near $\mathbf{B}_{\mathrm{ext}} = 0$ occur where all three T_{11} states are close to resonance with S_{11}. This is a consequence of Pauli-spin blockade where the leakage current is governed by the singlet-triplet couplings: the T_{11} triplets mix with S_{11} and because S_{11} is tunnel coupled to the other singlet S_{20}, the T_{11} triplets mix also with S_{20}. These mixings are strongest near the mutual resonances between S_{11} and T_{11} and zero far away from the corresponding resonances. As $|B_{\mathrm{ext}}|$ is increased the T_+ and T_- triplets are more and more detuned from S_{11}, their mixing with S_{20} also decreases, their decay ($\mathrm{T}_{11} \rightarrow \mathrm{S}_{20}$) slows down and they become the current limiting bottleneck states. Consequently, the current decreases. To illustrate this connection we numerically diagonalized the Hamiltonian in Eq. (1) and plot in Fig. 2(d) the energies of the four relevant (1,1) eigenstates versus B_{ext} for a sweep from negative to positive fields. The apparent avoided crossing at $B_{\mathrm{ext}} \simeq 20$ mT marks the point of minimal $\mathbf{B}_{\mathrm{ext}} + \mathbf{B}_{\mathrm{nm}}$, where $\overline{B}_z = 0$. This field coincides with the current maximum for $dB_{\mathrm{ext}}/dt > 0$ [blue in Fig. 2(c)], because here the $\mathrm{T}_\pm$-S_{20} mixing has its maximum. For $dB_{\mathrm{ext}}/dt < 0$ the nanomagnets would be magnetized in the opposite direction and the current maximum would occur at $B_{\mathrm{ext}} \simeq -20$ mT [as observed in the according measurement, red in Fig. 2(c)].

Continuing the sweep, we further increase $\mathbf{B}_{\mathrm{ext}}$ beyond the respective coercive fields of the two magnets where their magnetizations reverse and become again parallel to $\mathbf{B}_{\mathrm{ext}}$. This change of magnetization instantly rearranges the overall magnetic field at the QDs and causes a steplike characteristic of the eigenenergies at the coercive fields. We show below that because of the direct relation between the singlet-triplet mixing and the nanomagnets' configuration, this leads to the sudden changes of the measured current observed in Fig. 2(c), where we find coercive fields at $B_{\mathrm{ext}} \simeq 50$ mT for the wider and $B_{\mathrm{ext}} \simeq 80$ mT for the narrower magnet. These coercive fields are included in the numerics of Fig. 2(d).

We remark that the observed current jumps occur very abruptly as a function of $\mathbf{B}_{\mathrm{ext}}$. This underlines that the nanomagnets are single domain and the single-domain switches as a whole once the coercive field is reached.

To phenomenologically explain the current $I(B_{\mathrm{ext}})$ in Fig. 2(c), we assume four distinct current maxima corresponding to the four possible configurations of our nanomagnets. By sweeping $\mathbf{B}_{\mathrm{ext}}$ we can switch between these configurations which causes the actual current to jump between the four maxima at the corresponding coercive fields. This simple,

TABLE I. (Color online) Magnetic field components generated by the two nanomagnets (for parallel [⇉] vs antiparallel [⇄] magnetization) at the approximate QD positions marked in Fig. 5 by corresponding circles. Field values are calculated with OOMMF [24]; field strengths derived from measured EDSR resonances in parentheses.

Magnetiz.	QD	$B_{\rm nm}\|_x$	$B_{\rm nm}\|_y$	$B_{\rm nm}\|_z$	ΔB_x	ΔB_y	ΔB_z
Configuration I (single EDSR resonance)—$B_{\rm nm}$ (mT)							
⇉	L ●	−15	6	17 (19)	−3	7	5
	R ●	−12	−1	22			
⇄	L ●	−2	−7	9 (12)	1	2	8
	R ●	−3	−5	17			
Configuration II (two EDSR resonances)—$B_{\rm nm}$ (mT)							
⇉	L ●	14	19	10 (9)	−1	7	40 (46)
	R ●	13	26	50 (55)			
⇄	L ●	−10	−11	10	18	30	38
	R ●	8	29	48			

yet reasonable model is displayed in Fig. 2(f), where we plot two pairs of Lorentzians (gray) reflecting the symmetry properties of the problem. The larger maxima correspond to the parallel and the smaller ones to the antiparallel magnets' configurations. For better comparability with our measurements we have added two colored curves which mimic the actual current jumps between the Lorentzians. The identical curves are also shown in Fig. 2(c) as black lines, where they reveal good agreement with the measured data. The two Lorentzians describing the parallel or antiparallel magnets' configurations, respectively, are equal in amplitude and width. Most interesting is the observation that the overall current through the QD is considerably smaller if the two magnets are polarized antiparallel to each other compared to their parallel configurations. It suggests that the antiparallel magnetization causes a smaller singlet-triplet mixing of the bottleneck triplets $T_\pm$ than the parallel configuration. From our Hamiltonian in Eq. (1) we see that the coupling between the $T_\pm$ states and the singlet subspace is proportional to the difference of the magnetic field component perpendicular to the quantization axis (approximately parallel to $\mathbf{B}_{\rm ext}$) between the two QDs. Thus it suggests that the perpendicular component of the field difference between the two QDs is smaller when the magnetization of the magnets is antiparallel compared to the parallel configurations. To check this, we have approximately determined the location of the two QDs (as depicted in Fig. 5 below) taking into account the numerically calculated $\mathbf{B}_{\rm nm}$ combined with results of the EDSR measurements (discussed below), the gate voltage configuration (referred to as configuration I), and the measurement in Fig. 2(c). This information provides the magnetic field components in our Hamiltonian in Eq. (1) (see Table I) and allows us to calculate its eigenenergies, shown in Fig. 2(d), as well as the mixings between the four (1,1) states and S_{20}. The latter are visualized in the inset of Fig. 2(e) as a function of $B_{\rm ext}$ swept from negative towards positive fields. The main panel is a magnification showing the mixings of the two bottleneck states $T_\pm$ near the current steps in Fig. 2(c). It also shows a steplike characteristic at the coercive fields of the two magnets and is considerably reduced for the magnets in their antiparallel configuration, namely between the two coercive fields. This strengthens the Pauli-spin blockade and explains the reduced current for the antiparallel configuration of the nanomagnets in between the current steps in Fig. 2(c). We close this section by noting that an accurate prediction of the current which depends on $\mathbf{B}_{\rm nm}$, $\mathbf{B}_{\rm ext}$, ϵ, and $t_{\rm c}$ would require a detailed density matrix calculation which goes beyond the scope of this article.

V. ELECTRIC-DIPOLE-INDUCED SPIN RESONANCE MEASUREMENTS

Mixing between any two singlet and triplet states is strongly enhanced where their eigenenergies are nearly equal. If detuned from this resonance, it is possible to actively drive transitions between two levels in an EDSR experiment which regains the resonance condition by applying a proper rf magnetic field. We have performed our EDSR measurements in the (1,1) configuration with $\epsilon \simeq -100t_{\rm c}$ [lower red dot in Fig. 2(b)], where the two electrons are strongly localized in the two respective dots. Consequently, we expect to find two distinct EDSR resonances at the respective Zeeman energies in the two dots:

$$hf = |g\mu_{\rm B}\mathbf{B}^{\rm L,R}| \simeq g\mu_{\rm B}\left(B_{\rm ext} + B^{\rm L,R}_{\rm nm}|_z\right), \qquad (2)$$

where f is the modulation frequency, h is the Planck constant, and $B^{\rm L,R}_{\rm nm}|_z$ is the z component of $|\mathbf{B}^{\rm L,R}_{\rm nm}|$. The approximation in Eq. (2) is fair for $(B_{\rm ext} + B^{\rm L,R}_{\rm nm}|_z)^2 > B^{\rm L,R}_{\rm nm}|^2_x + B^{\rm L,R}_{\rm nm}|^2_y$. $B_{\rm ext}$ and $B^{\rm L,R}_{\rm nm}|_z$ can have identical or opposite signs depending on the magnets configuration. The resonance condition Eq. (2) allows us to directly probe the g factor as well as the z component of $\mathbf{B}_{\rm nm}$ in the two dots and therefore also ΔB_z.

Our experimental EDSR sequence is sketched in Fig. 3(a). We start at $\epsilon \gtrsim 0$ in the Pauli-spin blockade [upper red dot in Fig. 2(b)], which initializes the double QD with equal probabilities in one of the bottleneck states T_+ or T_-. [The other two (1,1) states, T_0 and S_{11}, decay quickly if occupied and eventually the system stalls in T_+ or T_-.] After 800 ns we isolate the two electrons by pulsing the double QD deep into Coulomb blockade to $\epsilon \simeq -100t_{\rm c}$ [lower red dot in Fig. 2(b)] by changing the gate voltages $V_{\rm R}$ and $V_\sim$ [see Fig. 1(a)] within $\simeq$2 ns. To avoid pulse transients effects we next wait 200 ns before we modulate $V_\sim$ for 500 ns with a sine wave which

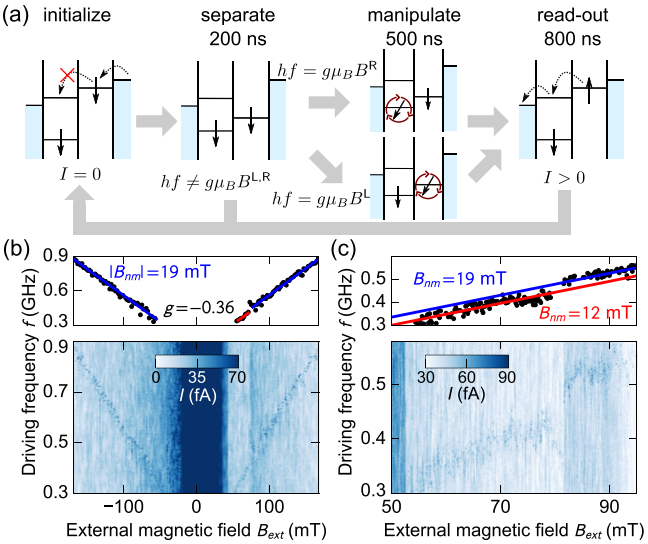

FIG. 3. (Color online) (a) EDSR measurement scheme, from left to right: initialization in Pauli-spin blockade → separation of the QD states from the leads (Coulomb blockade) → EDSR manipulation by rf-modulation of gate voltage → read-out ($I > 0$ for EDSR resonance) and re-initialization. (b) Current $I(B_{\rm ext}, f)$ through the DQD (bottom panel) and position of current maxima at EDSR resonance (top panel) while driving with the pulse sequence shown in (a). (c) Same as (b) but high resolution measurement near the coercive field of the left magnet $B_{\rm c}^{\rm L} \sim 80$ mT, where the resonance line forms a step.

causes both electrons to oscillate in real space. Due to the inhomogeneous $\mathbf{B}_{\rm nm}$ this rf modulation directly translates into oscillations of both $\mathbf{B}^{\rm L}$ and $\mathbf{B}^{\rm R}$. Finally, we pulse back to our starting point at $\epsilon \gtrsim 0$ for read-out. If the rf modulation in both dots is off-resonant the double QD stays in Pauli-spin blockade and no current flows. However, if the resonance condition Eq. (2) is fulfilled for one of the two electrons during the rf modulation, the S_{11} singlet state becomes occupied with a finite probability. As a consequence the Pauli-spin blockade is lifted during read-out. Performing a steady state measurement by periodically repeating this sequence at a frequency of $\simeq$670 kHz we then measure a small leakage current.

Typical results of such measurements are presented in Figs. 3(b) and 3(c), where the leakage current is plotted as function of $B_{\rm ext}$ and f. At $B_{\rm ext} \simeq 0$ the Pauli-spin blockade is lifted even without applying an rf modulation as already seen in Fig. 2(c) and discussed there. This effect gives rise to the broad frequency independent current maximum at $B_{\rm ext} \simeq 0$. The rf modulation, however, generates additional sharp but weak current maxima along straight lines, where the resonance condition in Eq. (2) is fulfilled. Whenever $\mathbf{B}_{\rm ext}$ causes one of the nanomagnets to reverse its magnetization the resonance frequency suddenly increases according to the increase of the Zeeman energy. In Fig. 3(b) $B_{\rm ext}$ was stepped from negative towards positive fields and hence the nanomagnets reverse their magnetizations at the positive fields, $B_{\rm ext} \simeq 50, 80$ mT. Figure 3(c) shows a high resolution measurement of part of Fig. 3(b). It reveals one of the expected jumps in resonance frequency at $B_{\rm ext} \simeq 80$ mT. Linear fits according to Eq. (2) suggest $|g| = 0.36 \pm 0.01$ and $B_{\rm nm}^{\rm L}|_z = 19 \pm 1$ mT if both magnets

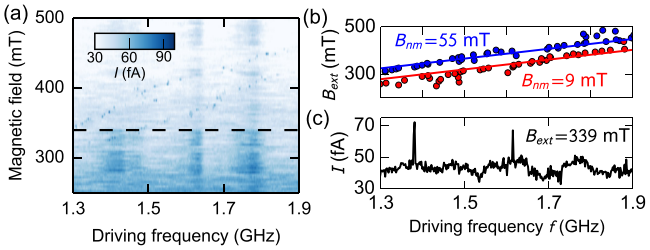

FIG. 4. (Color online) Coexistence of two EDSR resonances: (a) $I(B_{\rm ext}, f)$ through the DQD as in Figs. 3(b) and 3(c) but for a different gate voltage configuration (configuration II). (b) Position of the current maxima at EDSR resonances in (a). Lines indicate fits with Eq. (2). (c) Typical current trace at constant $\mathbf{B}_{\rm ext}$ along dashed line in (a).

are magnetized parallel to $\mathbf{B}_{\rm ext}$ and $B_{\rm nm}^{\rm L}|_z = 12 \pm 1$ mT if the narrower magnet (with the larger coercive field) is aligned antiparallel to $\mathbf{B}_{\rm ext}$.

Technical remark: To hereby determine the values of $|g|$ and the fields of the nanomagnets we have applied the linear least squares fitting method to our EDSR resonances as those shown in the upper panels of Fig. 3, averaging the virtually identical values for positive versus negative magnetic field. The slope of these fits gives the g factor and the offsets the field of the nanomagnets. From comparing measurements with mutually opposite sweep direction of $B_{\rm ext}$ and for various histories of $B_{\rm ext}(t)$ we exclude a possible hysteresis of the external magnet that could, in principle, cause an additional horizontal shift of the EDSR resonances.

We close the discussion of Figs. 3(b) and 3(c) with two remarks: first, the switching of the large magnet cannot be observed in this measurement because it is masked by the broad current maximum around $B_{\rm ext} = 0$. Second, in Figs. 3(b) and 3(c) we find only one EDSR resonance for this particular gate voltage configuration (configuration I). We will show below that it belongs to the left QD and under which conditions a second EDSR resonance can be observed.

In Fig. 4 we present a second EDSR measurement after retuning the double QD such that each QD is situated in close proximity to one of the two magnets. In this gate voltage configuration (II) the antiparallel magnetization of the nanomagnets did not result in clear EDSR resonances because of strong effects of DNSP at the required weak $\mathbf{B}_{\rm ext}$ values. Fortunately, the parallel magnetization of the nanomagnets allows for EDSR measurements at higher magnetic fields where DNSP is weak. In this regime we find two distinct EDSR resonances as can be seen in the raw data in Fig. 4(a) plotting $I(B_{\rm ext}, f)$, in Fig. 4(b) indicating the positions of sharp current maxima in Fig. 4(a) and also in Fig. 4(c) presenting a single frequency trace at constant $\mathbf{B}_{\rm ext}$. The latter contains two sharp current maxima clearly indicating two distinct EDSR resonances. Fitting Eq. (2) yields the same $|g| = 0.36 \pm 0.02$ as above, but $B_{\rm nm}^{\rm L}|_z = 9 \pm 2$ mT and $B_{\rm nm}^{\rm R}|_z = 55 \pm 3$ mT. The assignment of the EDSR resonances to either the left (L) or the right (R) QD is thereby based on our OOMMF simulations of $\mathbf{B}_{\rm nm}$.

In Figs. 5(a) and 5(b) we plot the $\mathbf{B}_{\rm nm}|_z$ component which is relevant for the $T_\pm \leftrightarrow S_{11}$ transitions considered here for

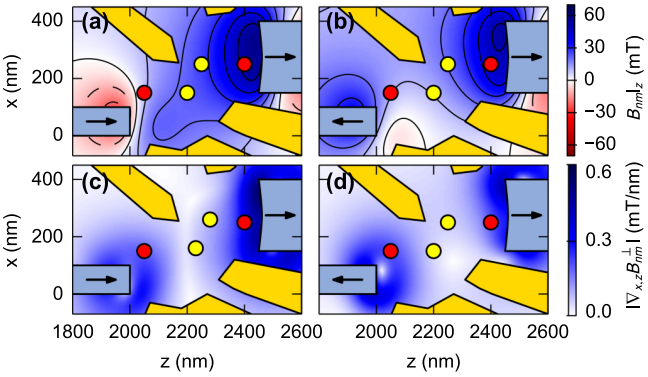

FIG. 5. (Color online) OOMMF simulations of $\mathbf{B}_{\rm nm}$ [24]. Magnetic field component $\mathbf{B}_{\rm nm}|_z$ along $B_{\rm ext}$ (z axis) for (a) parallel and (b) antiparallel magnetization of the two nanomagnets. $\mathbf{B}_{\rm nm}|_z$ is relevant for the EDSR resonance condition, Eq. (2). (c) and (d) Absolute value of the gradient of the perpendicular component $\mathbf{B}^{\perp}_{\rm nm}$ within the plane of the 2DES; $\mathbf{B}_{\rm nm} = \mathbf{B}_{\rm nm}|_z + \mathbf{B}^{\perp}_{\rm nm}$. The EDSR signal strength scales with $|\nabla_{x,z}\mathbf{B}^{\perp}_{\rm nm}|$. Colored circles in (a)–(d): Approximate QD center positions for the two different gate voltage tunings. Arrows indicate nanomagnets polarization directions.

the two cases, a parallel and an antiparallel magnetization of the nanomagnets.

Comparing our numerical results with our EDSR measurements we find the approximate center coordinates of the QDs, which are marked as red circles in Figs. 5(a)–5(d). The used gate voltages are in agreement with these locations, where details also depend on the disorder potential. The yellow circles in Figs. 5(a)–5(d) indicate the approximate positions of the QDs for the previous gate voltage configuration (I) discussed above.

The strength of each EDSR resonance [i.e., the height of each current maximum in Fig. 4(c)] should scale with the absolute value of the local gradient of the magnetic field component perpendicular to $\mathbf{B}_{\rm ext}$, i.e., $\mathbf{B}^{\perp}_{\rm nm}$, along each electron oscillation path caused by the rf modulation. As we do not know the exact pathways we plot in Figs. 5(c) and 5(d) the absolute value of the two-dimensional derivative within the plane of the 2DES, $|\nabla_{x,z}\mathbf{B}^{\perp}_{\rm nm}|$. The red circles in Figs. 5(c) and 5(d) are clearly near derivative extrema while the situation is not so clear for the yellow circles. This observation provides a possible explanation for the missing second EDSR resonance in our first gate voltage configuration (yellow circles). There we can assign the observed resonance to the left QD as the simulated $\mathbf{B}_{\rm nm}$ at the position of the left QD fits to the EDSR results for both magnet configurations but that of the right QD does not.

Our numerical results at the marked QD positions are summarized and compared to our experimental findings in Table I. Interestingly, for the parallel magnetization of the nanomagnets the difference fields ΔB_x and ΔB_y are quite weak compared to ΔB_z, while ΔB_x and ΔB_y are also sizable for the antiparallel magnetization. This implies that the dynamics of the $\mathrm{T}_\pm$ state is quite different for the two cases, as the coupling between $\mathrm{T}_\pm$ and S_{11} is mediated by ΔB_x and ΔB_y. For instance, antiparallel magnetization would be the better choice for defining a qubit based on the states $\mathrm{T}_\pm$ and S_{11}, while the parallel magnetization would be a good choice for a qubit based on T_0 and S_{11}.

VI. SAMPLES WITH ONE NANOMAGNET

In the following we discuss an EDSR measurement of a sample of our previous generation of double QD designs [27]. It contains just one single-domain nanomagnet [see Fig. 6(a)] located on top of a gold gate. The voltage on the same gate is modulated to drive EDSR. This design is especially simple as the magnet axis, the rf-modulated gate and the symmetry axis of the QD (z axis) coincide. It is justified to assume that the gate voltage modulation entails a motion of the QD electrons mostly also along the z axis. Simulations of the nanomagnet shown in Fig. 6(b) reveal a sizable magnetic field gradient at the left QD while it almost vanishes at the right QD at a larger distance to the magnet. Our measurements agree with the simulations and reveal an average field of approximately $|\mathbf{B}_{\rm nm}| \simeq 22$ mT within the left QD and a coercive field of the nanomagnet of 52 ± 2 mT. As in our EDSR experiments, the rf-magnetic field modulation is produced by driving an electron along a time-independent slanting magnetic field, only electrons in the left QD can be manipulated by EDSR. Consequently, in this sample only a single EDSR resonance corresponding to the left QD is expected. This is in contrast to our sample with two nanomagnets, which can be tuned such that a sizable field gradient exists in two QDs giving rise to two EDSR resonances associated with two separate QDs (see Fig. 4). As expected, we find only a single EDSR line in the experiment in Fig. 6(c). The g factor is identical to the one of our previous sample, $g = 0.36 \pm 0.01$, while both samples feature similar QDs based on the same wafer.

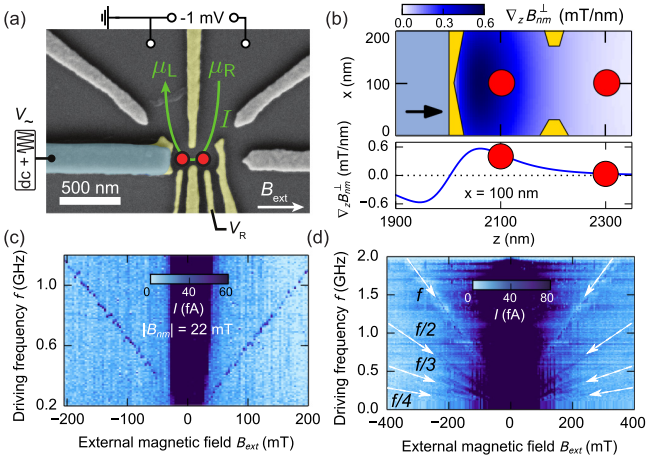

FIG. 6. (Color online) Double quantum dot with one instead of two single-domain nanomagnets reproduced from Ref. [27]. (a) Scanning electron microscope image; color coding analog to Fig. 1(a). (b) OOMMF simulations of the perpendicular field gradient along $\mathbf{B}_{\rm ext}$ aligned with the z axis. This is also the main direction of the rf electron displacement. The lower panel is a horizontal cross section of the color plot at $x = 100$ nm. (c) $I(\mathbf{B}_{\rm ext}, f)$ through the DQD as in Figs. 3(b) and 4(a) showing a single EDSR resonance at a modulation amplitude of $\simeq$15 mV. (d) Multiple EDSR resonances at about twice the modulation power.

In Fig. 6(d) we present a similar EDSR measurement as in Fig. 6(c), but with about twice the modulation power. We observe a transition from a single resonance at $\hbar\omega = g\mu_B B_{ext}$ at small modulation powers in Fig. 6(c) to multiple resonances at $n\hbar\omega = g\mu_B B_{ext}, n = 1,2,\ldots$ for larger modulation powers in Fig. 6(d). Such a behavior can be explained in terms of higher order harmonics generation and has also been observed to such a high order in comparable EDSR experiments in an InAs nanowire based double QD [28] and to second order in another GaAs based double QD [29]. A related example of higher order harmonics generation are Landau-Zener-Stückelberg-Majorana interference oscillations [30,31]. The multiple resonances here (with variable slopes) are fundamentally different from the two resonances (with identical slopes) observed in our previous sample with two nanomagnets discussed above. There they are caused by the different magnetic fields in two QDs and, in contrast to the higher harmonics, observable for low driving powers.

VII. CONCLUSIONS

In summary, we have explored a hybrid nanostructure consisting of a double QD incorporating two single-domain nanomagnets with different coercive fields. The magnets' properties agree well with numerical simulations. By sweeping an external field it is possible to reverse the magnet polarizations one-by-one and to directly measure their coercive fields. The magnetization of each nanomagnet switches almost instantly at its coercive field as expected for a single-domain magnet at very low temperature. Each switching event modifies the local magnetic field distribution and gives rise to a distinct current jump in a dc transport measurement in the Pauli-spin blockade regime. In a radio frequency EDSR experiment the switching of a magnet generates a shift of the resonance frequency. Compared to the larger multiple domain magnets our single-domain magnets generate sizable field gradients even at zero external field and therefore allow experiments in a regime where the relative field difference between adjacent QDs is stronger than the average field. In contrast to magnets with multiple domains, the single-domain nature guarantees a stable field distribution over a large range of external field values. The disadvantage of a somewhat smaller field gradient due to the smaller size of the magnet can be compensated by using multiple single-domain nanomagnets. The combination of several magnets provides a high degree of control of the overall field distribution as the coercive fields of each magnet can be predetermined by design. In summary, coupled QDs including multiple single-domain nanomagnets represent a promising approach for future spin qubit circuits desired for quantum information or related spintronics applications.

ACKNOWLEDGMENTS

We are grateful for financial support from the DFG via SFB-631 and the Cluster of Excellence *Nanosystems Initiative Munich*. S.L. acknowledges support via a Heisenberg fellowship of the DFG.

APPENDIX: METHODS

Magnetic field simulations were carried out with the 3D solver oxsii 1.2a5 of the OOMMF toolkit [24]. A simulation gridsize of 5 nm (in-plane) and 2.5 nm (out-of-plane) was chosen, comparable to the magnetic exchange length of ∼3.5 nm in cobalt. The exchange stiffness of cobalt, 30×10^{-12} J/m, as well as the saturation magnetization, 1.4×10^6 A/m, enter the simulation as external parameters. We included a reasonable 10° correction between the 2DES-plane and the direction of $\mathbf{B}_{ext}$ which provides the best fit to the measured sample characteristics.

[1] D. Loss and D. P. DiVincenzo, Phys. Rev. A **57**, 120 (1998).
[2] J. R. Petta, A. C. Johnson, J. M. Taylor, E. A. Laird, A. Yacoby, M. D. Lukin, C. M. Marcus, M. P. Hanson, and A. C. Gossard, Science **309**, 2180 (2005).
[3] F. H. L. Koppens, J. A. Folk, J. M. Elzerman, R. Hanson, L. H. W. van Beveren, I. T. Vink, H. P. Tranitz, W. Wegscheider, L. P. Kouwenhoven, and L. M. K. Vandersypen, Science **309**, 1346 (2005).
[4] J. M. Taylor, H. A. Engel, W. Dur, A. Yacoby, C. M. Marcus, P. Zoller, and M. D. Lukin, Nat. Phys. **1**, 177 (2005).
[5] Y. Tokura, W. G. van der Wiel, T. Obata, and S. Tarucha, Phys. Rev. Lett. **96**, 047202 (2006).
[6] F. H. L. Koppens, C. Buizert, K. J. Tielrooij, I. T. Vink, K. C. Nowack, T. Meunier, L. P. Kouwenhoven, and L. M. K.Vandersypen, Nature (London) **442**, 766 (2006).
[7] E. A. Laird, C. Barthel, E. I. Rashba, C. M. Marcus, M. P. Hanson, and A. C. Gossard, Phys. Rev. Lett. **99**, 246601 (2007).
[8] K. C. Nowack, F. H. L. Koppens, Y. V. Nazarov, and L. M. K. Vandersypen, Science **318**, 1430 (2007).
[9] R. Hanson, L. P. Kouwenhoven, J. R. Petta, S. Tarucha, and L. M. K. Vandersypen, Rev. Mod. Phys. **79**, 1217 (2007).
[10] M. Pioro-Ladriere, T. Obata, Y. Tokura, Y.-S. Shin, T. Kubo, K. Yoshida, T. Taniyama, and S. Tarucha, Nat. Phys. **4**, 776 (2008).
[11] S. Nadj-Perge, S. M. Frolov, E. P. A. M. Bakkers, and L. P. Kouwenhoven, Nature (London) **468**, 1084 (2010).
[12] T. Obata, M. Pioro-Ladriere, Y. Tokura, Y. S. Shin, T. Kubo, K. Yoshida, T. Taniyama, and S. Tarucha, Phys. Rev. B **81**, 085317 (2010).
[13] Y. S. Shin, T. Obata, Y. Tokura, M. Pioro-Ladriere, R. Brunner, T. Kubo, K. Yoshida, and S. Tarucha, Phys. Rev. Lett. **104**, 046802 (2010).
[14] H. Bluhm, S. Foletti, I. Neder, M. Rudner, D. Mahalu, V. Umansky, and A. Yacoby, Nat. Phys. **7**, 109 (2011).
[15] L. Gaudreau, G. Granger, A. Kam, G. C. Aers, S. A. Studenikin, P. Zawadzki, M. Pioro-Ladriere, Z. R. Wasilewski, and A. S. Sachrajda, Nat. Phys. **8**, 54 (2012).
[16] B. M. Maune, M. G. Borselli, B. Huang, T. D. Ladd, P. W. Deelman, K. S. Holabird, A. A. Kiselev, I. Alvarado-Rodriguez, R. S. Ross, A. E. Schmitz *et al.*, Nature (London) **481**, 344 (2012).
[17] H. Xiaojie, R. Rusko, X. Ming, T. Charles, and J. HongWen, Nat. Commun. **5**, 3860 (2014).

[18] E. Kawakami, P. Scarlino, D. R. Ward, F. R. Braakman, D. E. Savage, M. G. Lagally, M. Friesen, S. N. Coppersmith, M. A. Eriksson, and L. M. K. Vandersypen, Nat. Nano **9**, 666 (2014).

[19] J. Yoneda, T. Otsuka, T. Nakajima, T. Takakura, T. Obata, M. Pioro-Ladrière, H. Lu, C. J. Palmstrøm, A. C. Gossard, and S. Tarucha, Phys. Rev. Lett. **113**, 267601 (2014).

[20] L. Cywinski, W. M. Witzel, and S. Das Sarma, Phys. Rev. Lett. **102**, 057601 (2009).

[21] H. Bluhm, S. Foletti, D. Mahalu, V. Umansky, and A. Yacoby, Phys. Rev. Lett. **105**, 216803 (2010).

[22] G. Petersen, E. A. Hoffmann, D. Schuh, W. Wegscheider, G. Giedke, and S. Ludwig, Phys. Rev. Lett. **110**, 177602 (2013).

[23] The narrow stripe of $|I| > 0$ near $\epsilon = 0$ is weaker for the second triangle. Differences like this in the details of the current amplitudes within the two triangles are often observed. They are a consequence of (i) an asymmetric configuration of the dot-lead tunnel couplings in combination with (ii) the different charge configurations within the two alternative cycles. Such differences can be more or less visible depending on the choice of color scale.

[24] M. Donahue and D. Porter, Interagency Report NISTIR 6376, National Institute of Standards and Technology, Gaithersburg, MD (1999).

[25] K. Ono and S. Tarucha, Phys. Rev. Lett. **92**, 256803 (2004).

[26] T. Kobayashi, K. Hitachi, S. Sasaki, and K. Muraki, Phys. Rev. Lett. **107**, 216802 (2011).

[27] G. Petersen, Ph.D. thesis, Ludwig-Maximilians-Universität München, 2013.

[28] J. Stehlik, M. D. Schroer, M. Z. Maialle, M. H. Degani, and J. R. Petta, Phys. Rev. Lett. **112**, 227601 (2014).

[29] E. A. Laird, C. Barthel, E. I. Rashba, C. M. Marcus, M. P. Hanson, and A. C. Gossard, Semicond. Sci. Technol. **24**, 064004 (2009).

[30] F. Forster, G. Petersen, S. Manus, P. Hänggi, D. Schuh, W. Wegscheider, S. Kohler, and S. Ludwig, Phys. Rev. Lett. **112**, 116803 (2014).

[31] J. Danon and M. S. Rudner, Phys. Rev. Lett. **113**, 247002 (2014).

6 Dynamic nuclear spin polarization: Multistability and spin diffusion enhanced lifetimes

---

This chapter presents the results of

- Forster, F. *et al. Phys. Rev. B. 92.* 245303 (2015)

See section D for the contributions of each author.

6.1 Overview

In this chapter, we analyse the complex dynamics of nuclear spins interacting with electrons in a DQD in the presence of the highly inhomogeneous magnetic field distribution characterized in chapter 5. We polarize the nuclear spin bath dynamically via hyperfine interaction by driving a current through the DQD in PSB which causes the nuclear spins to arrange at one of a number of possible fixed points of their polarization distribution. By increasing an external magnetic field we can increase and modify the nuclear spin polarization. We use EDSR to directly measure the nuclear spin polarization and to monitor its decay. Combining two on-chip nanomagnets with dynamic nuclear spin polarization and EDSR is a new approach and our studies go well beyond previous experimental investigations of the nuclear spin dynamics in lateral QDs. We present a number of interesting observations: We establish multiple (at least 4) stable fixed points differing by their spatial nuclear spin distribution. The fixed points are stable but occur in subsequent measurements with nominally identical settings in random order, the reason possibly being related to random fluctuations in the initial conditions of the sweep related to charge noise or the residual nuclear fields. Nuclear spin diffusion is slowed down by the strongly inhomogeneous magnetic field generated by the nanomagnets. This leads to a quite stable cloud of nuclear spin polarization inside the dots but also in their surroundings, substantially slowing down the decay of nuclear spin polarization.

6.2 Theory

6.2.1 Nuclear spin bath

So far we treated the DQD as an isolated system only tunnel coupled to electron reservoirs. In a real solid state based DQD, the interactions with its environment can become crucial. If the atoms of the host material carry a nuclear spin, which is the case for all isotopes of the III-V semiconductor GaAs, the electron spins will interact with the nuclei via the hyperfine interaction [38]. In addition, the nuclei interact directly with each other, most prominently through magnetic dipole-dipole interaction among nuclear spins [39]. The quantum mechanical interaction of the electron with the multitude of nuclei can in principle lead to a complex entanglement between all particles and can give rise to exciting and complex many-body quantum physics involving both the electrons in the DQD and the nuclei (e.g. ref. [40–42]). However, the quantum mechanical treatment of the complete problem is consequently challenging and still under active research

in theory. To nevertheless make progress, we use a semi-classical model of the nuclear spin bath which can already explain many key observations of the experiments [4].

Let us consider the contact hyperfine interaction of one electron localized in a single QD. Since the confinement potential of the QD extents over many lattice positions of the host material, $N \simeq 10^6$ nuclei for the lateral QDs discussed here, the Hamiltonian consists of the sum of the hyperfine interaction between the electron and each individual nuclear spin [4, p. 1240],

$$H_{\mathrm{HF}} = \sum_k^N A_k \mathbf{I}_k \cdot \mathbf{s}, \tag{6.1}$$

where $\mathbf{s}$ is the spin operator for the electron and $\mathbf{I}_k$ the one for the k-th nucleus. The amplitude of each interaction A_k scales proportionally to the overlap squared of the wavefunction of the electron and the one of the nucleus k and depends on the isotope of the specific nucleus [38]. This renders the hyperfine interaction of electrons in GaAs important, since their s-like orbitals have a large overlap with the nuclei. In contrast, the contact hyperfine interaction for holes in the same material is much weaker due to their p-like orbital wavefunction [4, pp. 1240f]. Semi-classically, we neglect the quantum correlations between the electron and the nuclei and replace the operators $\mathbf{I}_k$ in (6.1) by its expectation value $\bar{\mathbf{I}}_k$ with $\bar{I}_k = 3/2$ in GaAs. We then write the semi-classical Hamiltonian as

$$H_{\mathrm{HF}} = \left(\sum_k^N A_k \bar{\mathbf{I}}_k \right) \cdot \mathbf{s} = \frac{g\mu_B}{\hbar} \mathbf{B}_{\mathrm{nuc}} \cdot \mathbf{s},$$

where the classical vector $\mathbf{B}_{\mathrm{nuc}}$ describing the nuclear interaction regarding the electron is an effective magnetic field, the so called Overhauser field [43]. Since the electron dynamics are much faster compared to the dynamics of $\mathbf{B}_{\mathrm{nuc}}$, the mean field approximation of a quasistatic $\mathbf{B}_{\mathrm{nuc}}$ is justified [44, 45]. Within the mean-field approach, we replace the interaction constant of each individual nucleus A_k with an average interaction constant A reflecting the natural abundance ν_i of the isotope type per nucleus (^{69}Ga: 0.3; ^{71}Ga: 0.2; ^{75}As: 0.5) and the average overlap of the wavefunction for each isotope $\overline{A_i}$ (^{69}Ga: 74 µeV; ^{71}Ga: 96 µeV; ^{75}As: 86 µeV [46]). The averaged interaction constant A is then calculated as the averaged root mean square of A_i, $A = \sqrt{\sum_i \nu_i \overline{A_i^2}} = 85\,\mu\mathrm{eV}$ [47]. The maximum value of $\mathbf{B}_{\mathrm{nuc}}$ is reached, when all nuclear spins are aligned (all $\bar{\mathbf{I}}_k$ are equal). The Overhauser field is then

$$B_{\mathrm{nuc}}^{\mathrm{max}} = \frac{\bar{I} A}{|g| \mu_B} = \frac{3/2 \cdot 85\,\mu\mathrm{eV}}{0.36 \mu_B} = 6.1\,\mathrm{T}.$$

We find that the size of the Overhauser field for a fully polarized nuclear spin ensemble is significant and exceeds several Tesla in GaAs.

At $\mathbf{B}_{\mathrm{ext}} = 0$, the mean value of the Overhauser field, $\langle \mathbf{B}_{\mathrm{nuc}} \rangle$, vanishes in thermal equilibrium, but the effective strength of the Overhauser field determined by its fluctuations $\sqrt{\langle \mathbf{B}_{\mathrm{nuc}}^2 \rangle} \sim B_{\mathrm{nuc}}^{\mathrm{max}} / \sqrt{N} \simeq 1\,\mathrm{mT}$ remains finite [16]. At $\mathbf{B}_{\mathrm{ext}} \neq 0$, the thermal distribution of nuclear spins causes a non-vanishing $\langle \mathbf{B}_{\mathrm{nuc}} \rangle$, but plays a negligible role considering the magnetic fields in our experiments: Even at cryogenic temperatures of 10 mK, the thermal energy ~1 µeV exceeds the nuclear Zeeman energy splitting, e.g. ~30 neV at 10 T, by far.

In conclusion, we obtain a finite effective magnetic field in each quantum dot due to the fluctuations, yielding the semi-classical hyperfine Hamiltonian for the DQD as

$$H_{\mathrm{HF}} = \frac{g\mu_B}{\hbar} \left(\mathbf{B}_{1,\mathrm{nuc}} \cdot \mathbf{s}_1 + \mathbf{B}_{2,\mathrm{nuc}} \cdot \mathbf{s}_2 \right),$$

where $\mathbf{B}_{1,\mathrm{nuc}}$ is the Overhauser field in the first, and $\mathbf{B}_{2,\mathrm{nuc}}$ the one in the second quantum dot. This Hamiltonian is analogous to H_{mag} (2.9) and has similar consequences for the electronic term-scheme: Even

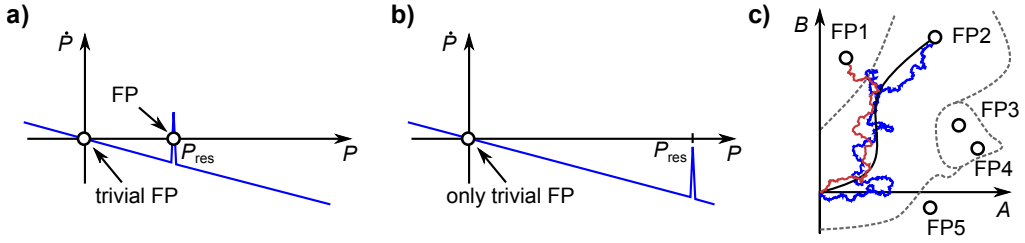

Figure 6.1: a) Result of a simple phenomenological model describing the dynamics of nuclear spin polarization P. It includes a polarization resonance at P_{res} and a constant decay rate and results in a stable fixed point (FP) defined by $\dot{P} = 0$ and $\ddot{P} < 0$ at finite P alongside the trivial fixed point at $P = 0$. In this simple model, the change of polarization depends only on a single variable, the polarization itself. b) Same as a, but for a different value of P_{res}. Here, only the trivial FP exists. c) Sketch of a 2D phase space where $\dot{P}$ depends on two independent variables A and B. Dashed gray lines separate regions, in which a different FP is most attractive. A trajectory towards FP 2 without fluctuations of the dynamic variables is shown in black. Stochastic fluctuations of A and B induced by the environment can disturb the trajectory and can lead to different ones, e.g. the ones in blue and red colour. Fixed points close to the undisturbed trajectory can potentially be reached because of fluctuations as sketched for the red curve.

without the presence of a real magnetic difference field $\Delta\mathbf{B}$, the singlet and triplet subsystems are coupled by the Overhauser field difference, and PSB is partially lifted.

In addition to the electron-nuclear interaction discussed above, the nuclear dipolar and quadrupolar interactions influence the Overhauser fields in the DQD. These mechanisms cause flip-flop processes between nuclear spins and can therefore lead to a spatial redistribution of nuclear spins [47]. In particular, it opens a decay channel for polarized nuclear spins through nuclear spin diffusion [39]. In this thesis, we apply a phenomenological rate model to describe a free decay of spin polarization (see below). We will, however, also find that this simple model can only partly explain our observations in the experiment.

6.2.2 Dynamic polarization

For the electron dynamics it does not seem to make a difference if the PSB is lifted by a real magnetic field or by an effective one, since both are captured equally in the semi-classical Hamiltonian. However, if the spin blockade is lifted by a flip-flop process of an electron with a nucleus, the overall spin needs to be conserved. As long as the system is completely symmetric, i. e. the spins in the left and in the right dot have equal probability to be flipped either up or down, the net transfer of spin between the electrons and the nuclear bath remains zero. If perfect symmetry is broken in the experiment, asymmetries in the DQD lead to a preferred spin flip direction. This effect can cause a sizeable net-polarization of the nuclear spin bath dynamically generated by a steady current flow through the DQD in PSB. This dynamic nuclear spin polarization (DNSP) can generate sizeable Overhauser fields in the quantum dots which contribute to both $\Delta\mathbf{B}$ and $\overline{\mathbf{B}}$ and therefore lead to complex hysteretic dynamics [30, 48, 49], since both parameters act on the current and therefore on the spin-flip rates themselves [50, 51]. At the same time, nuclear spin diffusion out of the dot depolarizes the nuclear spin ensemble and eventually, a stable steady state is reached, where the net-polarization rate is equal to the decay rate. In the most simple case, the existence of such fixed points (FPs) can be described by a phenomenological model, where the polarization rate Γ is proportional to the current I. When describing isolated current resonances, e.g. the resonance between $|S_+\rangle$ and $|T_-\rangle$ [30] or the EDSR resonance during rf driving [52] at sufficiently large magnetic field, the polarization dependent pump rate $\Gamma(P)$ is only different from zero near a resonance P_{res}, e.g. described by a Lorentzian resonance curve [8]. In addition, a decay of P with a rate $1/\tau$ is assumed which accounts for the diffusion of polarized nuclear spins out of the DQD. Then the rate equation for the dynamics reads [52]

$$\dot{P} = \Gamma(P) - \frac{1}{\tau}P.$$

This simple model results in the prediction sketched in figure 6.1(a): As main feature, we find two stable fixed points ($\dot{P} = 0$ and $\ddot{P} < 0$); the trivial one at zero polarization, but also another one at a finite polarization near P_{res}. The non-trivial FP can vanish, for example if P_{res} is located at larger P as shown in 6.1(b). Here, a larger peak value of Γ would reintroduce the fixed point. In the same spirit, the fixed point could be still found for a longer τ, which determines the slope of $\dot{P}$. While this simple model, in which $\dot{P}$ only depends on the single variable P, successfully predicts the existence of FPs in the polarization dynamics, it is far from complete: The current through the DQD and hence $\dot{P}$ in PSB depends crucially on the electronic spectrum and thus the magnetic field distribution as discussed in chapter 5. In particular, we know that the current is a function of $\overline{\mathbf{B}}$ and $\Delta\mathbf{B}$, which indicates that a single variable might not be sufficient to capture the dynamics of the full system, if $\overline{\mathbf{B}}$ and $\Delta\mathbf{B}$ are independent. Already the assumption of two independent variables A and B leads to a far more complex phase space, where more than one non-trivial FP exists [53], such as sketched in figure 6.1c. While the trajectory through the now 2D phase space is predefined by the attractiveness of each FP, small stochastic fluctations of A and B (of potentially quantum mechanical and classical kind induced by the environment) can lead to deviations between multiple experiments [black and blue curves in fig. 6.1(c)] and can in principle even lead to different fixed points (red curve in 6.1c). In the same spirit, if two or more FPs are very close to each other, blinking between these multistabilities can occur [54]. A common phenomenon is the intrinsic stabilization of the effective magnetic field by the polarization dynamics: Changes in the external (real) magnetic field can be compensated dynamically by the Overhauser field, such that the overall magnetic field remains unchanged [30, 52] which we will use to reach high Overhauser fields inside the DQD.

6.3 Measurement setup

The measurement setup is identical to the one of chapter 5, see section 5.3.

Multistability and spin diffusion enhanced lifetimes in dynamic nuclear polarization in a double quantum dot

F. Forster,[1] M. Mühlbacher,[1] D. Schuh,[2] W. Wegscheider,[3] G. Giedke,[4,5,6] and S. Ludwig[1,7]

[1]*Center for NanoScience and Fakultät für Physik, LMU-Munich, 80539 München, Germany*

[2]*Fakultät für Physik, Universität Regensburg, 93040 Regensburg, Germany*

[3]*Solid State Physics Laboratory, ETH Zurich, 8093 Zurich, Switzerland*

[4]*Max-Planck-Institut für Quantenoptik, 85748 Garching, Germany*

[5]*IKERBASQUE, Basque Foundation for Science, 48013 Bilbao, Spain*

[6]*Donostia International Physics Center, 20018 San Sebastián, Spain*

[7]*Paul-Drude-Institut für Festkörperelektronik, Hausvogteiplatz 5-7, 10117 Berlin, Germany*

(Received 26 August 2015; published 7 December 2015)

The control of nuclear spins in quantum dots is essential to explore their many-body dynamics and exploit their prospects for quantum information processing. We present a unique combination of dynamic nuclear spin polarization and electric-dipole-induced spin resonance in an electrostatically defined double quantum dot (DQD) exposed to the strongly inhomogeneous field of two on-chip nanomagnets. Our experiments provide direct and unrivaled access to the nuclear spin polarization distribution and allow us to establish and characterize multiple fixed points. Further, we demonstrate polarization of the DQD environment by nuclear spin diffusion which significantly stabilizes the nuclear spins inside the DQD.

DOI: 10.1103/PhysRevB.92.245303 PACS number(s): 72.25.Pn, 03.67.−a, 73.63.Kv

In III-V semiconductors the weak hyperfine interaction between nuclear and electron spins has a strong impact on the electron spin dynamics owing to the fact that each conduction band electron interacts with a large number of nuclei [1–4]. This situation can give rise to dynamic nuclear spin polarization (DNSP) [5–14] and exciting many-body quantum physics such as complex hysteretic dynamics [1,5,15], multistabilities [6,16], collectively enhanced transport [17], and dissipative phase transitions [18,19]. However, the thermal fluctuations of nuclear spins, even present at cryogenic temperatures, also cause decoherence of spin qubits [20,21]. Ignoring correlations, the influence of the nuclei on the electron spin dynamics is usually described within a semiclassical mean-field approach, which expresses the nuclear spin polarization in terms of an effective magnetic field for the electron spin, $\mathbf{B}_{\mathrm{nuc}}(\mathbf{r})$, the Overhauser field [22]. In a double quantum dot (DQD) charged by one electron in each dot, thermally fluctuating nuclear spins result in a field difference $\Delta\mathbf{B}_{\mathrm{nuc}}$ in the order of a few mT between the two dots [23]. In equilibrium, the time averages of $\mathbf{B}_{\mathrm{nuc}}(\mathbf{r})$ and $\Delta\mathbf{B}_{\mathrm{nuc}}$ vanish. This fluctuating field nevertheless causes a weak mixing of singlet and triplet states [3,24,25] being explored for quantum information processing [21,26]. To control this mixing, it would be necessary to stabilize the difference of the effective magnetic fields in the two dots, $\Delta\mathbf{B}_{\mathrm{nuc}}$.

Here, we combine DNSP with electric dipole induced spin resonance (EDSR) to study the dynamic polarization of nuclear spins on the one hand, and the decay of the polarization on the other hand. We demonstrate the existence of multiple attractive fixed points (FPs) in the steady-state solution of the driven system, where the decay of $\mathbf{B}_{\mathrm{nuc}}(\mathbf{r})$ is exactly canceled by its dynamical buildup [6,8,27]. Our results demonstrate that the FPs differ from each other by their spatial distributions of $\mathbf{B}_{\mathrm{nuc}}(\mathbf{r})$. Relevant for spin qubit applications, the singlet-triplet mixing of each FP can thereby be fine tuned by adjusting external parameters such as the external field B_{ext} [direction as in Fig. 1(a)] or the energy detuning ε between the two dots [i.e., the singlet configurations (1,1) and (2,0), where (n,m) denotes the number of electrons in the left (n) and right (m) dots]. Attractive FPs in DNSP are often characterized by a narrow nuclear spin distribution, hence sharply reduced nuclear spin fluctuations, which provides possible advantages for the preparation of coupled dots for quantum information applications [2,28]. Our measurements allow us to characterize FPs by their nuclear spin distribution, and their dynamic and static stability. In particular, we show that the diffusion of nuclear spins outside the DQD has a strong influence on the buildup and decay dynamics of their polarization inside the DQD which it further stabilizes. Such an enhanced stability of FPs promises positive impact on the coherence of the electron and nuclear spin states.

I. EXPERIMENTAL SETUP AND TECHNIQUES

Our DQD design, presented in Fig. 1(a), incorporates two single-domain nanomagnets. They generate an additional, static inhomogeneous field $\mathbf{B}_{\mathrm{nm}}(\mathbf{r})$, such that the total effective field difference is $\Delta\mathbf{B}_{\mathrm{eff}} = \Delta\mathbf{B}_{\mathrm{nuc}} + \Delta\mathbf{B}_{\mathrm{nm}}$. In equilibrium, the static $|\Delta\mathbf{B}_{\mathrm{nm}}| \simeq 45$ mT [29] exceeds the fluctuations of $\Delta\mathbf{B}_{\mathrm{nuc}}$ of ~ 2 mT [3] by far, degrading $\Delta\mathbf{B}_{\mathrm{nuc}}$ to a weak perturbation. Important for qubit applications this stabilizes the singlet-triplet splitting and yields advantages in controlling the nuclear spin dynamics [8]. Furthermore, our sizable $\Delta\mathbf{B}_{\mathrm{nm}}$ causes a corresponding separation of the Zeeman energy in the two dots and allows us to resolve EDSR experiments in the individual dots [29]. We operate our DQD in the vicinity of the $(1,1) \leftrightarrow (2,0)$ charge transition. In response to the applied voltage $V = (\mu_{\mathrm{R}} - \mu_{\mathrm{L}})/e = 1$ mV electrons tunnel one by one through the DQD via the cycle $(1,0) \rightarrow (1,1) \rightarrow (2,0) \rightarrow (1,0)$. We measure the resulting current which is, however, strongly suppressed by Pauli spin blockade (PSB) of the transition $(1,1) \rightarrow (2,0)$ [30]. In the stability diagram of our

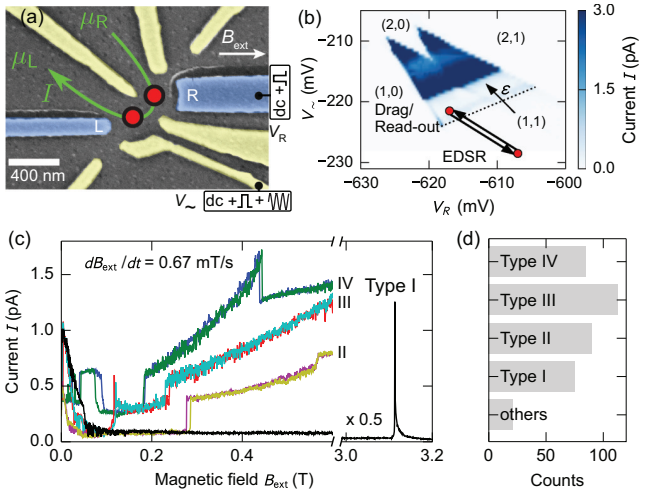

FIG. 1. (Color online) (a) Scanning electron microscope image of a DQD defined in a two-dimensional electron system 85 nm beneath the surface of a GaAs/AlGaAs heterostructure [29]: GaAs surface in gray, gold gates in yellow, cobalt gates in blue. Red circles indicate approximate quantum dot positions, green arrows the physical current direction for $\mu_R > \mu_L$, and a white arrow the direction of B_{ext}. (b) Charge stability diagram $I(V_\sim, V_R)$. An arrow marks the detuning axis, and a dotted line $\varepsilon = 0$. A double arrow indicates pulsing of gate voltages $V_\sim$ and V_R during an EDSR experiment [see labels in (a)]; the modulation $V_\sim = V_\sim^0 + v\ \sin(\omega t)$ with $v \simeq 3$ mV is applied at the red point labeled EDSR. (c) $I(B_{ext})$ as B_{ext} is swept. Variations suggest the existence of multiple FPs. (d) Distribution of current traces $I(B_{ext})$ corresponding to FPs I–IV and "others" (referring to traces which did not fit to types I–IV) detected within 384 sweeps.

DQD in Fig. 1(b), an extended region of PSB is clearly visible as reduced current at the base of the current-carrying double triangle. Details are explained in Ref. [29] for the identical sample.

We follow two complementary approaches to study the nuclear spin dynamics. First, we actively polarize the nuclear spins by sweeping B_{ext} and driving electrons through the DQD. We measure the background leakage current still flowing in PSB, which grows with increasing singlet-triplet mixing being proportional to the components of $\Delta\mathbf{B}_{eff}$ [8] (if we ignore weak influences of cotunneling and spin-orbit interaction). In our second approach, we let $\mathbf{B}_{nuc}(\mathbf{r})$ (produced as described above) decay and directly measure it by performing EDSR. We have experimented with several scenarios, but for better comparability here we discuss only measurements taken under the following conditions: we start with an initialization time $t_{init} = 180$ s with $B_{ext} = V = 0$ at $\varepsilon \simeq 0.1$ meV [red dot in Fig. 1(b) labeled "Drag"; the interdot tunnel coupling is tuned to $t_c \simeq 20\ \mu$eV] to let any remaining $\mathbf{B}_{nuc}(\mathbf{r})$ decay. Next, we apply $V = 1$ mV (at otherwise identical settings) and sweep B_{ext} at the rate 0.67 mT/s to a finite value and then sweep back to zero at -3.3 mT/s. To avoid complications by long-time memory effects, before each measurement series we preconditioned the system with a number of identical sweeps.

II. DYNAMIC NUCLEAR SPIN POLARIZATION – MULTIPLE FIXED POINTS

Figure 1(c) shows $I(B_{ext})$ during typical sweeps to $B_{ext}^{max} = 0.6$ T. Even though we keep dot and sweep parameters identical we find four different characteristic current traces, each one occurring multiple times [Fig. 1(d)] but in arbitrary order. Within each type $I(B_{ext})$ is reproducible, even including sudden current steps and the noise level [see Fig. 1(c)]. The different curve types $I(B_{ext})$ are stable over many minutes (jumps between them occur very rarely at sizable B_{ext}, not more than in one out of 50 sweeps). They strongly depend on B_{ext}, and persist even for very slow sweeps, but are lost if the sweep is performed too fast. We will show below, that the magnetic field sweeps are accompanied by a buildup of sizable (and type-dependent) nuclear polarizations.

Knowing that I scales with $\Delta\mathbf{B}_{eff}$, this all points to corresponding stable FPs with steady-state nuclear spin configurations $\mathbf{B}_{nuc}(\mathbf{r}, B_{ext})$. Traces II–IV contain sudden jumps (within less than a second), which might indicate reproducible transitions between some FPs at specific values of B_{ext}. Before each sweep we let $\mathbf{B}_{nuc}(\mathbf{r})$ decay by setting $V = 0$, hence $I = 0$, where DNSP is absent [and only the trivial FP in equilibrium with $\mathbf{B}_{nuc}(\mathbf{r}) = 0$ is left]. Our experiments indicate that within the first few seconds of $I \neq 0$ the nuclear spins arrange themselves at one of the FPs (even at $B_{ext} = 0$). Figure 1(d) presents a statistics of the rate of different curve types. It suggests that for our settings four FPs are almost equally likely occupied under these conditions. Interestingly, the order at which the different types occur is random, likely being related to random fluctuations. In our case these could be thermal fluctuations of $\mathbf{B}_{nuc}(\mathbf{r}, B_{ext})$ [2,31] or random telegraph noise in the local DQD potential, called charge noise [32–34].

Type I curves [see Fig. 1(c)] are characterized by a reduction of the current from $I \simeq 1$ pA at $B_{ext} \simeq 0$ to $I < 80$ fA at $B_{ext} > 0.1$ T. In Ref. [8], type I has been associated with the resonance between the T_+ triplet and the singlet state (both for one electron in each dot). In our system, the strong reduction of $I(B_{ext})$ implies that especially the components of $\Delta\mathbf{B}_{eff}$ perpendicular to B_{ext} should be reduced to $\Delta B_{eff}^{\perp} \simeq 0$. Likewise, the other FPs with larger currents correspond to more inhomogeneous $\mathbf{B}_{nuc}(\mathbf{r})$ at sizable B_{ext}.

III. FREE DECAY OF NUCLEAR SPIN POLARIZATION

Utilizing EDSR experiments, we can measure the effective magnetic field value to monitor $\mathbf{B}_{nuc}(\mathbf{r})$. Here, we measure its decay in the two dots after we have built up $\mathbf{B}_{nuc}(\mathbf{r})$ by DNSP. As sketched in Fig. 2(a), we start by sweeping B_{ext} to B_{ext}^{max} within t_{sweep} as described above. There, we hold B_{ext} and V constant during $t_{hold} = 120$ s. For the remainder of the experiment we keep $B_{ext} = B_{ext}^{max}$. Next, at $t = 0$, we initiate the decay of $\mathbf{B}_{nuc}(\mathbf{r})$ by switching V off to stop DNSP. After the waiting period t_w, we go back to $V = 1$ mV. If t_w was long enough, the FP is lost and $\mathbf{B}_{nuc}(\mathbf{r})$ continues decaying. To measure this, we perform EDSR by periodically pulsing to $\varepsilon \simeq -0.5$ meV [see Fig. 1(b)] and applying an rf modulation at a fixed frequency to the gate voltage $V_\sim$. Details of our EDSR procedure are explained in Ref. [29]. At $\varepsilon \ll -t_c$ the electrons, confined in the DQD and affected by EDSR, can be considered localized in

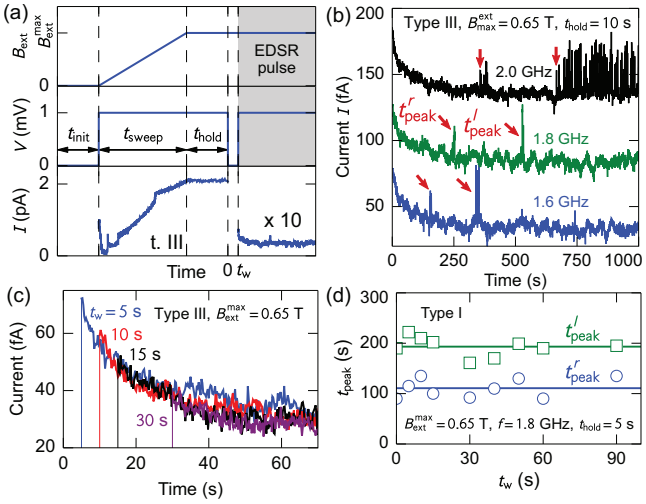

FIG. 2. (Color online) (a) Measuring scheme and an example current trace $I(t)$ (type III); $\mathbf{B}_{nuc}(\mathbf{r})$ begins to decay at $t = 0$ (see main text for details). (b) $I(t)$ during the decay of $\mathbf{B}_{nuc}(\mathbf{r})$ for various EDSR frequencies. Current peaks marked with red arrows indicate EDSR resonances. (For clarity the upper traces are vertically offset in steps of 50 fA.) (c) Initial current decay for various t_w. (d) EDSR resonance times t^r_{peak} and t^l_{peak} as a function of t_w. Horizontal lines are mean values.

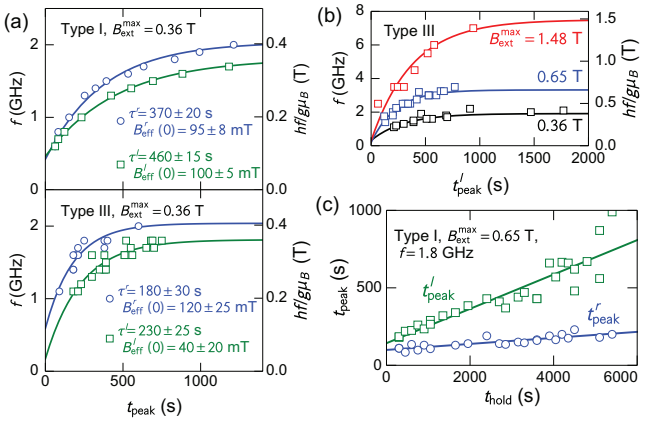

FIG. 3. (Color online) (a) EDSR resonance frequency versus time $f(t_{peak})$: t^r_{peak} (blue, right dot) and t^l_{peak} (green, left dot) for type I (III) curves in the upper (lower) panel. Lines are fits according to Eq. (1). (b) Type III decay curves $f(t^l_{peak})$ for various B_{ext}^{max}. (c) Slowing down the decay of the nuclear spin polarization: $t_{peak}(t_{hold})$.

the individual dots. As long as the rf bursts are off-resonance, I remains small, but whenever $hf = g\mu_B B_{eff}$ in one of the two dots, PSB is lifted and we expect enhanced current.

Typical traces $I(t)$ are plotted in Fig. 2(b) for the case of type III curves for three different frequencies and $B_{ext}^{max} = 0.65$ T. The frequency-independent gradual decrease of I within the first 250 s is related to the decay of $\mathbf{B}_{nuc}(\mathbf{r})$ away from the FP. It indicates that the FP is close to a singlet-triplet resonance, where I has a maximum. On top of this background, we observe current spikes indicating EDSR resonances [arrows in Fig. 2(b)]. Interestingly, we find two distinct resonances per decay curve, the first occurring at t^r_{peak} and the second at t^l_{peak}, which we assign to the right and left dots, respectively (see below). A resonant EDSR experiment can also lead to DNSP (more so at higher frequencies) [6,16,35–37]. The uppermost $I(t)$ curve in Fig. 2(b) measured at $f = 2$ GHz demonstrates this effect, where the second EDSR spike repeats multiple times and causes I to fluctuate strongly. Important for our analysis, no DNSP is induced as long as f is off-resonant. This is always the case in each dot before the corresponding current peak occurs the first time, marking the relevant t^l_{peak} and t^r_{peak}.

For measuring the undisturbed decay of $\mathbf{B}_{nuc}(\mathbf{r})$, it would be desirable to avoid any DNSP effects during the decay. As a continuous $V = 0$ and no rf modulation are no option, we carefully monitor and set up the experiments to avoid unwanted DNSP effects. In particular, we found that the background current does not cause any DNSP away from the FPs: for instance, variations of t_w (at $V = 0$) do not influence the initial decay of $I(t)$ [see Fig. 2(c)]. In addition, t^r_{peak} and t^l_{peak} are independent of t_w as demonstrated in Fig. 2(d). However, a correlation is evident in the jitter between t^r_{peak} and t^l_{peak} (the correlation coefficient is 0.87). Such a behavior is expected if the origin of the fluctuations is related to noise occurring with frequencies small compared to $1/(t^l_{peak} - t^r_{peak})$. This favors charge noise, which has its weight at long-time scales [32–34,38], over the thermal fluctuations of $\mathbf{B}_{nuc}(\mathbf{r})$, which are fast compared to $t^l_{peak} - t^r_{peak}$ [2]. Charge noise modulates the geometry of the confinement potential. The details of the latter determine parameters with a possibly strong impact on the static and dynamic properties of the FPs, including the detuning ε, the positions of the charge centers, consequently $\Delta\mathbf{B}_{nm}$, and the decay of $\mathbf{B}_{nuc}(\mathbf{r})$.

To map out the decay of $\mathbf{B}_{nuc}(\mathbf{r})$ in the two dots, we present t^r_{peak} and t^l_{peak} (x axis) of type I and III curves for various frequencies (y axis) and $B_{ext}^{max} = 0.36$ T in Fig. 3(a). The solid lines are theory curves, where we assume that $\mathbf{B}_{nuc}(\mathbf{r})$ is antiparallel to $\mathbf{B}_{ext}$ (an assumption fully compatible with our data [8]) and decays exponentially, such that

$$hf = \left|g\mu_B\left[B_{ext}^{max} + B_{nm}^z + B_{nuc}^z(t=0)\exp(-t/\tau)\right]\right|, \quad (1)$$

where we replaced vectors by their z components (along the external field), a good approximation for the data in Figs. 3(a) and 3(b) [39]. In accordance with EDSR measurements on this sample [29], we use $g = -0.36$ and $B_{nm}^z = 55$ mT vs 10 mT in the left vs right dot. Note that B_{nm}^z defines the long-time limit of the EDSR frequencies in each dot, and hence also the $t^l_{peak} - t^r_{peak}$ in this limit. The knowledge of $\mathbf{B}_{nm}(\mathbf{r})$ allows us to attribute the two EDSR resonances to the individual dots. We find that both, decay times and $\mathbf{B}_{nuc}(\mathbf{r})$ generally differ from FP to FP and between the two dots, see Fig. 3(a). In these measurements, decay times range from 3 min to almost 8 min, much longer than earlier findings in lateral dots [8,16].

For both types I and III, our measurements show the buildup of a strong nuclear polarization which partially compensates B_{ext} and B_{nm} as evidenced by the small values of B_{eff} [see Fig. 3(a)]. FP I is characterized by a nuclear spin polarization which tends to equalize B_{eff} in the two dots: From the small current, we already concluded that $\Delta B_{eff}^{\perp} \simeq 0$. From our EDSR measurements, we find $B_{nuc}^z = -(270 \pm 5)$ mT

vs $-(320 \pm 9)$ mT in the left vs right dot, corresponding to $\Delta B^{\parallel}_{\rm eff} = (-5 \pm 10)$ mT, hence $\Delta \mathbf{B}_{\rm eff} \simeq 0$. This complete compensation of $\mathbf{B}_{\rm ext} + \mathbf{B}_{\rm nm}(\mathbf{r})$ is surprising as the EDSR measurement is performed at dot positions shifted by $\sim$10 nm compared to where they are during polarization buildup. It is a first indication that nuclear spin polarization diffuses outside the dots. For FP III we find $B^{z}_{\rm nuc} = -(340 \pm 25)$ mT vs $-(290 \pm 20)$ mT in the left vs right dot, corresponding to $\Delta B^{\parallel}_{\rm eff} = (80 \pm 30)$ mT (with statistical errors from the fit procedure). Furthermore, FPs II and IV have similarly large leakage currents as FP III, indicating that these three FPs have in common a relatively large $\Delta \mathbf{B}_{\rm eff}$ at finite $B_{\rm ext}$. Unfortunately, we have not been able to reliably capture EDSR current peaks following DNSP traces II and IV as these resonances turned out to be too unstable.

In Fig. 3(b), we compare decay curves of the later occurring current maximum corresponding to the left dot for FP III and three different values of $B^{\rm max}_{\rm ext}$. We find equal decay times for relatively small $B^{\rm max}_{\rm ext}$, namely, $\tau = 230 \pm 20$ s for $B^{\rm max}_{\rm ext} = 0.36$ T and 0.65 T, but a longer $\tau = 400 \pm 60$ s for 1.48 T. This points to a stabilization mechanism of the nuclear spin polarization inside the dots for longer sweeps.

IV. LIFETIME ENHANCEMENT OF NUCLEAR SPIN POLARIZATION

To further explore the long decay times observed in Fig. 3(a) and the stabilization mechanism evidenced in Fig. 3(b) we continued polarizing with $V = 1$ mV at a fixed $B^{\rm max}_{\rm ext} = 0.65$ T and measured $t^{r}_{\rm peak}$ and $t^{l}_{\rm peak}$ as a function of the additional polarizing time $t_{\rm hold}$. As shown in Fig. 3(c) we find that both current maxima occur later in proportion to the increase of $t_{\rm hold}$. Similar lifetime enhancement of $\mathbf{B}_{\rm nuc}(\mathbf{r})$ was previously observed in bulk GaAs [40] and self-assembled quantum dots [41,42]. Our long polarization lifetimes of many minutes for large $t_{\rm hold}$ and the linear dependence of $t_{\rm peak}$ on $t_{\rm hold}$ confirm a significant polarization of the surroundings of the dots. The large and widely spread magnetic field inhomogeneity caused by our two nanomagnets further increases the lifetime by slowing nuclear spin diffusion via flip-flop processes. The latter are restricted by energy conservation but the nuclear spin state energies depend on the local magnetic and electric (and strain) fields, all having varying gradients throughout the DQD. In our system, the gradient of $B^{z}_{\rm nm}$ is around 0.2–1 mT/nm [29]. The ensuing difference in Zeeman energy between closest homonuclear atoms is several times larger than their nuclear spin dipole-dipole coupling and of the same order as the Knight-field gradient caused by the inhomogeneous electron wave function and estimated to reduce diffusion coefficients by factors of 2–10 [43]. Since the magnetic field gradient extends far beyond the dots [29], it also facilitates the polarization of their surroundings. Increasing $t_{\rm hold}$ from 0 to 100 min causes $t^{l}_{\rm peak}$ to be delayed by more than a factor of 4 while $t^{r}_{\rm peak}$ is only increased by 70 %. We ascribe this difference to asymmetries in geometry and magnetic field in the two dots.

V. CONCLUSION

In summary, we have dynamically polarized nuclear spins at a DQD and combined transport spectroscopy with electric-dipole-induced spin resonance to study the polarization and decay dynamics of nuclear spins. Measuring the leakage current through the DQD in Pauli-spin blockade, we find a remarkably complex current behavior during magnetic field sweeps. The statistical reoccurrence of four patterns in $I(B_{\rm ext})$ establishes the existence of multiple fixed points, one of which is always occupied as long as dynamical polarization is maintained. Our EDSR measurements reveal long decay times of the nuclear spin polarization, its stability being enhanced by the strongly inhomogeneous magnetic field distribution generated by two single-domain nanomagnets in an extended area including the DQD. In addition, the EDSR measurements confirm that the individual FPs substantially differ by their polarizations and dynamics of the nuclear spins. On one hand, our studies demonstrate that the existence of several FPs in dynamical nuclear spin polarization complicates the desired control of electron and nuclear spins in coupled quantum dots. On the other hand, our experiments present a salient advance in our understanding of the hyperfine induced dynamics in nanoelectronic circuits and brings us closer towards the desired fine control of the nuclear spins, important for quantum information applications.

ACKNOWLEDGMENTS

We are grateful for financial support from the DFG via SFB-631 and the Cluster of Excellence *Nanosystems Initiative Munich*. G.G. acknowledges support by the Spanish Ministerio de Economía y Competitividad (MINECO) through the Project FIS2014-55987-P. S.L. acknowledges support via a Heisenberg fellowship of the DFG.

[1] B. Urbaszek, X. Marie, T. Amand, O. Krebs, P. Voisin, P. Maletinsky, A. Högele, and A. Imamoğlu, Rev. Mod. Phys. **85**, 79 (2013).

[2] E. A. Chekhovich, M. N. Makhonin, A. I. Tartakovskii, A. Yacoby, H. Bluhm, K. C. Nowack, and L. M. K. Vandersypen, Nat. Mater. **12**, 494 (2013).

[3] J. M. Taylor, J. R. Petta, A. C. Johnson, A. Yacoby, C. M. Marcus, and M. D. Lukin, Phys. Rev. B **76**, 035315 (2007).

[4] W. A. Coish and J. Baugh, Phys. Status Solidi B **246**, 2203 (2009).

[5] K. Ono and S. Tarucha, Phys. Rev. Lett. **92**, 256803 (2004).

[6] J. Danon, I. T. Vink, F. H. L. Koppens, K. C. Nowack, L. M. K. Vandersypen, and Y. V. Nazarov, Phys. Rev. Lett. **103**, 046601 (2009).

[7] S. M. Frolov, J. Danon, S. Nadj-Perge, K. Zuo, J. W. W. van Tilburg, V. S. Pribiag, J. W. G. van den Berg, E. P. A. M. Bakkers, and L. P. Kouwenhoven, Phys. Rev. Lett. **109**, 236805 (2012).

[8] G. Petersen, E. A. Hoffmann, D. Schuh, W. Wegscheider, G. Giedke, and S. Ludwig, Phys. Rev. Lett. **110**, 177602 (2013).

[9] A. S. Bracker, E. A. Stinaff, D. Gammon, M. E. Ware, J. G. Tischler, A. Shabaev, A. L. Efros, D. Park, D. Gershoni, V. L. Korenev *et al.*, Phys. Rev. Lett. **94**, 047402 (2005).

[10] D. H. Feng, I. A. Akimov, and F. Henneberger, Phys. Rev. Lett. **99**, 036604 (2007).

[11] A. Högele, M. Kroner, C. Latta, M. Claassen, I. Carusotto, C. Bulutay, and A. Imamoglu, Phys. Rev. Lett. **108**, 197403 (2012).

[12] J. Iñarrea and G. Platero, J. Phys. D: Appl. Phys. **41**, 195104 (2008).

[13] M. Gullans, J. J. Krich, J. M. Taylor, H. Bluhm, B. I. Halperin, C. M. Marcus, M. Stopa, A. Yacoby, and M. D. Lukin, Phys. Rev. Lett. **104**, 226807 (2010).

[14] I. Neder, M. S. Rudner, and B. I. Halperin, Phys. Rev. B **89**, 085403 (2014).

[15] C. Latta, A. Högele, Y. Zhao, A. N. Vamivakas, P. Maletinsky, M. Kroner, J. Dreiser, I. Carusotto, A. Badolato, D. Schuh *et al.*, Nat. Phys. **5**, 758 (2009).

[16] I. T. Vink, K. C. Nowack, F. H. L. Koppens, J. Danon, Y. V. Nazarov, and L. M. K. Vandersypen, Nat. Phys. **5**, 764 (2009).

[17] M. J. A. Schuetz, E. M. Kessler, J. I. Cirac, and G. Giedke, Phys. Rev. B **86**, 085322 (2012).

[18] M. S. Rudner and L. S. Levitov, Phys. Rev. B **82**, 155418 (2010).

[19] E. M. Kessler, G. Giedke, A. Imamoglu, S. F. Yelin, M. D. Lukin, and J. I. Cirac, Phys. Rev. A **86**, 012116 (2012).

[20] J. Fischer, M. Trif, W. A. Coish, and D. Loss, Solid State Commun. **149**, 1443 (2009).

[21] H. Bluhm, S. Foletti, I. Neder, M. Rudner, D. Mahalu, V. Umansky, and A. Yacoby, Nat. Phys. **7**, 109 (2011).

[22] A. W. Overhauser, Phys. Rev. **92**, 411 (1953).

[23] $\mathbf{B}_{\mathrm{nuc}}(\mathbf{r})$ is the Overhauser field acting on an electron in the lowest orbital eigenstate of the QD centered at position $\mathbf{r}$. $\Delta\mathbf{B}_{\mathrm{nuc}}$ is the difference of $\mathbf{B}_{\mathrm{nuc}}(\mathbf{r})$ acting on two electrons, each located in one of the dots. $\Delta\mathbf{B}_{\mathrm{nm}}$ below is defined likewise.

[24] F. H. L. Koppens, J. A. Folk, J. M. Elzerman, R. Hanson, L. H. W. van Beveren, I. T. Vink, H. P. Tranitz, W. Wegscheider, L. P. Kouwenhoven, and L. M. K. Vandersypen, Science **309**, 1346 (2005).

[25] A. C. Johnson, J. R. Petta, J. M. Taylor, A. Yacoby, M. D. Lukin, C. M. Marcus, M. P. Hanson, and A. C. Gossard, Nature (London) **435**, 925 (2005).

[26] H. Ribeiro, J. R. Petta, and G. Burkard, Phys. Rev. B **82**, 115445 (2010).

[27] M. S. Rudner, F. H. L. Koppens, J. A. Folk, L. M. K. Vandersypen, and L. S. Levitov, Phys. Rev. B **84**, 075339 (2011).

[28] H. Bluhm, S. Foletti, D. Mahalu, V. Umansky, and A. Yacoby, Phys. Rev. Lett. **105**, 216803 (2010).

[29] F. Forster, M. Mühlbacher, D. Schuh, W. Wegscheider, and S. Ludwig, Phys. Rev. B **91**, 195417 (2015).

[30] K. Ono, D. G. Austing, Y. Tokura, and S. Tarucha, Science **297**, 1313 (2002).

[31] D. J. Reilly, J. M. Taylor, E. A. Laird, J. R. Petta, C. M. Marcus, M. P. Hanson, and A. C. Gossard, Phys. Rev. Lett. **101**, 236803 (2008).

[32] S. W. Jung, T. Fujisawa, Y. Hirayama, and Y. H. Jeong, Appl. Phys. Lett. **85**, 768 (2004).

[33] M. Pioro-Ladrière, J. H. Davies, A. R. Long, A. S. Sachrajda, L. Gaudreau, P. Zawadzki, J. Lapointe, J. Gupta, Z. Wasilewski, and S. Studenikin, Phys. Rev. B **72**, 115331 (2005).

[34] D. Taubert, M. Pioro-Ladrière, D. Schröer, D. Harbusch, A. S. Sachrajda, and S. Ludwig, Phys. Rev. Lett. **100**, 176805 (2008).

[35] E. A. Laird, C. Barthel, E. I. Rashba, C. M. Marcus, M. P. Hanson, and A. C. Gossard, Phys. Rev. Lett. **99**, 246601 (2007).

[36] M. Kroner, K. M. Weiss, B. Biedermann, S. Seidl, S. Manus, A. W. Holleitner, A. Badolato, P. M. Petroff, B. D. Gerardot, R. J. Warburton *et al.*, Phys. Rev. Lett. **100**, 156803 (2008).

[37] T. Obata, M. Pioro-Ladrière, Y. Tokura, and S. Tarucha, njp **14**, 123013 (2012).

[38] T. Fujisawa and Y. Hirayama, Appl. Phys. Lett. **77**, 543 (2000).

[39] We expect deviations if the quantization axis deviates from the z axis, which is never the case for our measurements taken at $hf \gg g\mu_B B_{\mathrm{nm}}^{\perp}$.

[40] D. Paget, Phys. Rev. B **25**, 4444 (1982).

[41] M. N. Makhonin, A. I. Tartakovskii, A. B. Van'kov, I. Drouzas, T. Wright, J. Skiba-Szymanska, A. Russell, V. I. Fal'ko, M. S. Skolnick, H.-Y. Liu *et al.*, Phys. Rev. B **77**, 125307 (2008).

[42] C. Latta, A. Srivastava, and A. Imamoğlu, Phys. Rev. Lett. **107**, 167401 (2011).

[43] C. Deng and X. Hu, Phys. Rev. B **72**, 165333 (2005).

7 Landau-Zener-Stückelberg-Majorana interferometry

This chapter presents the results of

- Forster, F. *et al. Phys. Rev. Lett. 112*. 116803 (2014)

See section D for the contributions of each author.

7.1 Overview

In recent years Landau-Zener-Stückelberg-Majorana (LZSM) interferometry has been developed by research groups into an established technique which mainly has been adopted in superconducting qubits as a proof of concept to demonstrate, more than analyze, coherent properties of these qubits [55–58]. Here, we present the first experiment in which LZSM interference is used as a practical tool beyond the mere measurement of an interference pattern. Our method is based on straightforward rf-driven steady-state measurements which are then analysed with a complete model using Floquet theory developed in collaboration with S. Kohler from Instituto de Ciencia de Materiales de Madrid. Our method especially allows us to decipher the details of the coupling of the qubit states to a noisy environment. We are able to determine the individual values of the inhomogeneous decay time T_2^* and the true (single-shot) qubit coherence time T_2. For the first time we succeeded to measure T_2 and T_2^* individually without the need of (much more difficult) pulsed-gate echo experiments. We implement our method in a two-electron DQD charge qubit and demonstrate the first direct determination of T_2 for a QD based charge qubit. Surprisingly, we find coherence times more than an order of magnitude longer than previously reported for similar devices. Further, we demonstrate that the electron-phonon interaction is the relevant decoherence source for our charge qubit even at cryogenic temperatures of 20 mK.

7.2 Theory

7.2.1 Landau-Zener-Stückelberg-Majorana physics

We already established the importance of the coupling of quantum states and showed how it leads to avoided crossings of the local basis states (section 2.2.1), and how it enables transitions between them, with the example of EDSR (section 5.2.1). We revisit the Hamiltonian of the singlet subsystem H_{el} (2.7), but we now introduce an experiment in which the detuning ε is varied and hence modelled by a time-dependent function $\varepsilon(t)$:

$$H_{\mathrm{LZ}}(t) \doteq \begin{pmatrix} 0 & t_c/2 \\ t_c/2 & -\varepsilon(t) \end{pmatrix} \tag{7.1}$$

In the most simple case, we assume a linear function for the detuning, $\varepsilon = vt$, and look at the probability P_{LZ} to remain in the same quantum state while ε is varied from $-\infty$ to ∞, e.g. $P_{\mathrm{LZ}} = \left|\langle S_{11}|\psi(t\to\infty)\rangle\right|^2$, if $|\psi(t\to-\infty)\rangle = |S_{11}\rangle$. Here, $v = d\varepsilon/dt$ has the interpretation of a sweep velocity. Intuitively, if the sweep

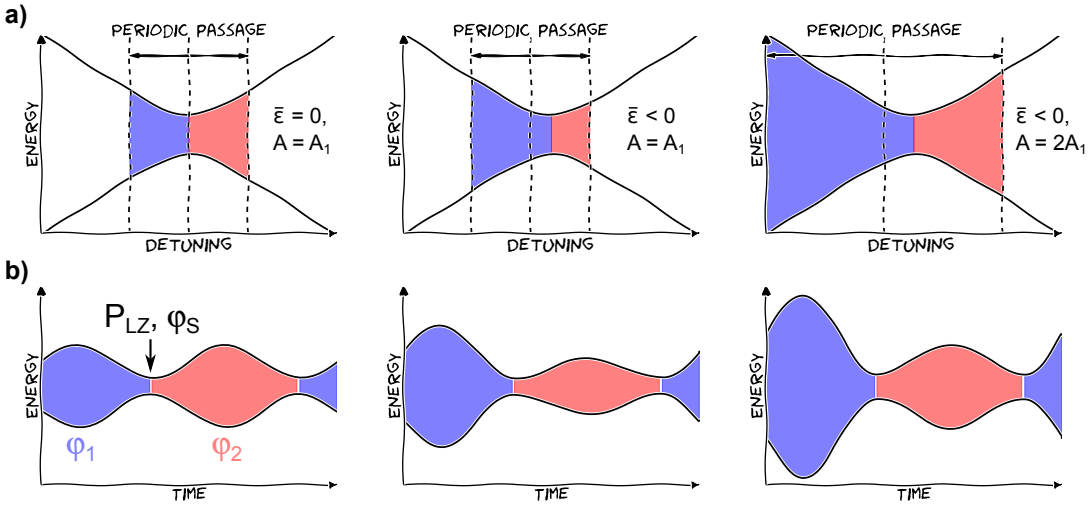

Figure 7.1: Illustration of the phase pick-up in the adiabatic impulse model. a) Sketch of the avoided crossing reached during the driving of the detuning parameter $\varepsilon(t) = \bar{\varepsilon} + A\cos\Omega t$ for different parameters A and $\bar{\varepsilon}$. b) Sketch of the energy levels over time for the parameters in a). The dynamical phases φ_1 and φ_2 corresponding to the area between the energy levels originate from the regions of the corresponding colours in a) and depend strongly on the parameter set. They contribute to the overall phase as well as the Stokes phase φ_S (impulse) at the avoided crossing.

is fast compared to the Rabi dynamics induced by t_c and hence v large, we expect that the system will remain in the state $|S_{11}\rangle$. In the opposite case, i.e. for small v, we expect the system to be able to follow adiabatically and thus to remain in the ground state at all times, which means a transition to $|S_{20}\rangle$. In the regime of intermediate v, we expect to find a solution in between the two extreme cases, i.e. to reach a superposition state of the two adiabatic states. Historically, the problem just described is known as the Landau-Zener problem, which is nowadays often called Landau-Zener-Stückelberg-Majorana problem to acknowledge all four independent solutions of the problem, which were all presented in 1932 [59–62]. The probability to remain in the same diabatic state is the Landau-Zener probability

$$P_{\mathrm{LZ}} = \exp\left(-\pi\frac{t_c^2}{2\hbar v}\right). \tag{7.2}$$

We see that $P_{\mathrm{LZ}} \to 1$ in the limit of $t_c^2 \ll \hbar v$, and $P_{\mathrm{LZ}} \to 0$ for $t_c^2 \gg \hbar v$, confirming our intuitive expectation. More interestingly, we indeed find a finite value between 0 and 1 for $t_c^2 \sim \hbar v$. It turns out that we can prepare an arbitrary superposition state by going through the avoided crossing at a defined velocity v. This result is independent from details of the avoided crossing itself, such as the coupling mechanism or the kind of states involved; therefore it is a general result applicable to all coupled two-level systems. In fact, we will apply this result not only to the just discussed charge qubit of $|S_{11}\rangle$ and $|S_{20}\rangle$, but also to the $|S_{11}\rangle$-$|T_+\rangle$ spin qubit.

7.2.2 Landau-Zener-Stückelberg-Majorana interferometry

An extension to the classical LZSM problem, where the avoided crossing is passed once, is multiple passages by a periodic drive. Here, we consider the driving $\varepsilon(t) = \bar{\varepsilon} + A\cos(\Omega t)$. An appealing approach to the physics of multiple passages is provided by the adiabatic-impulse model [10, 63]. Here, we assume that the experiment can be divided into two separate stages: First, at each passage a Landau-Zener transition changes the occupation of the quantum state according to P_{LZ} (7.2). This transition is treated as instantaneous, and is hence the impulse part of the model. The Landau-Zener transition also introduces the Stokes phase, which in the same spirit only depends on $t_c^2/\hbar v$ and is constant for each passage [64]. Second: Whenever

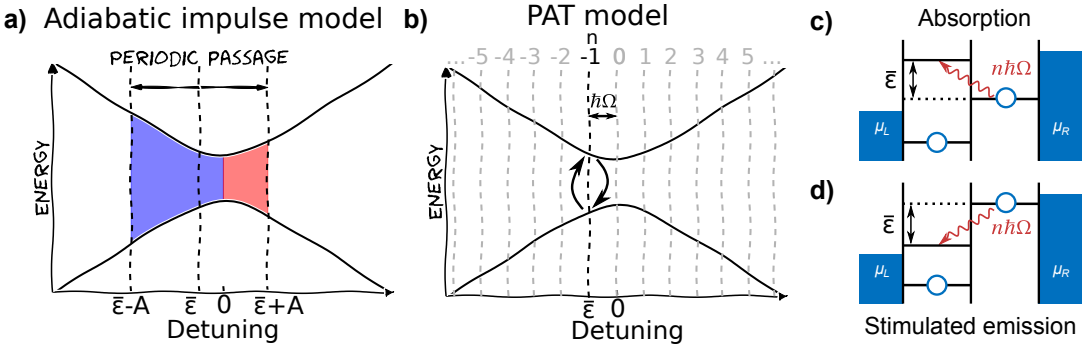

Figure 7.2: Comparison of the adiabatic impulse model and the photon assisted tunnelling model. a) Adiabatic impulse model. The detuning parameter $\varepsilon(t) = \bar{\varepsilon} + A\cos\Omega t$ is time dependent and the phase acquired during periodic passages of the avoided crossing determines the interference pattern (see fig. 7.1). b) Photon assisted tunnelling model. The detuning parameter itself is considered static and the driving enters as a photon source enabling absorption (c) and stimulated emission (d), possible if the driving frequency is resonant with the detuning, $\bar{\varepsilon} = n\hbar\Omega$, $n \in \mathbb{Z}$ (grey dashed lines). The specific case in black at $n = -1$ corresponds to a one photon process. c, d) Sketch of the charge transition in energy space of the DQD enabled by the absorption (c) or stimulated emission (d) of photons with energy $\hbar\Omega$.

the detuning is not at the avoided crossing, the time evolution of the superposition state generated by the Landau-Zener transition is described by the adiabatic time evolution of the state vector. This can be described by a phase pick-up at each side of the avoided crossing, which is called dynamical phase. This phase is given by the area between the energy levels over time and depends strongly on the parameters A and $\bar{\varepsilon}$ as depicted in figure 7.1b. The overall phase consisting of the dynamical phase and the Stokes phase can result in constructive or destructive interference depending on the aforementioned parameters. As a straightforward implication, there is no interference expected if $|\bar{\varepsilon}| > A$, since the avoided crossing is not reached. This leads to an interference pattern within a triangular region as a function of A and $\bar{\varepsilon}$. Note that the adiabatic-impulse model is only applicable if passing the avoided crossing is sufficiently well described by P_{LZ} and the Stokes phase, i.e. transient dynamics [65, 66] are negligible[(1)].

For drivings $\hbar\Omega > t_c$, the photon assisted tunnelling (PAT) interpretation offers a straightforward alternative description: In this model, the energy difference $\bar{\varepsilon}$, which is assumed to be static, is overcome by absorption and stimulated emission of n photons provided by the driving $A\cos\Omega t$. In this picture, transitions are allowed only at discrete $\varepsilon = n\hbar\Omega$, where $n \in \mathbb{Z}$, which is indeed observed. In the given regime, this is fully equivalent to the LZSM picture, where constructive interference only occurs at discrete values of $\bar{\varepsilon}$.

Our theory approach to numerically calculate the interference patterns harnesses the time periodicity of the Hamiltonian (7.1). Equivalent to the Bloch theorem for wavefunction of electrons of the periodic potential of a crystal, the Hamiltonian can be decomposed into the Floquet basis which facilitates the solution of the master equation of the system and is discussed at length in the supplement of the paper. This powerful approach enables us to go well beyond the adiabatic impulse model: It allows to include a dissipative environment and study its impact on the LZSM dynamics, which is the subject of the following section.

7.2.3 Coherence of a qubit

The general representation of the charge qubit's quantum state at a given time is

$$|\Psi\rangle = c_1|S_{11}\rangle + c_2|S_{20}\rangle = |c_1|\exp(i\phi_1)|S_{11}\rangle + |c_2|\exp(i\phi_2)|S_{20}\rangle,$$

(1) Formally, the applicability can be expressed in the condition $A^2 + t_c^2 \gg \Omega^2$; see reference [67] for a detailed discussion.

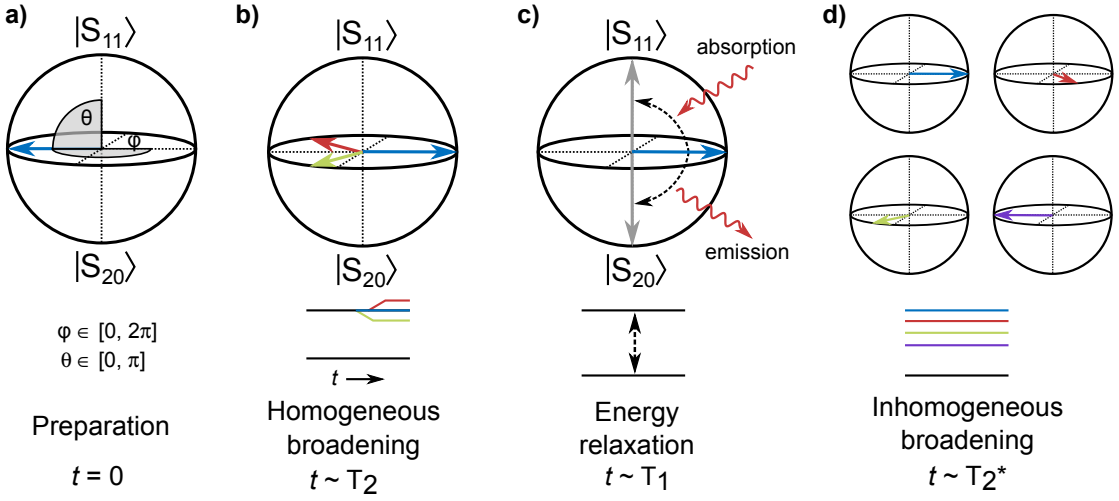

Figure 7.3: Illustration of the influence of noise on the time evolution of a qubit. a) Bloch representation of the state vector at the initialization $t = 0$. Equation (7.3) relates the polar angle θ to the population ratio of the quantum superposition and the azimuth angle ϕ to the corresponding phase. b) Decoherence: A homogeneous broadening of the electron levels causes a fluctuating Larmor frequency leading to different time evolutions of the state vector regarding the phase ϕ (different colours). c) Energy relaxation. Energy exchange with the environment destroys the superposition state (example in blue) and brings the Bloch vector to one of the poles of the sphere (dependening on whether energy is absorbed or emitted). d) An ensemble of qubits with constant, but different level energies (inhomogeneous broadening) [different colours] shows a stochastic distribution of phases. Note that each individual qubit is also subject to a homogeneous broadening and that T_2^* includes both broadenings.

which is completely defined by the two complex coefficients $c_{1,2}$. Since each complex number has two degrees of freedom, i.e. its absolute value $|c_i|$ and its phase ϕ_i, there are in principle four variables which define the quantum state. However, since the global phase has no physical meaning, we can eliminate one of the variables by multiplying the state with a global phase, e.g. $|\Psi\rangle \rightarrow \exp(-i\phi_1)|\Psi\rangle$ and define $\phi = (\phi_2 - \phi_1) \in [0,\, 2\pi]$ as the (relative) phase. In addition, the normalization condition for a quantum state, i.e. $|\langle\Psi|\Psi\rangle|^2 = |c_1|^2 + |c_2|^2 = 1$, removes another degree of freedom. We choose $c_1 = \cos\theta/2$ with $\theta \in [0,\, \pi]$, such that the quantum state reads

$$|\Psi\rangle = \cos\frac{\theta}{2}|S_{11}\rangle + \exp(i\phi)\sin\frac{\theta}{2}|S_{20}\rangle\,. \tag{7.3}$$

Our choice allows us to interpret θ and ϕ as coordinates on a sphere, the Bloch sphere, and represent the quantum state $|\Psi\rangle$ as a vector on this sphere as depicted in figure 7.3a. The time evolution of the quantum state can be depicted on the Bloch sphere, for example Rabi oscillations correspond to oscillations of the Bloch vector in longitudinal direction.

So far, we regarded the charge qubit as a perfectly isolated quantum system, where the dynamics of the two-level system is fully determined by the parameters t_c and ε in the 2x2 Hamiltonian (7.1). In an experiment, the two-level system is exposed to an uncontrolled environment which influences the time evolution of its state vector. In contrast to the *coherent* time evolution of the closed two-level system, we will call changes of the state vector caused by the environment in longitudinal direction (θ) *energy relaxation* and in transversal direction (ϕ) *decoherence*. Statistical fluctuations in t_c and ε change the coupling of the qubit as well as their energy levels and thus its Larmor frequency. A statistically fluctuating Larmor frequency leads to an uncontrolled phase ϕ, and hence decoherence, as shown in 7.3c. Exchanging energy with the environment, energy relaxation between the two qubit states become possible and cause transverse transitions of the state vector to the poles of the Bloch sphere, figure 7.3b.

It is not possible to describe the dynamics of such an open quantum system with the Schrödinger equation, whereas the density matrix offers an elegant and powerful formalism, which is able to capture

relaxation as well as decoherence [68]. The density operator combines the quantum mechanical uncertainty and the classical one and is defined as $\rho = \sum_i p_i |\Psi_i\rangle \langle\Psi_i|$, where each $|\Psi_i\rangle$ is a given quantum state and p_i its classical probability [15, p. 295]. For a pure quantum state, such as (7.3), we find the density matrix in the eigenbasis of the qubit

$$\rho \doteq \begin{pmatrix} \rho_{00} & \rho_{01} \\ \rho_{10} & \rho_{11} \end{pmatrix} = \begin{pmatrix} \cos^2\frac{\theta}{2} & \cos\frac{\theta}{2}\sin\frac{\theta}{2}\exp i\phi \\ \cos\frac{\theta}{2}\sin\frac{\theta}{2}\exp -i\phi & \sin^2\frac{\theta}{2} \end{pmatrix}. \tag{7.4}$$

To motivate the physical meaning of the diagonal and off-diagonal terms of the density matrix in the eigenbasis of the qubit, we compare the density matrix of the pure state (7.4) with a classical mixture, i.e. $|\Psi_i\rangle \in \{|S_{11}\rangle, |S_{20}\rangle\}$. For the pure state, $\rho_{00} = |\langle S_{11}|\Psi\rangle|^2$ and $\rho_{11} = |\langle S_{20}|\Psi\rangle|^2$ are the quantum mechanical probabilities to measure the respective state, while in the mixed state $\rho_{00} = p_{S_{11}}$ and $\rho_{11} = p_{S_{20}}$ are the corresponding classical probabilities. In both cases, the diagonal terms represent the populations of the system. The off-diagonal terms for the classical mixture however vanish while the ones for the pure state are finite. Therefore, these terms are a direct consequence of the quantum superposition of the pure state and the ability to show interference effects [15, p. 303]. For complete decoherence, i.e. a completely random phase between 0 and 2π, the (classical) expectation value of $\exp(\pm i\phi)$ becomes 0 which implicates all coherence terms are zero, and the system becomes identical to the classical mixture. We will denote the time scale related to the decay of the off-diagonal coherence terms with T_2. For an energy relaxation process, where $\theta \to \pi$, the populations $\rho_{00} \to 0$ and $\rho_{11} \to 1$ change as expected. The time scale for energy relaxation processes is denoted as T_1. Note that while decoherence can occur without a change of populations, relaxation always includes decoherence as relaxation processes will ultimately transform the pure state into a classical mixture. This connection between the decay of population and coherence terms is a fundamental property and one can show that $T_1 \geq 2T_2$ always holds [69].

Since the fluctuations of the environment can occur at very different time scales, it is important to relate these time scales to the time evolution of the qubit. In particular, we differ between the decoherence during a single time evolution of the qubit, here described by parameters t_c and ε fluctuating on the time scale of a single qubit experiment (homogeneous broadening), and the dephasing of a time ensemble of qubits, where in addition fluctuations of these parameters on longer time scales affect the averaged measurement outcome of the qubit state (inhomogeneous broadening) [figure 7.3d]. In our experiments, the measurement signal is the averaged result of typically $\sim 10^6$ single events and the inhomogeneous broadening is important. Since the inhomogeneous broadening is always on top of the homogeneous one, the ensemble coherence time, denoted with T_2^*, cannot exceed the one of a single time evolution and therefore $T_2^* \leq T_2$. While both broadenings cause dephasing of the qubit, it is possible to revert the inhomogeneous broadening's contribution by refocusing the state vector. This can be achieved by applying an echo sequence which lets the state vector propagate contrary to the original direction on the Bloch sphere thus compensating inhomogeneous broadening, a technique commonly applied in NMR imaging [70] and more recently also spin qubit experiments [9, 19]. For this reason, we use the term *decoherence* only for the single qubit, and *dephasing* as a more general term also for the ensemble.

While the T_2^* time of a charge qubit in a system such as ours has been successfully determined in the past to <10 ns [71, 72], T_2 remains elusive: An echo sequence requires a high degree of control over the system and can be difficult to realize, if the clock speed at which the qubit is operated is very fast. This is the case for our charge qubit, where the clock speed is in the order of several GHz[(2)]. Looking at the Larmor frequency,

$$\omega_L = (E_{S_{11}} - E_{S_{20}})/\hbar = \sqrt{\varepsilon^2 + t_c^2}/\hbar,$$

we find that the influence of fluctuations in ε is reduced near the avoided crossing itself, which poses a sweet point in terms of a fluctuating detuning ε: Since the level splitting exhibits a minimum at this point,

[(2)] In principle, the clock speed is connected to the tunnel coupling of the DQD which can be tuned in a wide range; however the coherence time limits the range of values useful for coherent qubit applications.

$\partial_\varepsilon \omega_L|_{\varepsilon=0} = 0$, first order variations vanish and do not cause a change in ω_L. Indeed, T_2^* has its maximum value at this point [72]. However, since fluctuations in t_c are still in effect, $\partial_{t_c} \omega_L|_{\varepsilon=0} \neq 0$, and higher order terms of ε fluctuations are not necessarily negligible, one still has to expect $T_2^* \neq T_2$ for this detuning. In fact, we find T_2 in our system to be two orders of magnitude larger than T_2^* measured at the sweet point in reference [72], which suggests that neglecting noise in t_c and ε in higher order is not a good approximation.

The two main noise sources are known to be interaction with bulk phonons [73] and fluctuating charges in the vicinity of the DQD which cause modifications of the local confinement potential, known as charge noise [74]. In our case, the time scale of a single qubit experiment can be estimated by the time an electron is typically inside the DQD, given by the tunnel rate between the quantum dot and its drain contact, $\Gamma_L \simeq 10\,\mathrm{MHz}$. Since charge noise has its weight at time scales corresponding to frequencies of $< 100\,\mathrm{kHz}$ [74], it mainly contributes to the inhomogeneous broadening of the qubit. Our approach to determine both T_2 and T_2^* is to decipher the information included in the LZSM interference pattern with the help of a theoretic model capturing both noise sources. To model the phonon bath, we apply a Caldeira-Leggett model [75] to couple the qubit to a bath of harmonic oscillators with an Ohmic spectrum. The validity of this model is confirmed by the very good agreement with our measurements, as presented in the main paper and discussed in more detail in section II D-F and III A of the supplement.

The key parameter of this model is a dimensionless coupling strength, α_z, which we use to calculate the T_2 coherence time of the undriven charge qubit (see section III of the supplement for a detailed description). The inhomogeneous broadening is captured by convolution of the numeric data obtained from the Caldeira-Legett model with a Gaussian, whose standard deviation λ^* gives direct access to $T_2^* = \hbar/\lambda^*$. The analysis how to obtain these parameters from the experiment is in detail explained in section II of the supplement. It involves the 2D Fourier transform of the interference pattern, a procedure suggested in reference [76] which reduces the complexity of the pattern in real space to single Lemon-shaped lines in Fourier space. The role of the Fourier transform and its dependence on the driving shape is a further topic of chapter 8.

7.3 Measurement setup

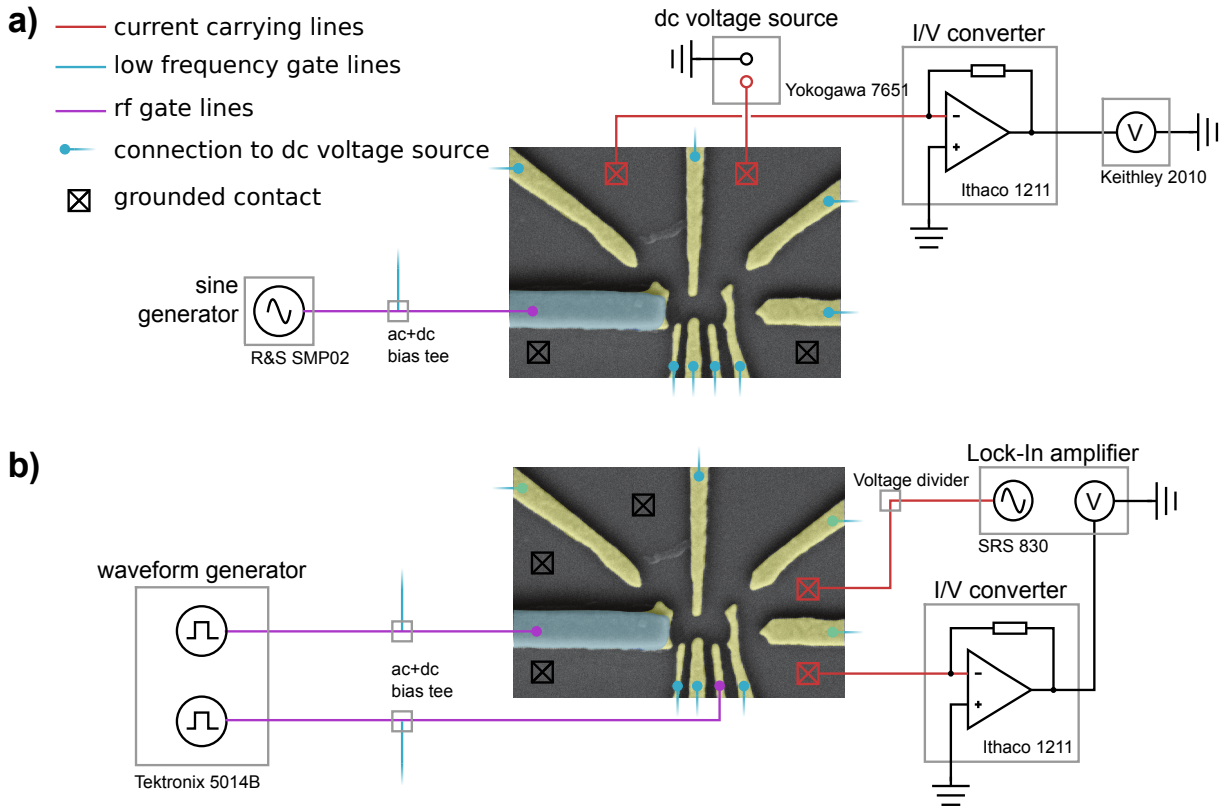

Figure 7.4: a) Electrical measurement setup for the LZSM experiment with the charge qubit. The single electron tunnelling current I through the double quantum dot defined by dc voltage sources connected to all gates is measured by an I/V converter, which amplifies current by a gain of 10^{10} and converts it to a voltage measured by a voltmeter. The sine generator applies an rf sine voltage to one of the gates. b) Setup for the LZSM experiment with the spin qubit. The average electron charge state in the DQD, which in our measurement scheme gives access to the spin state, is measured by its response on the current through a nearby quantum point contact. We use a Lock-in amplifier to measure the quantum point contact current by applying a bias modulated with a frequency of ~37 Hz. The current signal, which is pre-amplified by an I/V converter with a gain of 10^8, is processed by the Lock-In which only selects the part of the current signal which carries the modulation frequency. Pulses in the 100 MHz range are applied to two gates by an arbitrary waveform generator.

We employ two different measurements schemes: For the main experiment, where we measure LZSM interference of a charge qubit, we continuously modulate the voltage at one of the gates with a sine with a frequency of $2\pi\Omega$ to drive the detuning of the DQD as depicted in figure 7.4a. At the same time, we apply -1 mV dc bias to the DQD and measure the quantum dot's single electron tunnelling current with an Ithaco 1211 I/V converter similar to sections 5 and 6 and measure the steady state of the system. As an experimental detail, the output of the Rohde&Schwarz SMP02 sine generator does not support linear scaling of the output voltage. By using amplitude modulation with a dc voltage (not shown in the scheme), we were able to conveniently realize an effective linear scale. In this experiment, we also vary the temperature of the sample. This is achieved by using a heater in the mixing chamber connected to a PID loop of the Lakeshore 370AC resistance bridge used to measure the temperature in the mixing chamber via a calibrated resistor.

In the second measurement scheme, applied in the supplement to measure the Landau-Zener transition of the S-T^+ avoided crossing, we measure the average charge state of the quantum dot by its response to a

nearby QPC. We apply a low-frequency bias of 37 Hz with an amplitude of 50 μeV to the QPC[3]. Its resistance is measured with a lock-in amplifier (model SRS 830), where only current of the reference frequency is detected. The DQD is driven by a pulse scheme of rf voltages applied to two gates by the arbitrary waveform generator shown in figure 7.4b. This allows – in contrast to the steady state measurement of the charge qubit – clean initialization, manipulation, and read-out phases during the experiment (details in section I.C of the supplement below).

[3] A voltage divider is used to increase the resolution of the sine output of the SRS 830 source.

Characterization of Qubit Dephasing by Landau-Zener-Stückelberg-Majorana Interferometry

F. Forster,[1] G. Petersen,[1] S. Manus,[1] P. Hänggi,[2] D. Schuh,[3] W. Wegscheider,[3,4] S. Kohler,[5] and S. Ludwig[1]
[1]Center for NanoScience & Fakultät für Physik, LMU-Munich, 80539 München, Germany
[2]Institut für Physik, Universität Augsburg, 86135 Augsburg, Germany
[3]Fakultät für Physik, Universität Regensburg, 93040 Regensburg, Germany
[4]Solid State Physics Laboratory, ETH Zurich, 8093 Zurich, Switzerland
[5]Instituto de Ciencia de Materiales de Madrid, CSIC, 28049 Madrid, Spain
(Received 5 December 2013; published 19 March 2014)

Controlling coherent interaction at avoided crossings and the dynamics there is at the heart of quantum information processing. A particularly intriguing dynamics is observed in the Landau-Zener regime, where periodic passages through the avoided crossing result in an interference pattern carrying information about qubit properties. In this Letter, we demonstrate a straightforward method, based on steady-state experiments, to obtain all relevant information about a qubit, including complex environmental influences. We use a two-electron charge qubit defined in a lateral double quantum dot as test system and demonstrate a long coherence time of $T_2 \simeq 200$ ns, which is limited by electron-phonon interaction.

DOI: 10.1103/PhysRevLett.112.116803 PACS numbers: 73.63.Kv, 03.65.Yz, 03.67.-a

A qubit is a quantum mechanical two-level system characterized by its tunnel coupling and the detuning from its symmetry point at which the qubit levels form an avoided crossing. Dynamic control can be achieved by switching the detuning between finite values and zero at velocities ranging from almost sudden to adiabatically slow changes. A particularly intriguing dynamics was predicted by Landau, Zener, Stückelberg, and Majorana (LZSM) [1–4] for the intermediate (Landau-Zener) regime that is hallmarked by quantum superpositions. These give rise to interference for the case of periodic passages [5–11]. A particular application is LZSM interferometry, a double-slit kind of experiment that, in principle, can be realized with any qubit, while the specific measurement protocol might vary. Ours is based on two-electron states in a lateral double quantum dot (DQD) embedded in a two-dimensional electron system (2DES) (Fig. 1). Source and drain leads at chemical potentials $\mu_{S,D}$, each tunnel coupled to one dot, allow current flow by single-electron tunneling. Applying the voltage $V = (\mu_S - \mu_D)/e = 1$ mV across the DQD [Fig. 1(b)], we use this current to detect the steady-state properties of the driven system. We take the singlet S_{11} (one electron in each dot) and the singlet S_{20} (two electrons in the left dot) as charge qubit states. They form an avoided crossing [Fig. 1(c)], described by the Hamiltonian

$$H_{\text{qubit}} = \begin{pmatrix} 0 & \Delta/2 \\ \Delta/2 & -\varepsilon(t) \end{pmatrix}, \tag{1}$$

where we consider a variable energy detuning $\varepsilon(t)$ and a constant interdot tunnel coupling tuned to $\Delta \simeq 13$ μeV, corresponding to a clock speed of $\Delta/h \simeq 3.1$ GHz, where h is the Planck constant.

Let us first discuss a single sweep through the avoided crossing at $\varepsilon = 0$: as shown back in 1932 independently by Landau, Zener, Stückelberg, and Majorana, it brings the qubit into a superposition state [1–4], the electronic analog to the optical beam splitter [13–17]. The probability to remain in the initial qubit state $P_{\text{LZ}} = \exp(-\pi\Delta^2/2\hbar v)$ thereby grows with the velocity $v = d\varepsilon/dt$, here assumed to be constant [1–4]. Because the relative phase between the split wave packets depends on their energies, repeated passages by a periodic modulation $\varepsilon(t) = \bar{\varepsilon} + A\cos(\Omega t)$ give rise to so-called LZSM quantum interference [5–11]. We present a breakthrough that makes LZSM interferometry a powerful tool: it is based on systematic measurements together with a realistic model, which explicitly includes the noisy environment. We demonstrate how to decipher the detailed qubit dynamics and directly determine its decoherence time T_2 based on straightforward steady-state measurements.

Keeping the experiment simple, we detect the dc-current I through the DQD. It involves electron tunneling giving rise to the configuration cycle $(1,0) \to (1,1) \leftrightarrow (2,0) \to (1,0)$, where pairs of digits refer to the number of electrons charging the (left, right) dot [Fig. 1(b)]. The energetically accessible two-electron states include the singlets S_{11} and S_{20} but also three triplets T_{11} [Figs. 1(b), 1(c)]. These triplets are likely occupied during $(1,0) \to (1,1)$, and their decay via a spin flip $T_{11} \to S_{11}$ is hindered by a Pauli-spin blockade [18,19]. This slows down the transition $(1,1) \to (2,0)$ and thereby limits the current. To nevertheless quickly initialize the qubit and generate a measurable current, we lift the blockade using an on-chip nanomagnet [Fig. 1(a)] [12]. I is proportional to the occupation probability of S_{20} and serves as destructive qubit detector.

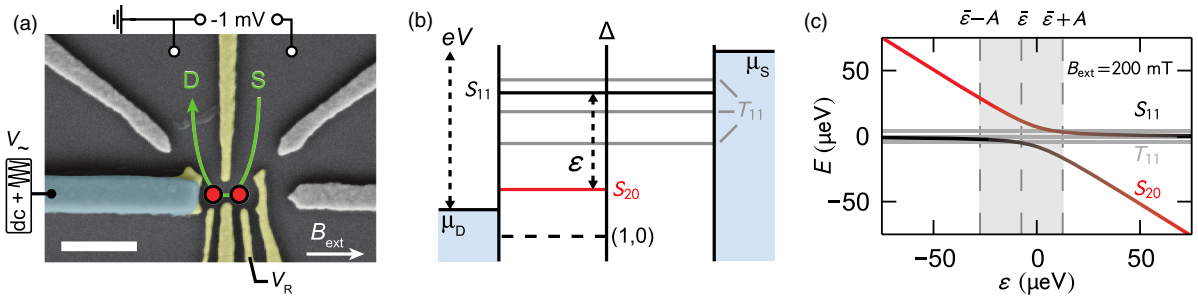

FIG. 1 (color online). Experimental setup. (a) Scanning electron micrograph showing Ti/Au gates, fabricated by electron-beam lithography, on the surface of a GaAs/AlGaAs heterostructure, grown by molecular beam epitaxy (500 nm scale bar). 85 nm beneath the surface it contains a 2DES with carrier density $n_e = 1.19 \times 10^{11}$ cm^2 and mobility $\mu = 0.36 \times 10^6$ cm^2 V^{-1} s^{-1}. Six of the Ti/Au gates (light yellow) are biased with negative voltages to electrostatically define a DQD in the 2DES, and the other gates are grounded. A cobalt single-domain nanomagnet (thick blue bar) produces an inhomogeneous magnetic field that slightly mixes singlet and triplet states of the DQD [12]. (b) Typical situation in our two-electron DQD: vertical lines indicate tunable tunnel barriers, horizontal lines mark the chemical potentials, blue areas are the degenerate 2DES leads. The voltage $V = (\mu_S - \mu_D)/e$ causes a single-electron tunneling current [green arrow in panel (a)]. (c) Energy diagram of the relevant two-electron DQD eigenstates. Singlets (the qubit states) are represented as black and red lines; triplets, which are Zeeman split, are represented as gray lines. Rf modulation of the gate voltage $V_\sim$ [panel (a)] results in a modulated detuning $\varepsilon(t)$, indicated by gray shading.

As it is possible to tune the relative couplings and the mean detuning $\bar{\varepsilon}$ of the singlet-singlet and singlet-triplet crossings by gate voltages and magnetic fields, our two-electron DQD opens two interesting perspectives: (i) LZSM interferometry involving multiple avoided crossings [8,20–23] and (ii) coherent Landau-Zener transitions between our charge qubit and the recently very successful spin-based qubits [24]; see the Supplemental Material [25], Sect. IIA for details.

Concentrating on the two-electron charge qubit, in Figs. 2(a) and 2(b) we display LZSM interference patterns measured at $T_{2DES} \simeq 20$ mK for two different modulation frequencies $\Omega/2\pi$. Within the triangle defined by $A \gtrsim |\bar{\varepsilon}|$, the qubit is periodically driven through the avoided crossing and the current oscillates between zero and distinct maxima indicating destructive and constructive interference [9,26]. An interpretation based on photon-assisted tunneling, which is for $\hbar\Omega \gtrsim \Delta$ fully equivalent to the LZSM picture discussed above, facilitates quantitative predictions: using Floquet scattering theory [27], we find for $\Delta \ll \hbar\Omega$ the current per spin projection

$$I(\bar{\varepsilon}, A) = \frac{e}{\hbar}\frac{\Gamma_{in}\Gamma_{out}}{4\gamma}\sum_{n=-\infty}^{\infty}\frac{\Delta_n^2}{(\bar{\varepsilon} - n\hbar\Omega)^2 + \Delta_n^2 + \gamma^2}, \qquad (2)$$

where Γ_{in} is the qubit initialization rate $(1,0) \to S_{11}$, Γ_{out} is the decay rate $(2,0) \to (1,0)$, and $\gamma = (1/2)(\Gamma_{in} + \Gamma_{out})$.

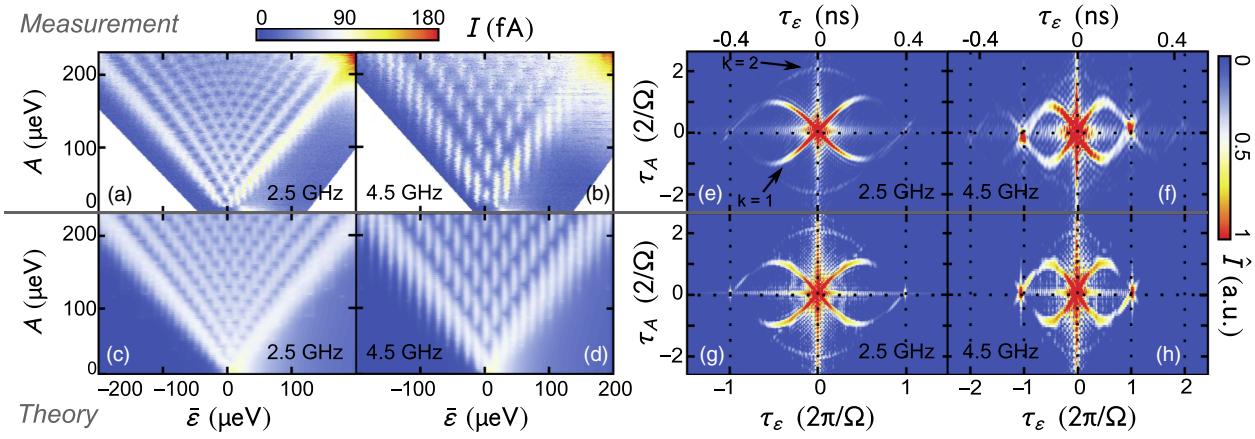

FIG. 2 (color online). LZSM interference. Measured current through the DQD as a function of mean detuning $\bar{\varepsilon}$ and modulation amplitude A at $T \simeq 20$ mK for the modulation frequencies 2.5 GHz (a) and 4.5 GHz (b). [(c), (d)] Corresponding numerically calculated current for realistic conditions. [(e)—(h)] Two-dimensional numerical Fourier transformed ($A \to \tau_A$, $\bar{\varepsilon} \to \tau_\varepsilon$, $I \to \hat{I}$) of measurements (upper panels) and theory (lower panels). The shape of the sinusoidal branches of enhanced $\hat{I}$ is determined by Ω; see Eq. (3). Their decay with increasing τ_ε encodes dephasing and decoherence. The horizontal and vertical lines of enhanced amplitude at $\tau_A = 0$ and $\tau_\varepsilon = 0$ are artifacts caused by the finite region of data being transformed.

The interdot tunnel coupling is renormalized with the nth-order Bessel function J_n of the first kind: $\Delta_n = J_n(A/\hbar\Omega)\Delta$. Equation (2) predicts Lorentz-shaped current maxima of width $\delta\bar{\varepsilon} = \sqrt{\Delta_n^2 + \gamma^2}$ at $\bar{\varepsilon} = n\hbar\Omega$, which for $\Delta \ll |\bar{\varepsilon}|$ corresponds to the bare n-photon resonance $\sqrt{\bar{\varepsilon}^2 + \Delta^2} = n\hbar\Omega$. The peaks are modulated by $J_n^2(A/\hbar\Omega)$ as a function of A. This scattering approach provides an appealing physical picture and describes the main features of the measured LZSM patterns as can be easily seen for the high-frequency limit $\hbar\Omega \gg \delta\bar{\varepsilon}$ (see the Supplemental Material [25], Fig. 5). For lower Ω, the distance between current peaks is smaller and, hence, the broadened resonances tend to merge [Fig. 2(a)].

The visibility of the LZSM pattern (i) depends on frequency and amplitude via the Landau-Zener probability P_{LZ} [captured in Eq. (2) by Δ_n], (ii) is strongest for $\Gamma_{\mathrm{in}} \simeq \Gamma_{\mathrm{out}}$, and (iii) is diminished for $\Delta < \gamma$, where the qubit decay is faster than its clock speed. However, Eq. (2) fails to predict the qubit coherence time as it ignores environmental noise. The nevertheless qualitative consent indicates that environmental noise can be treated perturbatively. In this spirit, we developed a complete model that goes beyond Eq. (2) by explicitly including all energetically accessible states of our driven DQD and, importantly, decoherence within a system-bath approach.

An evident source of decoherence is the interaction of the qubit electrons with bulk phonons [28], which entails quantum fluctuations to the DQD level energies. It enters our theory as dissipation kernel with a dimensionless electron-phonon coupling strength α_Z (see the Supplemental Material [25], Sect. III) derived from a system-bath approach, becoming the spin-boson model in the qubit subspace [29]. We assume for the coupling an Ohmic spectral density, which is justified by geometry considerations (see the Supplemental Material [25], Sect. III C) and also *a posteriori* by a surprisingly good agreement with our experimental results.

The second environmental component of our model is charge noise, well known to cause low-frequency fluctuations of the local confinement potential in semiconductor heterostructures [30,31]. Being slow compared to all relevant time scales of our experiment, they can be treated as static disorder leading in the ensemble average to an inhomogeneous, Gaussian broadening of width $\lambda^\star$.

To determine the key parameters $\lambda^\star$ and α_Z, we compare our measurements with theoretical results obtained within a Bloch-Redfield master equation which can be solved efficiently after a decomposition into the Floquet basis of the rf-driven DQD (see Supplemental Material [25], Sect. IV). The optimized result is displayed in Figs. 2(c) and 2(d) with $\lambda^\star = 3.5$ μeV and $\alpha_Z = 1.5 \times 10^{-4}$. Below, we illustrate the self-consistent fit procedure by first determining $\lambda^\star$ based on the final value of α_Z and then evaluating α_Z using the final value of $\lambda^\star$.

Figure 3(a) displays $I(\bar{\varepsilon})$ for $\Omega/2\pi = 2.75$ GHz and constant amplitude A, corresponding to a horizontal slice in the presentations of Figs. 2(a)–2(d). The measured data (dots) in Fig. 3(a) feature a beating of broadened and overlapping current peaks. The gray line is calculated for $\alpha_Z = 1.5 \times 10^{-4}$ and $\lambda^\star = 0$. Compared to our measurement, it shows a weaker broadening and a higher visibility. Much better agreement is reached for $\lambda^\star = 3.5$ μeV (blue line). This result is robust under moderate variations of α_Z and does not depend on frequency or temperature. Figure 3(b) underlines the good agreement between measured (dots) versus calculated (lines) data by presenting $I(A)$ at $\bar{\varepsilon} = n\hbar\Omega$ for various n [vertical slices in Figs. 2(a)–2(d)]. Owing to the electron-phonon interaction, the visibility of the interference pattern drops with increasing temperature [Fig. 3(c)].

To quantify α_Z with high accuracy, we use this temperature dependence and thereby capture global information of the extended LZSM patterns [Figs. 2(a)–2(d)] by performing two-dimensional Fourier transformations $I(\bar{\varepsilon}, A) \to \hat{I}(\tau_\varepsilon, \tau_A)$. The results, featured in Figs. 2(e)–2(h), are simple, lemon-shaped structures of local maxima $\hat{I}(\tau_\varepsilon, \tau_A)|_{\mathrm{lemon}}$. Transforming Eq. (2) yields an analytic formula describing these lemon arcs

$$\tau_A = \pm \frac{2k}{\Omega} \sin\left(\frac{\Omega\tau_\varepsilon + 2\pi k'}{2k}\right), \tag{3}$$

with $k = 1, 2, 3, \ldots$, $k' = 0, 1, 2, \ldots$, and $k' < k$. Arcs for $k > 1$ are a consequence of $\Delta \gtrsim \gamma$, a prerequisite for

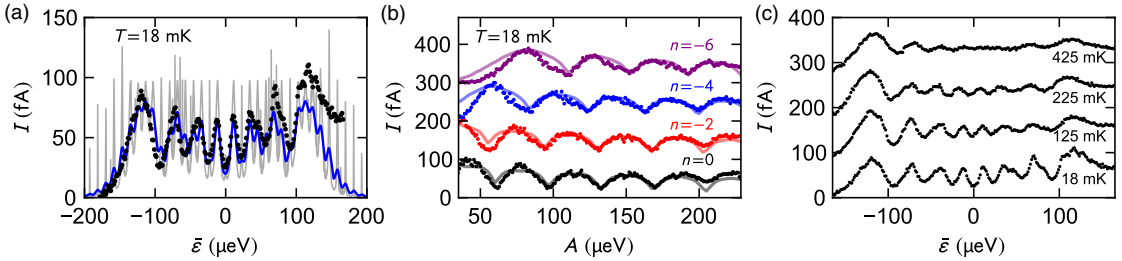

FIG. 3 (color online). Raw data analysis. Dots are measured at $\Omega/2\pi = 2.75$ GHz, lines numerical data for $\alpha_Z = 1.5 \times 10^{-4}$ and $\lambda^\star = 3.5$ μeV, whereas the gray line in panel (a) is for $\lambda^\star = 0$. (a) Horizontal slice through a LZSM pattern: $I(\bar{\varepsilon})$ for a constant $A = 130$ μeV. (b) Vertical slices through a LZSM pattern: $I(A)$ for $\bar{\varepsilon}/\hbar\Omega = 0, -2, -4, -6$. (c) Measured data as in panel (a) for various temperatures.

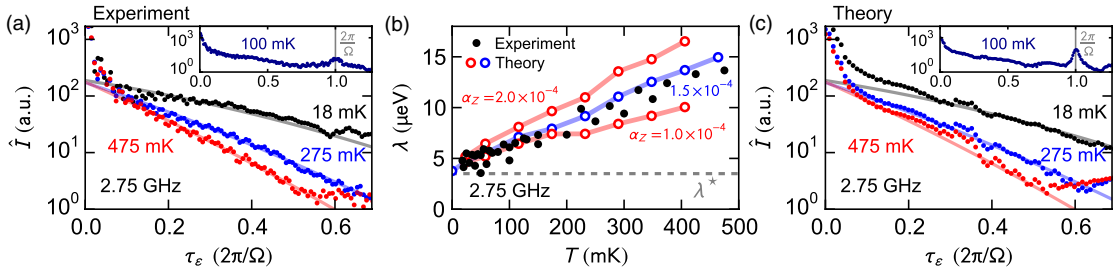

FIG. 4 (color online). Electron-phonon coupling. (a) Decaying region of the measured $\hat{I}(\tau_\varepsilon,\tau_A)|_{\text{lemon}}$ for three temperatures (dots). Lines are generated using Eq. (4) for $\lambda^\star = 3.5$ μeV and λ as a fit parameter. The inset shows a broader region including maxima at $\tau_\varepsilon = 0, 2\pi/\Omega$. (b) Measured decay rate $\lambda(T)$ (black dots) and corresponding numerical data (colored circles) based on $\lambda^\star = 3.5$ μeV (indicated as horizontal line) and $\alpha_Z = 1.0, 1.5, 2.0 \times 10^{-4}$. (c) Analog to panel (a) but based on numerical calculations. Solid lines are identical to those in (a). The numerical resolution is based on 100 data points sampling the Gaussian broadening in $\bar{\varepsilon}$ of width $\lambda^\star = 3.5$ μeV.

observing a pronounced interference pattern (see the Supplemental Material [25], Sect. II.E). [Arcs for $k > 1$ are weakly seen in Figs. 2(e)–2(h). In superconducting qubits they have been also observed but–considering $\Delta \ll \gamma$ [32]–not explained.] Concentrating on the principal lemon arc for $k = 1$, we find a nonmonotonic behavior of $\hat{I}(\tau_\varepsilon,\tau_A)|_{\text{lemon}}$ with maxima at the arc's intersections at $\tau_A = 0$ and τ_ε a multiple of $2\pi/\Omega$. Regions of decays in between have the form

$$\hat{I}(\tau_\varepsilon,\tau_A)|_{\text{lemon}} \propto e^{-\lambda|\tau_\epsilon|/\hbar} e^{-\frac{1}{2}(\lambda^\star\tau_\epsilon/\hbar)^2}, \tag{4}$$

where the exponential decay originates from the Lorentzian broadening due to electron-phonon coupling and the Gaussian term describes the inhomogeneous broadening caused by charge noise. Notice that τ_ε is a Fourier variable rather than a real time variable, and thus, λ should not be interpreted as physical decay rate. [Only for $\Delta \ll \gamma$, all Lorentzians in Eq. (2) possess the same width, so that $\hat{I}(\tau_\varepsilon,\tau_A)|_{\text{lemon}}$ is described by Eq. (4) with simply $\lambda = \gamma$ as suggested in Ref. [32].] In Figs. 4(a) and 4(c) we plot measured and calculated decays (dots), respectively, for various temperatures between 18 and 500 mK. The solid lines in panels (a) and (c) are identical and express Eq. (4) with λ as a fit parameter, while $\lambda^\star$ is kept fixed at 3.5 μeV. Figure 4(b) compares $\lambda(T)$ obtained by this procedure from our measurements (black dots) with the numerical results using three different values of α_Z. An outstanding agreement between theory and experiments is found at $\alpha_Z \simeq 1.5 \times 10^{-4}$ [blue in Fig. 4(b)]. This completes our set of model parameters needed to calculate LZSM patterns as in Figs. 2(c) and 2(d). $\lambda(T)$ increases linearly for $T \gtrsim 100$ mK, whereas it is bounded by $\lambda_{\text{min}} \simeq 4$ μeV at our lowest temperatures. This bound marks the intrinsic decay of $\hat{I}(\tau_\varepsilon,\tau_A)|_{\text{lemon}}$ present even in the low-temperature limit of our transport measurement but is not related to the low-temperature bound of the qubit coherence time T_2.

To actually identify $T_2(T)$, we use its dependence on α_Z in the spin-boson model. In the absence of rf modulation, it provides the analytical prediction [33]

$$T_2(T,\alpha_Z) = \frac{\hbar}{\pi\alpha_Z}\left[\frac{2k_BT\bar{\varepsilon}^2}{E^2} + \frac{\Delta^2}{2E}\coth\left(\frac{E}{2k_BT}\right)\right]^{-1}. \tag{5}$$

In the low-temperature limit $k_BT \ll E = \sqrt{\Delta^2+\bar{\varepsilon}^2}$ our undriven qubit has $T_2 = 2\hbar E/\pi\alpha_Z\Delta^2$. Assuming $\bar{\varepsilon} = 0$, we find $T_2 \simeq 0.2$ μs, which further increases at finite detuning. Alternatively, T_2 could be increased by decreasing Δ. This would, however, reduce the clock speed of the qubit. In the same spirit, the rf-induced renormalization of $\Delta \to \Delta_n$ stabilizes the qubit's coherence on the expense of a larger gate operation time [34].

Summarizing, we demonstrated that steady-state LZSM interferometry is a viable tool to fully characterize a qubit including its coupling to a noisy environment. The quantitative agreement between our experiments and our complete system-bath model analyzed with Floquet transport theory allows us to trace the origins of inhomogeneous broadening and decoherence. Thereby we determined the individual values of $T_2^\star = \hbar/\lambda^\star$ and T_2 of the qubit. Our steady-state method is remarkably simple compared to the alternative pulsed gate experiments. Our two-electron charge qubit is affected by slow charge noise limiting $T_2^\star$ to $\simeq$0.2 ns but a coherence time of $T_2 \simeq 0.2$ μs, being much longer than previously reported values in quantum dot charge qubits [17,35,36]. The clock speed of our qubit, $\Delta/h \simeq 3.1$ GHz, which limits T_2 at $T \simeq 20$ mK and $\bar{\varepsilon} = 0$, would then provide enough time for > 600 quantum operations. At higher temperatures or sizable $\bar{\varepsilon}$, decoherence is dominated by the electron-phonon coupling. Our method is simple, very general, and can be applied to arbitrary qubit systems. An extension including individually controlled Landau-Zener transitions and a combination with nonadiabatic pulses will open up alternative means of quantum information processing. Our two-electron qubit experiments illustrate an interesting approach for studying the interaction of qubits and complex many body quantum systems.

We wish to thank R. Blattmann, E. Hoffmann, M. Kiselev, J. Kotthaus, and P. Nalbach for valuable

discussions and are grateful for financial support from the DFG via SFB-631 and the Cluster of Excellence "Nanosystems Initiative Munich (NIM)" and by the Spanish Ministry of Economy and Competitiveness through Grant No. MAT2011-24331. S. L. acknowledges support via a Heisenberg fellowship of the DFG. F. F. and G. P. contributed equally to this work.

[1] L. D. Landau, Phys. Z. Sowjetunion **2**, 46 (1932).
[2] C. Zener, Proc. R. Soc. A **137**, 696 (1932).
[3] E. C. G. Stueckelberg, Helv. Phys. Acta **5**, 369 (1932).
[4] E. Majorana, Nuovo Cimento **9**, 43 (1932).
[5] W. D. Oliver, Y. Yu, J. C. Lee, K. K. Berggren, L. S. Levitov, and T. P. Orlando, Science **310**, 1653 (2005).
[6] M. Sillanpää, T. Lehtinen, A. Paila, Y. Makhlin, and P. Hakonen, Phys. Rev. Lett. **96**, 187002 (2006).
[7] C. M. Wilson, T. Duty, F. Persson, M. Sandberg, G. Johansson, and P. Delsing, Phys. Rev. Lett. **98**, 257003 (2007).
[8] D. M. Berns, M. S. Rudner, S. O. Valenzuela, K. K. Berggren, W. D. Oliver, L. S. Levitov, and T. P. Orlando, Nature (London) **455**, 51 (2008).
[9] S. N. Shevchenko, S. Ashhab, and F. Nori, Phys. Rep. **492**, 1 (2010).
[10] J. Stehlik, Y. Dovzhenko, J. R. Petta, J. R. Johansson, F. Nori, H. Lu, and A. C. Gossard, Phys. Rev. B **86**, 121303(R) (2012).
[11] E. Dupont-Ferrier, B. Roche, B. Voisin, X. Jehl, R. Wacquez, M. Vinet, M. Sanquer, and S. De Franceschi, Phys. Rev. Lett. **110**, 136802 (2013).
[12] G. Petersen, E. A. Hoffmann, D. Schuh, W. Wegscheider, G. Giedke, and S. Ludwig, Phys. Rev. Lett. **110**, 177602 (2013).
[13] J. R. Petta, H. Lu, and A. C. Gossard, Science **327**, 669 (2010).
[14] P. Huang, J. Zhou, F. Fang, X. Kong, X. Xu, C. Ju, and J. Du, Phys. Rev. X **1**, 011003 (2011).
[15] P. Nalbach, J. Knörzer, and S. Ludwig, Phys. Rev. B **87**, 165425 (2013).
[16] H. Ribeiro, G. Burkard, J. R. Petta, H. Lu, and A. C. Gossard, Phys. Rev. Lett. **110**, 086804 (2013).
[17] G. Cao, H.-O. Li, T. Tu, L. Wang, C. Zhou, M. Xiao, G.-C. Guo, H.-W. Jiang, and G.-P. Guo, Nat. Commun. **4**, 1401 (2013).
[18] M. Ciorga, A. S. Sachrajda, P. Hawrylak, C. Gould, P. Zawadzki, S. Jullian, Y. Feng, and Z. Wasilewski, Phys. Rev. B **61**, R16315 (2000).
[19] K. Ono, D. G. Austing, Y. Tokura, and S. Tarucha, Science **297**, 1313 (2002).
[20] Y. Wang, S. Cong, X. Wen, C. Pan, G. Sun, J. Chen, L. Kang, W. Xu, Y. Yu, and P. Wu, Phys. Rev. B **81**, 144505 (2010).
[21] A. M. Satanin, M. V. Denisenko, S. Ashhab, and F. Nori, Phys. Rev. B **85**, 184524 (2012).
[22] A. M. Satanin, M. V. Denisenko, A. I. Gelman, and F. Nori, arXiv:1305.4800.
[23] M. N. Kiselev, K. Kikoin, and M. B. Kenmoe, Europhys. Lett. **104**, 57004 (2013).
[24] H. Bluhm, S. Foletti, I. Neder, M. Rudner, D. Mahalu, V. Umansky, and A. Yacoby, Nat. Phys. **7**, 109 (2011).
[25] See the Supplemental Material at http://link.aps.org/supplemental/10.1103/PhysRevLett.112.116803 for details.
[26] Y. Kayanuma, Phys. Rev. A **50**, 843 (1994).
[27] M. Strass, P. Hänggi, and S. Kohler, Phys. Rev. Lett. **95**, 130601 (2005).
[28] G. Granger, D. Taubert, C. E. Young, L. Gaudreau, A. Kam, S. A. Studenikin, P. Zawadzki, D. Harbusch, D. Schuh, W. Wegscheider, Z. R.Wasilewski, A. A. Clerk, S. Ludwig, and A. S. Sachrajda, Nat. Phys. **8**, 522 (2012).
[29] A. J. Leggett, S. Chakravarty, A. T. Dorsey, M. P. A. Fisher, A. Garg, and W. Zwerger, Rev. Mod. Phys. **59**, 1 (1987).
[30] T. Fujisawa and Y. Hirayama, Appl. Phys. Lett. **77**, 543 (2000).
[31] C. Buizert, F. H. L. Koppens, M. Pioro-Ladrière, H.-P. Tranitz, I. T. Vink, S. Tarucha, W. Wegscheider, and L. M. K. Vandersypen, Phys. Rev. Lett. **101**, 226603 (2008).
[32] M. S. Rudner, A. V. Shytov, L. S. Levitov, D. M. Berns, W. D. Oliver, S. O. Valenzuela, and T. P. Orlando, Phys. Rev. Lett. **101**, 190502 (2008).
[33] U. Weiss and M. Wollensak, Phys. Rev. Lett. **62**, 1663 (1989).
[34] K. M. Fonseca-Romero, S. Kohler, and P. Hänggi, Chem. Phys. **296**, 307 (2004).
[35] T. Hayashi, T. Fujisawa, H. D. Cheong, Y. H. Jeong, and Y. Hirayama, Phys. Rev. Lett. **91**, 226804 (2003).
[36] K. D. Petersson, J. R. Petta, H. Lu, and A. C. Gossard, Phys. Rev. Lett. **105**, 246804 (2010).

Supplementary Information for "Characterization of Qubit Dephasing by Landau-Zener-Stückelberg-Majorana Interferometry"

F. Forster*,[1] G. Petersen*,[1] S. Manus,[1] P. Hänggi,[2] D. Schuh,[3] W. Wegscheider,[3,4] S. Kohler,[5] and S. Ludwig[1]

[1]*Center for NanoScience & Fakultät für Physik, LMU-Munich, 80539 München, Germany*
[2]*Institut für Physik, Universität Augsburg, 86135 Augsburg, Germany*
[3]*Fakultät für Physik, Universität Regensburg, 93040 Regensburg, Germany*
[4]*Solid State Physics Laboratory, ETH Zurich, 8093 Zurich, Switzerland*
[5]*Instituto de Ciencia de Materiales de Madrid, CSIC, 28049 Madrid, Spain*

Contents

I. OVERVIEW

In the main article we demonstrated that LZSM (Landau-Zener-Stückelberg-Majorana) interferometry is a viable tool to measure standard qubit properties and, beyond, to determine its coupling to a noisy environment. In our specific case of a double quantum dot (DQD) charge qubit we found two main noise sources: (i) slow environmental fluctuations resulting in an inhomogeneous Gaussian broadening, and (ii) the heat bath, resulting in a homogeneous Lorentzian broadening. In Sec. II we provide additional experimental results together with numerical data, which underlie our interpretations in the main article. Further, we detail our quantitative data analysis based on a self-consistent fitting procedure and numerical calculations resulting in the qubit-environment coupling constants, namely the standard deviation $\lambda^\star = \hbar/T_2^\star$ of the inhomogeneous broadening and the dimensionless dissipation strength α_Z of the coupling to the phonons.

In Sec. III we discuss the details of our model for the DQD and its coupling to the leads as well as to the phonons. Moreover, we sketch the Bloch-Redfield master equation approach by which we compute the asymptotic state of the DQD and the time-averaged current. This includes a discussion of how we extract the qubit's coherence time T_2 from α_Z and under which conditions this is an appropriate procedure. Note that we neglect a second component of the electron-phonon coupling, namely α_X which would mainly cause additional energy relaxation between the qubit states. An estimate of α_X and a discussion, which justifies its negligence, is provided in Sec. III.

Table I in Sec. IV summarizes all system parameters extracted from various measurements and used for the numerical calculations.

II. ADDITIONAL EXPERIMENTS AND DATA ANALYSIS

A. Initial tuning of the double quantum dot

Our experiments start by tuning the DQD by means of gate voltages. As an orientation, Fig. S1(a) displays a charge stability diagram of the unbiased DQD ($V = 0$) as function of the gate voltages $V_\sim$ and V_R. It has been measured using a quantum point contact (QPC) as charge detector. The sharp lines of local minima in its transconductance $\mathrm{d}I_{\mathrm{QPC}}/\mathrm{d}V_R$ are the charging lines of the two dots which separate regions of stable charge configurations ranging from $(0,0)$ to $(2,1)$. Figure S1(b)

*These authors contributed equally to this work.

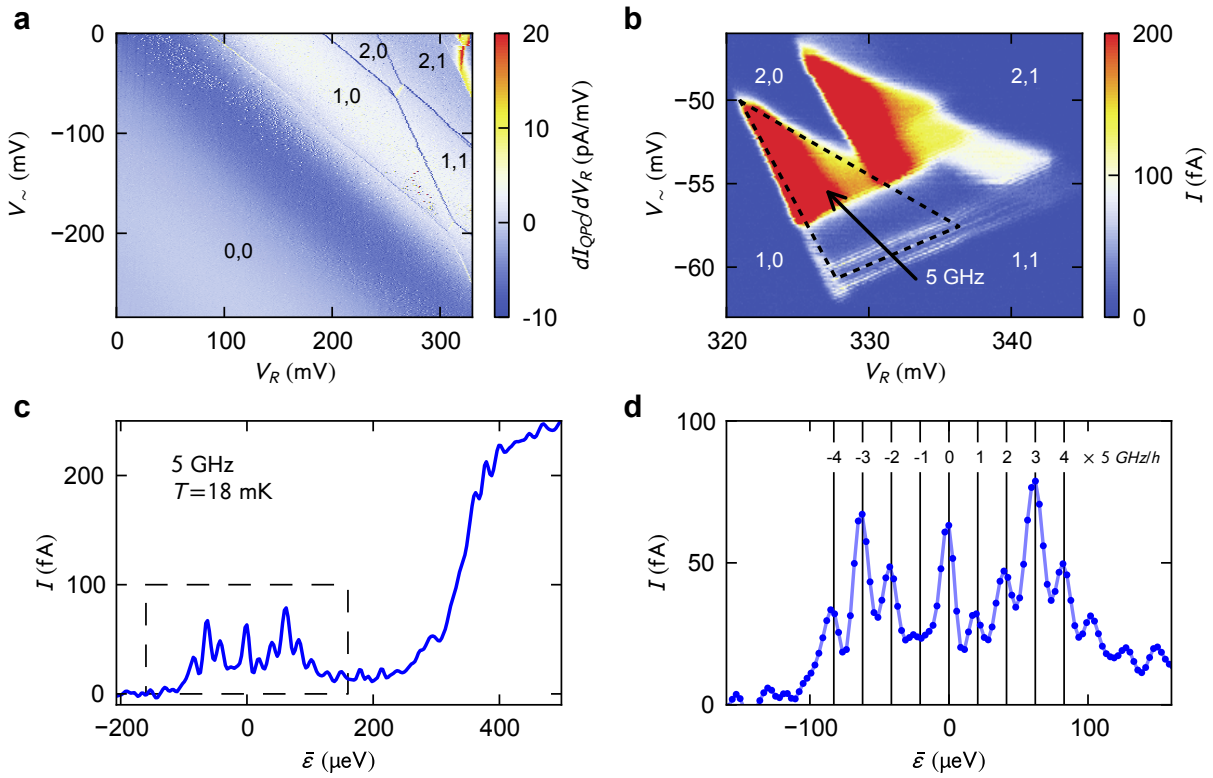

FIG. S1: Initial tuning of the qubit. (a) Charge stability diagram of the unbiased DQD ($V = 0$) as function of dc gate voltages [the gates are marked in Fig. 1(a) of the main article], measured by charge detection [1] at $T \simeq 20\,\mathrm{mK}$. In detail, the color scale displays the linear transconductance of a nearby almost pinched off quantum point contact. It has been defined in the two-dimensional electron system by $V_\sim$ and the upper left gate [gray in Fig. 1(a) of the main article]. Sharp lines of minimal transconductance are charging lines of the DQD which is empty [configuration $(0,0)$] in the lower left half of the plot. (b) Current I in the vicinity of the $(1,1) \leftrightarrow (2,0)$ transition of the charge stability diagram for $V = 1\,\mathrm{mV}$ applied across the DQD [see Fig. 1(a) of the main article] while $V_\sim$ was modulated with frequency $\Omega/2\pi = 5\,\mathrm{GHz}$ and amplitude $A \simeq 80\,\mu\mathrm{eV}$. The dashed triangle marks the region of current via $(1,0) \to (2,0) \leftrightarrow (1,1) \to (1,0)$. The black arrow indicates the detuning axis $\bar{\varepsilon}$ and its origin $\bar{\varepsilon} = 0$ at the intersection with the dashed line. (c) $I(\bar{\varepsilon})$ measured along the black arrow in (b). (d) Current around $\bar{\varepsilon} = 0$ corresponding to the region framed by a dashed box in (c). The current maxima close to $\bar{\varepsilon} = n\hbar\Omega$ with $n = 0, \pm1, \pm2, \pm3, \pm4$ (vertical lines) are caused by PAT.

details the region of the stability diagram near the transition $(1,1) \leftrightarrow (2,0)$, but it plots the current I measured through the DQD as a response to $V = 1\,\mathrm{mV}$ applied across the DQD [see Figs. 1(a,b) of the main article]. The finite current within the framed triangle is a consequence of the single-electron tunneling cycle $(1,0) \to (1,1) \leftrightarrow (2,0) \to (1,0)$, where the double arrow accounts for the fact that the interdot tunnel coupling is coherent and large compared to the dot-lead tunnel couplings. The transition $(1,1) \leftrightarrow (2,0)$ thereby divides into $\mathrm{S}_{11} \leftrightarrow \mathrm{S}_{20}$ and $\mathrm{T}_{11} \leftrightarrow \mathrm{T}_{20}$ while the coupling between singlet and triplet subspaces is forbidden by the Pauli principle. This is the configuration used for our LZSM interferometry measurements. The black arrow in Fig. S1(b) indicates the detuning axis. The current along this arrow, i. e. as a function of the mean detuning $\bar{\varepsilon}$, plotted in Fig. S1(c), shows two interesting features: (i) I is strongly suppressed for $\bar{\varepsilon} < 400\,\mu\mathrm{eV}$, because there the T_{20} state is beyond the transport window, while the transition $\mathrm{T}_{11} \to \mathrm{S}_{11}$ is hindered by Pauli-spin blockade [2, 3], which makes T_{11} a metastable state. In our case the spin blockade is partly lifted especially near $\bar{\varepsilon} = 0$ where the inhomogeneous field of our nanomagnet mixes T_{11} and S_{11}; spin relaxation, provided by the hyperfine interaction with nuclear spins [4] also contributes, but is weaker. The strong current increase at $\bar{\varepsilon} \simeq 400\,\mu\mathrm{eV}$ marks the onset of the T_{20} state contributing to the transport which then completely lifts the spin blockade via the triplet channel $(1,0) \to \mathrm{T}_{11} \leftrightarrow \mathrm{T}_{20} \to (1,0)$. (ii) In Fig. S1(b) we have, in addition, applied an rf-modulation of $V_\sim$ at the frequency of 5 GHz resulting in a modulation of the detuning with amplitude $A \simeq 80\,\mu\mathrm{eV}$. This gives rise to a pattern of photon assisted tunneling (PAT) current maxima appearing at $\bar{\varepsilon} = n\hbar\Omega$ with $n = 0, \pm1, \pm2, \ldots$. These PAT peaks in $I(\bar{\varepsilon})$, highlighted in Fig. S1(b), transform into the LZSM patterns observed in our 2D plots $I(\bar{\varepsilon}, A)$. Weaker PAT oscillations are also seen in panel c where the T_{20}-triplet starts to contribute to the current

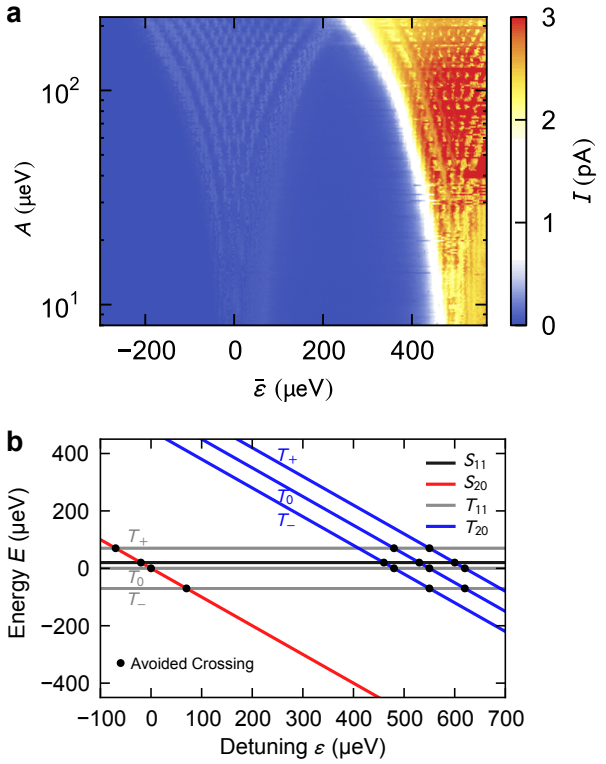

FIG. S2: LZSM patterns: singlets and triplets. (a) $I(\bar{\varepsilon}, A)$ at $\Omega/2\pi = 2.5\,\mathrm{GHz}$ and $T \simeq 20\,\mathrm{mK}$ (logarithmic amplitude axis). Not only for the singlets transition $S_{11} \leftrightarrow S_{20}$ (left) but also for the triplets transition $T_{11} \leftrightarrow T_{20}$ (right) a LZSM interference pattern is observed. (b) Energy eigenstates of our DQD neglecting the mixing between them (S_{11} is vertically shifted to separate it from T_0, similar as an exchange coupling would do). At the intersections marked by black dots, avoided crossings develop predominantly caused by the interdot tunnel coupling and magnetic field gradients between the two dots. The characteristic energy varies as it depends on the details of the coupled states.

near $\bar{\varepsilon} \simeq 400\,\mu\mathrm{eV}$. (The actual singlet-triplet splitting in the $(2,0)$-configuration is larger by the amplitude of $A = 80\,\mu\mathrm{eV}$ and accounts to $\simeq 480\,\mu\mathrm{eV}$.)

An example of measured LZSM interferometry is displayed in Fig. S2(a) using a logarithmic A-axis. It clearly shows LZSM interference patterns involving both transitions $S_{11} \leftrightarrow S_{20}$ around $\bar{\varepsilon} = 0$ as well as $T_{11} \leftrightarrow T_{20}$ at larger $\bar{\varepsilon}$ where the T_{20} state contributes to transport. In all other LZSM patterns presented in this article, the color scale is chosen to optimize the singlet contributions to the interference and the onset of the triplet channel is only seen as an asymmetry in $I(\bar{\varepsilon})$ at large A [increased current in the upper right corner of e. g. Figs. 2(a,b) of the main article].

With our setup it is also possible to perform LZSM interferometry in a one-electron DQD [5] and, moreover, to study the dynamics arising for two electrons when sweeping through multiple avoided crossings [6–9]. These can include not only the combination of singlet-singlet and singlet-triplet transitions around $\varepsilon = 0$ but also avoided crossings at higher detuning where the T_{20}-triplet enters the transport window [see Fig. S2(b)]. The LZSM patterns presented in Fig. S2(a) can be explained by only considering two separate avoided crossings (S_{11}-S_{20} around $\varepsilon = 0$ and a single triplet-triplet transition at larger ε). One way to combine transitions at several avoided crossings would obviously be to sweep through both by matching the Landau-Zener condition ($\hbar v \sim \pi\Delta^2$) at each avoided crossing. This could be done either by matching the characteristic energies (of the avoided crossings) or by varying the sweep speed to make up for different characteristic energies. Note, that the relative position of the avoided crossings can also be tuned via the magnetic field and the interdot tunnel coupling. An interesting application that could be studied at the avoided crossings involving the T_{20} triplets [at large positive detuning in Fig. S2(b)] is SU(3) LZSM interferometry [9]. Furthermore, combining singlet-singlet with singlet-triplet Landau-Zener transitions (charge qubit with spin-based qubit) would provide new possibilities for quantum information processing. Our experiments are a first step towards the realization of such ideas.

B. Energy calibration

In this section we briefly explain how we determine the detuning $\bar{\varepsilon}$ and the modulation amplitude A from gate voltages, the source-drain voltage V applied across the DQD and the modulation frequency $\Omega/2\pi$. The standard method is to use the current triangles in Fig. S1(b) which relate the known energy scale of the applied source-drain voltage eV to changes in gate voltages $V_\sim$ and V_R. The relations are linear with the mutual gate-dot capacities as proportionality factors [10]. Here, we can refine such a standard calibration based on the well known modulation frequency, which determines the LZSM interference patterns, in the following way: (i) The current maxima appear at $\bar{\varepsilon} = n\hbar\Omega$ with $n = 0, 1, 2, \ldots$ which we use to calibrate $\bar{\varepsilon}(V_R, V_\sim)$. (ii) The positions of the minima of the current as function of amplitude are also well known [see e. g. Eq. (2)] and we use them to calibrate $A(V_R, V_\sim)$. At small frequencies, where the interference patterns are less clear, the positions of the outermost current maxima (at $A \simeq \bar{\varepsilon}$) framing the region of finite current $I(\bar{\varepsilon}, A)$ [e. g. in Figs. 2(a,b)] can still be used for a calibration. As the transmission of the rf modulation to the sample depends on the frequency due to cable resonances in the experimental setup, the calibration of A has to be done separately for each frequency.

C. Determination of the system parameters

Using our model we aim at a quantitative prediction of the measured current. This requires knowledge of various system parameters such as the tunable tunnel barriers

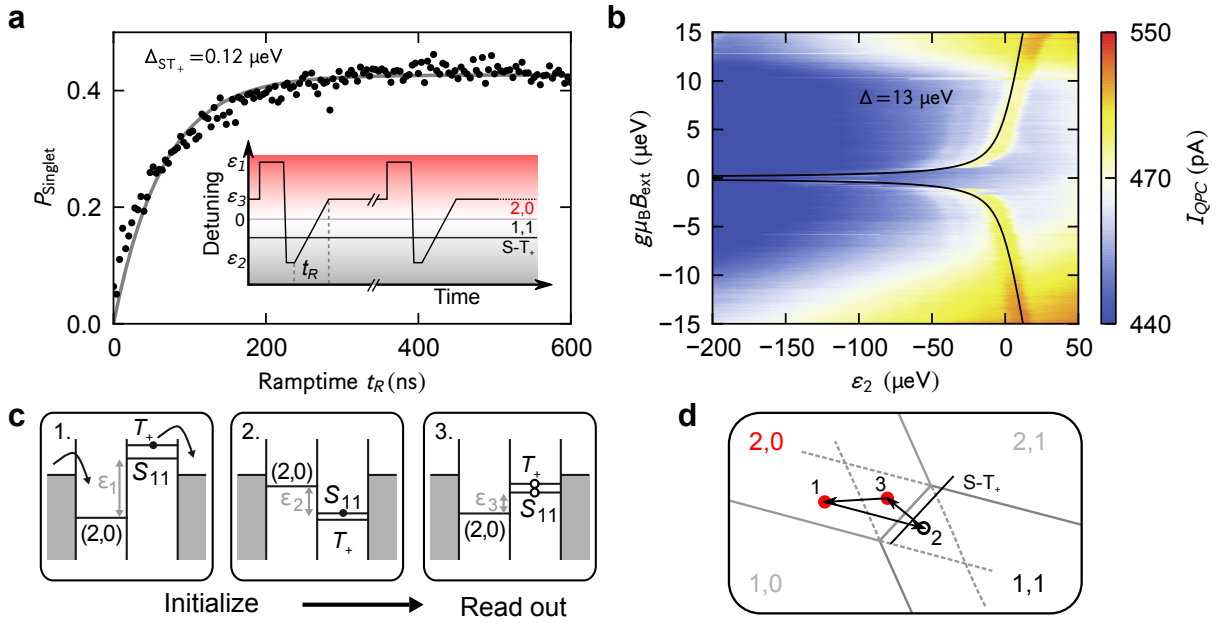

FIG. S3: Singlet-triplet and interdot tunnel couplings. (a) Probability to occupy the singlet state S_{11} after initialization in the same state and then sweeping across the S_{11}-T_+ avoided crossing (at $T \simeq 20\,\mathrm{mK}$) as a function of the ramp time t_R which is proportional to the inverse sweep speed v. From the theory (gray line) the singlet-triplet coupling is determined (details in bulk text). The inset sketches the pulse sequence. (b) Current I_{QPC}, measured at $T \simeq 20\,\mathrm{mK}$ through the detector quantum point contact, as function of an external magnetic field and detuning ε_2, where the entire pulse sequence shown in the inset of panel a is shifted vertically. Otherwise, the applied pulse sequence is the same as in a, but with a quick and constant ramp time $t_R \simeq 1.1\,\mathrm{ns}$. Enhanced current at the black lines (theory) mark singlet-triplet resonances. This so-called spin-funnel is used to determine the interdot-tunnel coupling Δ (details in bulk text). (c) Subfigures 1., 2., 3. sketch the chemical potentials (and dynamics) of the DQD at detunings ε_1, ε_2, ε_3 in the inset of panel a. (d) Sketch of the DQD charge stability diagram indicating the positions at detunings ε_1, ε_2, ε_3 during the pulse sequence sketched in the inset of panel a.

and transition rates between triplet and singlet states. All parameters used in our numerical calculations are summarized for convenience in Table I in Sec. IV. Henceforth, we describe our determination of those parameters, which are neither trivial nor described elsewhere in this article. The largest energy scales are the intradot and interdot Coulomb interactions $U \simeq 3.5\,\mathrm{meV}$ and $U' \simeq 0.8\,\mathrm{meV}$. Knowing the energy calibration (see last section) these values can be extracted from the charge stability diagram. In detail, U corresponds to the distance between charging lines in Fig. S1(a) and U' to the distance between the triangle tips in Fig. S1(b).

Next, we discuss the triplet-singlet coupling, which in our case originates from the hyperfine interaction between the electrons and many nuclei on the one hand and the inhomogeneous magnetic field of our nanomagnet, shown in Fig. 1(a) of the main article, on the other hand. The T_{11} triplets split into $T_+ = |\uparrow\uparrow\rangle$, $T_0 = (|\uparrow\downarrow\rangle + |\downarrow\uparrow\rangle)/\sqrt{2}$ and $T_- = |\downarrow\downarrow\rangle$. The couplings between T_+ and S_{11} and between T_- and S_{11} are identical and caused by field inhomogeneities parallel to the effective magnetic field [approximately parallel to $B_{ext} = 200\,\mathrm{mT}$, see Figs. 1(a,c)] of the main article, while T_0 and S_{11} are coupled by the perpendicular field inhomogeneities. We actually determine the T_+-S_{11} coupling by measuring the average charge occupation in a continuously pulsed gate experiment. Here, we use a quantum point contact as charge detector while no voltage is applied across the DQD, $V = 0$. As sketched in the inset of Fig. S3(a) and in the energy diagram in Fig. S3(d), we first initialize the DQD in S_{20} by applying a large positive detuning ε_1 where the transition $T_{11} \to S_{20}$ happens quickly via charge exchange with the leads: $T_{11} \to (1,0) \to S_{20}$; see left panel in Fig. S3(c). Next we prepare the DQD in the S_{11}-state at $\varepsilon = \varepsilon_2$ by sweeping the detuning from $\varepsilon_1 \to \varepsilon_2$ at a constant speed obeying $\Delta^2 \gg 2\hbar v/\pi \gg \Delta^2_{ST,\pm}$. During this sweep, the DQD is adiabatically transferred from the S_{20} to the S_{11} state while passing the S_{20}-S_{11} avoided crossing with coupling Δ. The DQD also passes the S_{11}-T_+ avoided crossing with coupling $\Delta_{ST,\pm}$; this passage is, however, non-adiabatic because $\Delta_{ST,\pm} \ll \Delta$ and, hence, the DQD remains in the S_{11}-state. After waiting a short time at ε_2 [center panel in Fig. S3(c)], we perform a Landau-Zener passage within the ramp time t_R through the S_{11}-T_+ avoided crossing up to $\varepsilon = \varepsilon_3$ where we spend a relatively long time in order to read out the charge state of the DQD [right panel in Fig. S3(c)]. We expect to find the charge configuration $(2,0)$ in case of a slow passage (with the DQD staying in the singlet subspace) and $(1,1)$ in case of a fast passage bringing the DQD into the T_+ state, because the decay $T_+ \to S_{11} \to S_{20}$

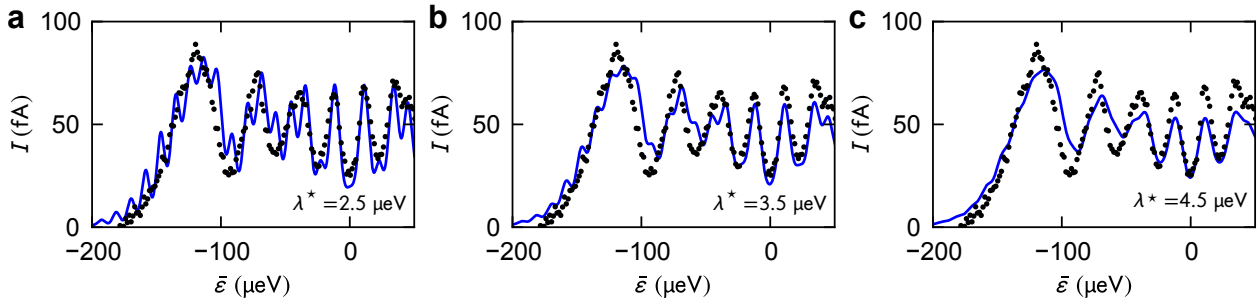

FIG. S4: Accuracy in determination of inhomogeneous broadening. $I(\bar{\varepsilon})$ at constant amplitude $A = 130\,\mu$eV and for $T = 18\,$mK and $\Omega/2\pi = 2.75\,$GHz as in Fig. 3(a) of the main article. The measured data (black dots) are identical in all three panels while the model curves (blue lines) are based on the same $\alpha_Z = 1.5 \times 10^{-4}$ (our final value) but use various values of $\lambda^\star$. Best agreement with the measured data is reached for $\lambda^\star = 3.5\,\mu$eV (panel b).

is hindered by Pauli-spin blockade. Figure S3(a) displays the probability to stay in the singlet subspace $P_{\rm singlet} = \alpha\,(1 - P_{\rm LZ}) = \alpha\left(1 - \exp\left[-\pi\Delta^2_{{\rm ST},\pm}/2\hbar v\right]\right)$ as a function of $t_{\rm R} = (\varepsilon_3 - \varepsilon_2)/v$. Fitting this function [gray line in Fig. S3(a)] to the measured singlet probability indicates our S_{11}-T_+ coupling of $\Delta_{{\rm ST},\pm} = (119 \pm 10)\,$neV, produced by our nanomagnet. The prefactor $\alpha \simeq 0.43$ accounts for the partial decay $T_+ \to S_{11}$ and depends on the duration of the readout period. Taking into account the interdot tunnel coupling which results in a reduced weight of S_{11} in the singlet eigenstate, this $\Delta_{{\rm ST},\pm}$ corresponds to a magnetic field difference in the two dots giving rise to $g\mu_{\rm B}\Delta B_x \simeq 0.2\,\mu$eV, smaller than previously measured in the same sample [4], which indicates a degradation by oxidation of the single domain properties of our nanomagnet during six months of shelf storage. Here, we used the g-factor $|g| = 0.36$ as determined for our DQD in Ref. [4] and Bohr's magneton $\mu_{\rm B}$. The hyperfine induced coupling contribution in our DQD is $\Delta_{\rm hyperfine} \simeq 60\,$neV [4] and results in a corresponding inhomogeneous broadening of the singlet-triplet coupling.

To determine the interdot tunnel coupling Δ we perform a so-called spin funnel experiment [11]. Thereby we repeat the same continuously pulsed gate measurements as above but with a short and fixed $t_{\rm R} = 1.1\,$ns so that all passages through the S_{11}-T_+ crossing are now equally non-adiabatic while the passage through the S_{11}-S_{20} crossing is still adiabatic [see inset of Fig. S3(a)]. Under this conditions, a pulse cycle $\varepsilon_1 \to \varepsilon_3 \to \varepsilon_2 \to \varepsilon_3$ [Fig. S3(d)] will usually bring the system back to the S_{20} singlet after preparing the S_{20} singlet at the detuning ε_1. A notable exemption occurs if ε_2 coincides with the singlet-triplet resonance, namely for $\pm g\mu_{\rm B}B_{\rm ext} = \frac{1}{2}(\pm\sqrt{\varepsilon_2^2 + \Delta^2} - \varepsilon_2)$, and if the system spends sufficient time ($> h/\Delta_{\rm ST}$) there to allow for a singlet-triplet transition. As a consequence, we measure a deviation from the S_{20} configuration at this resonance during the readout at ε_3, where the T_{11} triplet decays only slowly. To map out this condition we plot in Fig. S3(c) the current $I_{\rm QPC}$ through the detector QPC (corresponding to the average charge state of the DQD) as a function of $g\mu_{\rm B}B_{\rm ext}$ and ε_2. The two distinct lines of enhanced $I_{\rm QPC}$ correspond to a finite occupation of one of the $T^\pm$ triplets. By fitting the resonance condition (above) we find our tunnel coupling $\Delta = (13 \pm 1)\,\mu$eV [black lines in Fig. S3(c)].

The initialization and decay rates $\Gamma_{\rm in}$ and $\Gamma_{\rm out}$, respectively, are finally reconstructed from measuring the dc current through the DQD as a function of detuning and as a function of source drain voltage in forward and backward direction. An example of such a measurement is shown in Fig. S1(c), where in this case an rf-modulation was applied in addition. Since the current in backward direction [for $\mu_{\rm D} > \mu_{\rm S}$ in Fig. 1(b) of the main article] is practically independent of the spin relaxation, it allows us to determine the dot-drain coupling $\Gamma_{\rm out} = \Gamma_L$. In turn, the magnitude of the current in forward direction provides a faithful estimate for γ_σ and $\Gamma_{\rm in}$.

D. Origin of the inhomogeneous broadening

Compared to the measured LZSM patterns, our Floquet-Bloch-Redfield formalism, which already takes into account the realistic electron-phonon coupling α_Z and the DQD parameters summarized in Table I such as tunnel couplings, predicts a much higher visibility of the interference pattern resulting in sharper current maxima. This is evident in Fig. 3(a) of the main article which compares the measured interference at a constant modulation amplitude with calculated data. We resolved this caveat by introducing an additional Gaussian inhomogeneous broadening $\lambda^\star$ [Fig. 3(a)], where the final values $\alpha_Z = 1.5 \times 10^{-4}$ and $\lambda^\star = 3.5\,\mu$eV have been calculated self-consistently. Figure S4 demonstrates the convergence by plotting three calculated curves (lines) using various values of $\lambda^\star$ around its final value while the electron-phonon coupling is kept fixed at $\alpha_Z = 1.5 \times 10^{-4}$ [as also in Fig. 3(a)] of the main article. The model curve (blue line) in panel b using $\lambda^\star = 3.5\,\mu$eV fits best to the measured data (dots).

The inhomogeneous broadening is a result of the combination of slow charge noise and our time averaging dc measurement: The spectrum of charge noise has been

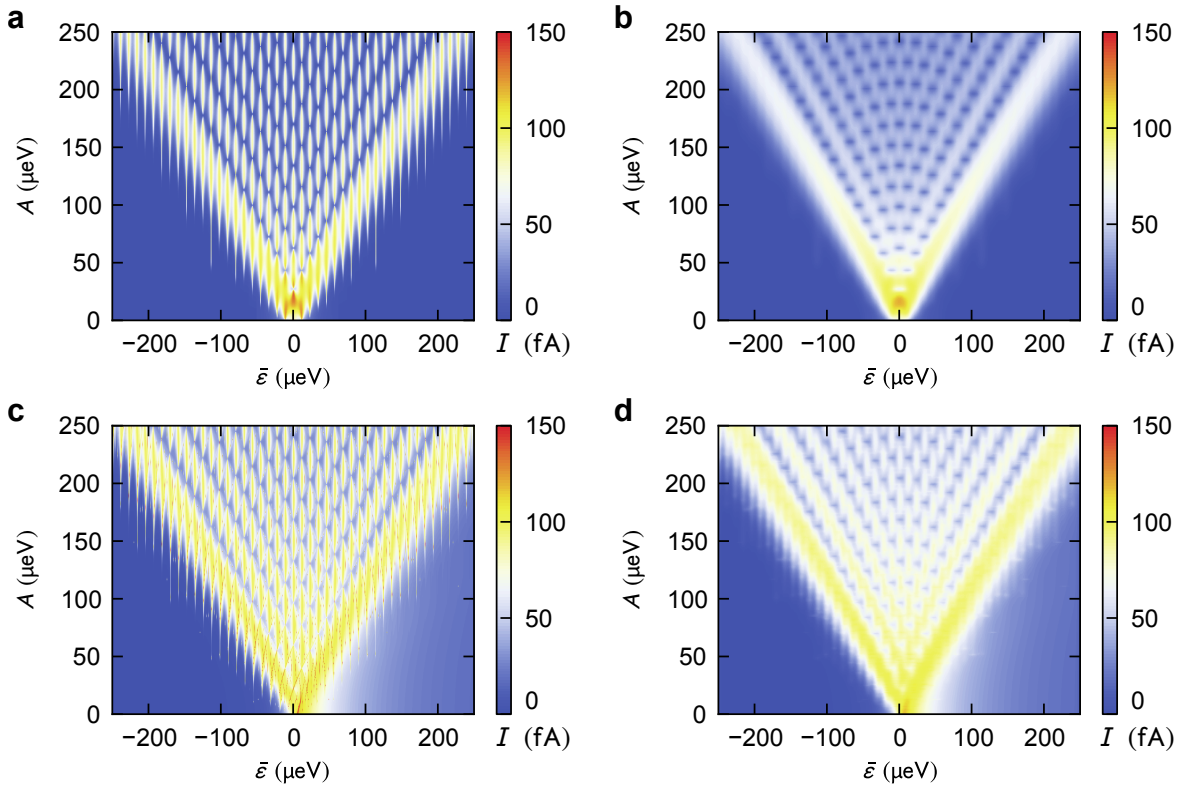

FIG. S5: Equation (2) versus full model. All data are calculated using $\Omega/2\pi = 2.75\,\mathrm{GHz}$ and system parameters as listed in Table I. (a) Analytical solution of Eq. (2). The width of the current peaks as function of $\bar{\varepsilon}$ is $\delta\bar{\varepsilon} = \sqrt{\Delta_n^2 + \gamma^2}$ (containing only tunneling rates), see Eq. (2). (b) Analytical solution of Eq. (2), as in panel a, but additionally convoluted with a Gaussian profile of width $\lambda^\star = 3.5\,\mu\mathrm{eV}$ to simulate the effect of an inhomogeneous broadening in a time ensemble measurement caused by slow charge noise. (c) Numerical solution of our full model, including electron-phonon coupling, at $T = 18\,\mathrm{mK}$ (with parameters from Table I) but using $\lambda^\star = 0$. (d) Numerical solution of our full model as in panel c but using $\lambda^\star = 3.5\,\mu\mathrm{eV}$. The similarity between the analytical solutions and the low temperature result of our full model, if comparing panel a with c and panel b with d, justifies our perturbative approach to treat the electron-phonon coupling.

measured in heterostructures similar to ours. It can be described as $1/f$-noise which typically occurs only at frequencies below 10 kHz [12–15]. The longest time scale of our experiment is the dwell time in the DQD of each electron, contributing to the measured current. It is in the order of $1\,\mu\mathrm{s}$, much shorter than the highest frequency components of charge noise. A single shot qubit measurement and hence T_2 are, consequently, unlikely to be affected by charge noise. However, in our steady state experiments each measured data point averages the dc current over 200 ms. Such an effective time ensemble measurement can be inhomogeneously broadened by charge noise, slow compared to T_2 but fast compared to the averaging time. Assuming a Markovian statistics, this inhomogeneous broadening is well described using a Gaussian distribution with standard deviation $\lambda^\star$.

E. Dissipation strength

In comparison, determining the dissipation parameter α_Z requires considerably more effort, experimentally and even more in theory, where it enters in a rather complex manner. We follow a route that is based on an idea by Rudner *et al.* [16], who showed analytically that the Fourier transformed $\widehat{I}(\tau_\varepsilon, \tau_A)$ of the dc current pattern exhibits a lemon-shaped structure, composed of sinusoidal branches. However, the treatment of Ref. [16] neglects the impact of the tunnel matrix element Δ on the dynamical phase which finally yields an expression similar to our Eq. (2), but with $\Delta_n^2 + \gamma^2$ in its denominator replaced by a phenomenological decay rate $\widetilde{\gamma}^2$. Thus, the result is a simple Lorentzian broadening of width $\widetilde{\gamma}$ giving rise to an exponential decay, $\propto \exp(-\widetilde{\gamma}|\tau_\varepsilon|)$, of the Fourier transformed including the lemon structure. This simplification allows an analytical solution of the problem for the price of limiting our horizon to an unrealistically weak inter-dot tunnel coupling and a convenient but just phenomenologically introduced broadening.

In our DQD we have $\Delta_n \gtrsim \gamma$ for all relevant resonances in the whole parameter range measured; more precisely the interdot tunnel coupling exceeds all broadening mechanisms including the initialization and decay rates, Γ_{in} and Γ_{out}, but also the broadening caused by

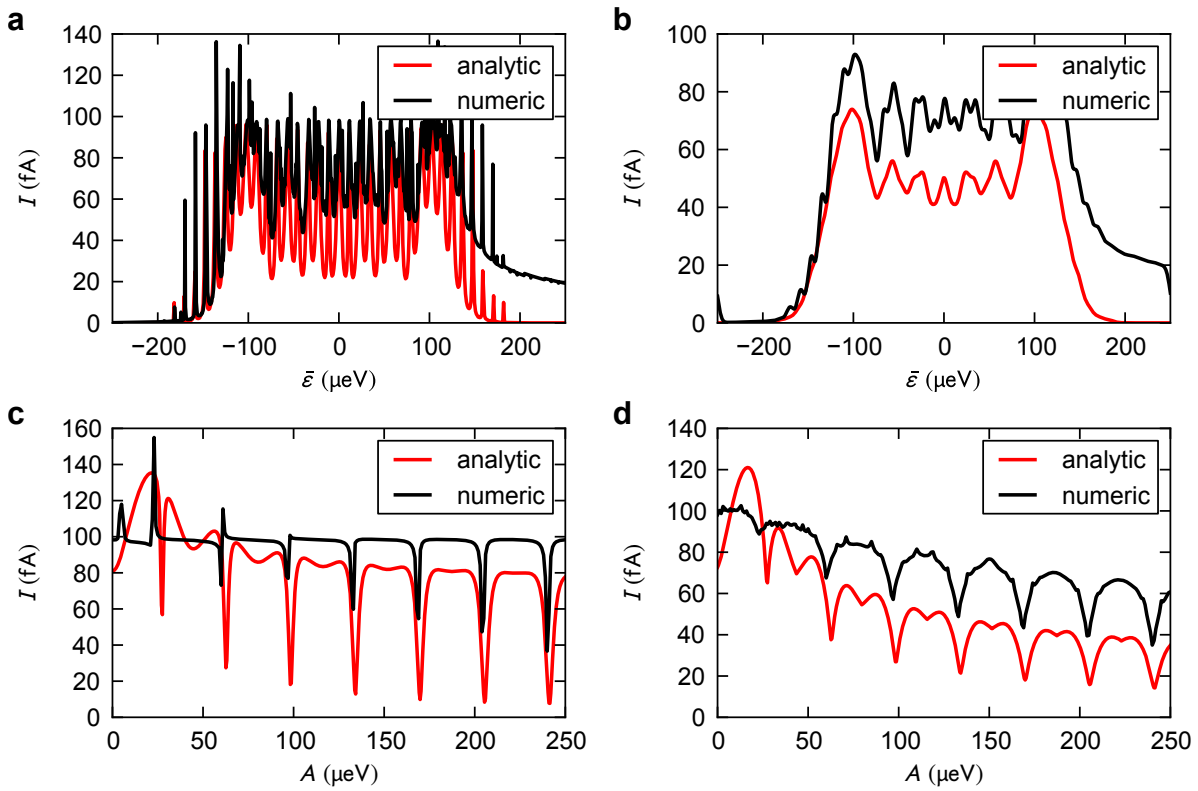

FIG. S6: Equation (2) versus full model — slices. Slices of the data in Fig. S5. Each panel compares the analytical predictions of Eq. (2) (marked as "analytic") with those of our full model for $\alpha_Z = 1.5 \times 10^{-4}$ and at $T = 18\,\mathrm{mK}$ ("numeric"). The modulation frequency is $\Omega/2\pi = 2.75\,\mathrm{GHz}$. (a) $I(\bar{\varepsilon})$ at $A \simeq 130\,\mu\mathrm{eV}$ using $\lambda^\star = 0$. (b) $I(\bar{\varepsilon})$ at $A \simeq 130\,\mu\mathrm{eV}$ using $\lambda^\star = 3.5\,\mu\mathrm{eV}$. (c) $I(A)$ for $\bar{\varepsilon} = 0$ using $\lambda^\star = 0$. (d) $I(A)$ for $\bar{\varepsilon} = 0$ using $\lambda^\star = 3.5\,\mu\mathrm{eV}$. For the agreement of the full model results with measured data, see Figs. 3(a,b) of the main text.

environmental influences. This guaranties a sufficiently long coherence time, $T_2 > \hbar/\Delta$, which is a necessary condition for qubit operation as $\Delta/\hbar$ is the qubit clock-speed.

Interestingly, the finite Δ_n in the denominator of Eq. (2) has a direct manifestation in the Fourier transformed of the measured LZSM patterns. It gives rise to extra features described in Eq. (3) present in both our measured and calculated data: cosine shaped arcs in the Fourier transformed (marked by black arrows) in Fig. 2(e,h) of the main article in addition to the principal lemon structure. These extra arcs are also evident in the measured data discussed in reference [16] but they have not been reproduced in the calculations there.

The analytical expression in Eq. (2) serves as a sign post for our analysis as it describes the main features of our measurements correctly. This is evident in Fig. S5 and Fig. S6 which provide a direct comparison between the predictions of Eq. (2) and our full model. The detailed comparison between our numerical calculations and measurements, provided in Figs. 3(a,b) of the main article, further demonstrates that our full model fits considerably better to our data than Eq. (2). The analytical expression in Eq. (2) only considers non-interacting electrons and, hence, fails to predict decoherence effects. A reliable physical interpretation including the observed temperature dependence [see main text, Figs. 3(c) and 4] requires a detailed analysis: First, it is necessary to explicitly consider all dot-lead and interdot tunnel couplings and the relevant energy spectrum of the DQD. Second, interaction effects have to be included which in our case comprise: (i) Coulomb-interaction giving rise to Coulomb blockade and the coupling to charge noise; (ii) exchange interaction causing Pauli-spin blockade, hyperfine interaction causing spin-flips and the mixing between singlet and triplet states by the inhomogeneous field of the nanomagnet; (iii) electron-phonon interaction resulting in decoherence. We focus on the latter. Our master equation formalism takes into account all these effects and allows us to numerically calculate $I(\bar{\varepsilon}, A)$ in the range in which we take our experimental data and compute its two-dimensional discrete Fourier transformation. Finally, a Fourier transformation of our data causes cut-off effects, because both measured and calculated data span only finite ranges in $\bar{\varepsilon}$ and A. Typical artefacts of the discrete Fourier transformation are avoided throughout our analysis as good as possible by using only data with sufficiently high resolution.

Next, we discuss the details of our data analysis: after calculating raw data resembling the measured LZSM pat-

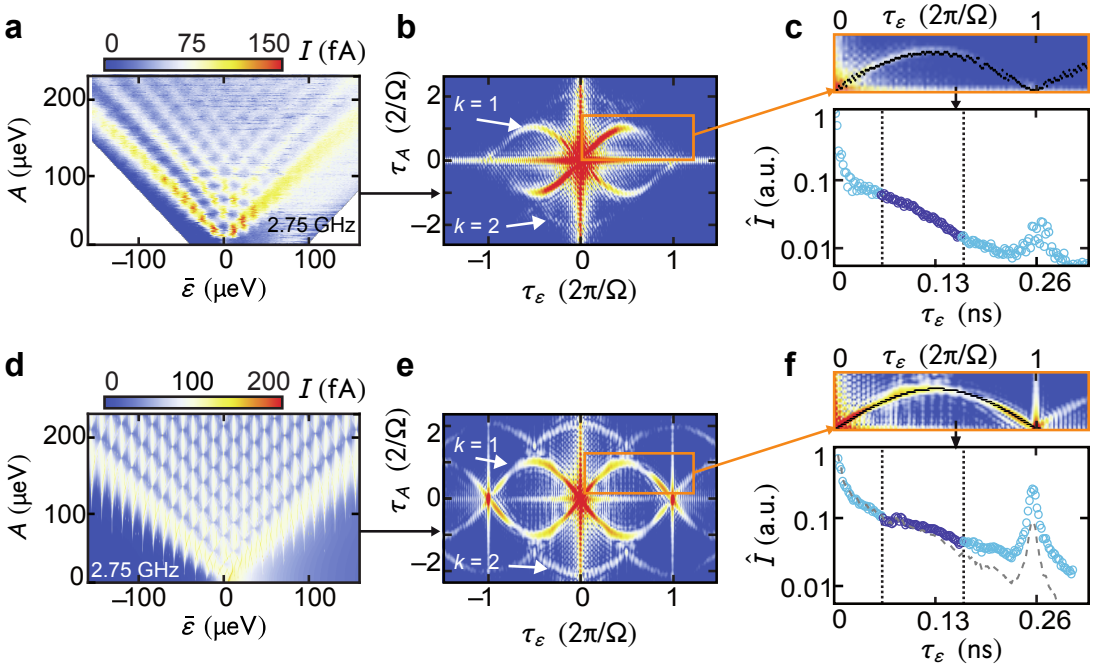

FIG. S7: Data analysis based on Fourier transformation. Analysis steps on measured data (a–c) versus theory (d–f) for $T \simeq 60\,\mathrm{mK}$ and $\Omega/2\pi = 2.75\,\mathrm{GHz}$ using the parameters listed in Table I for the numerical calculations. The numerical data in panels d–f are without the inhomogeneous broadening, i. e. for $\lambda^\star = 0$. (a,d) LZSM interference patterns $I(\bar{\varepsilon}, A)$. The measured data in panel a display a stronger asymmetry in $\bar{\varepsilon}$ compared to the numerical data in panel d, which is discussed in Sec. II H. (b,e) Two-dimensional Fourier transformed $\widehat{I}(\tau_\varepsilon, \tau_A)$ of the raw data in panels a and d. Clearly visible are the principal lemon arcs for $k = 1$ and those for $k = 2$ in Eq. (3). Horizontal and vertical lines at $\tau_\varepsilon = 0$ and $\tau_A = 0$, respectively, are artefacts caused by the discrete Fourier transformation. The color scales are in arbitrary units as the absolute amplitude of $\widehat{I}$ scales with the number of data points in the raw data and has no physical meaning. The higher visibility of the numerical data in panel e compared to the measured data in b is due to the negligence of the inhomogeneous broadening. (c,f) Decay of a quarter of the principal lemon arc in the range $0 \lesssim \tau_\varepsilon \lesssim 2\pi/\Omega$. The dashed line in the lowest panel is the data (open circles) multiplied by the Gaussian $\exp[-\frac{1}{2}(\lambda^\star \tau_\varepsilon/\hbar)^2]$ using $\lambda^\star = 3.5\,\mu\mathrm{eV}$ for direct comparison with the data in panel c. The region between the two vertical (dotted) lines is then fitted with Eq. (4) to determine λ.

terns, using estimated values for α_Z and $\lambda^\star$ we apply the identical analysis to experimental and numerical data. Then, we compare the results and repeat calculation and analysis of the numerical data with modified α_Z and $\lambda^\star$ in a self-consistent way until we find best agreement with the measured data. Figure S7 demonstrates the last step of this procedure, exemplarily, for a typical set of measured data in panels a–c and the corresponding calculated data, based on our model parameters listed in Table I, in panels d–f. The numerical data shown here neglect the inhomogeneous broadening, equivalent to using $\lambda^\star = 0$, as this is sufficient for evaluating λ from the numerical data. Measured and calculated data in Fig. S7, therefore, imply differences (details in figure caption); for a direct comparison including the inhomogeneous broadening in the numerical data we refer to Fig. 2 and Fig. 3 of the main article. Panels a and d of Fig. S7 show the measured and calculated $I(\bar{\varepsilon}, A)$, respectively, panels b and e the corresponding Fourier transformed $\widehat{I}(\tau_\varepsilon, \tau_A)$. Since the current is real-valued, the Fourier transformed pattern is point symmetric, while the approximate mirror symmetry at the A-axis relates the two independent branches. Therefore it is sufficient to restrict the analysis to the upper-right quarter as indicated in Figs. S7(c,f). The Fourier transformed of the current along the lemon arcs $\widehat{I}(\tau_\varepsilon, \tau_A)\big|_{\mathrm{lemon}}$ incorporate a decay between two maxima at the arcs intersections at $\tau_\varepsilon = 0$ and $\tau_\varepsilon = 2\pi/\Omega$. These maxima indicate a fast intrinsic decay and are related to Δ_n^2 dominating the denominator of Eq. (2) near the n-photon resonances. They are not a measure of the qubit decoherence. Note that finite range cut-off effects of the Fourier transformations cause the finite $\widehat{I}(\tau_\varepsilon, \tau_A)$ along $\tau_\varepsilon = 0$ and $\tau_A = 0$ in Figs. S7(b,e), which additionally obscure the maxima in $\widehat{I}(\tau_\varepsilon, \tau_A)\big|_{\mathrm{lemon}}$. For our further analysis we therefore only consider the decay of $\widehat{I}(\tau_\varepsilon, \tau_A)\big|_{\mathrm{lemon}}$ in the regions marked in Figs. S7(c,f). To determine λ the measured $\widehat{I}(\tau_\varepsilon, \tau_A)\big|_{\mathrm{lemon}}$ in Fig. S7(c) is fitted with Eq. (3) using $\lambda^\star = 3.5\,\mu\mathrm{eV}$ while the calculated data in Fig. S7(f) are just fitted with the exponentially decaying term in Eq. (3) using $\lambda^\star = 0$.

To accurately determine the electron-phonon coupling we consider the temperature dependence of $\lambda(\alpha_Z, T)$ rather than relying on a single LZSM pattern at low tem-

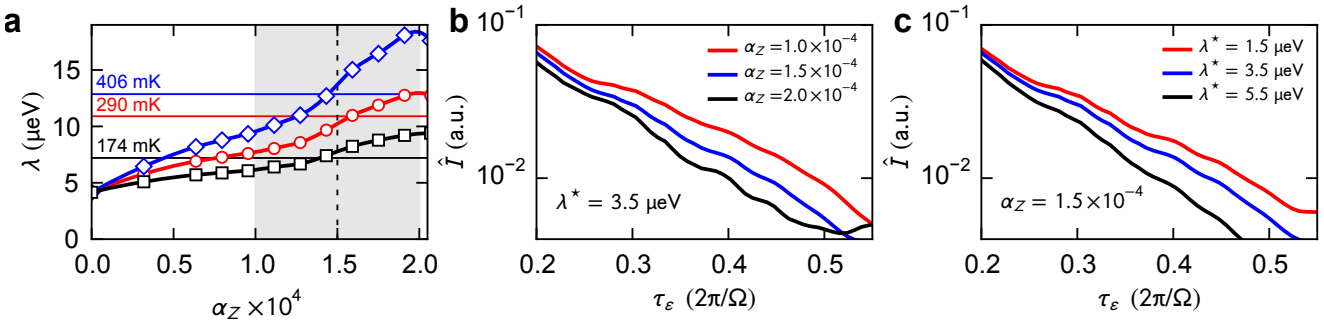

FIG. S8: Analysis of the Fourier transformed — electron-phonon coupling. (a) Decay rate $\lambda(\alpha_Z)$ for three different temperatures. The curves are numerically calculated using the fixed $\lambda^\star = 3.5\,\mu$eV but various values of α_Z. Horizontal lines indicate λ determined from our measured data for the same three temperatures. The vertical dashed line and the gray region indicate the best fitting α_Z and its accuracy. Also compare to Fig. 4(b) of the main article. (b) Numerically calculated decay of the principal lemon arc for $T = 295\,$mK using the fixed $\lambda^\star = 3.5\,\mu$eV but various values of α_Z [same as those in Fig. 4(b) of the main article]. (c) Numerically calculated decay of the principal lemon arc for $T = 295\,$mK using the fixed $\alpha_Z = 1.5 \times 10^{-4}$ but various values of $\lambda^\star$.

perature. This procedure allows us to properly separate the two main noise sources, the temperature independent charge noise giving rise to the inhomogeneous dephasing time $T_2^\star$ and the temperature dependent homogeneous broadening λ, which is directly related to α_Z and determines the qubit decoherence time T_2. (There are no indications for a temperature dependence of the charge noise for $T < 1\,$K). The details of this procedure are discussed in the main article around Fig. 4. In Fig. S8(a) we provide additional data on the determination of the electron-phonon coupling presenting $\lambda(\alpha_Z)$ for various temperatures. Each data point has been determined from fitting Eq. (4) to a principal lemon arc as the one in Fig. S7(f) calculated using the fixed $\lambda^\star = 3.5\,\mu$eV but various values of α_Z. Horizontal lines indicate λ determined from our measured data for the same three temperatures. Assuming a temperature independent α_Z we find best agreement to our data for $\alpha_Z = (1.5 \pm 0.2) \times 10^{-4}$ (vertical dashed line and gray region). Note that a similar information is contained in Fig. 4(b) of the main article. The saturation of $\lambda(T)$ for low temperatures at a value $\lambda_{\rm min} \simeq 4\,\mu$eV is a consequence of measuring PAT current peaks which possess the intrinsic width $\sqrt{\Delta_n^2 + \gamma^2}$ of $I(\bar{\varepsilon}, A)$ as a function of $\bar{\varepsilon}$ expressed in Eq. (2). As is evident from Fig. 4(b) of the main article the lower bound $\lambda_{\rm min}$ is also observed in our experiments. Figs. S8(b,c) demonstrate the robustness of our main model parameters α_Z and $\lambda^\star$, respectively, by varying each of the two parameters separately and comparing the decay of the principal lemon arcs.

F. Summary of data analysis

Summarizing our data analysis, we started by determining all important physical constants such as tunnel couplings and spin-flip rates based on a number of independent measurements on our double quantum dot device already tuned to the configuration used for the LZSM interferometry experiments. To determine the remaining key-parameters $\lambda^\star$ and α_Z we used a self-consistent approach within our model. It turned out that α_Z could be best determined from the two-dimensional Fourier transformed of LZSM interference patterns at various temperatures. In contrast, $\lambda^\star$, which causes a strong but temperature independent inhomogeneous broadening, could be equally well determined from the raw data. This allowed us to avoid a third fit parameter (besides λ and a prefactor) by which we would loose precision in finding α_Z. Specifically, by comparing the resulting decay rates $\lambda(T, \alpha_Z)$ with those extracted from our measurements [see Fig. 4(b) of the main article], we find that in our setup, decoherence can be described by a Caldeira-Leggett model with Ohmic spectral density and the dimensionless dissipation strength $\alpha_Z \simeq 1.5 \times 10^{-4}$.

G. LZSM interference at various frequencies

In the main article we already demonstrate that the LZSM interference pattern depends on frequency. In Fig. S9 we extend the frequency range presenting data between $1.5\,{\rm GHz} \leq \Omega/2\pi \leq 5.5\,{\rm GHz}$ all measured (upper line) or numerically calculated (lower line) at $T \simeq 20\,$mK. At the highest frequencies we observe clear PAT patterns as expected from Eq. (2) which distort increasingly as the frequency is lowered and neighbored PAT current peaks overlap. At $\Omega/2\pi = 1.5\,$GHz all interference signatures are (almost) lost as $\hbar\Omega \simeq 6\,\mu$eV is close to the broadening caused by the combination of our $\lambda^\star \simeq 3.5\,\mu$eV and $\lambda(T = 20\,{\rm mK}) \simeq 4\,\mu$eV.

It is instructive to estimate the Landau-Zener probability $P_{\rm LZ} = \exp(-\pi\Delta^2/2\hbar|v|)$ [17–21] for the Hamiltonian (6) with onsite-energy difference $\varepsilon(t) = \bar{\varepsilon} + A\cos(\Omega t)$ for the frequencies of the experiment and an intermediate amplitude, say $A = 100\,\mu$eV. Then the sweep velocity at

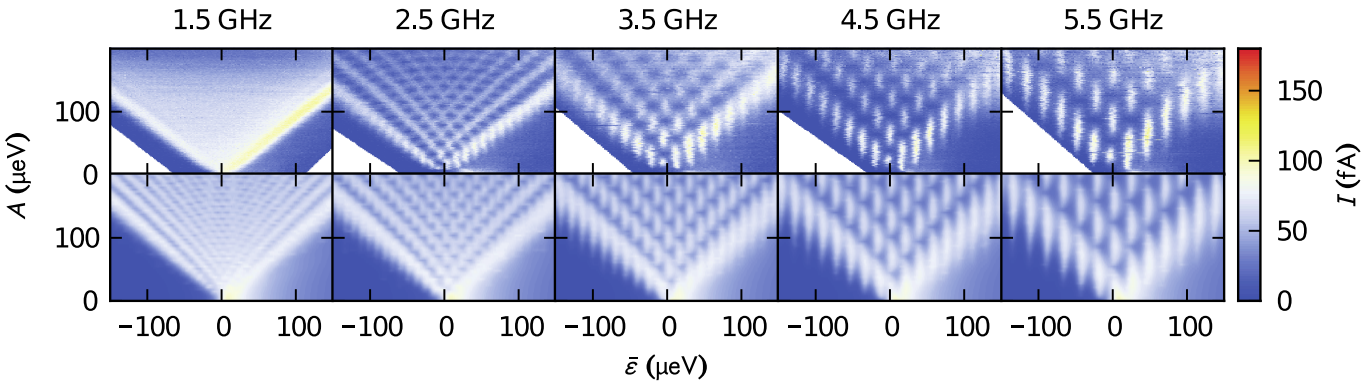

FIG. S9: LZSM interference patterns for various modulation frequencies. The upper row contains measured and the lower row calculated data, both for $T \simeq 20\,\mathrm{mK}$. Model parameters according to Table I.

the avoided crossing is $|v| = \Omega\sqrt{A^2 - \bar{\varepsilon}^2}$. Thus we find for the frequencies used in Fig. S9 and $\bar{\varepsilon} = 0$ Landau-Zener transition probabilities in the range $0.65 \lesssim P_{\mathrm{LZ}} \lesssim 0.89$ and $P_{\mathrm{LZ}} \simeq 0.79$ for $\Omega/2\pi = 2.75\,\mathrm{GHz}$ where we performed our temperature dependent measurements. For non-vanishing $\bar{\varepsilon}$, P_{LZ} is smaller, so that the average over all relevant crossings becomes of order $P_{\mathrm{LZ}} \simeq 1/2$ which ensures good visibility. For frequencies $\Omega/2\pi \lesssim 2\,\mathrm{GHz}$, the analytic estimate of Eq. (2) based on PAT becomes increasingly inaccurate and, consequently, our interpretation of the lemon arc decay given by Eq. (4) is not guaranteed.

H. Influence of dynamic nuclear polarization

The measured data, e. g. in Figs. 2(a,b) of the main article and in Figs. S9(a–e) contain two distinct features not included in our model. The first one is a pronounced asymmetry in $I(\bar{\varepsilon})$ in the limit of large amplitudes. It is considerably smaller in the theoretical data, which neglect the influence of the T_{20} triplet. The stronger asymmetry observed in measured data is indeed caused by the influence of the T_{20} state which grows with increasing positive detuning. The effect is clearly seen in Fig. S2 and has been discussed at the end of Sec. II A. The second feature occurs at very small amplitudes and appears as if the tip of the current triangle was shifted to slightly positive values of $\bar{\varepsilon}$. It is a signature of dynamic polarization of the nuclear spins caused by the hyperfine interaction between the current carrying electrons and the nuclear spins in the DQD. At very small A, the rf-modulation is practically off and we simply measure the current through the DQD while sweeping $\bar{\varepsilon}$ from positive towards negative values. As explained in detail in Ref. [4], the current maximum occurs at the value of $\bar{\varepsilon}$ that marks the resonance between the T_- and the singlet state. This resonance is shifted towards positive ε by dynamic nuclear polarization [4]. The fact that the shift only occurs at very small A indicates that the continuous rf-modulation effectively prevents the polarization of nuclear spins. We therefore, do not have to include this in our model as long as we concentrate on data with $A \gtrsim 20\,\mu\mathrm{eV}$.

I. Temperature dependence and limitations of our model

The temperature dependence of the LZSM patterns discussed in the main article in Fig. 3(c) and Fig. 4 is at the heart of our model as it is used to accurately determine the electron-phonon coupling and finally the qubit coherence time T_2. So far we have mostly concentrated on the temperature dependence of the principal lemon arc in the Fourier transformed of the LZSM patterns. Figure S10(a) shows LZSM patterns measured (upper line) versus calculated (lower line) at various temperatures. Figure S10(b) shows horizontal slices at $A = 130\,\mu\mathrm{eV}$ (dots are measured and lines present numerical data). To facilitate a quantitative comparison, we extract the visibility as well as the average current $\bar{I}$ in the region defined by $-70\,\mu\mathrm{eV} \le \bar{\varepsilon} \le 70\,\mu\mathrm{eV}$ and plot the temperature dependences of experimental versus numerical data in Fig. S10(c). The temperature dependence of the calculated visibility resembles the measured ones. However, the measured mean current is roughly temperature independent while the predicted mean current increases with temperature. Interestingly, the decay of the principal lemon arc of the Fourier transformed is strongly related to the visibility of a LZSM pattern but not at all to the mean current. Our model, therefore, describes the decoherence of the qubit correctly while it predicts an increase of the mean current with temperature that is stronger than in the measurements. A possible explanation for this discrepancy is that in the experiment, the spectral density of the phonons is not strictly ohmic as is assumed in our model, see Sec. III A 3. Consequently, our theoretical description may overestimate the thermal activation of some singlet-triplet transitions.

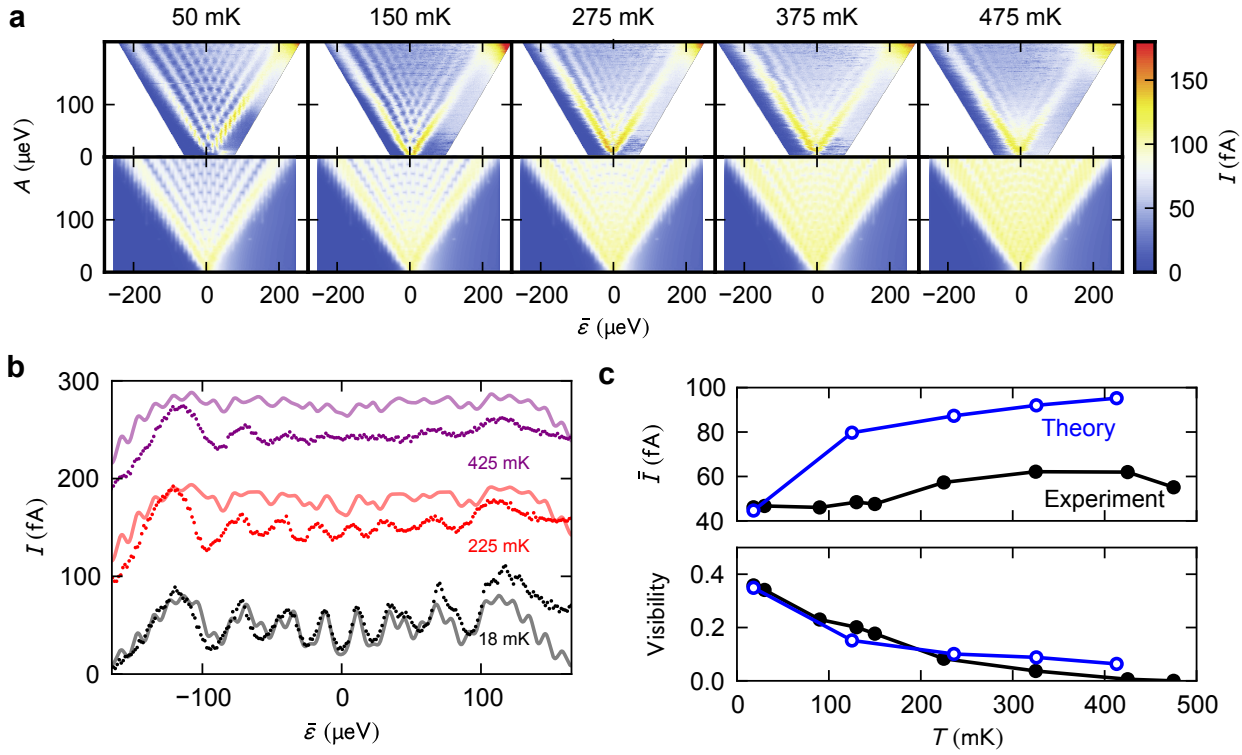

FIG. S10: Temperature dependence of raw data versus model. (a) LZSM interference patterns at $\Omega/2\pi = 2.75\,\mathrm{GHz}$ and various temperatures. The upper plots have been measured, the lower plots calculated using our full model with the parameters listed in Table I. (b) Horizontal slices from plots like those in panel a at $A = 130\,\mu\mathrm{eV}$. Dots correspond to measured and lines to numerical data. (c) Average current $\bar{I}$ (upper panel) and visibility $\nu = (I_{\max} - I_{\min})\,/\,(I_{\max} + I_{\min})$ (lower panel), extracted from the slices presented in panel b and similar data, as function of temperature. The data points are taken in the region $-100\,\mu\mathrm{eV} \leq \bar{\varepsilon} \leq 30\,\mu\mathrm{eV}$; this avoids the region of $\bar{\varepsilon} > 100\,\mu\mathrm{eV}$ where experimental data are influenced by the T_{20} triplet which is neglected in our model. Black dots are measured while blue open circles are calculated.

III. THEORETICAL MODELLING

Our aim is to compute the LZSM interference patterns using a realistic model and to compare the results with the measured ones. Therefore we need to consider besides our DQD also its coupling to electron source and drain contacts, as well as to environmental fluctuations. In order to realistically describe our measurements, performed in the regime of Pauli-spin blockade which is partly lifted by an inhomogeneous Zeeman field of an on-chip nanomagnet, we further include spin relaxation. Our model considers all energetically accessible DQD states and all processes which play a noticeable role in our experiment. Comparing our theoretical and experimental data we find two main contributions to a noisy environment: the first is slow charge noise [12–15] and can be described as an inhomogeneous broadening $\lambda^\star$, the second is the heat bath and contributes via the electron-phonon coupling α_Z. It is straightforward to independently extract other relevant system parameters from transport measurements, so that $\lambda^\star$ and α_Z are the only fit parameters left.

A. System-lead-bath model

1. *Double quantum dot Hamiltonian*

We include the single-particle energies ε_L and ε_R in the left / right dot, the electron-electron interactions neglecting the small exchange terms, inter-dot tunneling, and the inhomogeneous Zeeman field to obtain in second quantization the DQD Hamiltonian

$$\begin{aligned} H_{\mathrm{DQD}} = & \sum_{\ell=L,R} \varepsilon_\ell n_\ell + U \sum_{\ell=L,R} n_\ell(n_\ell - 1) + U' n_L n_R \\ & + \frac{\Delta}{2\sqrt{2}} \sum_{m=\uparrow,\downarrow} (c^\dagger_{Lm} c_{Rm} + c^\dagger_{Rm} c_{Lm}) \\ & + \frac{g\mu_{\mathrm{B}}}{2} \sum_{\ell=L,R} (c^\dagger_{\ell,\uparrow}, c^\dagger_{\ell,\downarrow})(\vec{B}_\ell \cdot \vec{\sigma})(c_{\ell,\uparrow}, c_{\ell,\downarrow})^T, \end{aligned} \tag{1}$$

where $n_\ell = \sum_{m=\uparrow\downarrow} c^\dagger_{\ell m} c_{\ell m}$ is the occupation of dot $\ell = L, R$ expressed with the usual fermionic creation and annihilation operators. The largest energy scales are the intra- and inter-dot Coulomb interactions U and U',

which define the diabatic basis states of our charge qubit with energies $\varepsilon(\mathrm{S}_{20}) = 2\varepsilon_L + U$ and $\varepsilon(\mathrm{S}_{11}) = \varepsilon_L + \varepsilon_R + U'$ and their mutual detuning $\bar{\varepsilon} \equiv \varepsilon(\mathrm{S}_{20}) - \varepsilon(\mathrm{S}_{11}) = \varepsilon_L - \varepsilon_R + U - U'$. The fourth term describes tunneling between the dots with the matrix element Δ defined such that it equals the energy splitting of the charge qubit formed by the singlets. The final Zeeman term affects the triplet states and, because of the inhomogeneous field contribution of our on-chip magnet, also mixes singlets with triplets. This mixing enables transitions between singlet and triplet states and may be rather sensitive to thermal exitations [22]. If a source-drain voltage is applied across the DQD, it causes a finite average current. Notice that also the hyperfine interaction causes electron spin-flips, which we capture by a phenomenological spin-flip rate γ_σ.

2. Dot-lead Hamiltonians

To model the single electron tunneling current through the DQD we have to consider its interaction with the two-dimensional leads. Starting from the configuration (1,0), the right quantum dot is loaded via the tunneling process $(0,1) \rightarrow (1,1)$ from the source contact, i. e. the right lead. The latter is modeled as non-interacting electrons with the Hamiltonian $H_{\mathrm{lead}} = \sum_{q,m=\uparrow\downarrow} E_q c^\dagger_{q,m} c_{q,m}$ while the dot-lead coupling terms reads

$$H_{\mathrm{dot-lead}} = \sum_{q,m=\uparrow\downarrow} V_q (c^\dagger_{R,m} c_{q,m} + c^\dagger_{q,m} c_{R,m}). \qquad (2)$$

Here, the lead-to-dot tunnel probability into a specific electronic dot state with energy E_q is proportional to the equilibrium population $\langle c^\dagger_{q,m} c_{q,m} \rangle = f(E_q - \mu_R)$ with the source contact characterized by the Fermi function $f(E-\mu_R) = [e^{(E-\mu_R)/k_\mathrm{B}T} + 1]^{-1}$ at temperature T and chemical potential μ_R. For simplicity, we assume within a wide-band approximation that the spectral density of the source contact is energy independent and find the tunnel coupling $\Gamma_R(E) = 2\pi \sum_q |V_q|^2 \delta(E - E_q) \equiv \Gamma_R$ between the right dot ond the source contact. The tunnel coupling between the left dot and the drain contact (left lead) is defined accordingly. Since the coupling term V_q is sample dependent and not a priory known (it can be tuned by gate voltages), we have determined the effective dot-lead tunnel couplings, Γ_L and Γ_R, experimentally by independent dc-measurements without applying an rf-field. Note that the decay rate used in the main article is $\Gamma_{\mathrm{out}} = \Gamma_L$, while the initialization rate Γ_{in} combines Γ_R with the singlet-triplet couplings in the last term of the Hamiltonian in Eq. (1).

3. System-bath Hamiltonian

A central aim of our study is to investigate our two-electron charge qubit and its decoherence, caused by the coupling to a dissipating environment, which is encoded in the LZSM pattern and its visibility. The details in the experimentally observed fading of the LZSM pattern with increasing temperature reveal two main environmental influences captured by $\lambda^\star$ and α_Z: the first one is an inhomogeneous broadening most likely caused by slow charge noise; the second influence is the phonon bath [23, 24] which yields quantum dissipation and direct decoherence. Another possible decoherence source is the coupling to circuit noise which is important for typically impedance matched superconducting qubits [25]. In our case, however, we expect this external noise source to be of minor relevance owing to a strong impedance mismatch.

For the inhomogeneous broadening, we assume that it stems from practically temperature independent slow fluctuations of the local potential that remain constant during the typical dwell time of an electron in the DQD. Therefore we can capture these fluctuations by convoluting their amplitude distribution with $I(\bar{\varepsilon}, A)$.

For describing decoherence that stems from the interaction between the DQD and bulk phonons, we employ a system-bath approach in the spirit of the Caldeira-Leggett model for the dissipative two-level system. This means that we couple the DQD to an ensemble of harmonic oscillators described by the Hamiltonian $H_{\mathrm{bath}} = \sum_\nu \hbar\omega_\nu a^\dagger_\nu a_\nu$, where $a^\dagger_\nu$ and a_ν are the usual bosonic creation and annihilation operators for a phonon of frequency ω_ν. The position operators of the bath oscillators couple to the occupation difference between the left and the right dot, $Z = n_L - n_R$, according to

$$H_{\mathrm{dot-bath}} = \sum_\nu \lambda_\nu (a^\dagger_\nu + a_\nu) Z\,. \qquad (3)$$

This electron-phonon coupling Hamiltonian describes the interaction of the DQD with environmental degrees of freedom. Its immediate effect is that fluctuations in the environment detune the electronic states which, in turn, results in a randomization of the relative phase in a superposition of states with distinct charge distribution, in particular of the singlets representing our qubit. The latter is therefore subject to decoherence. An important characteristic of a dissipating bath is its spectral density $J(\omega) = \pi \sum_\nu |\lambda_\nu|^2 \delta(\omega - \omega_\nu)$. As for the leads, we assume also for the phonon bath a continuum limit and replace $J(\omega)$ by the Ohmic spectral density $J(\omega) = \pi\alpha_Z\omega/2$. The dimensionless electron-phonon coupling strength α_Z reflects the dissipation strength, which together with the temperature parametrizes the decoherence due to the phonon bath. The Ohmic spectral density represents the natural choice which we have tested by performing additional numerical calculations using super-Ohmic spectral densities $J(\omega) \propto \omega^{s+1}$ with $s > 0$, which however failed to reproduce the experimentally observed fading of the LZSM pattern with increasing temperature. A possible explanation for the good agreement of our data with an Ohmic spectral phonon density is the quasi one-dimensional character of the electron-phonon interaction

in our DQD sample: decoherence is mainly caused by the one-dimensional subset of phonons with wavevector parallel to the line connecting the two quantum dots. For one-dimensional problems, the Ohmic spectral density of the electron-phonon coupling is microscopically justified [26].

While α_Z couples to the diagonal of the Hamiltonian in Eq. (1), one may in addition consider the off-diagonal coupling term, namely the coupling between phonons and the interdot tunnel barrier. For this purpose, one introduces a further dot–bath Hamiltonian like that in in Eq. (3) but with Z replaced by $X = \sum_{m=\uparrow,\downarrow}(c^\dagger_{Lm}c_{Rm} + c^\dagger_{Rm}c_{Lm})$ and the coupling strength denoted by α_X. Unlike the bath-coupling via Z, the bath now entails a fluctuating tunnel matrix element. Therefore, α_X, much more than α_Z, drives transitions between the quantum dots by phonon emission or absorption. Analyzing this effect, we found a significant asymmetry of the current as function of the detuning, which is in contrast to our experimental results. The quantitative comparison with our measurements revealed that α_X is roughly two orders of magnitude smaller than α_Z. In summary, α_X is of minor relevance for the qubit decoherence and need not be taken into account.

B. Charge qubit formed by two-electron singlet states

The simplest implementation of a DQD charge qubit is a single electron that tunnels between two dots. Nevertheless, here we consider the more complex case of two electrons charging a DQD. For the sake of applications, the two-electron state has the important advantage that it allows one to utilize both, charge and spin degrees of freedoms in a single DQD. This opens up a number of interesting possibilities, such as using either the singlet-singlet or one of the singlet-triplet transitions to define a qubit or even to combine both by subsequently sweeping through adjacent avoided crossings. Furthermore, the two-electron configuration constitutes the simplest possible many-body problem which yields a theoretically more interesting system compared to a single electron. Here, we focus on the two singlet states

$$|\mathrm{S}_{20}\rangle = c^\dagger_{L\uparrow}c^\dagger_{L\downarrow}|0\rangle, \tag{4}$$

$$|\mathrm{S}_{11}\rangle = \frac{1}{\sqrt{2}}(c^\dagger_{L\uparrow}c^\dagger_{R\downarrow} + c^\dagger_{L\downarrow}c^\dagger_{R\uparrow})|0\rangle, \tag{5}$$

which span the Hilbert space of our qubit, where $|0\rangle$ is the uncharged state of the DQD. In this singlet subspace, the double dot Hamiltonian defined in Eq. (1) reads

$$H_{\mathrm{qubit}} = \frac{\Delta}{2}\sigma_x + \frac{\varepsilon}{2}\sigma_z - \frac{\varepsilon}{2}\mathbb{1}, \tag{6}$$

[which is equivalent to Eq. (1)] with the unity matrix $\mathbb{1}$. The electron-phonon coupling operator defined in Eq. (3) then contains $Z = \sigma_z$. This leads us to the well-known spin-boson model with energy splitting $E = \sqrt{\Delta^2 + \varepsilon^2}$ and dissipation strength $\alpha = \alpha_Z$ defined in the usual way [27].

1. Qubit decoherence

The qubit reaches thermal equilibrium within the energy relaxation time T_1 while in the limit of weak dissipation, $\alpha_z k_\mathrm{B}T \ll E$, its pseudo-spin performs coherent oscillations which decay exponentially within the coherence time T_2 (assuming that the electron-phonon coupling is the main decoherence mechanism). From a corresponding Bloch-Redfield master equation (see below), both decay times can be determined [25, 28]:

$$T_1^{-1} = \frac{\pi\alpha_Z}{\hbar}\frac{\Delta^2}{E}\coth\Big(\frac{E}{2k_\mathrm{B}T}\Big), \tag{7}$$

$$T_2^{-1} = \frac{1}{2}T_1^{-1} + \frac{\pi\alpha_Z}{\hbar}\frac{2k_\mathrm{B}T\varepsilon^2}{E^2}. \tag{8}$$

In the high-temperature limit, $k_\mathrm{B}T \gg E$, the decoherence rate is proportional to the temperature: $T_2^{-1} = \pi\alpha_Z[1 + \varepsilon^2/E^2]k_\mathrm{B}T/\hbar$. In the low-temperature limit, $k_\mathrm{B}T \ll E$, quantum fluctuations take over and the coherence time becomes temperature independent, $T_2 = 2T_1 = (2\hbar/\pi\alpha_Z)(E/\Delta^2)$. For temperatures $T \gtrsim \hbar\Delta/k_B$, decoherence is weakest near $\varepsilon = 0$, while for $|\varepsilon| \gg \Delta$, the dephasing time decays proportional to $1/\varepsilon$. Thus, at these relatively high temperatures $\varepsilon = 0$ defines a sweet point for quantum operations provided that the environment predominantly couples via the occupation operator $Z = \sigma_z$, i. e., for $\alpha_X \ll \alpha_Z$ as assumed in Eqs. (7) and (8). In the opposite limit $\alpha_X \gg \alpha_Z$ a likewise spin-boson model would result in Eqs. (7) and (8), but with the parameters Δ and ε interchanged and α_Z replaced by α_X.

Equation (8) overestimates the coherence time of our specific charge qubit based on two-electron states in a DQD as it uses a two-level approximation which neglects spin flips and the triplet states. In order to determine the qubit dephasing beyond the two-level approximation, we follow the lines of Ref. [29] and employ the Bloch-Redfield formalism (see Sec. III C). In contrast to our transport calculations, we here disregard the dot-lead couplings and consider a qubit in a closed DQD configuration. We aim at obtaining the Liouville operator for the DQD coupled to the phonon bath and further including spin flips. Decoherence is manifest in the transient decay of off-diagonal density matrix elements. The coherence time, T_2, is straightforwardly found by computing the eigenvalues of the Liouville operator. To compute T_2 we, hence, evaluate the equation of motion of the total density operator beyond the rotating-wave approximation [see below and Eq. (10)], albeit using a time-independent Hamiltonian. One finds a pair of eigenvalues with imaginary parts close to $\pm E$ which correspond to coherent qubit oscillations. Their real parts are equal and can be identified as T_2^{-1}.

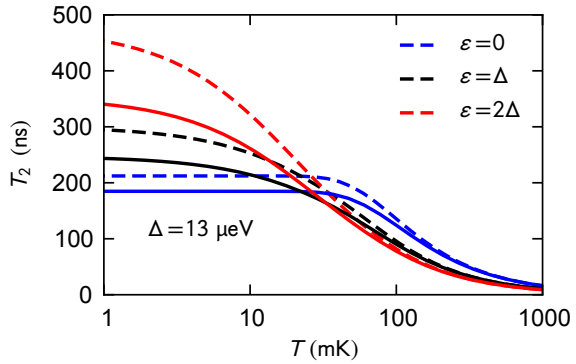

FIG. S11: Temperature dependence of the qubit coherence. Decoherence time T_2 for our S_{20}-S_{11} qubit for various values of the detuning ε. The dashed lines visualize Eq. (8) considering the electron-phonon coupling in a two-level model, while the solid lines are computed numerically for the full DQD Hamiltonian which, in addition, takes the triplet states and e. g. spin-flips into account.

In Fig. S11 we compare the coherence time T_2 as a function of temperature calculated analytically with Eq. (8) (weakly dissipative spin-boson model, two-level approximation), on the one hand, and the numerical result of the complete problem, on the other hand. This reveals that the two-level approximation overestimates T_2 by about 15% since it cannot capture incoherent singlet-triplet transitions induced by spin-flips and dephasing. For the temperature range of the experiment, $T \gtrsim 20\,\mathrm{mK}$, the sweet point at $\varepsilon = 0$ is most favorable and predicts T_2-times up to 200 ns which, however, become significantly smaller with increasing temperature and bias. In the sub milli-Kelvin regime, we observe the opposite. There the strongly biased situation corresponds to pure phase noise for which the spin-boson model predicts $T_2 \propto 1/k_B T$. This leaves some room for speculating about a coherence gain by further cooling. With such extrapolation, however, we leave the range in which our experiments justify the ohmic bath model.

2. *Advantage of a steady state experiment*

Previous measurements of the dephasing time [30, 31] relied on an explicit time-trace of Ramsey fringes, where for each instance of time a probability was reconstructed from a large number of destructive measurements of a transient. Such an averaging technique requires repeated identical preparation. Owing to the inhomogeneous broadening caused by slow noise, the time-trace of the averaged probability oscillations obtained typically decays on a much smaller time scale T_2^*, hence T_2 is not directly accessible. Our data, by contrast, are measured in the stationary state of a much simpler experiment. In the resulting LZSM pattern, inhomegeneous broadening and decoherence are manifest in separate ways. Crucially, as a consequence, $T_2^\star$ and T_2 can be distinguished in the analysis described in Sec. II and the main article.

C. Bloch-Redfield-Floquet theory

We aim at computing the time-averaged steady-state current through our strongly driven DQD including an appreciable number of levels coupled to the various environments, namely (i) the leads, (ii) slow charge noise, and (iii) the heat bath. Moreover, dealing with two-electron states we have to include spin flips which allow transitions between the triplet and singlet sub-spaces and resolve spin blockade. Our experimental results are consistent with the assumption that all these incoherent processes occur on time scales much larger than those of the coherent DQD dynamics, as is indicated by the following experimental observations: (i) the coupling to the leads and the spin relaxation rate ultimately determine the maximal current that we may observe. The latter is significantly smaller than the inter-dot tunnel frequency multiplied by the elementary charge, i. e., $\Gamma_{L/R} \ll \Delta$. (ii) Charge noise is rather slow as compared to all these tunneling processes. Therefore we can treat it as disorder that is constant during the dwell time of an electron in the DQD. In other words, it leads to an inhomogeneous broadening that does not affect the decoherence dynamics of the electrons. (iii) The appearance of an interference pattern indicates that the inter-dot tunneling must be predominantly coherent which excludes strong coupling to a heat bath. This is confirmed by our finding that the dimensionless dissipation strength is several orders of magnitude below the crossover to the so-called incoherent tunneling regime [28]. We can not a-priory exclude stronger coupling to a small number of individual (tunneling) defects, but the fact that we did not find any memory effects makes such a strong coupling scenario unlikely.

1. *Floquet ansatz*

To cope with the complex problem outlined above we use a reduced density matrix approach with the Floquet states of the driven system in the absence of the environments as basis states. These basis states already incorporate the rf-modulation and, therefore, allow us to apply a rotating-wave approximation, conveniently resulting in a time independent Liouville equation. This perturbative approach is reliable under the assumption of only weakly coupled environments. It has been applied in the past to both rf-driven dissipative quantum systems [32] and rf-driven quantum transport [33].

Floquet theory exploits the fact that a periodically time-dependent Schrödinger equation of the type $i\hbar\partial_t|\psi\rangle = H_{\mathrm{DQD}}(t)|\psi\rangle$ possesses a complete set of solutions of the form $|\psi(t)\rangle = e^{-i\omega t}|\phi(t)\rangle$, where $\hbar\omega$ is called

quasienergy. The Floquet state $|\phi(t)\rangle = |\phi(t+2\pi/\Omega)\rangle \equiv \sum_k e^{-ik\Omega t}|\phi_k\rangle$ is characterized by shareing the time-periodicity of the Hamiltonian. Therefore, it can be represented as Fourier series which, importantly, allows an efficient numerical treatment. In analogy to quasimomenta in Bloch theory employed for spatially periodic potentials, in Floquet theory the quasienergies can be divided into Brillouin zones of equivalent states. Thus, it is sufficient to solve the eigenvalue problem within one Brillouin zone, e. g. for $-\Omega/2 \leq \omega < \Omega/2$. By inserting the Floquet ansatz into the Schrödinger equation, we obtain the eigenvalue equation

$$\Big(H_{\rm DQD}(t) - i\hbar\frac{\partial}{\partial t}\Big)|\phi(t)\rangle = \hbar\omega|\phi(t)\rangle \tag{9}$$

from which we compute a complete set of Floquet states, $\{|\phi_n\rangle\}$, and the corresponding quasienergies $\hbar\omega_n$.

2. Bloch-Redfield theory

An established technique for studying a quantum system in weak contact with an environment is Bloch-Redfield theory. It is based on a treatment of the system-environment coupling operator V within second-order perturbation theory by which one finds for the total density operator the equation of motion [34]

$$\dot{R} = -\frac{i}{\hbar}[H_{\rm DQD}(t)+H_{\rm env}, R] - \frac{1}{\hbar^2}\int_0^\infty d\tau [V,[V(t-\tau,t),R]]\,. \tag{10}$$

The particular form of the coupling operator in the interaction picture, $V(t-\tau,t) = U^\dagger_{\rm DQD}(t-\tau,t)VU_{\rm DQD}(t-\tau,t)$, stems from the explicit time-dependence of the central quantum system. By tracing out the environmental degrees of freedom, one obtains an equation of motion for the reduced density operator of the system, ρ. This step requires one to specify the state of the environment. Here, we assume that it is in the grand canonical state $\rho^{\rm (eq)}_{\rm env}$ and that it is uncorrelated with the system, such that the total density operator factorizes into a system and an environment part, $R \simeq \rho\otimes\rho^{\rm (eq)}_{\rm env}$. Under this condition the decomposition into the Floquet basis provides a master equation of the form $\dot\rho = -i(\omega_n-\omega_m)\rho_{mn} + \sum_{n'm'} L_{nm,n'm'}\rho_{n'm'}$, where the Bloch-Redfield tensor $L_{nm,n'm'}$ follows in a straightforward way from Eq. (10). In the last step we assume that all matrix elements ρ_{nm} evolve much slower than the rf-field, which allows us to replace the Bloch-Redfield tensor by its time average. In this way we obtain a time-independent master equation describing the time evolution of the population of the (time dependent) Floquet states.

We are exclusively interested in the steady state of this master equation, which for weak dissipation eventually becomes diagonal in the Floquet basis. Exploiting this knowledge, we set the off-diagonal matrix elements to zero and arrive at a master equation of the form

$$\dot\rho_{nn} = \sum_{n'}\Big(W_{n\leftarrow n'}\rho_{n'n'} - W_{n'\leftarrow n}\rho_{nn}\Big)\,, \tag{11}$$

where ρ_{nn} are the populations of the Floquet states. In the following we present the results for the transition rates $W_{n\leftarrow n'}$ which have been evaluated as sketched above.

3. Coupling between the double quantum dot and the leads

To calculate the tunnel coupling between the right lead and the right quantum dot, we evaluate the coefficients of the master Eq. (11) by replacing V in Eq. (10) with the tunnel coupling between the right dot and the right lead given by Eq. (2). After some algebra, we arrive at the transitions rates

$$\begin{aligned} W^{\rm leads}_{n\leftarrow n'} = &\frac{\Gamma_R}{\hbar}\sum_k\Big|\sum_{k'}\langle\phi_{n,k'+k}|c^\dagger_R|\phi_{n',k'}\rangle\Big|^2 \\ &\times f(\omega_n-\omega_{n'}+k\Omega-\mu_R) \\ &+\frac{\Gamma_R}{\hbar}\sum_k\Big|\sum_{k'}\langle\phi_{n,k'+k}|c_R|\phi_{n',k'}\rangle\Big|^2 \\ &\times (1-f(\omega_n-\omega_{n'}+k\Omega-\mu_R)), \end{aligned} \tag{12}$$

where the first term describes tunneling from the right lead to the right dot, while the second term refers to the opposite process. The corresponding Liouvillian for coupling to the left lead is obtained in the same way with the accordingly modified dot-lead Hamiltonian. Owing to charge conservation, the time-averaged currents are the same at all interfaces. Here we evaluate it at the right dot-lead barrier and obtain it as the difference between the terms that describe in Eq. (12) tunneling from the lead to the dot and those describing the opposite process:

$$\begin{aligned} J_{n\leftarrow n'} = &-\frac{\Gamma_R}{\hbar}\sum_k\Big|\sum_{k'}\langle\phi_{n,k'+k}|c^\dagger_R|\phi_{n',k'}\rangle\Big|^2 \\ &\times f(\omega_n-\omega_{n'}+k\Omega-\mu_R) \\ &+\frac{\Gamma_R}{\hbar}\sum_k\Big|\sum_{k'}\langle\phi_{n,k'+k}|c_R|\phi_{n',k'}\rangle\Big|^2 \\ &\times (1-f(\omega_n-\omega_{n'}+k\Omega-\mu_R)), \end{aligned} \tag{13}$$

where $J_{n\leftarrow n} = 0$ due to vanishing matrix elements. Note that this expression can also be derived in a more formal way by introducing a counting variable for the lead electrons before tracing them out and, thus, it does not rely on any specific interpretation of the tunneling terms.

4. Coupling between the qubit states and the heat bath

A Liouvillian that describes the influence of the dissipating environment on the DQD is derived by the same

procedure, but using for V the electron-phonon Hamiltonian Eq. (2). We obtain

$$W^{\rm decoherence}_{n\leftarrow n'} = 2\sum_k \Big|\sum_{k'}\langle\phi_{n,k'+k}|Z|\phi_{n',k'}\rangle\Big|^2 \times N(\omega_n-\omega'_n+k\Omega), \tag{14}$$

where $N(\omega) = J(\omega)n_{\rm th}(\omega)$ with the bosonic thermal occupation number $n_{\rm th}(\omega) = [e^{\hbar\omega/k_{\rm B}T}-1]^{-1}$. In order to arrive at this convenient form, we have defined $J(-\omega) = -J(\omega)$, while the Bose function was extended by analytic continuation.

As already mentioned, a coherent tunnel process between the charge configurations (1,1) and (2,0) requires that the spin configuration of both states is equal, and in our case this includes only the singlet states S_{11} and S_{20}. The reason is, that the triplet T_{20} is too high in energy owing to the large intradot exchange interaction. In turn, a direct transition of the triplet states with (1,1) charge configuration to S_{20} is inhibited. As a consequence the transport process comes to a standstill until a transition to the S_{11} singlet occurs. In our setup, this spin blockade is resolved by two mechanisms. First, the Zeeman field of the nanomagnet close to the DQD possesses an inhomogeneity by which singlets and triplets mix. They form narrow avoided crossings at which spin blockade is resolved and a current peak emerges. This effect is fully coherent and contained in our DQD Hamiltonian, Eq. (1). Second, spin flips are induced by the hyperfine interaction with nuclear spins in the GaAs matrix, which we treat as incoherent relaxation. Therefore, thermal motion of the nuclear spins coupled via the hyperfine interaction represents a further dissipative environment. Our LZSM measurements do not provide clear experimental hints on memory effects (besides for very small modulation amplitudes A, where we find indications for dynamic nuclear spin polarization, see Sec. II H) or a significant temperature dependence of the spin flip rate within the probed temperature range. This allows us to avoid the theoretical difficulties of choosing a particular microscopic model and to capture spin flips by a Lindblad form with a rate γ_σ. Therefore, we add to the master equation the Liouvillean $L[\rho] = \frac{1}{2}\gamma_\sigma\sum_{\ell,m=\uparrow\downarrow}(2S_{\ell,m}\rho S^\dagger_{\ell,m} - S^\dagger_{\ell,m}S_{\ell,m}\rho - \rho S^\dagger_{\ell,m}S_{\ell,m})$ with the spin flip operator $S_{\ell,m} = c^\dagger_{\ell,\bar m}c_{\ell,m}$ for an electron on dot ℓ, where $m=\uparrow,\downarrow$ and $\bar m\neq m$. Decomposition into Floquet states followed by rotating-wave approximation yields the rate

$$W^{\rm spinflip}_{n\leftarrow n'} = \gamma_\sigma\sum_{m=\uparrow\downarrow}\sum_k\Big|\sum_{k'}\langle\phi_{n,k'+k}|S_{L,m}|\phi_{n',k'}\rangle\Big|^2. \tag{15}$$

In our numerical approach to the steady-state average current, we first compute the Floquet states which allows us to evaluate the transition probabilities:

$$W_{n\leftarrow n'} = W^{\rm leads}_{n\leftarrow n'} + W^{\rm decoherence}_{n\leftarrow n'} + W^{\rm spinflip}_{n\leftarrow n'}, \tag{16}$$

so that we obtain a specific expression for the master equation Eq. (11). The steady-state solution of this master equation, $\rho^{(\infty)}_{nn}$, follows straigtforwardly from the condition $\dot\rho^{(\infty)}_{nn} = 0 = \sum_{n'}(W_{n\leftarrow n'}\rho^{(\infty)}_{n'n'} - W_{n'\leftarrow n}\rho^{(\infty)}_{nn})$ together with the trace condition $\sum_n\rho^{(\infty)}_{nn} = 1$. Finally we arrive at the dc current $I = \sum_{nn'}J_{n\leftarrow n'}\rho^{(\infty)}_{n'n'}$.

IV. SYSTEM PARAMETERS

Table I summarizes the most important parameters which characterize our DQD, the two-electron qubit and its coupling to the environment that we used in our numerical calculations. For applying the scattering formula Eq. (2), we identified the initialization rate $\Gamma_{\rm in}$ for the process $(1,0)\to S_{11}$ with the spin relaxation rate γ_σ, while the decay $(2,0)\to(1,0)$ occurs at the dot-drain rate so that $\Gamma_{\rm out} = \Gamma_L$.

[1] M. Field, C. G. Smith, M. Pepper, D. A. Ritchie, J. E. F. Frost, G. A. C. Jones, and D. G. Hasko, Phys. Rev. Lett. **70**, 1311 (1993).

[2] M. Ciorga, A. S. Sachrajda, P. Hawrylak, C. Gould, P. Zawadzki, S. Jullian, Y. Feng, and Z. Wasilewski, Phys. Rev. B **61**, R16315 (2000).

[3] K. Ono, D. G. Austing, Y. Tokura, and S. Tarucha, Science **297**, 1313 (2002).

[4] G. Petersen, E. A. Hoffmann, D. Schuh, W. Wegscheider, G. Giedke, and S. Ludwig, Phys. Rev. Lett. **110**, 177602 (2013).

[5] J. Stehlik, Y. Dovzhenko, J. R. Petta, J. R. Johansson, F. Nori, H. Lu, and A. C. Gossard, Phys. Rev. B **86**, 121303(R) (2012).

[6] D. M. Berns, M. S. Rudner, S. O. Valenzuela, K. K. Berggren, W. D. Oliver, L. S. Levitov, and T. P. Orlando, Nature (London) **455**, 51 (2008).

[7] Y. Wang, S. Cong, X. Wen, C. Pan, G. Sun, J. Chen, L. Kang, W. Xu, Y. Yu, and P. Wu, Phys. Rev. B **81**, 144505 (2010).

[8] A. M. Satanin, M. V. Denisenko, S. Ashhab, and F. Nori, Phys. Rev. B **85**, 184524 (2012).

[9] Kiselev, M. N., Kikoin, K., and Kenmoe, M. B., EPL **104**, 57004 (2013).

[10] D. Taubert, D. Schuh, W. Wegscheider, and S. Ludwig, Review of Scientific Instruments **82**, 123905 (2011).

[11] J. R. Petta, A. C. Johnson, J. M. Taylor, E. A. Laird, A. Yacoby, M. D. Lukin, C. M. Marcus, M. P. Hanson, and A. C. Gossard, Science **309**, 2180–2184 (2005).

[12] T. Fujisawa and Y. Hirayama, Appl. Phys. Lett. **77**, 543 (2000).

[13] M. Pioro-Ladrière, J. H. Davies, A. R. Long, A. S.

DQD parameter	value in μeV	determined by
bias voltage V	1000	externally applied voltage
intra dot Coulomb energy U	3500 ± 350	charging diagram
inter dot Coulomb interaction U'	820 ± 80	charging diagram
inter-dot tunnel coupling Δ	13 ± 1	spin funnel, see Fig. S3(c)
source-dot tunnel rate Γ_R	0.1	estimated from current, of minor relevance
dot-drain tunnel rate Γ_L	$2 \times 10^{-3\dagger}$	from current without spin blockade
spin relaxation γ_σ	10^{-3}	from current with spin blockade
$T_\pm - S_{11}$ splitting	$0.12^\ddagger$	Landau-Zener transition, see Fig. S3(a)
external parameters	value in μeV	determined by
photon energy $\hbar\Omega$	6.2/11.4/18.7	at modulation frequency of 1.5/2.75/4.5 GHz
mean Zeeman splitting $g\mu_B B$	4.2	$g\mu_B B_{\rm ext}$; $\lvert g\rvert = 0.36$ and $B_{\rm ext} = 200\,$mT
thermal energy $k_B T$	1.7 – 40	cryostat and electron temperature
environmental influences	value	determined by
inhomogeneous broadening $\lambda^\star$	$3.5 \pm 0.5\,\mu$eV	from broadening in $I(\bar{\varepsilon})$ peaks
Caldeira-Leggett parameter α_Z	$(1.5 \pm 0.5) \times 10^{-4}$	decay of lemon arcs, temperature dependence
Caldeira-Leggett parameter α_X	$< 5 \times 10^{-6}$	asymmetry of LZSM pattern

TABLE I: Parameters used for the numerical calculations. † The data of Fig. 2 of the main article and Fig. S9 were measured with a slightly smaller dot-drain rate and, accordingly, the numerical data were computed with $\Gamma_R = 1.2 \times 10^{-3}\,\mu$eV. ‡ Note that the S-T splittings are reduced compared to $g\mu_B \Delta B_{x,z}$ according to the weight of S_{20} in the singlet state. In our case we have $g\mu_B \Delta B_x \simeq 0.2\,\mu$eV which reduces to the $T_\pm$-S_{11} splitting of $0.12\,\mu$eV.

Sachrajda, L. Gaudreau, P. Zawadzki, J. Lapointe, J. Gupta, Z. Wasilewski, and S. Studenikin, Phys. Rev. B **72**, 115331 (2005).

[14] C. Buizert, F. H. L. Koppens, M. Pioro-Ladrière, H.-P. Tranitz, I. T. Vink, S. Tarucha, W. Wegscheider, and L. M. K. Vandersypen, Phys. Rev. Lett. **101**, 226603 (2008).

[15] O. E. Dial, M. D. Shulman, S. P. Harvey, H. Bluhm, V. Umansky, and A. Yacoby, Phys. Rev. Lett. **110**, 146804 (2013).

[16] M. S. Rudner, A. V. Shytov, L. S. Levitov, D. M. Berns, W. D. Oliver, S. O. Valenzuela, and T. P. Orlando, Phys. Rev. Lett. **101**, 190502 (2008).

[17] L. D. Landau, Phys. Z. Sowjetunion **2**, 46 (1932).

[18] C. Zener, Proc. R. Soc. London, Ser. A **137**, 696 (1932).

[19] E. C. G. Stueckelberg, Helv. Phys. Acta **5**, 369 (1932).

[20] E. Majorana, Nuovo Cimento **9**, 43 (1932).

[21] S. N. Shevchenko, S. Ashhab, and F. Nori, Phys. Rep. **492**, 1 (2010).

[22] H. Ribeiro, J. R. Petta, and G. Burkard, Phys. Rev. B **87**, 235318 (2013).

[23] G. J. Schinner, H. P. Tranitz, W. Wegscheider, J. P. Kotthaus, and S. Ludwig, Phys. Rev. Lett. **102**, 186801 (2009).

[24] G. Granger, D. Taubert, C. E. Young, L. Gaudreau, A. Kam, S. A. Studenikin, P. Zawadzki, D. Harbusch, D. Schuh, W.Wegscheider, Z. R.Wasilewski, A. A. Clerk, S. Ludwig, and A. S. Sachrajda, Nature Phys. **8**, 522 (2012).

[25] Y. Makhlin, G. Schön, and A. Shnirman, Rev. Mod. Phys. **73**, 357 (2001).

[26] U. Weiss, *Quantum Dissipative Systems*, 2nd ed. (World Scientific, Singapore, 1998).

[27] A. J. Leggett, S. Chakravarty, A. T. Dorsey, M. P. A. Fisher, A. Garg, and W. Zwerger, Rev. Mod. Phys. **59**, 1 (1987).

[28] P. Hänggi, P. Talkner, and M. Borkovec, Rev. Mod. Phys. **62**, 251 (1990).

[29] K. M. Fonseca-Romero, S. Kohler, and P. Hänggi, Chem. Phys. **296**, 307 (2004).

[30] K. C. Nowack, F. H. L. Koppens, Yu. V. Nazarov, and L. M. K. Vandersypen, Science **318**, 1430 (2007).

[31] H. Bluhm, S. Foletti, I. Neder, M. Rudner, D. Mahalu, V. Umansky, and A. Yacoby, Nature Phys. **7**, 109 (2011).

[32] S. Kohler, T. Dittrich, and P. Hänggi, Phys. Rev. E **55**, 300 (1997).

[33] S. Kohler, J. Lehmann, and P. Hänggi, Phys. Rep. **406**, 379 (2005).

[34] K. Blum, *Density Matrix Theory and Applications*, 2nd ed. (Springer, New York, 1996).

8 Landau-Zener-Stückelberg-Majorana interferometry with bichromatic driving

---

This chapter presents the results of

- Forster, F. *et al. Phys. Rev. B. 92.* 245422 (2015)

See section D for the contributions of each author.

8.1 Overview

In this chapter, we expand the experimental technique of LZSM interferometry developed in chapter 7 to two driving frequencies applied simultaneously, i.e. a bichromatic drive, and investigate experimentally and theoretically the electron transport through a double quantum dot under this condition. In this collaboration, S. Kohler from Instituto de Ciencia de Materiales de Madrid developed a generalized Floquet formalism to address the effects of bichromatic driving. In particular, we reveal the importance of the ratio of the two frequencies, which can be commensurable or incommensurable, for the symmetry properties of the interference pattern, and provide experimental evidence for the predicted effects.

8.2 Measurement setup

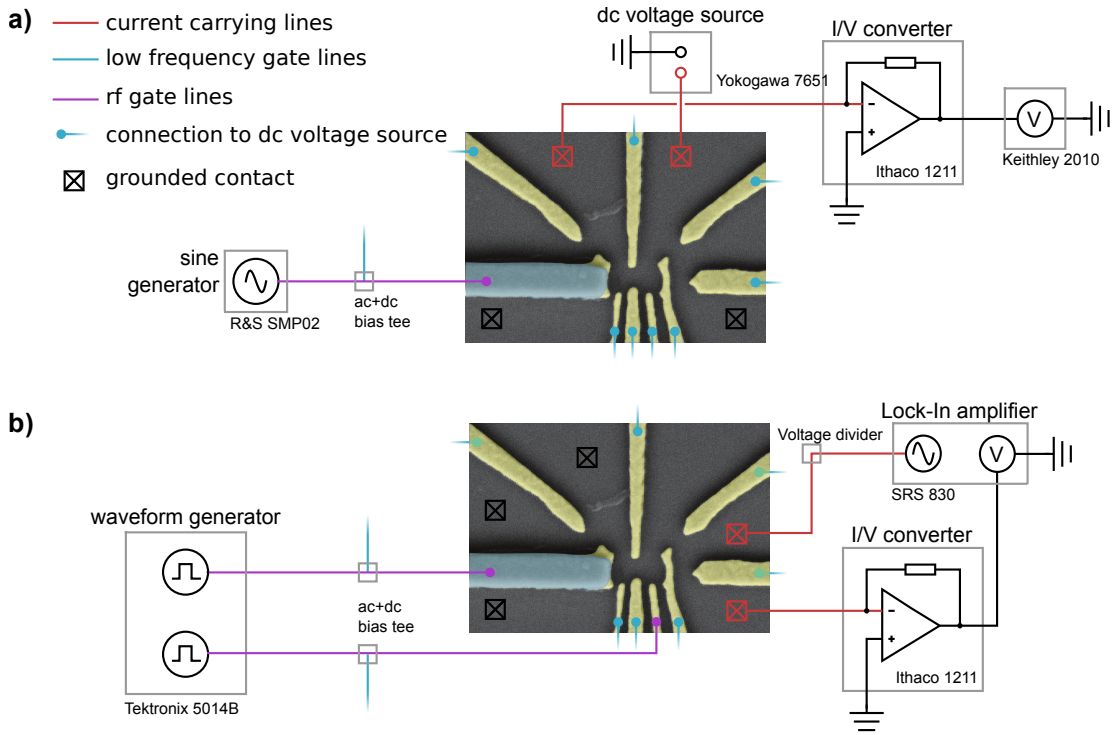

Figure 8.1: Electrical measurement setup for LZSM experiment using a bichromatic drive. The setup is extended compared to the one in 7.3 by combining the signal of a second sine generator (HP 83605B) synchronized in phase with the first one.

To apply a bichromatic drive, we extend the setup described in section 7.3 with a second sine generator and mix their outputs with a resistive combiner. To ensure the relative phase stability between the signal of both devices, we synchronize them by feeding the signal of the internal 10 MHz oscillator of one device to the other as depicted in figure 8.1. Since the output phase of the R&S SMP 02 can be tuned between 0 and 2π, we are able to achieve any relative phase value in the experiment. Even though the devices are synchronized and their outputs can be tuned to be in-phase, the phase at the sample is a priori unknown because of the unknown dispersion of the transmission lines. In section IV B of the paper, we present a method how to calibrate the value of the phase.

PHYSICAL REVIEW B **92**, 245422 (2015)

Landau-Zener interference at bichromatic driving

Florian Forster,[1] Max Mühlbacher,[1] Ralf Blattmann,[2] Dieter Schuh,[3] Werner Wegscheider,[4] Stefan Ludwig,[1,5] and Sigmund Kohler[6]

[1]*Center for NanoScience and Fakultät für Physik, LMU-Munich, 80539 München, Germany*
[2]*Department of Physics and Astronomy, Aarhus University, Ny Munkegade 120, 8000 Aarhus C, Denmark*
[3]*Fakultät für Physik, Universität Regensburg, 93040 Regensburg, Germany*
[4]*Solid State Physics Laboratory, ETH Zurich, 8093 Zurich, Switzerland*
[5]*Paul-Drude-Institut für Festkörperelektronik, Hausvogteiplatz 5–7, 10117 Berlin, Germany*
[6]*Instituto de Ciencia de Materiales de Madrid, CSIC, 28049 Madrid, Spain*

(Received 7 October 2015; revised manuscript received 1 December 2015; published 15 December 2015)

We investigate experimentally and theoretically the interference at avoided crossings which are repeatedly traversed as a consequence of an applied ac field. Our model system is a charge qubit in a serial double quantum dot connected to two leads. Our focus lies on effects caused by simultaneous driving with two different frequencies. We work out how the commensurability of the driving frequencies affects the symmetry of the interference patterns both in real space and in Fourier space. For commensurable frequencies, the symmetry depends sensitively on the relative phase between the two modes, whereas for incommensurable frequencies the symmetry of monochromatic driving is always recovered.

DOI: 10.1103/PhysRevB.92.245422 PACS number(s): 73.63.Kv, 03.67.−a, 03.65.Yz

I. INTRODUCTION

Landau-Zener-Stückelberg-Majorana (LZSM) interference protocols have been explored experimentally in various solid-state implementations ranging from Josephson junctions [1–8] to quantum dot based devices [9–12]. Besides demonstrating quantum coherence, LZSM interference allows one to explore dissipative effects in a predominantly coherent dynamics and determine system parameters such as the coherence time T_2 or the inhomogeneous decay time T_2^* [4,10,12]. Previous studies considered monochromatic driving, in one case with an additional sudden parameter switching at a low rate [8], which may be an insignificant restriction if one merely aims at studying the coherence and decoherence of solid-state qubits. Driving with two or more frequencies of the same order and different phases, however, allows the creation of doubly dressed states [13,14] and opens up a multitude of additional possibilities, which are worthwhile exploring, for instance, in the context of quantum simulations [15,16]. Since the phase between the components affects time-reversal symmetry, LZSM interference can mimic universal conductance fluctuations [17].

Building on two recent projects, one studying LZSM interference in a double quantum dot (DQD) charge qubit [12] and one applying bichromatic driving to a single dot realizing a Lissajous rocking ratchet [18], here, we combine bichromatic driving with LZSM interference in the DQD shown in Fig. 1(a) and explore the cases of commensurable versus incommensurable frequencies. Depending on the phase between its two components, bichromatic driving with commensurable frequencies may break time reversal symmetry, which is particularly visible in the Fourier transform of the LZSM interference pattern [19]. For the quasiperiodic driving with two incommensurable frequencies, by contrast, we find irrespective of the phase difference the symmetry properties of the monochromatic case.

The theoretical approaches exploring driven dissipative systems often rely on the time periodicity of the external field. Such methods applied in the context of LZSM interference include the mapping to a time-independent problem via a rotating-wave approximation [19–22], the computation of stationary phases [4,23], and the decomposition of a quantum master equation into the Floquet states of the central system [22,24]. For transport problems, LZSM patterns have been calculated ignoring interactions with Floquet scattering theory [25,26]. Taking into account two-particle interactions or a quantum heat bath, transport experiments can be described with a more realistic Floquet master equation approach [12]. While a Floquet ansatz can be generalized to bichromatic driving straightforwardly [27,28], the resulting scheme may be numerically demanding and only a few explicit results can be found in the literature [28]. Here, we develop a more efficient method including the case of driving with two incommensurable frequencies. It combines two known methods, namely a Floquet matrix representation [29] and the solution of a recurrence equation by matrix continued fractions [30].

This paper is arranged as follows. In Sec. II, we present our experimental setup. In Sec. III, we introduce our theoretical description and derive a Floquet method for the solution of master equations with two incommensurable drivings. Section IV is devoted to the analytical and numerical computation of LZSM interference patterns, their symmetries, and the comparison to the experimental results. Additional measured data can be found in Appendix A. Moreover, in Appendix B, we sketch the two Floquet methods for single-frequency driving that we combine to obtain our numerical scheme.

II. EXPERIMENT

In our experiments, we measured LZSM interference patterns at the avoided crossing of two charge states in the DQD presented in Fig. 1(a). The states are the singlets formed by (2,0) and (1,1), where (n_1,n_2) denotes the number of electrons in the left (n_1) and right (n_2) dot. The avoided crossing, sketched in Fig. 1(b) as a function of the detuning energy

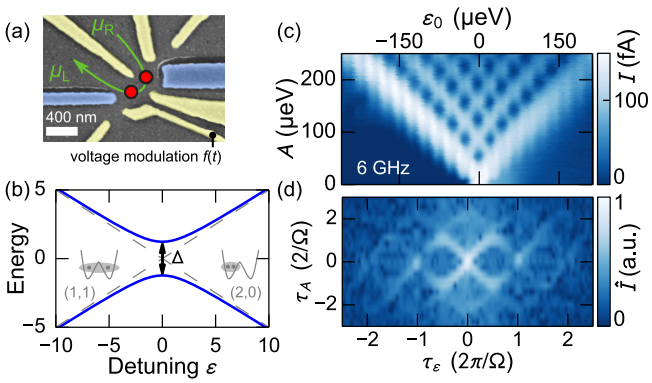

FIG. 1. (Color online) (a) Scanning electron micrograph of the wafer surface. The GaAs surface is dark gray, gold gates are shown in yellow and cobalt gates in blue. Red filled circles sketch the approximate quantum dot positions in the two-dimensional electron system 85 nm beneath the surface. The voltage on the lower right gate is radio frequency modulated with the function $f(t)$. (b) Avoided crossing of the eigenstates (solid lines) composed of the singlets (dashed lines) with charge configuration (1,1) and (2,0) (visualized in double well sketches), which mix via the interdot tunnel coupling Δ. (c) Measured LZSM pattern $I(\epsilon_0, A)$ for monochromatic driving with frequency 6 GHz. (d) Corresponding Fourier transformed LZSM pattern (plotted with a logarithmic color scale).

ϵ between the two singlets, is formed by the interdot tunnel coupling Δ. By modulating the voltage on one of the quantum dot defining gates, we modulate the detuning with a periodic function such that we repeatedly drive the system through the avoided crossing resulting in LZSM interference. The detuning thereby consists of a static component ϵ_0 and a time-dependent contribution with amplitude A,

$$\epsilon(t) = \epsilon_0 + A f(t). \tag{1}$$

Its shape is given by a bounded periodic or quasiperiodic function $f(t)$ with zero mean. To detect the electron charge state, we apply a constant voltage $V = (\mu_R - \mu_L)/e = 1$ mV across the DQD, where $\mu_{L,R}$ are the chemical potentials of the leads and measure the steady state current resulting from the combination of V and the rf modulation. We tuned our DQD such that the current is virtually exclusively caused by tunneling of single electrons via the configuration cycle $(1,0) \to (1,1) \leftrightarrow (2,0) \to (1,0)$. The current I is then proportional to the occupation of (2,0) and the current maxima and minima in Fig. 1(c) are a signature of the interference of the (2,0) and (1,1) singlet states as we periodically drive our DQD through their avoided crossing. Note that the transition $(1,1) \to (2,0)$ is initially slowed down by Pauli-spin blockade [31], i.e., as long as a (1,1) triplet is occupied no current flows. Primarily due to the inhomogeneous field of on-chip nanomagnets [marked blue in Fig. 1(a)] [32] the triplet eventually decays into the (1,1) singlet and sets off the interference dynamics observed here. The interference pattern as a function of ϵ_0 and A in Fig. 1(c) is a typical example for monochromatic driving of the form $f(t) = \sin(\Omega t)$, which is well understood and has been observed in various physical systems [1–10,12]. The interference pattern and even more its two-dimensional Fourier transform presented in Fig. 1(d) [4,5,12] exhibit a high degree of symmetry.

This paper is devoted to bichromatic driving of the form

$$f(t) = \sin(\Omega t) + \eta \sin(\Omega' t + \phi), \tag{2}$$

i.e., we augment monochromatic driving by a further contribution with relative strength η, frequency Ω', and a phase shift ϕ. Our main focus lies in two very different cases, namely commensurate versus incommensurate frequencies Ω and Ω'. The first corresponds to a rational Ω'/Ω and, thus, periodic driving, while the latter corresponds to an irrational Ω'/Ω and quasiperiodic driving. We will find that the two cases have quite different symmetry properties. Experimentally, one of the main challenges beyond monochromatic driving is to control the relative phases of different frequency components, a consequence of the dispersion of the transmission lines at radio frequencies. We will, however, present a straightforward method to calibrate relative phase differences by means of symmetry considerations. Before we present our experimental results, let us sharpen our expectations by introducing a general theory for bichromatic driving.

III. THEORETICAL DESCRIPTION

In our experiment, the electron transport from source to drain occurs via the DQD configuration cycle $(1,1) \to (2,0) \leftrightarrow (1,0) \to (1,1)$. Owing to the possible spin configurations, it consists of seven states. This makes the Floquet decomposition of the density operator a demanding task for bichromatic driving, where coherences described by off-diagonal density matrix elements play a decisive role. However, the coherent interdot tunneling relevant for the LZSM interference studied here is restricted to the singlet subspace [12] in which the left dot is always occupied and a single electron charge tunnels between the two dots. For our purposes, a simplifying description based on a single spinless electron tunneling between the two dots is sufficient. It is described by the Hamiltonian

$$H = \frac{\epsilon_0 + A f(t)}{2}(c_1^\dagger c_1 - c_2^\dagger c_2) + \frac{\Delta}{2}(c_1^\dagger c_2 + c_2^\dagger c_1) + U n_1 n_2 \tag{3}$$

with the electron creation operators $c_{1,2}^\dagger$. The last term contains the dot occupation numbers $n_i = c_i^\dagger c_i$ and expresses Coulomb blockade, where we assume that the Coulomb repulsion U is so strong that charge states different from those mentioned above are inaccessible.

A. Master equation

The DQD is coupled to a source and a drain, which we describe as a canonical ensemble of free electrons with chemical potentials that depend on the applied voltage. A tunnel coupling between the leads and the respective dot completes the model. With a standard second-order approach for the coupling, we eliminate the leads and obtain a Bloch-Redfield master equation for the reduced DQD density operator ρ [33,34]. Its incoherent terms typically depend on the details of the system and the leads such as the temperature, the chemical potentials $\mu_{L,R}$ of the left and right leads, the overlap between

the DQD eigenstates and the localized states, as well as the DQD eigenenergies [35].

If all DQD chemical potentials (which here are the energies of the single-particle states) are larger than μ_L and smaller than μ_R, the incoherent tunnel terms assume the convenient Lindblad form such that the master equation becomes [36]

$$\dot{\rho} = L\rho \equiv -\frac{i}{\hbar}[H(t),\rho] + \Gamma_L D(c_1)\rho + \Gamma_R D(c_2^\dagger)\rho, \quad (4)$$

with the Lindblad superoperator

$$D(x)\rho = \tfrac{1}{2}(2x\rho x^\dagger - x^\dagger x\rho - \rho x^\dagger x) \quad (5)$$

and the dot-lead rates $\Gamma_{L,R}$. The first term in Eq. (5) describes incoherent transitions induced by the operators c_1 and $c_2^\dagger$, i.e., tunneling between the DQD and the leads. This implies that the current superoperators are given by $J_L\rho = \Gamma_L c_1 \rho c_1^\dagger$ and $J_R\rho = \Gamma_R c_2^\dagger \rho c_2$, respectively. Owing to charge conservation, both yield the same time-averaged expectation value.

In quantum dots such as ours, the electrons are subjected to environmental fluctuations which affect the coherence of the DQD electrons. The environment can be described as a bath of harmonic oscillators that couple to an appropriate DQD degree of freedom. Formally, this coupling can be treated with Bloch-Redfield theory as the dot-lead coupling above. Then we obtain a further Liouvillian with temperature dependent coefficients, which allows one to determine the effective DQD-environment coupling strength by analyzing the fading of LZSM patterns with increasing temperature [12]. However, since such computation of the dissipative kernel is rather time consuming and beyond the present scope, we take a simpler route: within a standard approximation scheme [37], one can bring dissipation kernels to the Lindblad form

$$L_{\text{diss}} = \frac{\gamma}{2} D(x), \quad (6)$$

where x is the operator that induces dissipative transitions. In our system the relevant noise stems from charge fluctuations that couple to the DQD dipole moment. Therefore the coupling operator is proportional to the population imbalance $x = (n_1 - n_2)/2$ [38], while the effective rate γ collects all prefactors. For relatively low temperatures, γ depends on the detuning and the tunnel coupling and can be estimated as $\gamma = \pi\alpha\Delta^2/(\epsilon_0^2 + \Delta^2)^{1/2}$ [39]. The dimensionless dissipation strength in a similar system has been determined as $\alpha = 1.5 \times 10^{-4}$ [12]. We replace the decoherence rate by its average in the relevant range and use the value $\gamma = 1\,\text{neV}/\hbar$.

The coupling to the dissipative environment via the operator $n_1 - n_2$ is of the "longitudinal" type investigated in Ref. [19]. Purely "longitudinal" coupling results in triangular structures in $I(\epsilon_0, A)$ and antisymmetric line shapes in $I(\epsilon_0)$, in contrast to Lorentzians found in our data, e.g., for horizontal slices in Fig. 1(c). However, the Lorentzians are restored already by small additional decoherence such as a "transverse" coupling [19] or dot-lead tunneling [12]. In our case, the latter governs the shape of the peaks so that a possible tiny "transverse" coupling can be neglected.

B. Two-mode Floquet transport theory

From a formal perspective, we are interested in the solution of a master equation of the form $\dot{P} = L(t)P$, where P may be a reduced density operator or a distribution function. For single-frequency driving of the form $L_1 \sin(\Omega t)$, one can make use of the time-periodicity of the long-time solution and employ the ansatz $P(t) = \sum_k e^{ik\Omega t} p_k$ with the trace condition $\text{tr}\, p_k = \delta_{k,0}$. The resulting equation for the p_k can be solved in various ways. In particular, one may write it as a so-called Floquet matrix and numerically compute its kernel. Alternatively, one may exploit the tridiagonal block structure of the equations and solve them with matrix-continued fractions. For a short summary of each method, see Appendix B. Here we extend the first method to the case of bichromatic driving with commensurable frequencies for which the Liouvillian is still periodic. For the quasiperiodic with incommensurate frequencies, we combine both methods and thereby obtain an efficient numerical scheme.

1. Single-frequency driving and commensurable frequencies

Let us start the discussion for the limiting case of periodic and monochromatic driving with just one frequency Ω. Since in the Liouvillian in Eq. (4), the time dependence is fully contained in the DQD Hamiltonian, one possibility to make use of the Floquet theorem would be to compute the Floquet states of the Hamiltonian (3) and to use them as a basis [12,26]. This procedure is general and would allow us to consider a driving that shifts the DQD levels repeatedly across the chemical potentials of the leads, but it is numerically expensive. Since our experiment is operated with a large bias, so that such effects can be excluded we can take a more efficient route and employ the ideas of a Floquet approach directly to the master equation (4) [28]. The corresponding decomposition solution of the master equation is straightforward and is summarized in Appendix B 1. It yields a tridiagonal block matrix whose kernel corresponds to the steady-state solution of the master equation.

If one adds a nth harmonic to the system, i.e., a contribution with the time-dependence $\sin(n\Omega t + \varphi_n)$, the system remains $2\pi/\Omega$ periodic and one can still proceed as sketched above. Essentially, the Floquet matrix acquires a contribution in the nth diagonal of the block matrix, while the computation of the time-averaged steady state remains the same.

2. Incommensurable frequencies

We consider a master equation $\dot{P} = L(t)P$ with bichromatic driving for which the Liouvillian is of the form

$$L(t) = L_0 + L_1 \cos(\Omega t) + L_1' \cos(\Omega' t), \quad (7)$$

with nonrational Ω'/Ω. As we will argue below, for incommensurable frequencies the time-averaged steady-state solution does not depend on the relative phase between the two components of the driving. Thus, for convenience and in contrast to the rest of this work, we choose here particular phases such that the driving is given by cosine functions. Moreover, $L(t)$ is quasiperiodic rather than periodic and the usual Floquet ansatz with a periodic long-time solution is not justified. To circumvent this problem, we employ an idea on which a propagation scheme known as t-t' formalism [27,40]

is built. We replace in the last term of $L(t)$ the time variable by t' which we will treat as an independent angle variable, i.e., we assume that all functions of t' are $2\pi/\Omega'$ periodic. In doing so, we obtain the generalized Liouvillian

$$L(t,t') = L_0 + L_1\cos(\Omega t) + L_1'\cos(\Omega' t') \tag{8}$$

and postulate the generalized master equation

$$\left(\frac{\partial}{\partial t} + \frac{\partial}{\partial t'}\right) Q(t,t') = L(t,t')Q(t,t'). \tag{9}$$

From the chain rule of differentiation follows directly that if $Q(t,t')$ is a solution of the generalized master equation, then $P(t) = Q(t,t')|_{t'=t}$ solves the original master equation. By rewriting Eq. (9) as

$$\frac{\partial}{\partial t} Q(t) = \mathcal{L}(t)Q(t), \tag{10}$$

$$\mathcal{L}(t) = L_0 + L_1'\cos(\Omega' t') - \frac{\partial}{\partial t'} + L_1\cos(\Omega t), \tag{11}$$

we suppress the new coordinate t' in the master equation. In this way, we have obtained a time-periodic master equation with a periodic Liouvillian $\mathcal{L}(t) = \mathcal{L}(t + 2\pi/\Omega)$ for the price of an additional degree of freedom, namely t'. Accordingly, the generalized density operator Q can be decomposed as

$$Q(t) = \sum_k e^{-ik\Omega t} Q_k = \sum_{k,n} e^{-ik\Omega t} e^{-in\Omega' t'} q_{n,k}, \tag{12}$$

which corresponds to the ansatz proposed in Ref. [28]. In a formal consideration, Q is an element of the Sambe space $\mathcal{P}(\mathcal{H}) \otimes \mathcal{T}'$, which here is composed of the projective Hilbert space $\mathcal{P}(\mathcal{H})$ for the density operator and the space $\mathcal{T}'$ of $2\pi/\Omega'$ periodic functions.

The above transformation has a useful consequence, namely that $\mathcal{L}$ defines a time-periodic problem for which the common Floquet tools known from the literature apply. In particular, we can employ the matrix-continued fraction method summarized in Appendix B 2. For the generalized Liouvillian $\mathcal{L}$, the matrices A_n and B defined in Appendix B 2 become

$$\mathcal{A}_k = L_0 \otimes \mathbb{1} + \tfrac{1}{2}L_1' \otimes X + i\Omega' \mathbb{1} \otimes Z + ik\Omega \mathbb{1} \otimes \mathbb{1}, \tag{13}$$

$$\mathcal{B} = \tfrac{1}{2}L_1 \otimes \mathbb{1}, \tag{14}$$

where $\mathbb{1}$ denotes the unit matrices in the space indicated by the operator order. The matrices X and Z are defined by their elements $X_{kk'} = \delta_{k+1,k'} + \delta_{k-1,k'}$ and $Z_{kk'} = k\delta_{kk'}$. The last term in Eq. (13) corresponds to the decomposition of $-\partial/\partial t$. With $\mathcal{A}_k$ and $\mathcal{B}$, the recursion in Eqs. (B7)–(B9) provides $q_{n,0}$ and, finally, the time-averaged distribution $\overline{P(t)} = \overline{Q(t,t)} = q_{0,0}$.

Let us argue why $q_{0,0}$ does not depend on possible phases or time offsets in $L(t)$. A phase in the first time-dependent term of the Liouvillian (7) affects the recurrence relation on which the matrix-continued fractions are based. As such, it is not relevant for the iteration scheme, as shown rigorously in Appendix B 2. A phase φ' in the driving $L_1'\cos(\Omega' t)$ enters via $\mathcal{A}_k$ such that its second term becomes $L_1'(e^{i\varphi}\delta_{k+1,k'} + e^{-i\varphi}\delta_{k-1,k'})/2$. It can be removed by the transformation $q_{n,k} \to q_{n,k}e^{-ik\varphi}$, which does not change $q_{0,0}$.

One might be tempted to employ the ansatz (12) also for commensurable frequencies. Then, however, the time-dependent exponential functions on the right-hand side of Eq. (12) lose their linear independence. As a consequence, the Floquet representation is no longer unique and relations based on the orthogonality of the Floquet solutions will not hold. This is also manifest in the time-average of $e^{-in\Omega t - ik\Omega' t}$, which would be finite not only for $n = k = 0$, but also for other combinations of n and k.

IV. INTERFERENCE PATTERNS

Electron transport across the DQD requires interdot tunneling which is most pronounced when the DQD levels are in resonance with each other (and the electron tends to be delocalized between the two dots). At the resonance the adiabatic eigenstates form an avoided crossing. Our system reaches this resonance at times for which $\epsilon_0 + Af(t) = 0$ and traverses the resonance repeatedly for sufficiently large A such that

$$A\min[f(t)] < -\epsilon_0 < A\max[f(t)]. \tag{15}$$

At the crossings, the transitions follow the scenario considered by Landau, Zener, Stückelberg, and Majorana [41–44] in which the electron wave function is split into a superposition. Repeated sweeps through the crossing lead to interference, which may be constructive or destructive depending on the phase accumulated in between. Consequently, the current $I(\epsilon_0, A)$ exhibits an interference pattern in the triangle determined by Eq. (15). Analyzing this interference pattern and its Fourier transform can provide the complete information about the coherence properties of the DQD [12].

A measured example of the interference pattern and its Fourier transform for monochromatic driving $f(t)$ is presented in Figs. 1(c) and 1(d). The Fourier transform exhibits a characteristic arc structure with reflection symmetry at both the τ_ϵ axis and the τ_A axis and, consequently, with point symmetry at the origin. For the case of periodic bichromatic driving, i.e., with commensurable frequencies, the mirror symmetry is generally broken and the details of the symmetry properties depend on the phase difference between the two frequency components of $f(t)$, see, e.g., Fig. 4. For quasiperiodic bichromatic driving with incommensurable frequencies, by contrast, it turns out that the interference pattern and its Fourier transform regain the full reflection symmetries of the monochromatic case, see Fig. 5. Theoretically, the case of periodic driving can be treated correctly with the method presented in Ref. [19], while the quasiperiodic case (of incommensurable frequencies) reveals peculiarities which require the more general approach developed above.

A. Fourier transformed interference pattern: analytical approach to the arc structure

In the absence of interaction, Floquet scattering theory [26,45] can be employed to find an analytic expression for the dc current $I(\epsilon_0, A)$ through a driven DQD [25], which exhibits the main features of the characteristic interference pattern apparent in Fig. 1(c). Further, dissipation has been approximately taken into account in several analytic expressions

of the interference pattern [4,19,22]. Computing the Fourier transform of these expressions provides the arc structure. A solution for monochromatic driving has been obtained in a stationary-phase calculation [4] and a more general solution for arbitrary periodic driving has been derived recently using the Floquet ansatz [19]. These analytic solutions are all based on the condition $\Delta \ll \Gamma$, i.e., so weak interdot tunneling that it provides the bottleneck for electron transport. As a consequence they typically describe the principal arcs correctly but all fail to predict additional higher-order arcs, which are seen in experiments and found in complete numerical models [12,19].

Within the limit $\Delta \ll \Gamma$, we next generalize the approach introduced in Ref. [19] to include quasiperiodic driving. To describe the relevant interdot tunneling, it is sufficient to consider one-electron states of the DQD for which the second quantized Hamiltonian (3) in the localized basis reads

$$H(t) = \frac{\hbar}{2}\begin{pmatrix} \epsilon_0 + Af(t) & \Delta \\ \Delta & -\epsilon_0 - Af(t) \end{pmatrix}. \tag{16}$$

Assuming $\Delta \ll \Gamma$, we treat the interdot tunneling Δ within perturbation theory while considering the diagonal part, $H_0(t) = \hbar[\epsilon_0 + Af(t)]\sigma_z/2$, exactly. The corresponding interaction-picture Hamiltonian reads $\tilde{H}(t) = U_0^\dagger(t) H_1 U_0(t) = \hbar\tilde{\Delta}(t)\sigma_-/2 + \text{H.c.}$, with $H_1 = \Delta\sigma_x/2$, $U_0(t)$ being the propagator corresponding to $H_0(t)$, and H.c. the Hermitian conjugate. The emerging time-dependent tunnel matrix element

$$\tilde{\Delta}(t) = e^{-i\epsilon_0 t - iAF(t)}\Delta \tag{17}$$

is governed by the dynamic phase $\epsilon_0 t + AF(t)$ of the time evolution where $dF/dt = f$. For convenience, we choose the integration constant such that $F(t)$ vanishes on average.

For the analytic analysis we assume that the tunnel processes are much slower than the driving (i.e., the nonadiabatic limit which does not influence the course of the principle arcs) and replace $\tilde{\Delta}(t)$ by its time average $\bar{\Delta}$. Then according to Fermi's golden rule, we expect interdot tunneling with a rate $\gamma \propto |\bar{\Delta}|^2/\Gamma$, where the effective density of final states $\propto 1/\Gamma$ reflects the broadening of the DQD states due to the dot-lead coupling Γ. Consequently, for $\gamma \ll \Gamma$, the current through the DQD obeys the proportionality

$$I(\epsilon_0, A) \propto |\bar{\Delta}|^2 \propto \int dt\, dt' e^{i\epsilon_0(t-t') + iAF(t) - iAF(t')}, \tag{18}$$

where the integral may have to be regularized by an appropriate cutoff.

Notice that for a rigorous application of Fermi's golden rule, the final states must have a continuous spectrum. We achieve this by considering the relevant states of the still separate quantum dots after coupling them to the respective lead which yields a Lorentzian spectral density with a peak value $2/\pi\Gamma$. For an explicit calculation of a time-averaged current in this spirit, see Sec. 5.2 of Ref. [26]. Here, we do not attempt to compute the prefactor, because it is irrelevant for the structure of the LZSM pattern.

To obtain the Fourier transformed pattern

$$\hat{I}(\tau_\epsilon, \tau_A) = \int d\epsilon_0\, dA\, e^{-i\epsilon_0\tau_\epsilon - iA\tau_A} I(\epsilon_0, A), \tag{19}$$

we insert Eq. (18) and notice that both the ϵ_0 integration and the A integration yield δ functions. One of them reads $\delta(\tau_\epsilon - t + t')$ and allows us to directly evaluate the t' integral so that we remain with the expression

$$\hat{I}(\tau_\epsilon, \tau_A) \propto \int dt\, \delta(\tau_A - F(t + \tau_\epsilon/2) + F(t - \tau_\epsilon/2)) \tag{20}$$

$$\propto \sum_i \frac{1}{|f(t_i + \tau_\epsilon/2) + f(t_i - \tau_\epsilon/2)|}. \tag{21}$$

The sum has to be taken over all times t_i for which the argument of the δ function in Eq. (20) vanishes.

The two alternative expressions for $\hat{I}(\tau_\epsilon, \tau_A)$ in Eqs. (20) and (21) provide the desired information about the interference pattern in Fourier space. First, Eq. (20) specifies the times t_i at which the δ function contributes. Second, Eq. (21) lets us conclude that the most significant contributions stem from regions in which the denominator vanishes. Thus the structure in Fourier space is peaked on manifolds (τ_ϵ, τ_A) on which the conditions

$$\tau_A = F(t + \tau_\epsilon/2) - F(t - \tau_\epsilon/2), \tag{22}$$

$$0 = f(t + \tau_\epsilon/2) - f(t - \tau_\epsilon/2) \tag{23}$$

are fulfilled. While these conditions are formally the same as those in Ref. [19], we like to emphasize that the present derivation extends their range of validity from periodic driving to quasiperiodic driving. Henceforth we restrict ourselves to bichromatic driving as defined in Eq. (2).

1. *Commensurable frequencies*

Commensurable frequencies generally result in periodic driving, $f(t) = f(t + T)$, where T is determined by the greatest common divisor of the frequencies. The corresponding solution of Eqs. (22) and (23) has been addressed in Ref. [19]. For later reference, we outline its main aspects. First, the T periodicity of f implies that if t_1 solves Eq. (23), then $t_2 = t_1 + T/2$ fulfills this condition as well. Therefore the arcs come in pairs shifted by $T/2$, as is visible in Fig. 1(d). Second, generally Eq. (23) is transcendental and one has to resort to a numerical solution. Nevertheless, there exists a particular case that can be solved analytically. For a driving symmetric at $t = t_0$, i.e., for $f(t_0 + t) = f(t_0 - t)$, one finds the roots $t_1 = t_0$ and $t_2 = t_0 + T/2$. They provide the arcs $\tau_A^{(1)} = 2F(t_0 + \tau_\epsilon/2)$ and $\tau_A^{(2)} = 2F(t_0 + T/2 + \tau_\epsilon/2)$.

As in our experiment, we focus on the case

$$\Omega' = n\Omega \tag{24}$$

with integer n. Then $f(t)$ is symmetric at $t_0 = T/4$ for $\phi = (\pm 1 - n)\pi/2$ and one finds the arcs

$$\tau_A^{(1,2)} = \pm\frac{2}{\Omega}\sin\left(\frac{\Omega\tau_\epsilon}{2}\right) + (-1)^n\frac{2\eta}{n\Omega}\sin\left(\frac{n\Omega\tau_\epsilon}{2}\right). \tag{25}$$

As we will see in both our numerical and in our measured data, the solution presented by Eq. (25) is incomplete even

within the approximation $\Delta \ll \Gamma$. Depending on the value of the amplitude ratio η one may find further solutions [19].

2. *Incommensurable frequencies*

When Ω and Ω' are incommensurable, one cannot exploit symmetries such as periodicity and time reversal. To nevertheless make progress, we insert the driving shape (2) into Eqs. (22) and (23) to obtain with the functional relations of the trigonometric functions the conditions

$$\tau_A = \frac{2}{\Omega}\sin(\Omega t)\sin\left(\frac{\Omega\tau_\epsilon}{2}\right) + \frac{2\eta}{\Omega'}\sin(\Omega' t+\phi)\sin\left(\frac{\Omega'\tau_\epsilon}{2}\right), \tag{26}$$

$$0 = \cos(\Omega t)\sin\left(\frac{\Omega\tau_\epsilon}{2}\right) + \eta\sin(\Omega' t+\phi)\cos\left(\frac{\Omega'\tau_\epsilon}{2}\right). \tag{27}$$

While it is practically impossible to determine all roots t_i of the second equation, we can restrict ourselves to those t_i for which both terms in Eq. (27) vanish individually. This happens when in each term the cosine becomes zero. Then the corresponding sines in Eq. (26) assume the values ± 1. Therefore we can conjecture four arcs

$$\tau_A^{(\pm,\pm)} = \pm\frac{2}{\Omega}\sin\left(\frac{\Omega\tau_\epsilon}{2}\right) \pm \frac{2\eta}{\Omega'}\sin\left(\frac{\Omega'\tau_\epsilon}{2}\right), \tag{28}$$

where both $\pm$ signs are independent of each other. Moreover, in accordance with the general deliberations below, the arcs turn out to be independent of ϕ.

Thus, in contrast to the commensurable case, we find four independent arcs. While this reasoning does not exclude the existence of further solutions, our numerical and experimental results for $\hat{I}(\tau_\epsilon,\tau_A)$ below confirm that the main structure of the Fourier transformed LZSM patterns for incommensurable frequencies is well described by Eq. (28).

3. *Symmetries of the LZSM patterns*

We start our symmetry considerations by noticing that the analytically predicted arcs for periodic driving in Eqs. (25) and quasiperiodic driving in Eq. (28) are all point symmetric with respect to the origin, i.e., they are invariant under the simultaneous inversion of the τ_ϵ and τ_A axes—a feature that extends beyond these two special cases. Indeed, both the numerical and the measured Fourier transforms $\hat{I}(\tau_\epsilon,\tau_A)$ of the interference patterns possess point symmetry, as can be appreciated in Figs. 3–5.

Theoretically, the point symmetry at the origin, $\hat{I}(\tau_\epsilon,\tau_A) = \hat{I}(-\tau_\epsilon,-\tau_A)$, is evident from the definition of $\hat{I}(\tau_\epsilon,\tau_A)$ in Eq. (19) together with the analytic approximation (18) for the current: inverting in the definition the signs of τ_ϵ and τ_A can be compensated by inverting in Eq. (18) the signs of ϵ_0 and A together with interchanging the integration variables t and t'. This is also seen in Eq. (20) which, owing to the symmetry of the δ function, is invariant under inverting the signs of both τ_ϵ and τ_A. For the curves $\tau_A(\tau_\epsilon)$ defined as the solutions of Eqs. (22) and (23), the point symmetry is manifest in the relation $\tau_A(-\tau_\epsilon) = -\tau_A(\tau_\epsilon)$ which is obviously fulfilled by the explicit analytical predictions of the arcs in Eqs. (25) and (28).

For antisymmetric driving with commensurable frequencies (e.g., for $\Omega' = 2\Omega$ with $\phi = 0$ or π), we find in addition reflection symmetry at the τ_A axis, see Fig. 4. Together with the point symmetry discussed above, this implies reflection symmetry at the τ_ϵ axis as well. In these specific cases, periodic bichromatic driving recovers the symmetry properties found for monochromatic driving. For a proof, we notice that an antisymmetric driving shape $f(t) = -f(-t)$ corresponds to a symmetric $F(t) = F(-t)$. Then the integral in Eq. (20) is invariant under $\tau_\epsilon \to -\tau_\epsilon$ since the sign of the integration variable t can be changed by substitution. With the same argument, we can invert in Eq. (18) the sign of the detuning ϵ_0. Thus, in the validity regime of our analytical approximation, for antisymmetric driving the interference pattern in real space, $I(\epsilon_0, A)$, must be symmetric with respect to the A axis at $\epsilon_0 = 0$ [46].

For driving with incommensurable frequencies, we will see below that reflection symmetry in τ_ϵ and τ_A is fully recovered. Our analytic conjecture (28) yields the striking result, that the arcs in Fourier space do not dependent on the phase ϕ between the driving components (we used this fact for testing the numerical implementation). This conjecture is confirmed by general considerations based on the fact that in ergodic systems time-averaged expectation values do not depend on a time offset. To demonstrate the independence of ϕ, we consider a time delay by $2\pi\ell/\Omega$ with integer ℓ. This does not affect the first term in Eq. (28), while the second term acquires a phase $\phi(\ell) = 2\pi\ell\Omega'/\Omega \pmod{2\pi}$. For incommensurable Ω and Ω', there always exists an integer n that brings $\phi(\ell)$ arbitrarily close to a given $2\pi - \phi$ for $0 \leqslant \phi < 2\pi$. This means that any phase ϕ in $f(t)$ can be compensated by a proper time shift, hence the time averaged expectation values are phase independent.

In the commensurable case, by contrast, the phase $\phi(\ell) = 2\pi\ell\Omega'/\Omega \pmod{2\pi}$ assumes only a finite number of values given by the denominator k that appears when expressing the frequency ratio as a fraction of integers, $\Omega'/\Omega = k'/k$ (for $\Omega' = n\Omega$, we have $k = 1$, which implies $\phi(\ell) = 0$ for all ℓ). Therefore the phase in $f(t)$ generally cannot be compensated by a time shift so that the interference patterns for periodic driving will depend on ϕ.

This phase independence for incommensurable frequencies readily explains the reflection symmetry observed in Figs. 5(b) and 5(d), which fully resembles the symmetry properties obtained for monochromatic driving. For $\phi = \pi\Omega'/2\Omega$, the driving shape $f(t)$ is antisymmetric. Therefore, according to the above reasoning for antisymmetric driving (which did not make use of the commensurability), we can immediately conclude that the LZSM pattern must be reflection symmetric. Since the pattern does not depend on ϕ, this symmetry for incommensurable frequencies must be generic.

Finally, let us emphasize that our symmetry considerations are based on the assumption that the two-level Hamiltonian (16) describes the relevant part of the transport process. In practice, the reflection symmetry with respect to the detuning may be compromised by dissipative processes or the influence of states not considered in our model. However, as we will see below, our measured results substantiate our simplifying approach by displaying a convincing agreement with our predictions.

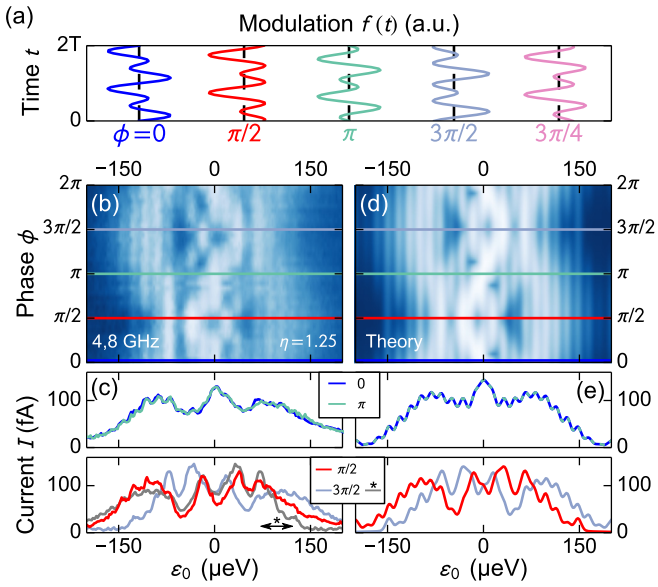

FIG. 2. (Color online) (a) Shape of the ac driving, $f(t) = \sin(\Omega t) + 1.25\sin(2\Omega t + \phi)$, for various phases ϕ. For $\phi = \pi/2$ and $3\pi/2$, $f(t)$ possesses reflection symmetry at specific times, for $\phi = 0$ and π, $f(t)$ is antisymmetric in time, while for other phases in the range $0 \leqslant \phi < 2\pi$ symmetry is lost. (b) Phase dependent LZSM interference for $f(t)$ as in (a), constant amplitude $A = 57$ μeV, $\eta = 1.25$, and $\Omega/2\pi = 4$ GHz ($\Omega' = 2\Omega$). (c) Interference patterns $I(\epsilon_0)$ at the phases of enhanced symmetry along horizontal lines in (b) [color coded]. The gray line in the lower panel of (c) is the blueish curve after reflection at the $\epsilon_0 = 0$ axis. (d) and (e) Theory data corresponding to the measurements in (b) and (c) for interdot and dot-lead tunnel couplings $\Delta = 8$ μeV and $\Gamma_L = \Gamma_R = 0.002$ μeV, decoherence rate $\gamma = 0.001$ μeV, and inhomogeneous broadening $\gamma^* = 5$ μeV. Colorscales in panels (b) and (d) as in Fig. 1(c).

B. Results for commensurable frequencies

To test our general considerations above, we next consider a representative case of two commensurate frequencies, namely a fundamental mode and its second harmonic, i.e., $\Omega' = 2\Omega$. In our experiment, the phase difference between the harmonics acquired along the dispersive transmission line through which we drive the gate voltages is not *a priori* known and has to be calibrated. With this purpose we display in Fig. 2(b) the current as a function of the static detuning ϵ_0 and the phase ϕ for the amplitude ratio $\eta = 1.25$. $I(\epsilon_0,\phi)$ has maxima of constructive and minima of destructive interference. Closer inspection reveals varying symmetry properties of the interference pattern $I(\epsilon_0)$ as function of ϕ as expected from the symmetry considerations above.

To explore, how the symmetry of the interference is related to that of the driving function, in Fig. 2(a), we sketch $f(t)$ at five different phases. Generally, $f(t)$ is asymmetric but it has enhanced symmetry at four special phases in the range $0 \leqslant \phi < 2\pi$: $f(t)$ is reflection symmetric for $\phi = \pi/2$ or $3\pi/2$ and antisymmetric for $\phi = 0$ or π (with respect to distinct points along the time axis). For a direct comparison we present in Fig. 2(c) also $I(\epsilon_0)$ at these four special phases, i.e., along the (color coded) horizontal lines in Fig. 2(b). The point symmetries of $f(t)$ at $\phi = 0$ or π expresses itself in

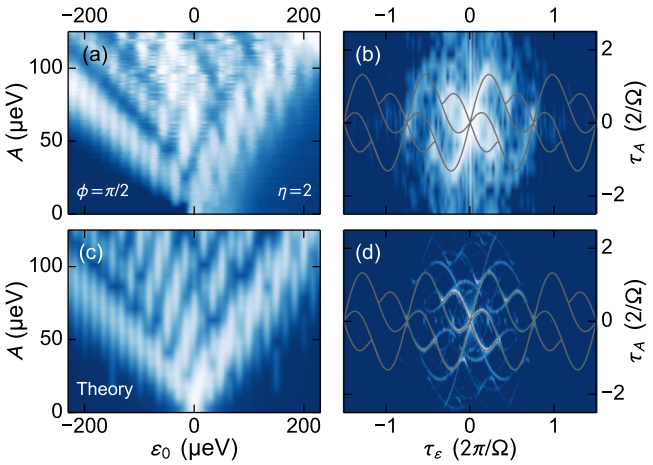

FIG. 3. (Color online) Measured and computed LZSM pattern in real space (a) and (c) and in Fourier space (b) and (d) for the phase $\phi = \pi/2$ and the amplitude ratio $\eta = 2$. All other parameters are as in Fig. 2, the color scales are as in Fig. 1(c). The enhanced resolution of the theory data in Fourier space is achieved by considering data beyond the range shown in (c).

$I(\epsilon_0)$ as reflection symmetries, see upper panel of Fig. 2(c). In contrast to this antisymmetric driving, reflection symmetry in $f(t)$ at $\phi = \pi/2$ or $3\pi/2$ does not lead to a symmetric $I(\epsilon_0)$, see lower panel of Fig. 2(c). Moreover, the current traces are identical for $\phi = 0$ and π but not for $\phi = \pi/2$ and $3\pi/2$. However, $I(\epsilon_0)$ at $\phi = 3\pi/2$ matches that at $\phi = \pi/2$ after reflection at $\epsilon_0 = 0$ (gray curve). These differences are directly related to the symmetry properties of $f(t)$ as we discussed in more detail in Sec. IV A 3 above. [Note that the measured $I(\epsilon_0)$ curves are subject to a global asymmetry caused by higher-order contributions to transport, such as co-tunneling via triplet states. This explains specifically the differences between the red curve (at $\phi = \pi/2$) and the gray curve (at $\phi = 3\pi/2$ and mirrored).]

Shifting the ϕ axis in panel (b) such that the symmetry properties match the corresponding phases concludes our phase calibration. Figures 2(d) and 2(e) display comparable theory data calculated as described in Sec. III B. The fit procedure allows us to determine important experimental parameters, namely the interdot and dot-lead couplings as well as decoherence and inhomogeneous broadening, see Ref. [12] for a discussion of a very similar fit procedure and the caption of Fig. 2 for fit parameters. The encountered parameters agree with our expectations from transport measurements and the agreement between the theory and experimental data is very good.

As an example of a LZSM interference pattern for bichromatic driving we present in Fig. 3 the current as a function of the driving amplitude A and the averaged detuning ϵ_0 for $\Omega/2\pi = 4$ GHz, $\Omega' = 2\Omega$, $\eta = 2$, and $\phi = \pi/2$. Measured data and their Fourier transform are presented in the upper panels and compared to numerical data below. In contrast to monochromatic driving (see Fig. 1) neither the data in real space (left) nor the Fourier transform (right) obey reflection symmetry but the Fourier transform has point symmetry, all in good agreement with theory [bottom panels] and with our expectations from Sec. IV A 3.

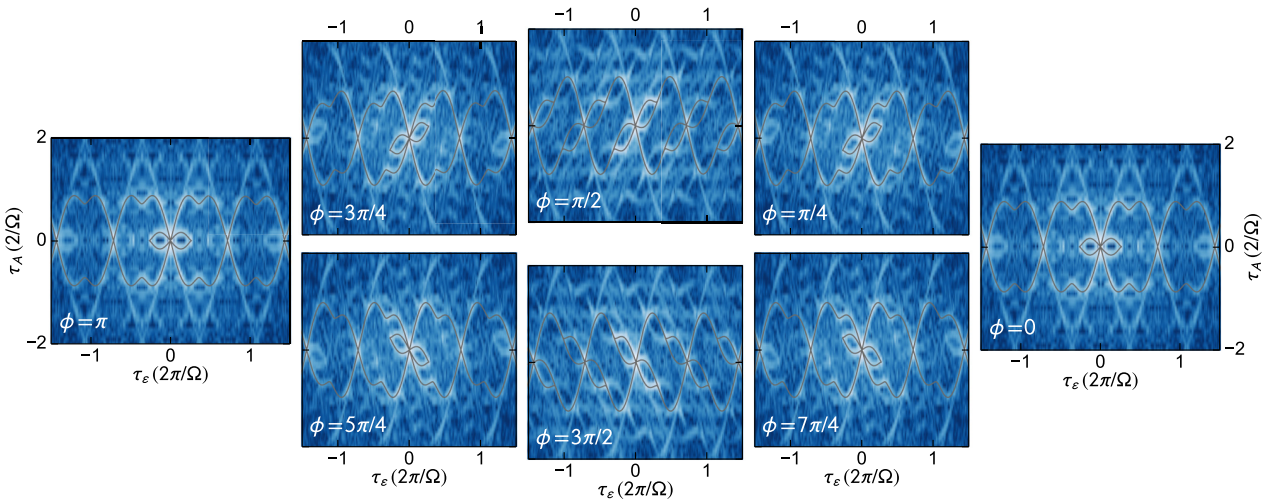

FIG. 4. (Color online) Theoretical LZSM patterns in Fourier representation for bichromatic driving with commensurable frequencies for various relative phases. The driving frequencies are $\Omega/2\pi = 4$ GHz and $\Omega'/2\pi = 8$ GHz, while the amplitude ratio is $\eta = 1.25$. The gray lines are the solutions of Eqs. (22) and (23). The phases $\phi = \pi/2$ and $\phi = 3\pi/2$ correspond to symmetric driving for which part of the structure is given by the analytic expression (25).

In real space [Figs. 3(a) and 3(c)], the patterns show clear resonance peaks which are located at detunings at which the energy quanta of the driving match the level splitting, i.e., when the condition $(n\Omega)^2 = \Delta^2 + \epsilon_0^2$ is fulfilled for any integer n. The triangle in which the current assumes an appreciable value confirms the prediction given in Eq. (15), which follows from the condition that the amplitude must be so large that the time-dependent detuning $\epsilon_0 + Af(t)$ reaches at least one avoided crossing. Since generally $|\min f(t)| \neq |\max f(t)|$, the parameter region in which interference takes place is asymmetric. In panels (a) and (c) of Fig. 3, we observe a clear tilt of the triangle to the left. This is a direct consequence of the asymmetry in driving with $|\min f(t)| > |\max f(t)|$, see Fig. 2(a). Within the triangle, the resonance lines are vertical and modulated. The physical pictures of the vanishing current at the minima is that of coherent destruction of tunneling [47,48], which occurs when the time-average of the tunnel matrix element defined in Eq. (17) vanishes.

Figure 4 shows theoretical LZSM patterns in Fourier space for distinct phases chosen to emphasize the symmetry properties. As expected, we always find point symmetry independent of the phase and, in addition, reflection symmetry for $\phi = 0$ and π corresponding to antisymmetric driving $f(-t) = -f(t)$. Gradually increasing the phase from 0 to π (or from π to 2π) first distorts the patterns and then brings them back to their original shape.

Concerning the semi-analytical calculation of the arcs structure (gray lines), these results confirm the predictions of Ref. [19]. There, however, the patterns depict the nonequilibrium population of a driven spin-boson model, while the present results stem from a transport theory for an open DQD, which allows for particle exchange between the system and fermionic reservoirs. Therefore we can conclude that a simple description with a closed two-level model provides a valid prediction of LZSM patterns also for open systems.

C. Results for incommensurable frequencies

Finally, we present our results for the case of incommensurate frequencies. Because of the finite broadening one might ask the question of how well we can experimentally (and numerically) differentiate between the periodic and the quasiperiodic case. For practical purposes, the numerical calculations are performed with rational approximations with a finite number of digits. We nevertheless use the terms "irrational" and "incommensurable." The differences to the commensurable case is typically best visible if one chooses for Ω'/Ω the "most irrational number," namely, the golden ratio $g = (1+\sqrt{5})/2 \simeq 1.618$ [49].

In Fig. 5, we present measured and calculated data for $\Omega'/\Omega = g$. As expected from our discussion in Sec. IV A 3 for incommensurable frequencies the data in real space recover reflection symmetry in respect to the A axis at $\epsilon_0 = 0$, while the Fourier transform exhibits reflection symmetry in regard to both axis. A further remarkable difference to the commensurable case with vertical resonance lines of enhanced current in the real space interference pattern is that the latter are tilted while the pattern nevertheless shows a regular structure. The agreement between theory and experiment is good even on a quantitative level.

In Fourier space [see Figs. 5(b) and 5(d)], the arcs follow by and large the prediction in Eq. (28) (gray lines). Taking into account that the analytical derivation of the structure was based on the *ad hoc* assumption that the main contribution stems from those roots of Eq. (27) for which both terms vanish individually, the agreement between measured and calculated data in Fourier space is surprisingly good. Note that the stronger broadening of the measured data in Fourier space compared to the calculated ones is mainly caused by the smaller range probed for ϵ_0 and A in real space, which determines the resolution in Fourier space.

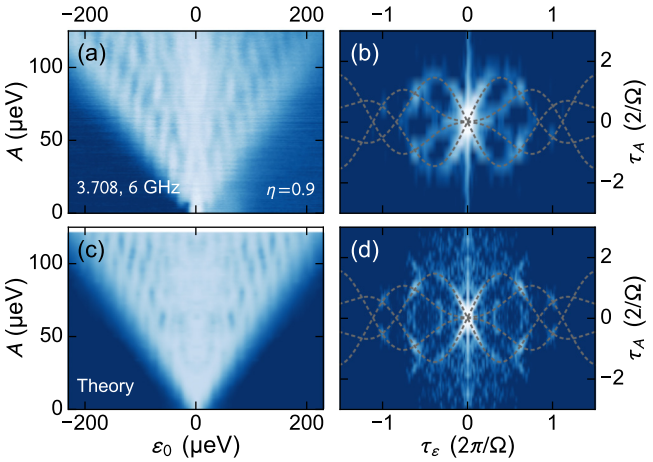

FIG. 5. (Color online) Experiment [(a) and (b)] and theory [(c) and (d)] for the driving frequencies $\Omega = 3.708$ GHz, $\Omega' = 6$ GHz, and the amplitude ratio $\eta = 0.9$. The frequency ratio approximates the golden mean with a precision of 10^{-4}. All other parameters are as in Fig. 2, the color scales are as in Figs. 1(c) and 1(d). Dashed lines visualize the analytical prediction in Eq. (28).

V. CONCLUSIONS

We have extended theoretically and experimentally LZSM interference from the already known monochromatic case to bichromatic driving. Studying quantum transport through a strongly biased DQD ($V = 1$ mV), we measured the dc current in the steady state and explored LZSM interference as a function of the DQD detuning and the driving amplitude.

The interference patterns in our measurements and their two-dimensional Fourier transforms exhibit characteristic symmetry properties, which we have confirmed in our analytical and numerical predictions: bichromatic driving with commensurable frequencies causes a reduction of the symmetry compared to the monochromatic case (except for two specific phase relations, only point symmetry in Fourier space survives). Interestingly, for driving with incommensurable frequencies, the full reflection symmetries observed for monochromatic driving are retained, although the interference patterns are more complex.

Our theoretical approaches exploit the Floquet theorem for time-dependent master equations that include the incoherent dot-lead tunneling. For the periodic driving with commensurable frequencies, the long-time solution obeys the periodicity of the Liouvillian and, thus, can be decomposed into a Fourier series. Then the master equation can be written with the help of a block-diagonal Floquet matrix. For the quasiperiodic driving with two incommensurable frequencies, we have developed an efficient numerical scheme for the computation of the long-time solution. It is based on a two-color Floquet theory for which we have combined a Floquet matrix decomposition with ideas adopted from the t-t' formalism. In doing so, we have mapped the bichromatically time-dependent master equation to a monochromatically driven problem in a higher dimensional space. This allowed us to find a solution based on known Floquet methods for periodic driving.

Experimentally, the phase dependence of the interference patterns for bichromatic driving with commensurable frequencies can be used to accurately calibrate phase differences caused by frequency dispersion. This is an important advantage for quantum measurements and related applications in quantum information where accurate knowledge of phase relations is crucial. To properly fit our measured interference patterns in our model, we needed to take into account decoherence and an inhomogeneous line broadening. Our results here quantitatively confirm our earlier findings in a similar system [12].

We have theoretically predicted and experimentally confirmed a strong relevance of commensurability effects in coherent nanoelectronics. Our results will be relevant for applications based on coherent driving with more than one frequency.

ACKNOWLEDGMENTS

We thank Mónica Benito for helpful discussions. This work was supported by the Spanish Ministry of Economy and Competitiveness through Grant No. MAT2014-58241-P and by the DFG via LU 819/4-1, SFB 631, and the Cluster of Excellence "Nanosystems Initiative Munich (NIM)". SL acknowledges support by the DFG via a Heisenberg fellowship.

APPENDIX A: ADDITIONAL DATA

1. Commensurate frequencies for various phases

In Fig. 6, we present additional measured data for three different phases at $\Omega' = 2\Omega$. The data clearly confirm the predicted point symmetries, albeit the Fourier transformation causes an additional broadening due to the relatively small

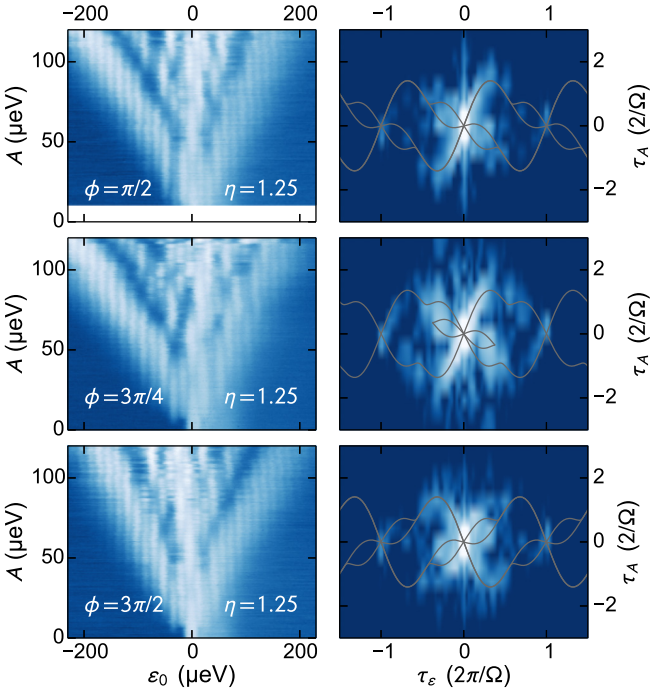

FIG. 6. (Color online) Measured LZSM pattern in real space and in Fourier space for commensurable frequencies $\Omega/2\pi = 4$ and 8 GHz and the phases and amplitude ratios displayed in the graphics. The gray lines indicate the arcs predicted by Eqs. (22) and (23).

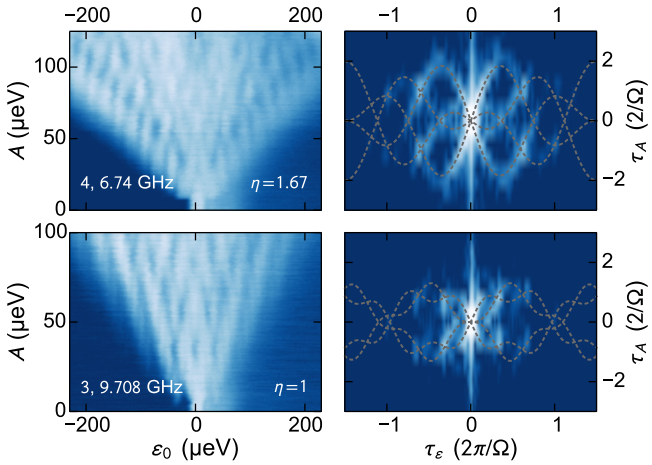

FIG. 7. (Color online) Measured LZSM pattern in real space and in Fourier space for the incommensurate frequencies with ratios g (the golden mean) and $2g$ and amplitude ratios displayed in the graphics. The gray lines indicate the arcs predicted by Eq. (28).

amount of data points. The theoretical predictions for the arcs result from a numerical solution of Eqs. (22) and (23). They are in accordance with the structure observed in the measured data.

2. Further combinations of incommensurate frequencies

Figure 7 depicts further experimental data for incommensurable frequencies. In the upper row, the frequency ratio is the golden mean, $\Omega'/\Omega = g$. As compared to Fig. 5, the frequencies are slightly smaller, while the amplitude ratio η is significantly larger. In the lower row, the frequency ratio is twice the golden mean, $\Omega'/\Omega = 2g$. The findings are consistent with the predictions in Sec. IV C: they confirm the symmetry in real space (left column), and the theoretical prediction (28) for the arcs in Fourier space (right column). Moreover, the Fourier transform of the pattern is most pronounced when two arcs cross each other.

APPENDIX B: FLOQUET THEORY FOR MASTER EQUATIONS WITH MONOCHROMATIC DRIVING

We consider the periodically time-dependent master equation $\dot{P} = L(t)P$ with a Liouvillian of the form

$$L(t) = L_0 + L_1 \cos(\Omega t + \varphi). \tag{B1}$$

In the case of a quantum master equation, the "distribution function" is the reduced density operator, which generally possesses off-diagonal matrix elements. We are interested in its long-time limit, the steady-state solution $P_\infty(t)$. Due to the linearity of the master equation, the steady state solution obeys the periodicity of the Liouvillian, i.e.,

$$P_\infty(t) = P_\infty(t + 2\pi/\Omega) = \sum_k p_k e^{-ik\Omega t}. \tag{B2}$$

The trace condition of the density operator leads for the Fourier coefficients to the normalization $\mathrm{tr}\, p_k = \delta_{k,0}$. Our main interest lies in time-averaged expectation values where the time-dependence is fully contained in the density operator $P_\infty(t)$. Hence $\overline{P_\infty(t)} = p_0$ contains all relevant information.

1. Master equation in Sambe space

A conceptually straightforward way to compute the p_k is to write the master equation in Fourier space where it reads $\sum_{k'} \mathcal{L}_{kk'} p_{k'} = 0$, where $\mathcal{L}$ denotes the Fourier representation of the superoperator $\mathcal{L} = L(t) - \partial/\partial t$ with the components [30]

$$\mathcal{L}_{kk'} = (L_0 + ik\Omega)\delta_{kk'} + \frac{L_1}{2}(e^{i\varphi}\delta_{k+1,k'} + e^{-i\varphi}\delta_{k-1,k'}). \tag{B3}$$

It can be written as tridiagonal block matrix, the so-called Floquet matrix. Its diagonal blocks are $L_0 + ik\Omega$, while its first diagonals are given by the driving L_1. The kernel of the Floquet matrix is a vector that contains the Fourier coefficients p_k of the steady state solution. The Fourier representation of the Liouvillian can be understood as extending the space in which the density operator is defined by the space of $2\pi/\Omega$-periodic functions (Sambe space) [29,50]. For numerical computations, one has to truncate the Floquet matrix setting $p_k = 0$ for all $k < -k_0$ and $k > k_0$. For a driving amplitude A, the value at which one reaches numerical convergence usually scales as $k_0 \propto A/\Omega$.

In the presence of higher harmonics $L(t) \to L(t) + L_n \cos(n\Omega t + \varphi_n)$ with a phase lag φ_n, the nth secondary diagonals become

$$\frac{L_n}{2}\left(e^{i\varphi_n}\delta_{k+n,k'} + e^{-i\varphi_n}\delta_{k-n,k'}\right). \tag{B4}$$

For a generalization of this method to the case of two commensurable driving frequencies Ω_i, one works in the Sambe space whose frequency Ω is a common divisor of the Ω_i such that $\Omega_i = n_i\Omega$. Then the secondary diagonals with indices n_i are nonvanishing.

2. Matrix-continued fraction

For large driving amplitudes or small frequencies, the Floquet matrix can become quite large. Then a more efficient way to compute the steady state p_0 is the matrix-continued fraction method widely applied in the context of Brownian motion [51,52]. For the single-frequency driving underlying the Floquet matrix (B3), it is based on the fact that the linear equation for the Fourier coefficients p_k corresponds to the tridiagonal recurrence relation

$$e^{i\varphi}Bp_{k+1} + A_k p_k + e^{-i\varphi}Bp_{k-1} = 0, \tag{B5}$$

where $A_k = L_0 + ik\Omega$ and $B = L_1/2$. The truncation of the Floquet matrix (B3) corresponds to assuming $p_k = 0$ for $|k| > k_0$.

The direct solution of the recurrence relation (B5) is hindered by the fact that the matrix B generally does not possess an inverse. This problem can be circumvented by

defining transfer matrices S_k and R_k via

$$p_k = \begin{cases} R_k e^{i\varphi} B p_{k+1} & \text{for } k < 0, \\ S_k e^{-i\varphi} B p_{k-1} & \text{for } k > 0. \end{cases} \tag{B6}$$

This allows us to substitute in the recurrence relation the terms $Bp_{k\pm1}$ by expressions proportional to p_k. Compliance of this ansatz with Eq. (B5) is ensured for

$$S_k = -(A_k + BS_{k+1}B)^{-1}, \tag{B7}$$

$$R_k = -(A_k + BR_{k-1}B)^{-1}, \tag{B8}$$

while p_0 obeys

$$(BR_{-1}B + A_0 + BS_1B)p_0 = 0. \tag{B9}$$

In a numerical calculation, one starts with $S_{k_0+1} = R_{-(k_0+1)} = 0$ and iterates Eqs. (B7) and (B8) to obtain S_1 and R_{-1}. Finally, one obtains p_0 by solving Eq. (B9) under the trace condition $\mathrm{tr}\, p_0 = 1$. Notice that the iteration scheme and, thus, the time averaged steady-state distribution do not depend on φ.

[1] W. D. Oliver, Y. Yu, J. C. Lee, K. K. Berggren, L. S. Levitov, and T. P. Orlando, Science **310**, 1653 (2005).
[2] M. Sillanpää, T. Lehtinen, A. Paila, Y. Makhlin, and P. Hakonen, Phys. Rev. Lett. **96**, 187002 (2006).
[3] C. M. Wilson, T. Duty, F. Persson, M. Sandberg, G. Johansson, and P. Delsing, Phys. Rev. Lett. **98**, 257003 (2007).
[4] M. S. Rudner, A. V. Shytov, L. S. Levitov, D. M. Berns, W. D. Oliver, S. O. Valenzuela, and T. P. Orlando, Phys. Rev. Lett. **101**, 190502 (2008).
[5] D. M. Berns, M. S. Rudner, S. O. Valenzuela, K. K. Berggren, W. D. Oliver, L. S. Levitov, and T. P. Orlando, Nature (London) **455**, 51 (2008).
[6] A. Izmalkov, S. H. W. van der Ploeg, S. N. Shevchenko, M. Grajcar, E. Il'ichev, U. Hübner, A. N. Omelyanchouk, and H.-G. Meyer, Phys. Rev. Lett. **101**, 017003 (2008).
[7] J. Li, M. P. Silveri, K. S. Kumar, J.-M. Pirkkalainen, A. Vepsäläinen, W. C. Chien, J. Tuorila, M. A. Sillanpää, P. J. Hakonen, E. V. Thuneberg, and G. S. Paraoanu, Nat. Commun. **4**, 1420 (2013).
[8] M. P. Silveri, K. S. Kumar, J. Tuorila, J. Li, A. Vepsäläinen, E. V. Thuneberg, and G. S. Paraoanu, New J. Phys. **17**, 043058 (2015).
[9] J. Stehlik, Y. Dovzhenko, J. R. Petta, J. R. Johansson, F. Nori, H. Lu, and A. C. Gossard, Phys. Rev. B **86**, 121303(R) (2012).
[10] E. Dupont-Ferrier, B. Roche, B. Voisin, X. Jehl, R. Wacquez, M. Vinet, M. Sanquer, and S. De Franceschi, Phys. Rev. Lett. **110**, 136802 (2013).
[11] G. Cao, H.-O. Li, T. Tu, L. Wang, C. Zhou, M. Xiao, G.-C. Guo, H.-W. Jiang, and G.-P. Guo, Nat. Commun. **4**, 1401 (2013).
[12] F. Forster, G. Petersen, S. Manus, P. Hänggi, D. Schuh, W. Wegscheider, S. Kohler, and S. Ludwig, Phys. Rev. Lett. **112**, 116803 (2014).
[13] A. P. Saiko, R. Fedaruk, and S. A. Markevich, J. Phys. B **47**, 155502 (2014).
[14] S. N. Shevchenko, G. Oelsner, Y. S. Greenberg, P. Macha, D. S. Karpov, M. Grajcar, U. Hübner, A. N. Omelyanchouk, and E. Il'ichev, Phys. Rev. B **89**, 184504 (2014).
[15] I. M. Georgescu, S. Ashhab, and F. Nori, Rev. Mod. Phys. **86**, 153 (2014).
[16] G. S. Paraoanu, J. Low Temp. Phys. **175**, 633 (2014).
[17] S. Gustavsson, J. Bylander, and W. D. Oliver, Phys. Rev. Lett. **110**, 016603 (2013).
[18] S. Platonov, B. Kästner, H. W. Schumacher, S. Kohler, and S. Ludwig, Phys. Rev. Lett. **115**, 106801 (2015).
[19] R. Blattmann, P. Hänggi, and S. Kohler, Phys. Rev. A **91**, 042109 (2015).
[20] K. M. Fonseca-Romero, S. Kohler, and P. Hänggi, Chem. Phys. **296**, 307 (2004).
[21] T. M. Stace, A. C. Doherty, and S. D. Barrett, Phys. Rev. Lett. **95**, 106801 (2005).
[22] S. N. Shevchenko, S. Ashhab, and F. Nori, Phys. Rep. **492**, 1 (2010).
[23] Y. Kayanuma, Phys. Rev. A **50**, 843 (1994).
[24] A. Ferrón, D. Domínguez, and M. J. Sánchez, Phys. Rev. Lett. **109**, 237005 (2012).
[25] M. Strass, P. Hänggi, and S. Kohler, Phys. Rev. Lett. **95**, 130601 (2005).
[26] S. Kohler, J. Lehmann, and P. Hänggi, Phys. Rep. **406**, 379 (2005).
[27] P. Hänggi, in *Quantum Transport and Dissipation* (Wiley-VCH, Weinheim, 1998), Chap. 5, pp. 249–286.
[28] S. I. Chu and D. A. Telnov, Phys. Rep. **390**, 1 (2004).
[29] H. Sambe, Phys. Rev. A **7**, 2203 (1973).
[30] T.-S. Ho, K. Wang, and S.-I. Chu, Phys. Rev. A **33**, 1798 (1986).
[31] K. Ono, D. G. Austing, Y. Tokura, and S. Tarucha, Science **297**, 1313 (2002).
[32] F. Forster, M. Mühlbacher, D. Schuh, W. Wegscheider, and S. Ludwig, Phys. Rev. B **91**, 195417 (2015).
[33] A. G. Redfield, IBM J. Res. Develop. **1**, 19 (1957).
[34] K. Blum, *Density Matrix Theory and Applications*, 2nd ed. (Springer, New York, 1996).
[35] R. Hussein and S. Kohler, Phys. Rev. B **89**, 205424 (2014).
[36] S. A. Gurvitz and Ya. S. Prager, Phys. Rev. B **53**, 15932 (1996).
[37] H.-P. Breuer and F. Petruccione, *Theory of Open Quantum Systems* (Oxford University Press, Oxford, 2003).
[38] T. Brandes, Phys. Rep. **408**, 315 (2005).
[39] U. Weiss and M. Wollensak, Phys. Rev. Lett. **62**, 1663 (1989).
[40] U. Peskin and N. Moiseyev, J. Chem. Phys. **99**, 4590 (1993).
[41] L. D. Landau, Phys. Z. Sowjetunion **2**, 46 (1932).
[42] C. Zener, Proc. R. Soc. London A **137**, 696 (1932).
[43] E. C. G. Stueckelberg, Helv. Phys. Acta **5**, 369 (1932).
[44] E. Majorana, Nuovo Cimento **9**, 43 (1932).
[45] L. Arrachea and M. Moskalets, Phys. Rev. B **74**, 245322 (2006).
[46] A. M. Satanin, M. V. Denisenko, A. I. Gelman, and F. Nori, Phys. Rev. B **90**, 104516 (2014).

[47] F. Grossmann, T. Dittrich, P. Jung, and P. Hänggi, Phys. Rev. Lett. **67**, 516 (1991).
[48] F. Großmann and P. Hänggi, Europhys. Lett. **18**, 571 (1992).
[49] H. G. Schuster, *Deterministic Chaos: An Introduction* (VCH Verlagsgesellschaft, Weinheim, 1995).
[50] J. H. Shirley, Phys. Rev. **138**, B979 (1965).
[51] H. Risken, *The Fokker-Planck Equation*, Springer Series in Synergetics Vol. 18, 2nd ed. (Springer, Berlin, 1989).
[52] P. Jung, Phys. Rep. **234**, 175 (1993).

9 Summary and conclusion

In this thesis, I presented the results of several electron transport experiments carried out in a driven few-electron double quantum dot (DQD) with focus on two different aspects. On one hand, I investigated the influence of a strongly inhomogeneous magnetic field across the DQD and the dynamic nuclear spin polarization (DNSP) in such a sample. On the other hand, I probed the coherent Landau-Zener-Stückelberg-Majorana dynamics of a two-electron charge qubit and presented a detailed analysis of the interference patterns providing access to the decoherence mechanisms. In the following, I will give a summary of the results of the experiments and connect them to the results of other recent experiments in this field.

The spin in quantum dots has been used to demonstrate a high degree of quantum control which is one of the key requirements for quantum information applications [6]. As an example, coherent single spin manipulation by electron dipole spin resonance (EDSR) has been demonstrated [33, 34, 36]. Various techniques to employ the time-dependent magnetic fields to drive the electron spins in QDs were developed [33, 34, 36]. As a globally applied ac magnetic field is unfavourable in a low-temperature setup due to heating effects and mechanical instabilities, most techniques aim to employ a (real or effective) magnetic field modulated locally at the QD site. Three successfully applied techniques are the usage of an Oersted field of a current through a wire near the QD [33], the effective field created by the spin-orbit interaction of a moving electron [34], and the periodic driving of an electron through a local magnetic field gradient provided by an on-chip magnet [36]. The third technique has been of recent interest. As an advantage, on-chip magnets can provide different static magnetic field values at the site of each individual QD facilitating to address each qubit individually even when they are both subject to the driving [27, 35, 78]. In the case of DQDs, two-electron spin states, i.e. singlet and triplet states, are of interest for qubit applications [19, 20, 79]. Here, the difference of the magnetic field at the sites of the two QD is essential, since it provides the coupling between the involved singlets and triplets [16]. In GaAs based DQDs, the nuclear hyperfine interaction of the localized electron with $\sim 10^6$ nuclei provides an effective magnetic field, the Overhauser field, whose thermal fluctuations are strong enough to provide a field difference of a few mT. In addition, we can harness the inhomogeneous field of a nanomagnet to enhance the singlet-triplet coupling, especially useful in materials whose main isotopes do not have a nuclear spin, such as SiGe or carbon based materials.

Previous realizations of on-chip magnet are large multi-domain magnets with laterial dimensions of several microns on top of the QDs separated by an insulating layer [27, 36, 78, 80, 81]. This micromagnet has the advantages of relatively easy fabrication and a potentially strong magnetic field, but the disadvantages of multiple domains which makes it sensitive to changes in the external magnetic field[(1)] leading to a small uncontrollable magnetization at small external magntic fields. The concept used in this thesis utilizes the field of much smaller bar-shaped nanomagnets whose dimensions of $\sim 2\,\mu\text{m} \times 100\,\text{nm} \times 50\,\text{nm}$ lead to a single magnetic domain even at no external magnetic field. The initial idea of the preceding PhD thesis by G. Petersen (ref. [8]), where one single-domain nanomagnet on top of a DQD gate provided the inhomogeneous field, was refined: First, we incorporated the nanomagnets directly into the existing layout of the gates defining the DQD by replacing one the gold gates by a cobalt gate allowing for a stronger field at the site of the QD. Second, we added a second nanomagnet of different width which leads to a different coercive field compared to the other magnet. This allowed us to access two different magnetic field regimes with very different singlet-triplet coupling constants, given by the parallel and the anti-parallel magnetization configuration of the two magnets, in the same sample. In the experiment, we characterized

[(1)] in the field regime where not all domains are aligned, i.e. small external fields

the magnetic field distribution of our nanomagnets by EDSR, which gives direct access to the size of the magnetic field inside each quantum dot, and measurement of the direct current through the DQD which in the given regime of Pauli spin blockade is highly dependent on the coupling between the singlet and triplet states. As a the main result, we found that our novel approach to integrate the nanomagnets as gates into the device was successful. It was possible to reverse the magnet polarizations one-by-one by sweeping an external magnetic field and to directly measure the coercive fields: As each switching event modified the local magnetic field distribution, it gave rise to a distinct current jump in a dc transport measurement. In a radio frequency EDSR experiment the sudden modification of the local magnetic field distribution generated a shift of the resonance frequency. We also found a distinct individual resonance for each dot and demonstrated that the disadvantage of a somewhat smaller field gradient due to the smaller size of the single-domain magnet compared to the conventional multi-domain magnet can be compensated by using multiple magnets. Overall, we managed to achieve a good agreement with numerically calculated field distributions. The experiment carried out establishes a high degree of control of the overall field distribution for future experiments. By designing the inhomogeneous field and thus the singlet-triplet coupling strength, it is now possible to access the regime of qubit-clock speeds much higher than the one given by the natural Overhauser field. Since the field gradient across the DQD provided by the nanomagnets (we found up to 40 mT) can be more than a magnitude larger than the one provided by the Overhauser field in GaAs, the nanomagnets provide a more robust coupling mechanism: as the fluctuations of the Overhauser field, which are a major dephasing source in GaAs spin qubits [16, 21, 82], become just small perturbations to a now much larger gradient, this coupling method should also prove beneficial in the context of spin based quantum computing in reducing dephasing.

The Overhauser contribution is significant when the nuclear spins are polarized, as a fully polarized nuclear bath corresponds to a magnetic field of around 6 T[(2)]. An elegant way to polarize the nuclear spins in a transport experiment is dynamic nuclear spin polarization (DNSP) by a current through a DQD in the Pauli spin blockade regime. As the spin blockade can be lifted by the hyperfine interaction, semi-classically described as flip-flop process between the electron and the nuclear spin, a net-polarization of the nuclear spin bath can be build up [17, 30, 49]. In this case, the polarization rate is on the one hand strongly dependent on the current and hence the electronic spectrum of the DQD. On the other hand, the polarization built up modifies the electronic spectrum itself, such that a very complex dynamics arises even when only considering the semi-classical description of the nuclear spins as Overhauser field.

For this thesis, I employed a polarization technique during which the external magnetic field is slowly ramped up after locking the DQD onto a fixed point to a DQD with a strong inhomogeneous field provided by two single-domain nanomagnets (see above). This technique was developed during the preceding PhD thesis by G. Petersen (ref. [8]) and enables high nuclear spin polarizations exceeding 50% which is by far the highest value reached in lateral DQDs [30]. Measuring the leakage current through the DQD in Pauli spin blockade, I found a remarkably complex current behaviour during magnetic field sweeps. In particular, the statistical reoccurrence of four distinct patterns in the current establishes the existence of multiple fixed points, one of which is always occupied as long as dynamical polarization is maintained. While at nominally the same starting conditions all of the fixed points were reached with roughly equal probabilities, the fixed points proved remarkably stable during the magnetic field sweeps. In addition, I measured the Overhauser field by means of EDSR during its free decay after the buildup. The EDSR measurements reveal long decay times of the nuclear spin polarization, its stability being enhanced by the strongly inhomogeneous magnetic field distribution generated by two single-domain nanomagnets. The nuclear polarization was even further stabilized during the experiment by polarizing for an extended time. I found that this leads to an extended area of polarization around the DQD. In addition, the EDSR measurements confirmed that the individual fixed points differed substantially by their polarizations and, remarkably, dynamics of the nuclear spins. The studies demonstrate that the existence of several fixed points in dynamical nuclear spin polarization

[(2)] See sec. 6.2.1.

complicates the desired control of electron and nuclear spins in coupled quantum dots. However, the experiments present an advance in the understanding of hyperfine induced dynamics in nanoelectronic circuits. For future studies, an independent access to the nuclear spins could be desirable. For example by introducing NMR techniques, one could influence the dynamical buildup of polarization and probe the stability of the system. The full understanding and the control of nuclear spins in electric nanocircuits, however, remains a desired and challenging goal.

A different approach to qubit physics in DQDs explored in this thesis is the charge qubit [71, 83]. Here, the two qubit states are given by different charge configurations of the DQD, for instance a DQD charged by a single electron which is localized in the left dot (first state) or in the right dot (second state) [72] or, as realised in this thesis, two singlet states of a two-electron DQD. Unlike for the singlet-triplet spin qubit, the coupling of the qubit states can be well defined and controlled by gate voltages during the experiment, as it is given by the tunnel coupling between the two dots. This renders it a qubit system interesting for applications, since it is relatively easy to define qubits with couplings in the order of a few GHz, hence fast clock speeds. However, the charge qubit is also more prone to noise from the environment, as fluctuating charges in the vicinity of the DQD deform the confinement potential and hence modify the qubit [74], and the charge states couple to bulk phonons [73]. These interactions make it experimentally significantly more difficult to achieve a high degree of quantum control comparable to spin qubits. In fact, even the accurate determination of the coherence time for a single charge qubit (T_2) had not been achieved before this thesis, as past experiments only considered the dephasing of a (time) ensemble of qubits (T_2^*) which includes inhomogeneous line broadening of the qubit's states [71, 72]. In principle, the influence of inhomogeneous line broadening can be compensated by echo techniques known from NMR imaging [70] and successfully applied to spin qubits [9, 19]. The relatively short coherence times in charge qubits, however, demand very fast pulsing capabilities and echoes sequences have not yet been successfully applied to charge qubits in GaAs. In this thesis, I presented a new and very general method applicable to any qubit system to nevertheless quantify the influence of inhomogeneous broadening and determine the coherence time for a single qubit experiment. By driving the biased qubit with a monochromatic drive repeatedly through its avoided crossing and measuring the steady state current of the qubit, I measured Landau-Zener-Stückelberg-Majorana (LZSM) interference [10, 59–62]. In contrast to sophisticated echo sequences, only a simple sinusoidal driving is needed for this method (in addition to the dc voltage needed here for the qubit read-out). The resulting interference patterns contain the coherence of the qubit, but the coherence parameters are not accessible in a straightforward manner. However, the initial complexity of the interference pattern can be significantly reduced by a two-dimensional Fourier analysis [76]. Furthermore, we collaborated with S. Kohler from Instituto de Ciencia de Materiales de Madrid to develop a complete system-bath model analyzed with Floquet transport theory and achieved a good quantitative agreement between experiment and theory which allowed us to trace the origins of inhomogeneous broadening and decoherence. We determined the individual values of T_2^* and T_2 of the qubit and find that our two-electron charge qubit is affected by slow charge noise limiting T_2^* to $\simeq 0.2\,\mathrm{ns}$ but a much longer coherence time of $T_2 \simeq 0.2\,\mu\mathrm{s}$ limited by the electron-phonon interaction even at cryogenic temperatures of 20 mK.

In a second step, we extended the previous LZSM technique of monochromatic driving (with a single frequency) to bichromatic driving (with two concurrent frequencies) and also extended the theory to capture the more complex driving. As before, we measured the dc current in the steady state and explored LZSM interference as a function of the DQD detuning and the driving amplitude. The interference patterns in our measurements and their Fourier transforms exhibit characteristic symmetry properties which were confirmed by our model's predictions: bichromatic driving with commensurable frequencies causes a reduction of the symmetry compared to the monochromatic case. Interestingly, for driving with incommensurable frequencies the full reflection symmetries observed for monochromatic driving are retained, although the interference patterns are more complex. In the case of commensurable frequencies, the interference patterns are highly sensitive to the phase dependence which can be harnessed to accurately calibrate phase differences caused by frequency dispersion. This is an important result for quantum measurements and

related applications where accurate knowledge of phase relations is crucial.

For future experiments (aside from transfering this technique to other qubit systems), the LZSM technique established here offers a variety of possibilities. For the charge qubit, one could further explore the electron-phonon interaction by introducing a quantum point contact as a tunable non-thermal phonon source [25, 73] and investigate its impact on the coherent dynamics. In the same spirit, one could simulate additional charge noise by applying noise to the gate voltages defining the confinement potential of the DQD and study the influence of noise in the coupling and the detuning parameter separately. Furthermore, one could combine the charge and spin qubit concepts by passing subsequent avoided crossings, e.g. a first one formed by two singlets and a second one formed by one singlet and one triplet, in the electron term scheme. The difference in coupling strength between the spin and charge states leading to different clock speeds of the qubits can be partly remedied by enhancing the coupling of the spin states by the inhomogeneous field of on-chip nanomagnets as discussed above.

A Calculations

A.1 Diagonalization of a two-level Hamiltonian

The Hamiltonian for a two-level system is given by

$$H = E_1 |1\rangle\langle 1| + t|1\rangle\langle 2| + t^* |2\rangle\langle 1| + E_2 |2\rangle\langle 2|.$$

Here, t is the coupling constant and E_1 and E_2 are the eigenenergies for the uncoupled system ($t = 0$). We choose the representation $|1\rangle \doteq \begin{pmatrix}1\\0\end{pmatrix}$ and $|2\rangle \doteq \begin{pmatrix}0\\1\end{pmatrix}$ and a real coupling constant $t = t^*$ to explicitly write the Hamiltonian as 2x2 matrix,

$$H \doteq \begin{pmatrix}E_1 & t\\ t & E_2\end{pmatrix}.$$

We will now carry out the analytic diagonalization of the Hamiltonian to obtain its eigenenergies and eigenstates. We start by calculating

$$\det(H - \mathbb{1}\varepsilon_\pm) = \begin{vmatrix}E_1 - \varepsilon_\pm & t\\ t & E_2 - \varepsilon_\pm\end{vmatrix} = \varepsilon_\pm^2 + \varepsilon_\pm(E_1 + E_2) + E_1E_2 - t^2 = 0,$$

which directly yields the eigenenergy

$$\varepsilon_\pm = \frac{1}{2}\left((E_1 + E_2) \pm \sqrt{(E_1 - E_2)^2 + 4t^2}\right). \tag{A.1}$$

For the eigenstate belonging to ε_+, we choose the first equation of the two linear dependent rows of the matrix,

$$\begin{pmatrix}E_1 - \varepsilon_+ & t\\ t & E_2 - \varepsilon_+\end{pmatrix}\begin{pmatrix}\alpha\\ \beta\end{pmatrix} = 0 \quad \Leftrightarrow \quad (E_1 - \varepsilon_+)\alpha + t\beta = 0, \quad \Rightarrow \quad \frac{\beta}{\alpha} = \frac{\varepsilon_+ - E_1}{t}$$

and further choose α and β to be real. Since we also want the eigenstate to be normalized, i.e. $\alpha^2 + \beta^2 = 1$, we choose $\alpha = \cos\theta$ and $\beta = \sin\theta$ which readily fulfils this condition. To determine θ, we just use the previous expression and read

$$\frac{\beta}{\alpha} = \tan\theta = \frac{\varepsilon_+ - E_1}{t}, \quad \theta \in \left[0, \frac{\pi}{2}\right].$$

We can find the useful representation of 2θ using $\Delta = E_1 - E_2$ and $\Sigma = E_1 + E_2$ with

$$\begin{aligned}
\tan(2\theta) = \frac{2}{\cot\theta - \tan\theta} &= \frac{2t(\varepsilon_+ - E_1)}{t^2 - (\varepsilon_+ - E_1)^2} = 2t \cdot \frac{\varepsilon_+ - E_1}{t^2 - \varepsilon_+^2 + 2E_1\varepsilon_+ - E_1^2}\\
&= 2t \cdot \frac{\varepsilon_+ - \frac{1}{2}(\Delta + \Sigma)}{t^2 - \frac{1}{4}\left[\Sigma^2 + 2\Sigma(2\varepsilon_+ - \Sigma) + \Delta^2 + 4t^2\right] + (\Delta + \Sigma)\varepsilon_+ - \frac{1}{4}(\Delta + \Sigma)^2}\\
&= 2t \cdot \frac{\varepsilon_+ - \frac{1}{2}(\Delta + \Sigma)}{-\frac{1}{4}\left[2\Sigma\Delta + 2\Delta^2 - 4\Delta\varepsilon_+\right]}\\
&= 2t \cdot \frac{\varepsilon_+ - \frac{1}{2}(\Delta + \Sigma)}{\Delta\left[\varepsilon_+ - \frac{1}{2}(\Delta + \Sigma)\right]}\\
&= \frac{2t}{\Delta}
\end{aligned} \tag{A.2}$$

Since H is a Hermitian matrix, its eigenvectors for distinct eigenvalues are orthogonal to each other, so we can just construct the eigenstate for the eigenenergy ε_- by satisfying

$$\begin{pmatrix}\cos\theta\\ \sin\theta\end{pmatrix}\cdot\begin{pmatrix}\gamma\\ \delta\end{pmatrix}=0.$$

We easily see that $\gamma=-\sin\theta$ and $\delta=\cos\theta$ is a solution with the desired normalization to unity. By using the basis representation $|1\rangle\doteq\begin{pmatrix}1\\0\end{pmatrix}$ and $|2\rangle\doteq\begin{pmatrix}0\\1\end{pmatrix}$, we end up with the final result for the eigenstates

$$\begin{aligned}|+\rangle&=\cos\theta\,|1\rangle+\sin\theta\,|2\rangle\,,\\ |-\rangle&=-\sin\theta\,|1\rangle+\cos\theta\,|2\rangle\,.\end{aligned}\tag{A.3}$$

Example: H_{el} We apply the results calculated above to find the eigenstates and eigenenergies of H_{el} (2.7) of the main text. There, we have

$$E_1=0,\quad E_2=-\varepsilon,\quad t=t_c/2,\quad |1\rangle=|S_{11}\rangle\,,\quad |2\rangle=|S_{20}\rangle\,.$$

Using (A.1) and (A.3), we find

$$\begin{aligned}|S_+\rangle&=\sin\theta\,|S_{20}\rangle+\cos\theta\,|S_{11}\rangle\,,\quad \varepsilon_+=\frac{1}{2}\left(-\epsilon+\sqrt{\varepsilon^2+t_c^2}\right),\\ |S_-\rangle&=\cos\theta\,|S_{20}\rangle-\sin\theta\,|S_{11}\rangle\,,\quad \varepsilon_-=\frac{1}{2}\left(-\epsilon-\sqrt{\varepsilon^2+t_c^2}\right),\end{aligned}$$

with $\tan(2\theta)=t_c/\varepsilon$ (A.2).

A.2 Two spin-1/2 particles in a static magnetic field

In this section, we will sketch the calculation of the Hamiltonian of two spins in an inhomogeneous magnetic field. We use the expressions $|\uparrow\rangle$ for a spin-up state, and $|\downarrow\rangle$ for a spin-down state in Dirac notation. We choose the $|\uparrow\rangle\doteq\begin{pmatrix}1\\0\end{pmatrix}$ and $|\downarrow\rangle\doteq\begin{pmatrix}0\\1\end{pmatrix}$ representation to describe a single spin-1/2 particle. In this basis, the spin operator for a single particle is given by $\mathbf{s_i}=\frac{\hbar}{2}\begin{pmatrix}\sigma_x & \sigma_y & \sigma_z\end{pmatrix}^T$, where σ_i are the Pauli matrices

$$\sigma_x=\begin{pmatrix}0&1\\1&0\end{pmatrix},\quad \sigma_y=\begin{pmatrix}0&-\mathrm{i}\\ \mathrm{i}&0\end{pmatrix},\quad \sigma_z=\begin{pmatrix}1&0\\0&-1\end{pmatrix}.\tag{A.4}$$

Two-particle spin states are mathematically described by the tensor product of the single spin operators acting on the subspace of a single spin; e.g.

$$|\uparrow\uparrow\rangle\equiv|\uparrow\rangle\otimes|\uparrow\rangle\doteq\begin{pmatrix}1\\0\end{pmatrix}\otimes\begin{pmatrix}1\\0\end{pmatrix}=\begin{pmatrix}1&0&0&0\end{pmatrix}^T\equiv\mathbf{e_1}.$$

Similarly, we find the representation of the other basis states $|\uparrow\downarrow\rangle\doteq\mathbf{e_2}$, $|\downarrow\uparrow\rangle\doteq\mathbf{e_3}$, and $|\downarrow\downarrow\rangle\doteq\mathbf{e_4}$. In this basis, we find the single spin operators by calculating the tensor product with the 2x2 unit matrix in the correct

order, e.g. $s_{1x} = \frac{\hbar}{2}\sigma_x \otimes \mathbb{1}$ and $s_{2x} = \mathbb{1} \otimes \frac{\hbar}{2}\sigma_x$. Explicitly, this yields

$$\begin{aligned} s_{1x} &= \frac{\hbar}{2}\begin{pmatrix} 0 & 0 & 1 & 0 \\ 0 & 0 & 0 & 1 \\ 1 & 0 & 0 & 0 \\ 0 & 1 & 0 & 0 \end{pmatrix}, \quad s_{1y} = \frac{\hbar}{2}\begin{pmatrix} 0 & 0 & -i & 0 \\ 0 & 0 & 0 & -i \\ i & 0 & 0 & 0 \\ 0 & i & 0 & 0 \end{pmatrix}, \quad s_{1z} = \frac{\hbar}{2}\begin{pmatrix} 1 & 0 & 0 & 0 \\ 0 & 1 & 0 & 0 \\ 0 & 0 & -1 & 0 \\ 0 & 0 & 0 & -1 \end{pmatrix}, \\ s_{2x} &= \frac{\hbar}{2}\begin{pmatrix} 0 & 1 & 0 & 0 \\ 1 & 0 & 0 & 0 \\ 0 & 0 & 0 & 1 \\ 0 & 0 & 1 & 0 \end{pmatrix}, \quad s_{2y} = \frac{\hbar}{2}\begin{pmatrix} 0 & -i & 0 & 0 \\ i & 0 & 0 & 0 \\ 0 & 0 & 0 & -i \\ 0 & 0 & i & 0 \end{pmatrix}, \quad s_{2z} = \frac{\hbar}{2}\begin{pmatrix} 1 & 0 & 0 & 0 \\ 0 & -1 & 0 & 0 \\ 0 & 0 & 1 & 0 \\ 0 & 0 & 0 & -1 \end{pmatrix}. \end{aligned} \tag{A.5}$$

We can also calculate $\mathbf{s}_1^2 = s_{1x}^2 + s_{1y}^2 + s_{1z}^2 = \mathbf{s}_2^2 = \frac{3}{4}\hbar^2\mathbb{1}$. Since s_{iz} and $\mathbf{s}_i^2$ are diagonal in this basis, we find that the single-spin basis states are the eigenstates of these operators. However, if we want to describe our system in terms of the total spin, we need to look at the eigenvectors of the total spin operator, $\mathbf{s}^2 = (\mathbf{s}_1 + \mathbf{s}_2)^2 = \mathbf{s}_1^2 + \mathbf{s}_2^2 + 2(s_{1x}s_{2x} + s_{1y}s_{2y} + s_{1z}s_{2z})$. By using the matrices of (A.5), we obtain

$$\mathbf{s}^2 = \hbar^2\begin{pmatrix} 2 & 0 & 0 & 0 \\ 0 & 1 & 1 & 0 \\ 0 & 1 & 1 & 0 \\ 0 & 0 & 0 & 2 \end{pmatrix},$$

which is obviously not diagonal in the single-spin basis. The eigenvalues and -vectors of this matrix are

$$\begin{aligned} |T_+\rangle = |\uparrow\uparrow\rangle &\doteq \begin{pmatrix} 1 & 0 & 0 & 0 \end{pmatrix}^T && s = 1, m = 1; \\ |T_0\rangle = \frac{1}{\sqrt{2}}(|\uparrow\downarrow\rangle + |\downarrow\uparrow\rangle) &\doteq \frac{1}{\sqrt{2}}\begin{pmatrix} 0 & 1 & 1 & 0 \end{pmatrix}^T && s = 1, m = 0; \\ |T_-\rangle = |\downarrow\downarrow\rangle &\doteq \begin{pmatrix} 0 & 0 & 0 & 1 \end{pmatrix}^T && s = 1, m = -1; \\ |S\rangle = \frac{1}{\sqrt{2}}(|\uparrow\downarrow\rangle - |\downarrow\uparrow\rangle) &\doteq \frac{1}{\sqrt{2}}\begin{pmatrix} 0 & 1 & -1 & 0 \end{pmatrix}^T && s = 0, m = 0. \end{aligned}$$

Here, $s(s+1)\hbar^2$ is the eigenvalue of $\mathbf{s}^2$, and $m\hbar$ is the eigenvalue of s_z. As discussed in the main text in section 2.1.3, these states are called singlet and triplet states of the system, which we want to choose for our new basis.

The Hamiltonian for two spin-1/2 particles inside an arbitrary magnetic field is given by

$$H_{\text{mag}} = \frac{g\mu_B}{\hbar}(\mathbf{B_1}\cdot\mathbf{s_1} + \mathbf{B_2}\cdot\mathbf{s_2}) = \frac{g\mu_B}{\hbar}\left[\overline{\mathbf{B}}\cdot(\mathbf{s_1} + \mathbf{s_2}) + \Delta\mathbf{B}\cdot(\mathbf{s_1} - \mathbf{s_2})\right],$$

where we defined $\overline{\mathbf{B}} = (\mathbf{B_1} + \mathbf{B_2})/2$ and $\Delta\mathbf{B} = (\mathbf{B_1} - \mathbf{B_2})/2$ and used the g-factor g and the Bohr magneton μ_B. To calculate this Hamiltonian, for which we know the representation in the single-spin basis, in the singlet-triplet basis, we use the transformation matrix U with $U_{mn} = \langle a_m | b_n \rangle$, where $|a_m\rangle$ are the single-spin basis states represented by $\mathbf{e}_m$ and $|b_n\rangle$ are the total-spin basis states in the order $(|T_+\rangle, |T_0\rangle, |T_-\rangle, |S\rangle)$. This yields

$$U \doteq \begin{pmatrix} 1 & 0 & 0 & 0 \\ 0 & 1/\sqrt{2} & 0 & 1/\sqrt{2} \\ 0 & 1/\sqrt{2} & 0 & -1/\sqrt{2} \\ 0 & 0 & 1 & 0 \end{pmatrix}.$$

We then use the operator representation of (A.5) to write H_{mag} in the single-spin basis and transform it to

the singlet-triplet basis by using U. We get the final result

$$H_{\text{mag}} = U^\dagger H_{\text{mag}} U \doteq g\mu_B \begin{pmatrix} \overline{B}_z & \overline{B}_-/\sqrt{2} & 0 & -\Delta B_-/\sqrt{2} \\ \overline{B}_+/\sqrt{2} & 0 & \overline{B}_-/\sqrt{2} & \Delta B_z \\ 0 & \overline{B}_+/\sqrt{2} & -\overline{B}_z & \Delta B_+/\sqrt{2} \\ -\Delta B_+/\sqrt{2} & \Delta B_z & \Delta B_-/\sqrt{2} & 0 \end{pmatrix},$$

where we used the abbreviations $\overline{B}_\pm = \overline{B}_x \pm i\overline{B}_y$ and $\Delta B_\pm = \Delta B_x \pm i\Delta B_y$.

A.3 A single spin-1/2 particle in a time-dependent magnetic field

A.3.1 Ideal driving

We will now consider a single spin-1/2 particle in a time-dependent magnetic field,

$$\mathbf{B}(t) = \mathbf{B}_{\text{ext}} + \mathbf{B}_{\text{ac}}(t) = B_z \begin{pmatrix} 0 \\ 0 \\ 1 \end{pmatrix} + B_0 \begin{pmatrix} \cos\omega t \\ \sin\omega t \\ 0 \end{pmatrix}. \tag{A.7}$$

The Hamiltonian of the system is therefore given by

$$H(t) = \frac{g\mu_B}{\hbar} \mathbf{s} \cdot \mathbf{B}(t) = \omega_z s_z + \omega_0 (\cos(\omega t) s_x + \sin(\omega t) s_y), \tag{A.8}$$

where $\mathbf{s}$ is the spin operator of a single spin with its projections s_x, s_y, s_z and we introduced the abbreviations $\omega_i = g\mu_B B_i/\hbar$. The solution of the Schrödinger equation,

$$i\hbar \left|\psi(t)\right\rangle = H(t) \left|\psi(t)\right\rangle,$$

becomes simplest when going to the rotating frame, where $H(t) \to \tilde{H}$ is no longer time-dependent. With the unitary rotational operator $R(t) = \exp(i\omega t s_z/\hbar)$, which describes a time-dependent rotation around the z-axis with the frequency ω [15, p. 698], we transform the Schrödinger equation to

$$\begin{aligned} i\hbar\partial_t \left|\tilde{\psi}(t)\right\rangle &= i\hbar\partial_t \left(R(t) \left|\psi(t)\right\rangle\right) \\ &= i\hbar R(t)\partial_t \left|\psi(t)\right\rangle + i\hbar\partial_t(R(t)) \left|\psi(t)\right\rangle \\ &= R(t)H(t) \left|\psi(t)\right\rangle - \omega s_z R(t) \left|\psi(t)\right\rangle \\ &= \left[R(t)H(t)R^\dagger(t) - \omega s_z\right] R(t) \left|\psi(t)\right\rangle \\ &\equiv \tilde{H} \left|\tilde{\psi}(t)\right\rangle \end{aligned}$$

Expressing $H(t)$ and $R(t)$ in the Cartesian basis with the Pauli matrices (A.4), we find

$$H(t) \doteq \frac{\hbar}{2} \begin{pmatrix} \omega_z & \omega_0 \exp(-i\omega t) \\ \omega_0 \exp(i\omega t) & -\omega_z \end{pmatrix}, \quad R(t) \doteq \begin{pmatrix} \exp(i\omega t/2) & 0 \\ 0 & \exp(-i\omega t/2) \end{pmatrix},$$

where we used $\exp(a\sigma_z) = \cos(a)\,\mathbb{1} + i\sin(a)\,\sigma_z$ to calculate the representation of $R(t)$ [15, p. 985]. In total, this yields indeed a time-independent $\tilde{H}$,

$$\tilde{H} = R(t)H(t)R^\dagger(t) - \omega s_z \doteq \frac{\hbar}{2} \begin{pmatrix} \Delta\omega & \omega_0 \\ \omega_0 & -\Delta\omega \end{pmatrix}, \tag{A.14}$$

with $\Delta\omega = \omega_z - \omega$, which is a standard Rabi problem [15, p. 413]. We find the eigenenergies and eigenstates according to (A.1) and (A.3)

$$\begin{aligned}
\left|\tilde{\phi}_+\right\rangle &= \cos\theta\,|\uparrow\rangle + \sin\theta\,|\downarrow\rangle, \qquad E_+ = \frac{\hbar}{2}\sqrt{(\Delta\omega)^2+\omega_0^2} \\
\left|\tilde{\phi}_-\right\rangle &= -\sin\theta\,|\uparrow\rangle + \cos\theta\,|\downarrow\rangle, \qquad E_- = -\frac{\hbar}{2}\sqrt{(\Delta\omega)^2+\omega_0^2}
\end{aligned}$$

with $\tan 2\theta = \omega_0/\Delta\omega$ (A.2). From these eigenstates of $\tilde{H}$, we can construct the time-dependent solution of the Schrödinger equation,

$$\left|\tilde{\psi}(t)\right\rangle = \sum_{n\in\{\pm\}} \exp(-iE_n t/\hbar) c_n(t=0) \left|\tilde{\phi}_n\right\rangle$$

We rewrite the solution in the basis of $|\uparrow\rangle$ and $|\downarrow\rangle$, and find

$$\begin{aligned}
\left|\tilde{\psi}(t)\right\rangle &= \left[\exp(-iE_+ t/\hbar)c_+\cos\theta - \exp(-iE_- t/\hbar)c_-\sin\theta\right]|\uparrow\rangle + \\
&\quad \left[\exp(-iE_+ t/\hbar)c_+\sin\theta + \exp(-iE_- t/\hbar)c_-\cos\theta\right]|\downarrow\rangle \\
&= \tilde{c}_\uparrow(t)\,|\uparrow\rangle + \tilde{c}_\downarrow(t)\,|\downarrow\rangle,
\end{aligned}$$

where $c_\pm$ depend on the boundary conditions at $t=0$. Finally, we can transform back to our stationary frame and get the time-dependent solution

$$\begin{aligned}
\left|\psi(t)\right\rangle &= R^\dagger(t)\left|\tilde{\psi}(t)\right\rangle \\
&= \exp(-i\omega t/2)\tilde{c}_\uparrow(t)\,|\uparrow\rangle + \exp(i\omega t/2)\tilde{c}_\downarrow(t)\,|\downarrow\rangle.
\end{aligned}$$

We are now interested in the dynamics of the system which is at $t=0$ in a pure state, in our case $|\uparrow\rangle$. For this boundary condition, we determine $c_\pm$

$$\begin{aligned}
\left|\psi(0)\right\rangle &= \tilde{c}_\uparrow(0)\,|\uparrow\rangle + \tilde{c}_\downarrow(0)\,|\downarrow\rangle \\
&= \underbrace{[c_+\cos\theta - c_-\sin\theta]}_{1}\,|\uparrow\rangle + \underbrace{[c_+\sin\theta + c_-\cos\theta]}_{0}\,|\downarrow\rangle \\
&\Rightarrow \quad c_+ = \cos\theta \quad \wedge \quad c_- = -\sin\theta.
\end{aligned}$$

We now calculate the projection of the spin direction $|\downarrow\rangle$, which is opposite to our initial state $|\uparrow\rangle$, and hence describes the probability to measure a spin-flip at time t.

$$\begin{aligned}
\left|\langle\downarrow|\psi(t)\rangle\right|^2 &= \left|\langle\downarrow|\tilde{\psi}(t)\rangle\right|^2 \\
&= \left|\exp(-iE_+ t/\hbar)\cos\theta\sin\theta - \exp(-iE_- t/\hbar)\sin\theta\cos\theta\right|^2 \\
&= \left|\cos\theta\sin\theta\left[\exp(-iE_+ t/\hbar) - \exp(-iE_- t/\hbar)\right]\right|^2 \\
&= \frac{1}{4}\sin^2 2\theta\left|\left[1-\exp(-i(E_+-E_-)t/\hbar)\right]\right|^2 \\
&= \frac{1}{4}\sin^2 2\theta\left[(1-\cos(E_+-E_-)t/\hbar)^2 + \sin^2(E_+-E_-)t/\hbar\right] \\
&= \frac{1}{2}\sin^2 2\theta\,[1-\cos(E_+-E_-)t/\hbar] \\
&= \sin^2 2\theta\sin(E_+-E_-)t/2\hbar
\end{aligned}$$

By using the explicit E_+ and E_- and using $2\theta = \arctan(\omega_0/\Delta\omega)$, we obtain Rabi's formula as the final result,

$$\left|\langle\downarrow|\psi(t)\rangle\right|^2 = \frac{\omega_0^2}{\omega_0^2+\Delta\omega^2}\sin^2\left(\frac{1}{2}\sqrt{\omega_0^2+\Delta\omega^2}\,t\right).$$

A.3.2 Realistic driving

So far, we discussed the case that $\mathbf{B}_{\mathrm{ac}}(t)$ describes a rotation around the z-axis while its absolute value remains independent of t. In our experiment, we provide an inhomogeneous magnetic field $\mathbf{B} = \mathbf{B}(\mathbf{r})$ and move the electron through the field gradient, i.e. $\mathbf{r} = \mathbf{r}(0) + \Delta\mathbf{r}(t)$. This is realised by applying a voltage $V_{\sim}(t) = V_0 \sin\omega t$ at one of the quantum dot gates. The total magnetic field obtained by Taylor expansion is given by

$$\mathbf{B}(t) = \mathbf{B}_{\mathrm{ext}}(\mathbf{r}(0) + \Delta\mathbf{r}(t)) = \mathbf{B}_{\mathrm{ext}}(\mathbf{r}(0)) + [\mathbb{J}\mathbf{B}(\mathbf{r})]|_{\mathbf{r}=\mathbf{r}(0)}\Delta\mathbf{r} + \mathcal{O}(\Delta\mathbf{r}^2),$$

where $\mathbb{J}$ is the Jacobian matrix [84, p. 535]. We can identify the first term as the static magnetic field and second term as the driving field. We explicitly write the driving field as

$$\mathbb{J}\mathbf{B}(\mathbf{r})|_{\mathbf{r}=\mathbf{r}(0)}\Delta\mathbf{r} = \begin{pmatrix} \partial_x B_x \Delta r_x + \partial_z B_x \Delta r_z \\ \partial_x B_y \Delta r_x + \partial_z B_y \Delta r_z \\ \partial_x B_z \Delta r_x + \partial_z B_z \Delta r_z \end{pmatrix} = V_0 \sin(\omega t) \begin{pmatrix} \partial_x B_x \beta_x + \partial_z B_x \beta_z \\ \partial_x B_y \beta_x + \partial_z B_y \beta_z \\ \partial_x B_z \beta_x + \partial_z B_z \beta_z \end{pmatrix} \equiv \sin(\omega t) \begin{pmatrix} \Delta B_x \\ \Delta B_y \\ \Delta B_z \end{pmatrix},$$

where we used that movement of the electrons $\Delta\mathbf{r}$ is restricted to the plane of the 2DES (x,z-plane) and that $\Delta\mathbf{r} = \boldsymbol{\beta} V_0 \sin(\omega t)$, where we assumed an anisotropic, but linear dependency of the displacement $\Delta\mathbf{r}$ on the gate voltage. Here, ΔB_i has the meaning of a field difference between the static position of the electron and its maximum displacement induced by the driving voltage. Since $\Delta B_z \ll B_z$ for all relevant cases, we approximate $\Delta B_z \approx 0$. By rotating the coordinate system around the z-axis, such that $\Delta\tilde{B}_x = \sqrt{\Delta B_x^2 + \Delta B_y^2} \equiv 2B_0$ and $\Delta\tilde{B}_y = 0$, we simplify the complete magnetic field to

$$\mathbf{B}(t) = \mathbf{B}_{\mathrm{ext}} + \mathbf{B}_{\mathrm{ac}}(t) = B_z \begin{pmatrix} 0 \\ 0 \\ 1 \end{pmatrix} + 2B_0 \begin{pmatrix} \cos wt \\ 0 \\ 0 \end{pmatrix}.$$

We also shifted the time by $\pi/2\omega$ for a stronger resemblance with (A.7). We then write the Hamiltonian H' as an analogue to (A.8),

$$\begin{aligned} H'(t) &= \omega_z s_z + 2\omega_0 \cos(\omega t) s_x = \omega_z s_z + \omega_0 \left[(\cos(\omega t) s_x + \sin(\omega t) s_y) + (\cos(\omega t) s_x - \sin(\omega t) s_y) \right] \\ &= H(t) + \omega_0 (\cos(\omega t) s_x - \sin(\omega t) s_y) \\ &= H(t) + H_{\mathrm{osc}}(t). \end{aligned}$$

We retrieved the Hamiltonian for the ideal driving $H(t)$ (A.14) and a second term $H_{\mathrm{osc}}(t)$. Finally, we transform it to the rotating frame as before, and find

$$\tilde{H}'(t) = \tilde{H} + R(t) H_{\mathrm{osc}}(t) R^{\dagger}(t) \doteq \frac{\hbar}{2} \begin{pmatrix} \Delta\omega & \omega_0 \\ \omega_0 & -\Delta\omega \end{pmatrix} + \frac{\hbar}{2} \begin{pmatrix} 0 & \omega_0 \exp(i2\omega t) \\ \omega_0 \exp(-i2\omega t) & 0 \end{pmatrix}.$$

For a sizeable ω, especially near the Rabi resonance where $\omega \sim \omega_z$, $\tilde{H}_{\mathrm{osc}}(t)$ oscillates so fast that its impact on the overall dynamics is negligible. By dropping this term, we perform a rotating wave approximation [85, p. 99] and obtain the same solution for the remaining Hamiltonian as before for an ideal driving.

B Process parameters

B.1 Sample *Ziege*

Used in chapters 5, 6, 8. See ref. [26, pp. 49ff.].

B.1.1 Material

Wafer: D080311D grown by D. Schuh and W. Wegscheider at the University of Regensburg.

Material	Thickness (nm)
GaAs	5
$Al_{0.3}Ga_{0.7}As$	40
Si	δ doping
$Al_{0.3}Ga_{0.7}As$	40
GaAs	500
GaAs /AlGaAs superlattice	3/7 (x 100)
GaAs	500

B.1.2 Mesa

- Shipley 1813 photoresist 3 s @ 800 rpm, 30 s @ 5000 rpm, bake 90 s @ 115 °C
- Exposure: 22 s, $\lambda = 405$ nm (Karl Suss MJB3 mask aligner)
- Development: Shipley Microposit 351 B (diluted with purified H_2O 1:3) for 30 s
- Etching: H_2O:H_2SO_4:H_2O_2 (100:3:1) for 95 s @ 0.95 nm/s

B.1.3 Ohmic contacts

- MicroChem LOR 3B lift-off photoresist 3 s @ 800 rpm, 30 s @ 4000 rpm, bake 90 s @ 150 °C
- Shipley 1813 photoresist 3 s @ 800 rpm, 30 s @ 5000 rpm, bake 90 s @ 115 °C
- Exposure: 22 s, $\lambda = 405$ nm (Karl Suss MJB3 mask aligner)
- Development: Shipley Microposit 351 B (diluted with purified H_2O 1:3) for 30 s
- Metal deposition: 60 nm AuGe, 10 nm Ni, 60 nm AuGe
- Lift-off: 45 min DMSO @ 80 °C, afterwards rinsing with Acetone and isopropyl alcohol
- Annealing: 5 min @ 110 °C, 4 min @ 360 °C, 1.5 min @ 420 °C

B.1.4 Coarse gates

- MicroChem LOR 3B lift-off photoresist 3 s @ 800 rpm, 30 s @ 4000 rpm, bake 90 s @ 150 °C
- Shipley 1813 photoresist 1 s @ 800 rpm, 30 s @ 5000 rpm, bake 90 s @ 115 °C
- Exposure: 22 s, $\lambda = 405$ nm (Karl Suss MJB3 mask aligner)
- Development: Shipley Microposit 351 B (diluted with purified H_2O 1:3) for 30 s
- Cleaning: 40 s O_2 plasma etching @ 200 W (GigaEtch)
- Metal deposition: 10 nm Ti, 90 nm Au
- Lift-off: 45 min DMSO @ 80 °C, afterwards rinsing with Acetone and isopropyl alcohol

B.1.5 Nano magnets

- PMMA 950 K, 4% in MIBK, 1 s @ 800 rpm, 30 s @ 5000 rpm, bake 90 s @ 170 °C
- Exposure: 5 kV, 10 µm aperture, 90 µC/cm^2 (narrow magnet), 75 µC/cm^2 (larger magnet), 160 µm × 160 µm write field
- Development: MIBK (diluted with isopropyl alcohol 1:3) for 40 s
- Metal deposition: 50 nm Co (thermal evaporation, current 135 A → 1 Å/s growth rate; around 10 pauses of 30 s during evaporation process), 5 nm Au
- Lift-off: Acetone (several hours) followed by 1 min ultrasonic bath on low power to remove residues

B.1.6 Nano meter sized gates

- PMMA 950 K, 4% in MIBK, 1 s @ 800 rpm, 30 s @ 5000 rpm, bake 90 s @ 170 °C
- Exposure: 5 kV, 10 µm aperture, 100 µC/cm^2 (196 µC/cm^2 at the tips), 160 µm × 160 µm write field
- Development: MIBK (diluted with isopropyl alcohol 1:3) for 45 s
- Metal deposition: 5 nm Ti, 35 nm Au
- Lift-off: Acetone (several hours)

B.2 Sample *Barney*

Used in chapter 7. Also see ref. [8, pp. 121ff.].

B.2.1 Material

Wafer: D080311D grown by D. Schuh and W. Wegscheider at the University of Regensburg. See B.1.1 for further details.

B.2.2 Mesa

- Shipley 1813 photoresist 1 s @ 800 rpm, 30 s @ 6000 rpm, bake 90 s @ 115 °C
- Exposure: 25 s, $\lambda = 405$ nm (Karl Suss MJB3 mask aligner)
- Development: Shipley Microposit 351 B (diluted with purified H_2O 1:3) for 25 s
- Etching: H_2O:H_2SO_4:H_2O_2 (100:3:1) for 80 s @ 1.25 nm/s

B.2.3 Ohmic contacts

- Shipley 1813 photoresist 1 s @ 800 rpm, 30 s @ 4500 rpm, bake 90 s @ 115 °C
- Exposure: 25 s, $\lambda = 405$ nm (Karl Suss MJB3 mask aligner)
- Development: Shipley Microposit 351 B (diluted with purified H_2O 1:3) for 25 s
- Metal deposition: 60 nm AuGe, 10 nm Ni, 60 nm AuGe
- Annealing: 5 min @ 110 °C, 4 min @ 360 °C, 1.5 min @ 420 °C

B.2.4 Coarse gates

- Shipley 1813 photoresist 1 s @ 800 rpm, 30 s @ 6000 rpm, bake 90 s @ 115 °C
- Exposure: 23 s, $\lambda = 405$ nm (Karl Suss MJB3 mask aligner)
- Development: Shipley Microposit 351 B (diluted with purified H_2O 1:3) for 15 s
- Metal deposition: 5 nm Ti, 90 nm Au

B.2.5 Nano meter sized gates

- PMMA 500 K, 4% in MIBK, 1 s @ 800 rpm, 30 s @ 5000 rpm, bake 90 s @ 170 °C
- Exposure: 5 kV, 10 µm aperture, 45 µC/cm^2, 160 µm × 160 µm write field
- Development: MIBK (diluted with isopropyl alcohol 1:3) for 25 s
- Metal deposition: 5 nm Ti, 35 nm Au

B.2.6 Nano magnet

- PMMA 150 K, 4% in MIBK, 1 s @ 800 rpm, 30 s @ 4000 rpm, bake 90 s @ 170 °C
- PMMA 500 K, 4% in MIBK, 1 s @ 800 rpm, 30 s @ 5000 rpm, bake 90 s @ 170 °C
- Exposure: 5 kV, 10 µm aperture, 45 µC/cm^2, 160 µm × 160 µm write field
- Development: MIBK (diluted with isopropyl alcohol 1:3) for 25 s
- Metal deposition: 25 nm Co, 2 min pause, 25 nm Co, 5 nm Au (e-beam evaporation with water cooled shutter)

C Setup parameters for wiring and filtering

Table C.1: Resistances and capacitances in the lines optimized for gate voltages. The bias tee is present for four of the 16 lines.

Component	Resistance (Ω)	Capacitance to ground (F)
Double shielded coax	1	100 p
Filter box	100 k	1 μ
Double shielded coax	1	100 p
Cu/NbTi loom	<10	300 p
Low temperature filtering	330 k	230 n
(Bias tee)	(2.2 k)	
Σ	430 (432) k	1.2 μ

Table C.2: Resistances and capacitances in the lines optimized for current flow.

Component	Resistance (Ω)	Capacitance to ground (F)
Double shielded coax	1	100 p
Filter box	2.2 k	2.36 n
Double shielded coax	1	100 p
Cu coax/Janis SS coax	200	250 p
Low temperature filtering	1 k	500 p
Σ	3.4 k	3.31 n

D List of publications

This section provides a list with the publications used in this thesis and acknowledges the contribution of each author.

- Chapter 5: Forster, F. *et al. Phys. Rev. B. 91*. 195417 (2015)

  F. Forster carried out the experiment, analysed the data and prepared the data visualization for publication. M. Mühlbacher fabricated and tested the sample. D. Schuh and W. Wegscheider provided the wafer material. F. Forster, and S. Ludwig wrote the manuscript. S. Ludwig supervised the project.

- Chapter 6: Forster, F. *et al. Phys. Rev. B. 92*. 245303 (2015)

  F. Forster carried out the experiment, analysed the data and prepared the data visualization for publication. M. Mühlbacher fabricated and tested the sample. D. Schuh and W. Wegscheider provided the wafer material. G. Giedke advised on the underlying theory. F. Forster, G. Giedke, and S. Ludwig wrote the manuscript. S. Ludwig supervised the project.

- Chapter 7: Forster, F. *et al. Phys. Rev. Lett. 112*. 116803 (2014)

  F. Forster and G. Petersen carried out the experiment and analysed the data. G. Petersen fabricated the sample. F. Forster prepared the data visualization for publication. S. Manus provided essential council regarding the rf measurement setup. P. Hänggi advised during the writing process. D. Schuh and W. Wegscheider provided the wafer material. S. Kohler developed the theory and calculated the interference patterns. F. Forster, S. Kohler, and S. Ludwig wrote the manuscript. S. Ludwig supervised the project.

- Chapter 8: Forster, F. *et al. Phys. Rev. B. 92*. 245422 (2015)

  F. Forster carried out the experiment, analysed the data and prepared the data visualization for publication. M. Mühlbacher fabricated the sample. R. Blattmann advised on the experimental parameters and helped developing the theory. D. Schuh and W. Wegscheider provided the wafer material. F. Forster, S. Ludwig, and S. Kohler wrote the manuscript. S. Ludwig supervised the experiment. S. Kohler developed the main theory, calculated the interference patterns and supervised the project.

Bibliography

1. Feynman, R. P., Leighton, R. B. & Sands, M. L. *The Feynman lectures on physics* (pub-AW, pub-AW:adr, 1963–1965).
2. Van Melsen, A. *From Atomos to Atom: The History of the Concept Atom* ISBN: 9780486495842 (Dover Publications, 1953).
3. Van der Wiel, W. G. *et al. Rev. Mod. Phys. 75*. 1–22 (2002).
4. Hanson, R., Kouwenhoven, L. P., Petta, J. R., Tarucha, S. & Vandersypen, L. M. K. *Rev. Mod. Phys. 79*. 1217–1265 (2007).
5. Urbaszek, B. *et al. Rev. Mod. Phys. 85*. 79–133 (2013).
6. DiVincenzo, D. P. *Science. 270*. 255–261 (1995).
7. Loss, D. & DiVincenzo, D. P. *Phys. Rev. A. 57*. 120–126 (1998).
8. Petersen, G. *Decoherence mechanisms of laterally defined double quantum dot qubits coupled to the environment* PhD thesis (Ludwig-Maximilians-Universität München, 2013).
9. Bluhm, H., Foletti, S., Mahalu, D., Umansky, V. & Yacoby, A. *Phys. Rev. Lett. 105*. 216803 (2010).
10. Shevchenko, S., Ashhab, S. & Nori, F. *Physics Reports. 492*. 1 –30 (2010).
11. Ashoori, R. C. *Nature. 379*. 413–419 (1996).
12. Kouwenhoven, L. P., Austing, D. G. & Tarucha, S. *Rep. Prog. Phys. 64*. 701 (2001).
13. Taubert, D. *Electronic transport experiments on low-dimensional nanostructures at non-equilibrium conditions* PhD thesis (Ludwig-Maximilians-Universität München, 2011).
14. Taubert, D., Schuh, D., Wegscheider, W. & Ludwig, S. *Review of Scientific Instruments. 82*. (2011).
15. Cohen-Tannoudji, C., Diu, B. & Laloë, F. *Quantum mechanics* ISBN: 9780471164333 (Wiley, 1977).
16. Taylor, J. M. *et al. Phys. Rev. B. 76*. (2007).
17. Koppens, F. H. L. *et al. Science. 309*. 1346–1350 (2005).
18. De Franceschi, S. *et al. Phys. Rev. Lett. 86*. 878–881 (2001).
19. Petta, J. R. *et al. Science. 309*. 2180–2184 (2005).
20. Petta, J. R., Lu, H. & Gossard, A. C. *Science. 327*. 669–672 (2010).
21. Bluhm, H. *et al. Nature Physics. 7*. 109–113 (2011).
22. Maune B. M. *et al. Nature. 481*. 344–347 (2012).
23. Forster, F. *et al. Phys. Rev. Lett. 112*. 116803 (2014).
24. Adachi, S. *Journal of Applied Physics. 58*. R1–R29 (1985).
25. Harbusch, D. *Hochfrequente Anregung einzelner Elektronen und Rückkopplungen eines Ladungsdetektors in gekoppelten Quantenpunkten* PhD thesis (Ludwig-Maximilians-Universität München, 2011).
26. Mühlbacher, M. *Lateral definierte Spinqubits mit einem Paar von on-chip Nanomagneten* MA thesis (Ludwig-Maximilians-Universität München, 2014).

27. Yoneda, J. *et al. Phys. Rev. Lett. 113*. 267601 (2014).
28. Engel-Herbert, R. & Hesjedal, T. *Journal of Applied Physics. 97*. 1–4 (2005).
29. Donahue, M. & Porter, D. *OOMMF User's Guide, Version 1.0* Interagency Report NISTIR 6376 (National Institute of Standards and Technology, Gaithersburg, MD, 1999).
30. Petersen, G. *et al. Phys. Rev. Lett. 110*. 177602 (2013).
31. Pobell, F. *Matter and Methods at Low Temperatures* (Springer, 1992).
32. Forster, F., Mühlbacher, M., Schuh, D., Wegscheider, W. & Ludwig, S. *Phys. Rev. B. 91*. 195417 (2015).
33. Koppens F. H. L. *et al. Nature. 442*. 766–771 (2006).
34. Nowack, K. C., Koppens, F. H. L., Nazarov, Y. V. & Vandersypen, L. M. K. *Science. 318*. 1430–1433 (2007).
35. Laird, E. A. *et al. Phys. Rev. Lett. 99*. 246601 (2007).
36. Pioro-Ladriere M. *et al. Nat Phys. 4*. 776–779 (2008).
37. Forster, F. *et al. Phys. Rev. B. 92*. 245303 (2015).
38. Abragam, A. *Principles of Nuclear Magnetism* (Oxford University Press, 1961).
39. Deng, C. & Hu, X. *Phys. Rev. B. 72*. 165333 (2005).
40. Schuetz, M. J. A., Kessler, E. M., Cirac, J. I. & Giedke, G. *Phys. Rev. B. 86*. 085322 (2012).
41. Kessler, E. M., Yelin, S., Lukin, M. D., Cirac, J. I. & Giedke, G. *Phys. Rev. Lett. 104*. 143601 (2010).
42. Rudner, M. S. & Levitov, L. S. *Phys. Rev. B. 82*. 155418 (2010).
43. Overhauser, A. W. *Physical Review. 92*. 411–415 (1953).
44. Khaetskii, A. V., Loss, D. & Glazman, L. *Phys. Rev. Lett. 88*. (2002).
45. Merkulov, I. A., Efros, A. L. & Rosen, M. *Phys. Rev. B. 65*. 205309 (2002).
46. Paget, D., Lampel, G., Sapoval, B. & Safarov, V. I. *Phys. Rev. B. 15*. 5780–5796 (1977).
47. Coish, W. A. & Baugh, J. *physica status solidi (b). 246*. 2203–2215 (2009).
48. Pfund, A., Shorubalko, I., Ensslin, K. & Leturcq, R. *Phys. Rev. Lett. 99*. (2007).
49. Kobayashi, T., Hitachi, K., Sasaki, S. & Muraki, K. *Phys. Rev. Lett. 107*. 216802 (2011).
50. López-Monís, C., Iñarrea, J. & Platero, G. *New Journal of Physics. 13*. 053010 (2011).
51. Rudner, M. S., Koppens, F. H. L., Folk, J. A., Vandersypen, L. M. K. & Levitov, L. S. *Phys. Rev. B. 84*. 075339 (2011).
52. Vink, I. T. *et al. Nature Physics. 5*. 764–768 (2009).
53. Rudner, M. S., Vandersypen, L. M. K., Vuletic, V. & Levitov, L. S. *Phys. Rev. Lett. 107*. 206806 (2011).
54. Danon, J. *et al. Phys. Rev. Lett. 103*. 046601 (2009).
55. Oliver, W. D. *et al. Science. 310*. 1653–1657 (2005).
56. Sillanpää, M., Lehtinen, T., Paila, A., Makhlin, Y. & Hakonen, P. *Phys. Rev. Lett. 96*. 187002 (2006).
57. Wilson, C. M. *et al. Phys. Rev. Lett. 98*. 257003 (2007).
58. Berns, D. M. *et al. Nature. 455*. 51–57 (2008).
59. Landau, L. D. *Phys. Z. Sowjetunion. 2*. 46 (1932).
60. Zener, C. *Proceedings of the Royal Society of London A: Mathematical, Physical and Engineering Sciences. 137*. 696–702 (1932).
61. Stückelberg, E. C. G. *Helvetica Physica Acta. 5*. 369 (1932).

62. Majorana, E. *Nuovo Cimento. 9*. 43–50 (1932).
63. Damski, B. & Zurek, W. H. *Phys. Rev. A. 73*. 063405 (2006).
64. Wubs, M., Saito, K., Kohler, S., Kayanuma, Y. & Hänggi, P. *New Journal of Physics. 7*. 218 (2005).
65. Mullen, K., Ben-Jacob, E., Gefen, Y. & Schuss, Z. *Phys. Rev. Lett. 62*. 2543–2546 (1989).
66. Zenesini, A. *et al. Phys. Rev. Lett. 103*. 090403 (2009).
67. Garraway, B. M. & Vitanov, N. V. *Phys. Rev. A. 55*. 4418–4432 (1997).
68. Marquardt, F. & Püttmann, A. *Introduction to dissipation and decoherence in quantum systems* 2008.
69. Wang, X. R., Zheng, Y. S. & Yin, S. *Phys. Rev. B. 72*. 121303 (2005).
70. Meiboom, S. & Gill, D. *Review of Scientific Instruments. 29*. 688–691 (1958).
71. Hayashi, T., Fujisawa, T., Cheong, H. D., Jeong, Y. H. & Hirayama, Y. *Phys. Rev. Lett. 91*. 226804 (2003).
72. Petersson, K. D., Petta, J. R., Lu, H. & Gossard, A. C. *Phys. Rev. Lett. 105*. 246804 (2010).
73. Granger, G. *et al. Nat Phys. 8*. 522–527 (2012).
74. Fujisawa, T. & Hirayama, Y. *Applied Physics Letters. 77*. 543–545 (2000).
75. Leggett, A. J. *et al. Rev. Mod. Phys. 59*. 1–85 (1987).
76. Rudner, M. S. *et al. Phys. Rev. Lett. 101*. 190502 (2008).
77. Forster, F. *et al. Phys. Rev. B. 92*. 245422 (2015).
78. Shin, Y. S. *et al. Phys. Rev. Lett. 104*. 046802 (2010).
79. Kawakami, E. *et al. Nat Nano. 9*. 666–670 (2014).
80. Obata, T. *et al. Phys. Rev. B. 81*. 085317 (2010).
81. Neumann, R. & Schreiber, L. R. *Journal of Applied Physics. 117*. (2015).
82. Yao, W., Liu, R. B. & Sham, L. J. *Phys. Rev. B. 74*. 195301 (2006).
83. Fujisawa, T., Hayashi, T., Cheong, H., Jeong, Y. & Hirayama, Y. *Physica E: Low-dimensional Systems and Nanostructures. 21*. 1046 –1052 (2004).
84. Felsager, B. *Geometry, Particles, and Fields* ISBN: 9781461206316 (Springer New York, 2012).
85. Kraus, R., Espy, M., Magnelind, P. & Volegov, P. *Ultra-Low Field Nuclear Magnetic Resonance: A New MRI Regime* ISBN: 9780199347889 (Oxford University Press, 2014).